IN-SITU AND *IN-OPERANDO* TECHNIQUES FOR MATERIAL CHARACTERIZATIONS DURING BATTERY OPERATION, 2nd Edition

EDITED BY: Verónica Palomares and Neeraj Sharma

PUBLISHED IN: Frontiers in Energy Research

frontiers Research Topics

ISSN 1664-8714
ISBN 978-2-8325-2641-5
DOI 10.3389/978-2-8325-2641-5

About Frontiers

Frontiers is more than just an open-access publisher of scholarly articles: it is a pioneering approach to the world of academia, radically improving the way scholarly research is managed. The grand vision of Frontiers is a world where all people have an equal opportunity to seek, share and generate knowledge. Frontiers provides immediate and permanent online open access to all its publications, but this alone is not enough to realize our grand goals.

Frontiers Journal Series

The Frontiers Journal Series is a multi-tier and interdisciplinary set of open-access, online journals, promising a paradigm shift from the current review, selection and dissemination processes in academic publishing. All Frontiers journals are driven by researchers for researchers; therefore, they constitute a service to the scholarly community. At the same time, the Frontiers Journal Series operates on a revolutionary invention, the tiered publishing system, initially addressing specific communities of scholars, and gradually climbing up to broader public understanding, thus serving the interests of the lay society, too.

Dedication to Quality

Each Frontiers article is a landmark of the highest quality, thanks to genuinely collaborative interactions between authors and review editors, who include some of the world's best academicians. Research must be certified by peers before entering a stream of knowledge that may eventually reach the public - and shape society; therefore, Frontiers only applies the most rigorous and unbiased reviews.
Frontiers revolutionizes research publishing by freely delivering the most outstanding research, evaluated with no bias from both the academic and social point of view. By applying the most advanced information technologies, Frontiers is catapulting scholarly publishing into a new generation.

What are Frontiers Research Topics?

Frontiers Research Topics are very popular trademarks of the Frontiers Journals Series: they are collections of at least ten articles, all centered on a particular subject. With their unique mix of varied contributions from Original Research to Review Articles, Frontiers Research Topics unify the most influential researchers, the latest key findings and historical advances in a hot research area! Find out more on how to host your own Frontiers Research Topic or contribute to one as an author by contacting the Frontiers Editorial Office: researchtopics@frontiersin.org

IN-SITU AND *IN-OPERANDO* TECHNIQUES FOR MATERIAL CHARACTERIZATIONS DURING BATTERY OPERATION, 2nd Edition

Topic Editors:
Verónica Palomares, University of the Basque Country UPV/EHU, Spain
Neeraj Sharma, University of New South Wales, Australia

This book aims to illustrate the state of the art for *in operando* techniques and the results from these techniques applied to battery research. Fundamental understanding of the battery materials composition and structure at different length scales makes possible to predict or understand their properties and propose changes to improve their electrochemical behavior. In this sense, the use of *in-situ* or *in operando* characterization techniques provides a unique way of understanding materials performance or evolution during battery operation.

The contents of this eBook comprise different *in situ* techniques used to study Li-ion electrode battery materials or full Li-ion cells (Neutron depth profiling, Transmission X-Ray Microscopy, Raman Spectroscopy, Neutron Diffraction, etc.). The scope of this Research Topic also covers *in operando* characterization methods applied to other energy storage systems, such as high temperature thermal systems or novel air cathode batteries. Papers report new findings as well as discussions about specific cell designs for various techniques.

Publisher's note: In this 2nd edition, the following article has been added: Gustafsson O, Schökel A and Brant WR (2022) Mind the miscibility gap: Cation mixing and current density driven non-equilibrium phase transformations in spinel cathode materials. *Front. Energy Res*. 10:1056260. doi: 10.3389/fenrg.2022.1056260

Citation: Palomares, V., Sharma, N., eds. (2023). *In-situ* and *In-operando* Techniques for Material Characterizations during Battery Operation, 2nd Edition. Lausanne: Frontiers Media. doi: 10.3389/978-2-8325-2641-5

Table of Contents

SECTION 3
OTHER BATTERY SYSTEMS

frontiers in Energy Research

EDITORIAL
published: 15 February 2019
doi: 10.3389/fenrg.2019.00010

Editorial: *In-situ* and *In-operando* Techniques for Material Characterizations During Battery Operation

Verónica Palomares[1,2]* *and Neeraj Sharma*[3]

[1] Inorganic Chemistry Department, University of the Basque Country/Euskal Herriko Unibertsitatea UPV/EHU, Bilbao, Spain, [2] BCMaterials, Bld. Martina Casiano, UPV/EHU Science Park, Leioa, Spain, [3] School of Chemistry, University of New South Wales, Sydney, NSW, Australia

Keywords: *operando* and *in situ* measurements, battery, materials characterization techniques, electrochemistry, structure-property relationship

Editorial on the Research Topic

In-situ and *In-operando* Techniques for Material Characterizations During Battery Operation

Batteries are prevalent in society and there is a need to develop better batteries to meet future demands. To build better batteries it is crucial to understand how components within real devices function and interact during use. This provides significantly more insight into function compared to isolated and idealized laboratory conditions. Electrochemical cells, whether half cells or full cells can be developed at various scales, depending on the desired application or research question. Electrochemical methods provide insight on the reactions and the potentials at which they happen, energy storage density, retention over cycling, rate capability to name a few parameters. They can be used to derive the impedance of the cell and back calculated to investigate interfacial and charge resistance phenomena. These methods are critical in understanding the electrochemistry of the batteries and are being widely used in research and development, however they only provide a narrow view of the materials response and function in the device. If the electrochemistry can be coupled with another analytical technique, such as spectroscopy, imaging, or diffraction while the device is operating, the insight gained into materials function is enhanced. The additional analytical techniques can be used to understand the electrochemistry with a totally different perspective, for example an atomic scale perspective on electrochemistry.

It is this ability to gain unparalleled insight into materials function within devices that have led researchers to push the boundaries of *in situ* and *operando* methods. These methods couple the electrochemical measurements or stimuli with another analytical technique(s). They often gain both electrochemical and structural or spectroscopic data which can be directly correlated. Thus providing two or more views on the function of the material and increasing the parameter space that can be measured in one experiment and correlated. These experiments by definition need to be conducted in an electrochemical cell environment (to run electrochemistry) while another measurement is occurring, with say X-rays or laser light impinging on the electrode of interest to through the entire device. Ideally full cells or commercially equivalent batteries should be used, however these in most cases are perfected for electrochemistry but not very well suited for other analytical methods. Therefore, specially designed electrochemical cells are often used, where the cell is optimized to achieve the best from both worlds, electrochemistry and the other analytical technique. This typically requires compromises, reducing the electrochemical performance to obtain better signal from the analytical method or vice versa. However, researchers are constantly trying to minimize the changes and maximize both the electrochemical performance and signal observed in the analytical method,

OPEN ACCESS

Edited by:
Soorathep Kheawhom, Chulalongkorn University, Thailand

Reviewed by:
Ryan Corpuz, Mindanao State University, Iligan Institute of Technology, Philippines
Maiyalagan Thandavarayan, University of Texas at Austin, United States

***Correspondence:**
Verónica Palomares
veronica.palomares@ehu.eus

Specialty section:
This article was submitted to Electrochemical Energy Conversion and Storage, a section of the journal Frontiers in Energy Research

Received: *14 January 2019*
Accepted: *28 January 2019*
Published: *15 February 2019*

Citation:
Palomares V and Sharma N (2019) Editorial: In-situ and In-operando Techniques for Material Characterizations During Battery Operation. Front. Energy Res. 7:10. doi: 10.3389/fenrg.2019.00010

thereby obtaining the best of both worlds. It is interesting to note, how routine such *in situ* and *operando* measurements are becoming for techniques like *in situ* X-ray diffraction, Raman spectroscopy, or FTIR as examples. With such works catalyzing significant development in relatively newer methods such as *in situ* electron microscopy.

The field is truly very exciting, new developments, new methods, combining of techniques, and gaining amazing insight into materials function in devices.

This selection of articles explores a variety of *in situ* characterization techniques, such as *operando* X-ray or neutron powder diffraction, Raman spectroscopy, neutron depth profiling, or *in situ* transmission X-ray microscopy. These techniques are analyzed from different approaches, either as original research work, review, or perspective article and cover very different battery systems, from more classical Li-ion half and full cell batteries, all solid state thin film batteries, or high temperature thermal batteries to newer systems such as air cathode batteries.

We hope that you enjoy these articles and appreciate the great work these researchers and other researchers engaged in *in situ* and *operando* methods are doing both from method development to a materials function point of view. We also thank the authors and reviewers for their contributions to this work.

AUTHOR CONTRIBUTIONS

All authors listed have made a substantial, direct and intellectual contribution to the work, and approved it for publication.

Conflict of Interest Statement: The authors declare that the research was conducted in the absence of any commercial or financial relationships that could be construed as a potential conflict of interest.

frontiers in Energy Research

ORIGINAL RESEARCH
published: 03 July 2018
doi: 10.3389/fenrg.2018.00062

Operando Neutron Depth Profiling to Determine the Spatial Distribution of Li in Li-ion Batteries

Tomas W. Verhallen[1], *Shasha Lv*[2] *and Marnix Wagemaker*[1]*

[1] Department of Radiation Science and Technology, Delft University of Technology, Delft, Netherlands, [2] The State Key Laboratory of New Ceramics and Fine Processing, School of Materials Science and Engineering, Tsinghua University, Beijing, China

Neutron Depth Profiling (NDP) allows determination of the spatial distribution of specific isotopes, via neutron capture reactions. In a capture reaction charged particles with fixed kinetic energy are formed, where their energy loss through the material of interest can be used to provide the depth of the original isotope. As lithium-6 has a relatively large probability for such a capture reaction, it can be used by battery scientists to study the lithium concentration in the electrodes even during battery operation. The selective measurement of the ^{6}Li isotope makes it a direct and sensitive technique, whereas the penetrative character of the neutrons allows practical battery pouch cells to be studied. Using NDP lithium diffusion and reaction rates can be studied operando as a function of depth, opening a large range of opportunities including the study of alloying reactions, metal plating, and (de) intercalation in insertion hosts. In the study of high rate cycling of intercalation materials the relatively low Li density challenges counting statistics while the limited change in electrode density due to the Li-ion insertion and extraction allows straightforward determination of the Li density as a function of electrode depth. If an electrode can be (dis)charged reversibly, data can be acquired and accumulated over multiple cycles to increase the time resolution. For Li metal plating and alloying reactions, the large lithium density allows good time resolution, however the large change of the electrode composition and density makes extracting the Li-density as a function of depth more challenging. Here an effective method is presented, using calibration measurements of the individual components, based on which the ratio of the components as a function of depth can be determined as well as the total Li-density. The same principles can be applied to insertion host materials, where the differences in density due to electrolyte infiltration yield the electrode porosity as a function of depth. This is of particular importance for battery electrodes where porosity has a direct influence on the energy density and charge transport.

Keywords: lithium-ion batteries, operando techniques, neutron depth profiling, electrode porosity, lithium concentration, spatial distribution, high rate materials, lithium metal plating

OPEN ACCESS

Edited by:
Neeraj Sharma,
University of New South Wales, Australia

Reviewed by:
William Robert Brant,
Department of Chemistry, Uppsala University, Sweden
Mogens Christensen,
Aarhus University, Denmark

***Correspondence:**
Marnix Wagemaker
m.wagemaker@tudelft.nl

Specialty section:
This article was submitted to Energy Storage, a section of the journal Frontiers in Energy Research

Received: *04 April 2018*
Accepted: *12 June 2018*
Published: *03 July 2018*

Citation:
Verhallen TW, Lv S and Wagemaker M (2018) Operando Neutron Depth Profiling to Determine the Spatial Distribution of Li in Li-ion Batteries. Front. Energy Res. 6:62. doi: 10.3389/fenrg.2018.00062

INTRODUCTION

Neutron Depth Profiling (NDP), developed in 1972 (Ziegler et al., 1972), allows the detection of a small concentration of a certain isotope as function of sample depth, via neutron capture reactions (Downing et al., 1993). Applications range from boron impurity determination in silicon to boron nitrogen ratios in coatings (Ziegler et al., 1972; Downing et al., 1993; Ünlü et al., 1999). Whitney et al. (2009), first suggested using the ^{6}Li capture reaction for NDP on lithium ion battery systems. The technique offers the unique ability to quantitatively measure lithium concentrations, as function of depth, independent of oxidation state, during battery cycling (Oudenhoven et al., 2011; Wang et al., 2014; Harks et al., 2015; Liu and Co, 2016). Techniques allowing direct, non-invasive lithium detection operando are limited, as a result NDP was quickly adopted by a number of research groups in to order to study problems such as degradation (Nagpure et al., 2011) and charge transport limitations (Zhang et al., 2015). In the coming years the technique will become even more effective with the interest in light weight, high capacity anodes (Zuo et al., 2017), and cathodes, facilitating NDP measurements and the development of dedicated Li-battery setups (Çetiner et al., 2008; Tomandl et al., 2017). However, interpretation of the results will be more challenging as the electrode properties are dynamic, expanding, and contracting under the influence of lithium content (Mohanty et al., 2013; Liu et al., 2015; Liu and Co, 2016)

NDP exploits the neutron capture reaction of the lithium-6 isotope, which is 7.5% abundant in natural lithium. Hence it measures ^{6}Li atoms only, regardless of their oxidation state, ensuring selectivity and low noise. The capture reaction is initiated by the absorption of a thermal neutron resulting in two charged particles with a well-defined energy: (Ziegler et al., 1972; Whitney et al., 2009).

$$^6Li + n_{thermal} \xrightarrow{yields} {}^3H^+ \left(2727.88\, keV\right) + He^{2+}\,(2055.12\, keV)$$

White beam thermal neutron fluxes at the Reactor Institute in Delft are in the order of 10^7 neutrons/ cm^2 /s at the NDP the sample position. The neutron capture cross section of lithium-6 is 940 barns (Kopecky, 1997) the absorption rate is one reaction per 10^{15} 6-lithium atoms per second. This ^{6}Li consumption rate is negligible making NDP a non-destructive technique. Moreover as a white beam is used, no neutron optics are necessary, making the technique one of the most compact and cheapest amongst available experimental neutron set-ups (Utsuro and Ignatovich, 2010; Wang et al., 2012). A major advantage of using neutrons is the fact that they have a large penetration depth in materials, allowing relatively simple sample environments (Wang et al., 2012).

A typical set-up is depicted in **Figure 1**, adapted from Zhang et al. (2015). A charged particle detector is placed at a well-defined distance, thereby decreasing the opening angle such that particles arrive almost perpendicular to the detector plane, implying that the ^{3}H and He particle trajectories make 90° with the sample plane. The detector measures the kinetic energy of the incoming helium and tritium particles, which has decreased because of interactions with the materials in the battery along their trajectory. The amount of material it encounters depends on the depth of the original Li; hence the energy loss is related to this depth. The energy loss of the ^{3}H and He particles, which depends on the composition and density of the battery electrode, is quantified by the stopping power. Therefore the stopping relates the measured energy loss to the depth position of Li. Using NDP a cross sectional averaged Li concentration profile is determined as a function of depth, the axis perpendicular to the sample surface (Whitney et al., 2009).

The stopping power depends on the density of charges, associated with the atoms, it is independent of the chemical nature of the surroundings, thus the stopping power of a mixture of materials is equal to the sum of volume ratio times the stopping power of the components (Ziegler, 1985; Ziegler et al., 2010):

$$S_t = \sum_{i=1}^{n} \nu_i \cdot S_i \tag{1}$$

Where S represents the stopping power, ν the volume fraction and i the different components, which in a Li-ion battery electrode would typically be carbon black, binder, electrolyte and active material. Accurate determination of the stopping power is paramount to achieve an accurate Li concentration profile and depth calibration. Electrons make up most of the matter volume and therefore the electron density dominates the stopping power, especially at high particle energies (Lindhard et al., 1963). At lower ^{3}H and He kinetic energies the type of bond of the electrons becomes relevant, where in the case of organic materials a correction factor of up to 20% is necessary to compensate for the decrease in electron energy with respect to the atomic state (Ziegler et al., 2010). Only at low particle kinetic energies do the atom cores start to contribute significantly to the stopping power (Wilson et al., 1977). As a consequence the stopping power is strongly dependent on the particle energy, being large for small kinetic energies and small for large kinetic energies. The consequence is that the depth resolution increases with increasing depth, assuming a constant energy resolution of the detector. This results in more counts per detector energy channel for larger energies and lower counting rates at lower energies, hence the standard error in the measurement is constant over the detector channels (Ziegler et al., 2010; Zhang et al., 2015). As the amount of detected particles is a function of energy accurate determination of the stopping power is necessary to achieve quantitative results from NDP, in addition to the geometric, background and detector corrections (Lindhard et al., 1963; Wilson et al., 1977; Ziegler, 1985; Maki et al., 1986; Ziegler et al., 2010).

Based on the well-defined kinetic energy of the ^{3}H and He particles after the capture reaction with ^{6}Li, see Equation (1), there is a maximum depth from which the ^{3}H and He particles can exit the sample, which depends on the stopping power of the sample. Due to the larger charge of the (Ziegler et al., 2010; Zhang et al., 2015) ^{4}He^{2+} particle as compared

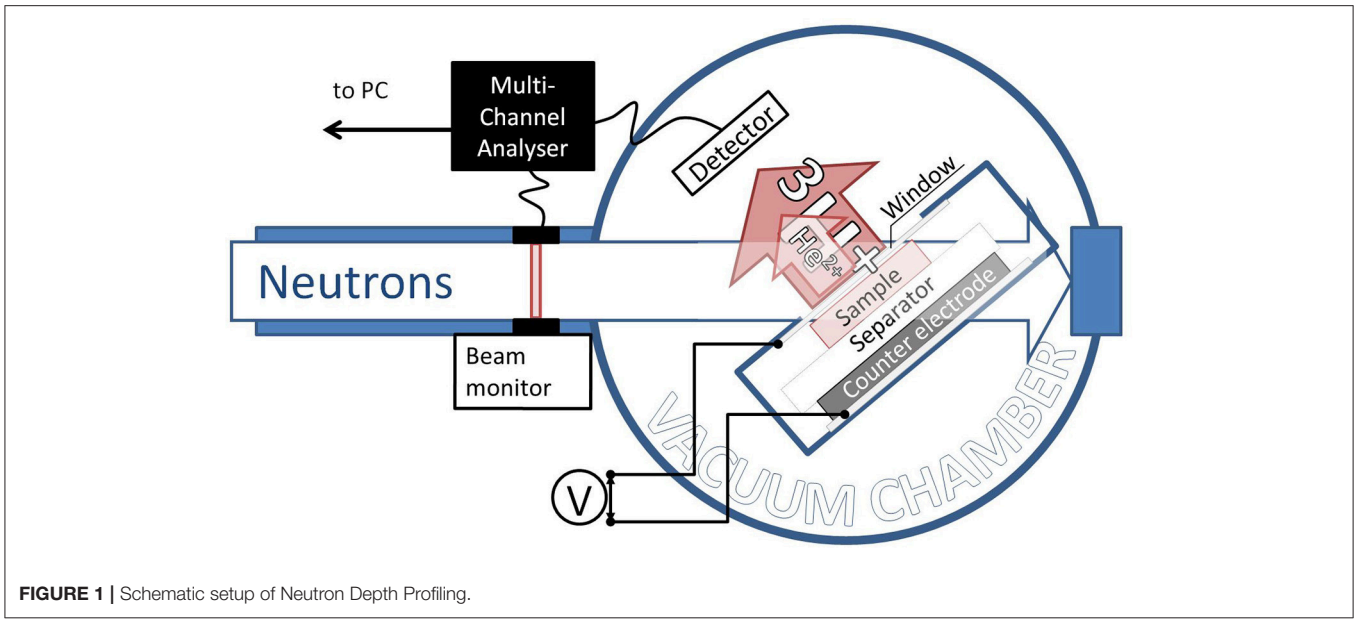

FIGURE 1 | Schematic setup of Neutron Depth Profiling.

to the $^{3}H^{+}$ particle, the stopping power for $^{4}He^{2+}$ is larger, and consequentially the escape depth for $^{4}He^{2+}$ is smaller and the depth resolution is larger, making $^{4}He^{2+}$suitable for the study of thin layers (Ziegler et al., 2010; Zhang et al., 2015). For energies smaller than the maximum energy of the $^{4}He^{2+}$ particle, 2056.12 keV, the measured ^{3}H and He signals overlap. Based on the ratio of the stopping power of the two particles, the two signals can be unraveled, methods for this can be found in Maki et al. (1986) and Liu et al. (2016). There is thus an intrinsic energy resolution associated with the material and particle through its stopping power, which through the detector resolution results in the depth resolution. For NDP the measurement time and the depth resolution are directly connected (Downing et al., 1993). Increasing the sample to detector distance, leads to higher resolution but fewer counts. However the relatively low beam intensity as compared to photon techniques is considered to be a common drawback of neutron techniques (Harks et al., 2015; Itkis et al., 2015). As a result, high resolution set-ups employ multiple detectors to improve counting statistics (Parikh et al., 1990; Mulligan et al., 2012). Another strategy to increase the count rate is to enrich the ^{6}Li contents of the materials under investigation (Downing et al., 1987; Oudenhoven et al., 2011) as the natural abundancy of the ^{6}Li isotope is only 7.5% (Hutchison, 1954). Hence replacing all ^{7}Li with ^{6}Li would increase count rates by a factor of 13.

The typical NDP operating conditions have implications for the operando/*in situ* battery research. An important implication of the geometrical resolution is that the detector is typically positioned at several centimeteres from the sample. This requires the setup to be operated under vacuum conditions to avoid parasitic energy absorption of the ^{3}H and He particles by the air (Hutchison, 1954; Downing et al., 1987; Oudenhoven et al., 2011). The vacuum conditions of the setup is one of the major obstacles for batteries containing liquid electrolytes, (Nagpure et al., 2014; Zhang et al., 2015) as most electrolytes contain solvents with a large vapor pressure, the evaporation of which leads to contact loss between the electrodes and the electrolyte, severely hindering battery performance (Zhang et al., 2015; Liu et al., 2016). To solve this Nagpure et al., have designed an experimental setup employing low density gasses at atmospheric pressures (Nagpure et al., 2014). Another approach is to work near the electrolyte vapor pressure, typically around 0.1 bar, allowing the particles to reach the detector with an acceptable loss in kinetic energy. Regardless of the operando set-up, a window is required to protect the unstable materials and supply electrons to the active material under study. This window is as thin as possible, reducing kinetic energy losses, while thick enough to withstand any pressure differences. For most cathode materials, aluminum is a straightforward choice (Zhang et al., 2015), as it is used in industry and provides low density and reasonable strength. For most anodes however, aluminum is not an option, enforcing the use of a metal/kapton combination for strength, conductivity and low density and thus stopping power (Liu D. X. et al., 2014; Wang C. et al., 2017).

Despite these challenges the technique is welcomed by the battery field, which is readily explained by the limited amount of techniques that are able to quantify both the amount and position of Li. Being a light element, lithium is difficult to detect with X-rays, for which reason most photon techniques typically use the change in oxidation state of the heavier ions to observe lithium intercalation (Nonaka et al., 2006; Katayama et al., 2014) or changes in interatomic spacing upon lithium insertion or extraction (Ganapathy et al., 2014; Zhang et al., 2014). Neutrons probe atom cores and therefore favor detection of the lighter elements compared to X-rays (Itkis et al., 2015). Also the penetrative nature of

neutrons and selectivity of the technique allows for probing small lithium concentrations in realistic battery pouch and coin cell set-ups without the introduction of noise (Whitney et al., 2009; Zhang et al., 2015; Vasileiadis et al., 2018). Furthermore the technique provides a unique relation between bulk properties, such as lithium concentration, and local sub-micron, depth dependent effects such as Ohmic potential drop or electrolyte concentration gradients (Zhang et al., 2015; Liu et al., 2016).

Previous operando NDP work has revealed a wealth of information. Oudenhoven et al. (2011)who were one of the first groups to perform operando NDP on a lithium ion cell, performed *in situ* lithium metal plating from a $LiCoO_2$ cathode through a lipon solid electrolyte in a thin film system using the increased depth resolution of the $^4He^{2+}$ spectrum. Moreover by using different isotopes the authors demonstrated that lithium ion exchange between cathode and electrolyte is almost non-existent in the pristine cell, due lack of lithium vacancies (Oudenhoven et al., 2011). It is noteworthy that the change in stopping power are marginal for Li-ion insertion hosts, making quantitative analysis straightforward. The first operando study on a liquid electrolyte cell was performed by Liu D. X. et al. (2014), their cell consisted of a 12.5 micron thick Sn anode. Their data clearly shows the expansion of the anode material, however the changes in the stopping power were not considered by the authors as the associated error in depth would stay within 10%, which was deemed acceptable (Liu D. X. et al., 2014). In a later study, concerning the intercalation of lithium in $LiFePO_4$, these problems where avoided as the changes in stopping power and morphology are negligible (Zhang et al., 2015). However, as typical for the low Li-density insertion hosts, the time resolution is poor, 10–60 min for operando (dis)charging (Zhang et al., 2015; Liu et al., 2016). Enriching samples with Li-6 provides the opportunity to improve this, however it adds the complication of relaxation and homogenization effects if not all components are enriched (Oudenhoven et al., 2011). As shown recently,Li-metal plating is a process where full enrichment is achieved relatively easy (Lv et al., 2018). Furthermore, the intrinsically high lithium densities in these systems allow for a good time resolution, down to 60 s. However, for these systems the challenge is correctly assessing the large changes in morphology for the calculation of the stopping power (Bieker et al., 2015; Liu et al., 2015; Cheng et al., 2017; Lv et al., 2018; Zhang, 2018). Challenges for Li-metal anodes include excessive growth of the solid electrolyte interface (SEI) and loss of active material, hindering its practical application (Zhang, 2018; Zhang et al., 2018). NDP is an ideal tool to study these problems but an effective strategy for determining the stopping power in these evolving electrode microstructures is paramount to obtain quantitative results.

At present two challenges are addressed in the operando study of batteries using NDP, aiming to demonstrate the possibilities for operando battery research. Firstly, building up statistics by repeated cycling is demonstrated as approach to improve the time resolution, making it possible to study Li-transport at high cycling rates, most relevant for insertion host electrode materials. Secondly, for electrodes that display large changes in morphology upon cycling, including Li-air, Li-S, Li-metal, and alloying anodes, an approach for calculating the stopping power during operando experiments is demonstrated, making quantitative analysis possible (Wang et al., 2014; Kang et al., 2016; Asadi et al., 2018; Lv et al., 2018). Finally, the stopping power correction strategy brought forward makes it possible to determine the depth resolved porosity of electrodes, an important property for the charge transport in electrodes that is not straightforward by other techniques. By means of these examples the aim of the present work is to demonstrate the possibilities, measurement, and data analysis strategies relevant to operando NDP for Li-ion battery work.

METHODS

To illustrate the possibilities and stopping power strategies of operando NDP experiments three examples performed at the dedicated NDP beamline of the Reactor institute are reported and discussed. The set-up consists of an aluminum vacuum chamber where a Canberra PIPS detector is used to measure the energy of the emitted ^3H particles, as illustrated in **Figure 1**. All results are based on measurements on pouch cells (Gustafsson et al., 1992; Yu et al., 2006; Mohanty et al., 2013; Lv et al., 2018), also known as coffee bag cells (Singh et al., 2015), their flexible design allows the straightforward sealing of current collector window (Villevieille, 2015), as is also described in Zhang et al. (2014). Also pouch cell type constructions are common practice in industrial applications (Trask et al., 2014). Moreover reducing the amount of material is advisable as neutron activation can lead to samples emitting hazardous radiation. Pouch cells introduce negligible background by other isotopes as they consist from plastic coated aluminum foil.

The electrodes used are prepared by NMP based slurries cast onto 11 micron aluminum foil, in the first example a 90% $Li_4Ti_5O_{12}$ (Phostech), 3% SuperP carbon and 7% PVDF binder was used and in the third example, the double layer electrode with a first coating of 60% $LiFePO_4$ (Phostech) active material, 25% carbon species [of which 10% SuperP and 15% KS4 (Timcal)] and 15% PVDF binder and the second layer containing 80% of active material, 10% SuperP carbon and binder. The second layer was applied when the first was dry. Particle sizes of commercial powders are poorly defined, but XRD refinement showed an domain size of ∼140 nm for both the $LiFePO_4$ and the $Li_4Ti_5O_{12}$.(Singh et al., 2013a,b) In the second example bare 10 micron copper foil was used as current collector and window and ^{6}Li-enriched Li-metal foil was used as counter electrode. 1M $LiPF_6$ in EC/DMC (Sigma Aldrich) served as the electrolyte in all examples. By measuring around the electrolyte vapor pressure in the NDP setup, contact loss between the electrodes of the pouch cell, signified by an increase in the overpotential, is avoided. The stopping power increases with decreasing particle energy, as a consequence conversion between energy and depth yields a nonlinear depth axis and a concentration profile that needs to

be corrected in a subsequent step. A more direct method is to calculate the energy width (Equation 2.2) at a constant depth step (Equation 2.1) and then assign the corresponding counts (Equation 2.3) resulting in a linear depth axis and preserving the total counts.

$$dx = x_{n+1} - x_n \tag{2.1}$$

$$E_{n+1} = E_n - \frac{\partial E(E_n)}{\partial x} dx \tag{2.2}$$

$$C_n = \int_{E_n}^{E_{n+1}} C(E) dE \tag{2.3}$$

The step size, *dx*, is chosen, based on statistics and sample thickness. Depending on the stopping power the resolution for $^3H^+$ can be around 50 nm and even better for He^{2+}. However practical considerations such as counting rate and surface roughness generally compromise the resolution. A table containing stopping powers as a function of particle energy is obtained (Wang and Hong, 2007; Zhang et al., 2015; Liu and Co, 2016; Liu et al., 2016) using the open software package SRIM (Ziegler et al., 2010). Electrons associated in a molecular bond are delocalized and have significantly different binding energies. Hence to correct for materials with covalent bonds, such as the electrolyte, a compound correction factor is calculated (Ziegler et al., 2010). The resulting table shows the stopping power due to electrons as well as due to atom cores, the contributions are independent and can thus be summed, similar to mixtures. The approach for a two component system is similar to that described by Equations (2.1–2.3), the difference lies in an extra parameter ρ, used to define the ratio between the two components (electrolyte and Li metal for instance for Li-metal anodes);

$$dx = x_{n+1} - x_n \tag{3.1}$$

$$E_{n+1} = E_n - (\rho_n \frac{\partial E(E_n)}{\partial x}|_{Li} + (1-\rho_n) \frac{\partial E(E_n)}{\partial x}|_{El}) dx \tag{3.2}$$

$$C_n = \int_{E_n}^{E_{n+1}} C(E) dE \tag{3.3}$$

The extra parameter results in an unsolvable set of equations, which can be resolved when the composition of the individual components is known, where:

$$C_n = \rho_n C_{n,Li} + (1-\rho_n) C_{n,\,El} \tag{3.4}$$

Valid under the assumption that the measured concentration is solely due to the two components obtained previously. Similarly the depth dependent porosity can be deduced. As the amount of lithium contained within the electrolyte is considered negligible compared to pristine or discharged insertion hosts, the material quantity in both measurements, i.e., dry and filled with electrolyte is equal. Thus the integrated spectrum intensity is equal, and solely the stopping power is changed, spreading the signal. To find this addition in stopping power the equations must be solved in reverse order, starting from the counts obtained in the first measurement.

$$C_{n,\,dry} = C_{n,filled} = \int_{E_n}^{E_{n+1}} C(E)\, dE|_{filled} \tag{4.1}$$

$$\Delta E_{El} = (E_{n+1} - E_n)_{filled} - (E_{n+1} - E_n)_{dry} \tag{4.2}$$

$$dx_{n,\,filled} = dx_{dry} + \frac{\Delta E_{El}}{\frac{\partial E(E_n)}{\partial x}|_{El}} \tag{4.3}$$

$$\rho_n = 1 - \frac{dx_{dry}}{dx_{n,filled}} \tag{4.4}$$

Now due to the electrolyte filling the energy difference associated with the same amount of material, or counts, will be larger due to the larger stopping power, as is described by Equation (4.2). This energy difference is divided by the stopping power associated with the electrolyte, resulting in a pore length, or addition to the depth increment, Equation (4.3). The outcome of Equation (4.3) is a modified and non-linear depth axis, where the change in depth step reflects the local density.

RESULTS AND DISCUSSION

The possibilities of operando NDP, including the challenges in achieving good counting statistics and quantitative results through calculating the stopping power will be illustrated through three examples. Firstly, operando NDP of fast cycling $Li_4Ti_5O_{12}$ electrodes is achieved, where the challenge is the counting statistics and where the limited change in stopping power due to the Li-ion insertion and extraction allows straightforward determination of the Li density as a function of electrode depth. Secondly, operando Li-metal plating is used to demonstrate the stopping power correction strategy necessary to achieve quantitative results for systems where the electrode composition changes strongly. At same time the large Li density results in high count rates and good time resolution during operando experiments. Thirdly, the stopping power calculation can also be used to quantify the change in stopping power of a porous Li-ion battery electrode due to filling with a Li containing electrolyte, providing the opportunity to determine the depth resolved porosity, demonstrated for $LiFePO_4$ electrodes.

One of the major obstacles in the operando study of high rate intercalation materials with NDP is time resolution. First and foremost the number of detectors can be increased or the neutron intensity via focusing optics. If the electrode can be cycled reversibly another approach is to accumulate statistics over several cycles (Meija et al., 2016). Spinel $Li_4Ti_5O_{12}$ (LTO) shows almost no strain upon (de)lithiation and its relatively high voltage prevents decomposition of typical Li-ion battery electrolytes (Tang et al., 2009; Odziomek et al., 2017; Wang S. et al., 2017). These properties ensure excellent rate capabilities, stable cycling and a long cycle life (Singh et al., 2013b). Previous measurements on another high rate material, $LiFePO_4$ (Wang and Hong, 2007), revealed that at high currents, 20C, and larger (Liu et al., 2016), ionic conduction in the electrolyte is the limiting factor as indicated by the enormous differences in concentration and local current near the electrolyte compared

to the current collector. Similar limitations may be expected to arise in LTO electrodes at comparable C-rates and particle sizes (Yu et al., 2015). However the limited time resolution restricts measurement possibilities at high C-rates.

Instead it is proposed to use the stable cycling of LTO and accumulate NDP measurements over several subsequent cycles at 30C, 0.0045 A/cm^2, and thereby achieve sufficient counting statistics in combination with the required time resolution (30 s in this case). The stable cycling of the LTO electrode in the operando NDP cell is demonstrated in **Figure 2A**, displaying almost no change in the voltage characteristic during the 20 cycles, even at the reduced pressure condition required for operando NDP operation. Furthermore, denoted by the black squares, the change in state of charge, reflected in terms of occupied sites, as obtained from the NDP spectra measured every 30 s, confirms the consistent behavior, reaching a site occupancy of 4.2–6.5 almost every time. The local, depth dependent, site occupancy or state of charge is found by comparing measurements to the lithium distribution after a low rate (dis)charge when all available active material is either filled, $Li_x = 7$, or emptied, $Li_x = 4$, completely. This allows the direct study of the active particle fraction as background noise due to the electrolyte lithium salt is subtracted. This method was previously described by Zhang et al. (2015).

Data obtained during these 20 charge-discharge cycles is ordered according to the voltage, where measurements within similar voltage ranges are averaged, reducing the noise, the result of which is shown in **Figure 2B**. The current collector is located on the left side at zero depth and the interface with the electrolyte at the right, approximately at 15 microns depth. Previous experiments observed large differences in concentration between the current collector and the interface with the electrolyte when $LiFePO_4$ electrodes were charged with a 20C rate (Zhang et al., 2015; Liu et al., 2016). Close examination of **Figure 2B** and especially comparing electrolyte side and current collector side, reveals that there are almost no significant differences between these two regions of the electrode. The lithium concentration is in fact homogenously distributed throughout the electrode as opposed to that for $LiFePO_4$ electrodes (by *ex-situ* measurements). This signifies the excellent rate performance of LTO electrodes, potentially explained by a better Li-ion transport network available through the particles (Lee et al., 2009; Tanida et al., 2016) or/and transport is facilitated due to a different morphology even though the particle size is comparable (Singh et al., 2013a,b). The particle size could also govern the kinetics, allowing a homogenous distribution since the larger particles do not have enough surface sites to accommodate larger reaction rates (Wang et al., 2016; Vasileiadis et al., 2018). The differences between the rate limiting mechanisms testifies to the extraordinary nature of these high rate insertion materials.

When electrode/electrolyte materials undergo changes during cycling, merging data over multiple cycles is not permitted and alternative strategies to improve the NDP measuring count rate are required. Decreasing the applied current might be the most straightforward strategy, alternatively the ^{6}Li concentration can be enriched or a neutron beam with a higher flux should be selected. A drawback is that unless all components have the same li-6 concentration, some degree of homogenization (Oudenhoven et al., 2011) will occur during cycling, complicating quantitative data interpretation. In the study of lithium metal plating, this is straightforwardly resolved as there is no lithium containing electrode, reducing one ^{7}Li reservoir. Electrolyte enrichment is achieved by exposure to an abundance of ^{6}Li metal (96% pure), before use in the operando NDP cell. For these specific measurements the use of ^{6}Li allows measurement times

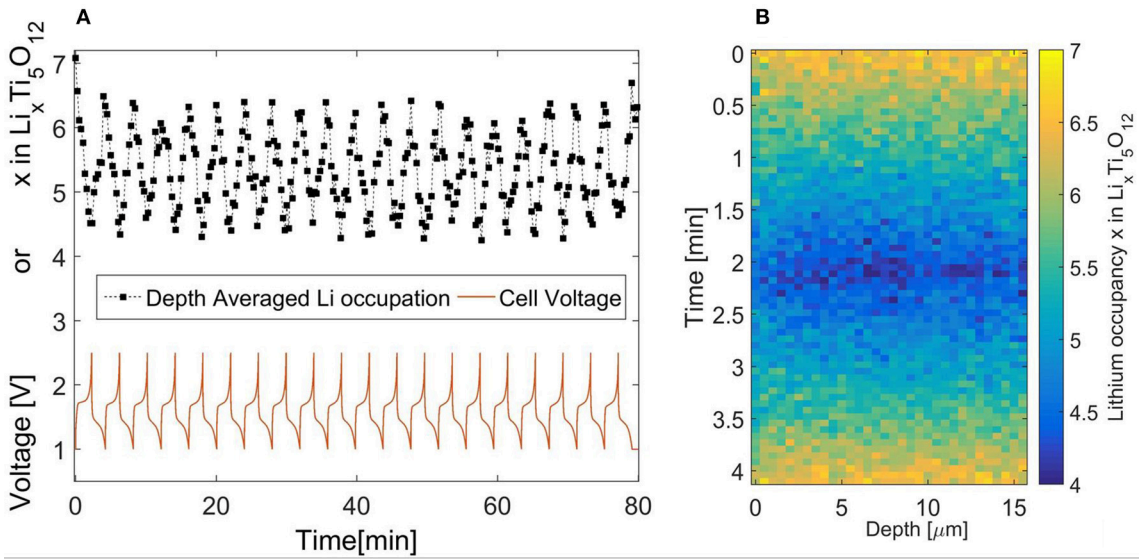

FIGURE 2 | (A) Reversible cycling of $Li_4Ti_5O_{12}$ during operando NDP experiments at a 30C rate. **(B)** Operando NDP of LTO during 30C cycling, based on accumilated data over 20 cycles. The current collector at zero depth and the electrolyte/seperator at 15 micron depth.

as short as 60 s (Lv et al., 2018). The challenge for these operando experiments is accurate calculation of the stopping power. Stopping powers of pure lithium and electrolyte are obtained straightforwardly using SRIM, shown in **Figure 3.** However determining the thickness and the concentration of the plated lithium layer requires knowledge of the ratio between the two components. Our proposed strategy is as follows, by obtaining spectra of both components, the local volume fraction of lithium and electrolyte can be fitted for any third measurement, as is described in Equations (3.1–3.4) found in methods. Obtaining the electrolyte spectra is straightforward as before cycling no lithium is plated and all counts are due to Li containing salts in the electrolyte.

Independently, NDP measurement of ^{6}Li-metal is performed to provide the second component for the stopping power calculation. As ^{6}Li metal is a strong thermal neutron absorber the neutron beam intensity drops significantly along the sample thickness, (**Figure 1**), furthermore chances of recording a coincidence as a single event increase. The energy recorded will then equal the sum of the energy of the two particles, a detailed explanation of the implications for signal analysis can be found in the Supplementary Information. The decrease in neutron beam intensity will effectively result in a decreased measurement (**Figure 1**). This effectively results in a decreased measurement efficiency of the deeper parts of the sample as demonstrated in **Figure 4A**. The Li density for the uncorrected data, gray triangles, decreases as a function of depth, whereas for the Li metal it should be constant at 4.64×10^{22} atoms per cm^3, based on the ^{6}Li metal density (0.353 g/cm^3, Lord, 1992) and its molar weight 6.941 g/mol (Meija et al., 2016). The first iteration, indicated by the black dots, corrects the count rate by the loss in neutron intensity based on the ^{6}Li cross-section of 940 barns (Kopecky, 1997). However, these atoms also absorb neutrons, thus a second iteration is necessary. Furthermore a small fraction is ^{7}Li, hence the theoretical value, as is indicated by the dashed line in the **Figure 4A,** is obtained after the second iteration, indicated by the black squares, this results in the constant Li density, accounting for both ^{6}Li and ^{7}Li.

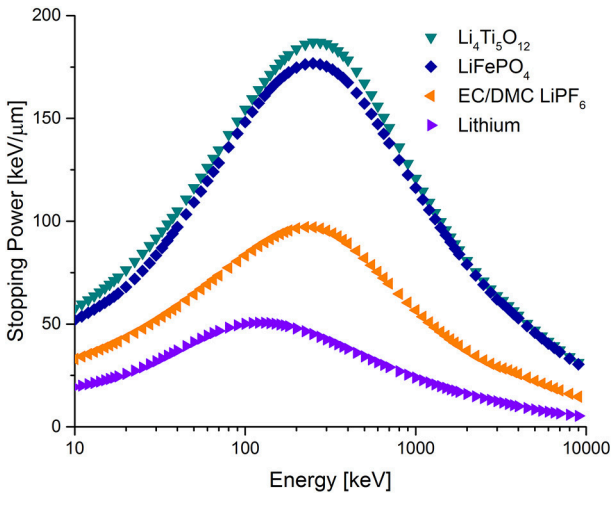

FIGURE 3 | Selected stopping powers. The transition metal insertion hosts have twice as high stopping compared the commonly used EC/DMC electrolyte, which in turn is almost twice as high as metallic lithium.

The concentration increase at the interface with the Cu current collector should resemble a step function however as shown in **Figure 4A,** smooth increase is observed. Firstly, this is the consequence of the larger stopping power of the copper current collector/window, which pushes the signal to lower energies. Secondly, the lower stopping power of the lithium metal spreads the measurement inaccuracies across multiple microns.

In **Figure 4B** the ratio between Li-metal and electrolyte is shown at two moments during an operando Li-metal plating experiment. Firstly after a plating current of 1 mA/cm^2 for 1 h, at this maximum capacity, only 30% of the volume is filled by Li-metal. From this data, averaged over approximately 1 cm^2 it is impossible to conclude if the Li-metal is plated as dense pillars or a porous network. SEM images, performed *ex-situ* on layers that were plated in the same electrolyte on bare copper, e.g., shown in Bieker et al. (2015) and Zhang et al. (2018), confirm that the electrochemically deposited Li-metal is highly porous. This porous layer will, to some extent, contain a solid electrolyte interphase, which is not taken into account in the stopping power analysis. The overall capacity as measured by NDP coincides with that applied electrochemically, indicating that no extra electrons are consumed by direct electrolysis of the electrolyte for instance. However it is difficult from NDP to obtain what fraction of Li is chemically decomposed. The lithium distribution after charge can be divided by the concentration after plating, as is shown in **Figure 4C**, providing an indication of the local charging efficiency and thus the ratio between lithium metal plated and inactive Li-metal/SEI layer formed. In the first few microns, on the left side near the current collector, there is a small plateau after which the ratio increases with increasing depth, indicating an increase of inactive material toward the electrolyte/separator on the right side. This indicates that plating results in dendrite like growing structures, whereas stripping induces thinning of these structures, resulting in the observed inactive layer covering the copper current collector. Although inactive Li in the SEI/Li metal morphology is not taken into account at present, the distribution and growth can be measured after each charge. These possibilities indicate that operando NDP can be used to providing vital experimental data on the distribution and growth at intermediate states of inactive Li (SEI and dead Li-metal) upon cycling of Li metal anodes.

In the lithium plating example discussed above, the stopping power of two known components was used in order to find the local ratio between the two during the operando NDP measurement. The same approach can be used to quantify the change in stopping power of a known porous Li-ion battery electrode due to filling with a Li containing electrolyte, providing the opportunity to determine the depth resolved porosity. In **Figure 5A** two ^{3}H count rates vs. particle kinetic energy loss are shown, one representing the dry electrode, in blue, and, in red, the same electrode impregnated by the electrolyte. The difference in NDP signal is due to the change in stopping power caused by the electrolyte filling the porous electrode. The data is corrected for the Al current collector, making direct comparison of the

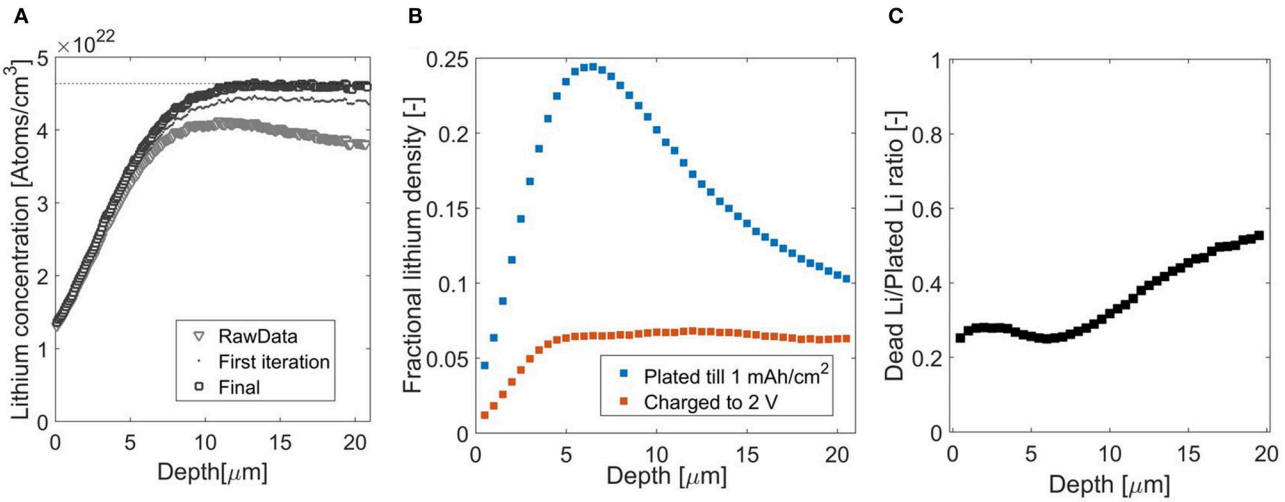

FIGURE 4 | (A) NDP spectra for lithium-6 metal foil, gray triangles indicate original, this data was corrected for reduced neutron intensity, dark gray dots, and finally for reduced neutron intensity and the small, unreactive ^{7}li fraction, black squares. **(B)** Lithium concentration after plating (blue) and stripping (red) at 1 mAh/cm^2 for 1 h. The unit of vertical axis, fractional lithium density is defined as the observed Li-density devided by the Li-density of Li-metal. **(C)** Fraction of inactive Li, with respect to plated Li-metal with 1 mAh/cm^2 for 1 h on copper.

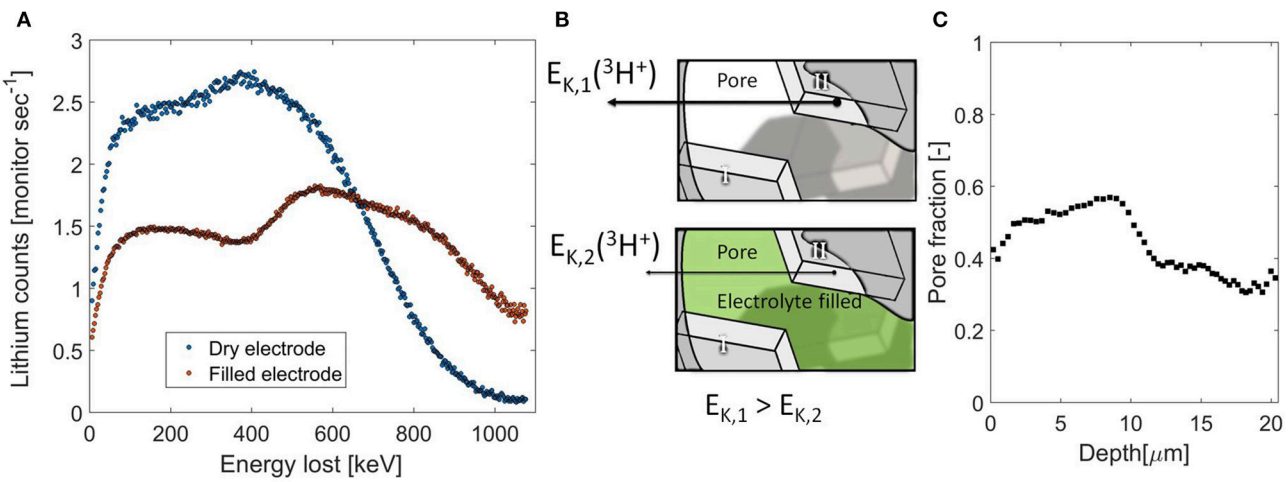

FIGURE 5 | (A) ^{3}H count rate vs. particle kinetic energy loss, the raw NDP data, of a double layer $LiFePO_4$ electrode, measured without electrolyte (blue) and measured with electrolyte (red). **(B)** Schematic representation of the influence of the change in stopping power due to filling of the electrode pores with electrolyte. The tetragonal shapes indicate lithium containing active material, the arrows indicate particle kinetic energy, indicating that as the electrolyte fills the pores particles from crystallite II will lose more energy than without, allow discrimination between crystallite I & II. **(C)**. Local porosity distribution as a function of depth. The sudden change in the middle reflects the transition into the second layer.

energy loss with and without the presence of the electrolyte possible. The electrode is built up by two layers of coating, the first layer on the Al current collector contains 60% of active material, 25% carbon species, 15% PVDF binder, and the second layer on top of that contains 80% of active material, 10% carbon, and binder. The two layers can be distinguished by NDP based on the difference in Li density, reflected in the step in ^{3}H count rate, especially when the electrode pores are filled with the electrolyte.

The electrolyte fills the pores in the electrode that would otherwise not contribute to the stopping power as schematically indicated in **Figure 5B**. Hence the stopping power is increased and the signal is spread across a larger number of energy channels, as is described in Equations (4.1–4.4). The total amount of lithium is only increased marginally (∼5%) by adding the electrolyte (Zhang et al., 2015). Indeed the total amount of ^{3}H counts is equal and the increase in stopping power by adding the electrolyte results in a larger distribution in energy loss detected. This is a direct measure of the amount and distribution of the electrolyte through the electrode, from which the depth resolved pore filling fraction can be determined.

The result, shown in **Figure 5C**, indicates that the porosity is much higher in the first layer. This demonstrates that an increased carbon content also increases the porosity due to the

large carbon black porosity. This readily provides an additional explanation why high carbon content electrodes exhibit high rate capabilities (Kang and Ceder, 2009; Liu H. et al., 2014). Also the porosity is relatively large at the vicinity of the interface between the two layers. This is probably a consequence of the double layer casting, where one layer is dried before the next is casted, resulting in more void space at the interface. For the second layer, having a closer to standard formulation of active material, carbon and binder, an average porosity of 0.36 is found, which is in good agreement with literature values (Singh et al., 2013a,b; Liu et al., 2016). Furthermore with this approach we measure the relevant porosity for the use as electrode porosity, the porosity that can be accessed by the electrolyte in question, which is different compared to what is measure by BET for instance (Klinkenberg, 1941). Electrode porosity is a crucial electrode parameter as it strongly influences battery performance (Fongy et al., 2010a,b; Strobridge et al., 2015; Just, 2016; Liu et al., 2017). Generally, a larger porosity favors Li-ion transport allowing larger (dis)charge (Singh et al., 2013b; Just, 2016) at the expense of the volumetric density (Liu et al., 2016; Singh et al., 2016) and electrical conductivity of the electrode (Wang and Hong, 2007; Fongy et al., 2010a). The optimum seems to be reached by a certain porosity gradient (Du et al., 2017; Liu et al., 2017). For measuring the porosity numerous methods are available, both bulk methods (DuBeshter et al., 2014; Li et al., 2014) as well as methods with a submicron resolution, such as tomography (Ge et al., 2014; Harks et al., 2015) and FIB-SEM (Hutzenlaub et al., 2014; Liu et al., 2016). The advantage of using NDP is the combination of both length scales, as this measurement represents an average over 1.1 cm^2 electrode, the bulk average porosity is determined with a sub-micron resolution along an axis of interest. Moreover the measurement is performed in a non-destructive manner, allowing direct continuation of battery cycling, where the (de)lithiation as a function of depth and local porosity can now be studied.

CONCLUSION

Direct observation of Li concentration vs. electrode depth in working Li-ion batteries is possible with NDP through the capture reaction of the thermal neutrons by the ^{6}Li isotope. Although the large attenuation length of neutrons in most materials allows diverse sample environments, the relatively low neutron intensity requires smart experimental design. The translation toward quantitative results requires detailed consideration of the stopping power of the battery electrodes ^{6}Li enrichment is an effective solution but not always practical to achieve. Here we demonstrate that accumulation of NDP data over repeated battery cycling enables operando investigations of intercalation materials at a rate of 30C, avoiding complexity of ^{6}Li homogenization that comes along with enrichment and allowing for the use of commercially produced powders.

The charged particles formed in the neutron capture reaction during NDP measurements allow straightforward detection of Li, where their energy loss is a direct measure for the point of origin and hence for the depth. Their kinetic energy limits the escape depth and therefore the depth of view, which demands smart design of the battery window and current collector, in particular in the low pressure NDP environment. Accurate determination of the stopping power of the battery electrode, which may change upon cycling, is vital to achieve the quantitative Li density as a function of depth. In particular for the cases that electrochemical cycling leads to large changes in the composition, a stopping power calculation strategy is developed to result in quantitative results. This is demonstrated lithium metal plating, where operando NDP is able to provide insight in the growth and development of the evolution of inactive Li.

Furthermore it is demonstrated that the change in NDP signal due to filling of the porous electrode by the electrolyte can be used to determine the depth resolved filling fraction or porosity. This is in particular important for battery electrodes where porosity has a direct influence on the energy density and charge transport, hence determining the rate capability of battery electrodes.

AUTHOR CONTRIBUTIONS

TV and MW wrote the manuscript. TV developed data treatment methods. Designed and conducted the experiments used in example 1 & 3 using intercalation materials, concerning $Li_4Ti_5O_{12}$ and the porosity determination. SL conducted the lithium plating experiment.

FUNDING

The research leading to these results has received funding from the European Research Council under the European Union's Seventh Framework Programme FP/2007-2013)/ERC Grant Agreement No. [307161] of MW Financial support from the Advanced Dutch Energy Materials (ADEM) program of the Dutch Ministry of Economic Affairs, Agriculture and Innovation is gratefully acknowledged. Financial support of the KNAW for the joint research project under the scientific cooperation between China and the Netherlands, project number 530-5CDP10 is gratefully acknowledged. SL is grateful for the financial support by National Key R&D Plan of China (No. 2017YFB0702201).

ACKNOWLEDGMENTS

The technical staff at the Reactor Institute Delft (RID) is gratefully acknowledged for their all-round support, most notable Michel Steenvoorden and Freek Labohm for maintaining the NDP set-up running and Frans Ooms for the pouch cell facilities.

SUPPLEMENTARY MATERIAL

The Supplementary Material for this article can be found online at: https://www.frontiersin.org/articles/10.3389/fenrg.2018.00062/full#supplementary-material

REFERENCES

Asadi, M., Sayahpour, B., Abbasi, P., Ngo, A. T., Karis, K., et al. (2018). A lithium–oxygen battery with a long cycle life in an air-like atmosphere. *Nature* 555:502. doi: 10.1038/nature25984

Bieker, G., Winter, M., and Bieker, P. (2015). Electrochemical *in situ* investigations of SEI and dendrite formation on the lithium metal anode. *Phys. Chem. Chem. Phys.* 17, 8670–8679. doi: 10.1039/C4CP05865H

Çetiner, S. M., Ünlü, K., and Downing, R. G. (2008). Development and applications of time-of-flight neutron depth profiling (TOF-NDP). *J. Radioanal. Nuclear Chem.* 276:623. doi: 10.1007/s10967-008-0609-7

Cheng, X.-B., Zhang, R., C.-,Zhao, Z., and Zhang, Q. (2017). Toward safe lithium metal anode in rechargeable batteries: a review. *Chem. Rev.* 117, 10403–10473. doi: 10.1021/acs.chemrev.7b00115

Downing, R. G., Lamaze, G. P., Langland, J. K., and Hwang, S. T. (1993). Neutron depth profiling: overview and description of NIST facilities. *J. Res. Natl. Instit. Stand. Technol.* 98, 109–126. doi: 10.6028/jres.098.008

Downing, R., Maki, J., and Fleming, R. (1987). Analytical applications of neutron depth profiling. *J. Radioanal. Nucl. Chem.* 112, 33–46. doi: 10.1007/BF02037274

Du, Z., Wood, D. L., Daniel, C., Kalnaus, S., and Li, J. (2017). Understanding limiting factors in thick electrode performance as applied to high energy density Li-ion batteries. *J. Appl. Electrochem.* 47, 405–415. doi: 10.1007/s10800-017-1047-4

DuBeshter, T., Sinha, P. K., Sakars, A., Fly, G. W., and Jorne, J. (2014). Measurement of tortuosity and porosity of porous battery electrodes. *J. Electrochem. Soc.* 161, A599–A605. doi: 10.1149/2.073404jes

Fongy, C., Gaillot, A. C., Jouanneau, S., Guyomard, D., and Lestriez, B. (2010a). Ionic vs electronic power limitations and analysis of the fraction of wired grains in LiFePO4 composite electrodes. *J. Electrochem. Soc.* 157, A885–A891. doi: 10.1149/1.3432559

Fongy, C., Jouanneau, S., Guyomard, D., Badot, J. C., and Lestriez, B. (2010b). Electronic and ionic wirings versus the insertion reaction contributions to the polarization in LiFePO4 composite electrodes. *J. Electrochem. Soc.* 157, A1347–A1353. doi: 10.1149/1.3497353

Ganapathy, S., Adams, B. D., Stenou, G., Anastasaki, M. S., Goubitz, K. X., et al. (2014). Nature of Li2O2 oxidation in a Li–O2 battery revealed by operando x-ray diffraction. *J. Am. Chem. Soc.* 136, 16335–16344. doi: 10.1021/ja508794r

Ge, M., Lu, Y., Ercius, P., Rong, J., Fang, X., Mecklenburg, M., et al. (2014). Large-scale fabrication, 3D tomography, and lithium-ion battery application of porous silicon. *Nano Lett.* 14, 261–268. doi: 10.1021/nl403923s

Gustafsson, T., Thomas, J. O., Koksbang, R., and Farrington, G. C. (1992). The polymer battery as an environment for *in situ* X-ray diffraction studies of solid-state electrochemical processes. *Electrochimica Acta* 37, 1639–1643. doi: 10.1016/0013-4686(92)80128-9

Harks, P. P., Mulder, F. M., and Notten, P. H. L. (2015). *In situ* methods for Li-ion battery research: a review of recent developments. *J. Power Sourc.* 288, 92–105. doi: 10.1016/j.jpowsour.2015.04.084

Hutchison, D. A. (1954). Natural abundance of the lithium isotopes. *Phys. Rev.* 96, 1018–1021. doi: 10.1103/PhysRev.96.1018

Hutzenlaub, T., Thiele, S., Paust, N., Spotnitz, R., Zengerle, R., and Walchshofer, C. (2014). Three-dimensional electrochemical Li-ion battery modelling featuring a focused ion-beam/scanning electron microscopy based three-phase reconstruction of a LiCoO2 cathode. *Electrochimica Acta* 115, 131–139. doi: 10.1016/j.electacta.2013.10.103

Itkis, M. D., Velasco Vélez, J., Knop-Gericke, A., Vyalikh, A. V., Avdeev, M., and Yashina, L. (2015). Probing operating electrochemical interfaces by photons and neutrons. *ChemElectroChem* 2, 1427–1445. doi: 10.1002/celc.201500155

Just, P. (2016). A method to quantify coating thickness and porosity of electrodes for lithium-ion-batteries. *Measurement* 89:312. doi: 10.1016/j.measurement.2016.04.001

Kang, B., and Ceder, G. (2009). Battery materials for ultrafast charging and discharging. *Nature* 458:190. doi: 10.1038/nature07853

Kang, H. S., Park, E., Hwang, J., Y., Kim, H., Aurbach, D., et al. (2016). A scaled-up lithium (ion)-sulfur battery: newly faced problems and solutions. *Adv. Mater. Technol.* 1:1600052. doi: 10.1002/admt.201600052

Katayama, M., Sumiwaka, K., Miyahara, R., Yamashige, H., Arai, H., Uchimoto, Y., et al. (2014). X-ray absorption fine structure imaging of inhomogeneous electrode reaction in LiFePO4 lithium-ion battery cathode. *J. Power Sourc.* 269, 994–999. doi: 10.1016/j.jpowsour.2014.03.066

Klinkenberg, L. J. (1941). *The Permeability Of Porous Media To Liquids And Gases. Drilling and Production Practice*. New York, NY, American Petroleum Institute.

Kopecky, J. (1997). *Atlas of Neutron Capture Crossections*. Vienna:IAEA Nuclear Data Section.

Lee, K. T., Kan, W. H., and Nazar, L. F. (2009). Proof of intercrystallite ionic transport in LiMPO4 electrodes (M = Fe, Mn). *J. Am. Chem. Society* 131, 6044–6045. doi: 10.1021/ja8090559

Li, X., Gu, M., Hu, S., Kennard, R., Yan, P., Chen, X., et al. (2014). Mesoporous silicon sponge as an anti-pulverization structure for high-performance lithium-ion battery anodes. *Nat. Commun.* 5:4105. doi: 10.1038/ncomms5105

Lindhard, J., Scharff, M., and Schioett, H. E. (1963). Range concepts and heavy ion ranges (notes on atomic collisions, II). *Kgl. Danske Videnskab. Selskab. Mat. Fys. Medd.* 33, 1–42.

Liu, D. X., and Co, A., C. (2016). Revealing chemical processes involved in electrochemical (De)lithiation of Al with *in situ* neutron depth profiling and X-ray diffraction. *J. Am. Chem. Soc.* 138, 231–238. doi: 10.1021/jacs.5b10295

Liu, D. X., Cao, L. R., and Co, A. C. (2015). *In Situ Neutron Depth Profiling of Lithium Transport Within Aluminum and Tin.* Meeting Abstracts MA2015-01(2), 649.

Liu, D. X., Wang, J., Pan, K., Qiu, J., Canova, M., Cao, L., et al. (2014). *In situ* quantification and visualization of lithium transport with neutrons. *Angew. Chem. Internat. Editn* 53, 9498–9502. doi: 10.1002/anie.201404197

Liu, H., Strobridge, F. C., Borkiewicz, O. J., Wiaderek, K. M., Chapman, K. W., et al. (2014). Capturing metastable structures during high-rate cycling of LiFePO₄ nanoparticle electrodes. *Science* 344:6191. doi: 10.1126/science.1252817

Liu, L., Guan, P., and Liu, C. (2017). Experimental and simulation investigations of porosity graded cathodes in mitigating battery degradation of high voltage lithium-ion batteries. *J. Electrochem. Soc.* 164, A3163–A3173. doi: 10.1149/2.1021713jes

Liu, Z., Verhallen, T. W., Singh, D. P., Wang, H. Q., Wagemaker, M., and Barnett, S. (2016). Relating the 3D electrode morphology to Li-ion battery performance; a case for LiFePO4. *J. Power Sourc.* 324, 358–367. doi: 10.1016/j.jpowsour.2016.05.097

Lord, A. M. J., (1992). *Macmillan's Chemical and Physical Data*. London: Macmillan.

Lv, S., Verhallen, T., Vasileiadis, A., Ooms, F., Xu, Y., Li, Z., et al. (2018). Operando monitoring the Lithium spatial distribution of Lithium metal anodes. *Nat. Commun.* 9:2152. doi: 10.1038/s41467-018-04394-3

Maki, J. T., Fleming, R. F., and Vincent, D. H. (1986). Deconvolution of neutron depth profiling spectra. *Nucl. Instr. Methods Phys. Res. Sec. B* 17, 147–155. doi: 10.1016/0168-583X(86)90077-7

Meija, J., Coplen Tyler, B., Berglund, M., Brand Willi, A., De Bièvre, P., Gröning, M., et al. (2016). Atomic weights of the elements 2013 (IUPAC Technical Report). *Pure Appl. Chem.* 88:265. doi: 10.1515/pac-2015-0305

Mohanty, D., Kalnaus, S., Meisner, R. A., Rhodes, K. J., Li, J., et al. (2013). Structural transformation of a lithium-rich Li1.2Co0.1Mn0.55Ni0.15O2 cathode during high voltage cycling resolved by *in situ* X-ray diffraction. *J. Power Sourc.* 229, 239–248. doi: 10.1016/j.jpowsour.2012.11.144

Mulligan, P. L., Cao, L. R., and Turkoglu, D. (2012). A multi-detector, digitizer based neutron depth profiling device for characterizing thin film materials. *Rev. Sci. Instr.* 83:8. doi: 10.1063/1.4732168

Nagpure, S. C., Downing, R. G., Bhushan, B., Babu, S. S., and Cao, L. (2011). Neutron depth profiling technique for studying aging in Li-ion batteries. *Electrochim. Acta* 56, 4735–4743. doi: 10.1016/j.electacta.2011.02.037

Nagpure, S. C., Mulligan, P., Canova, M., and Cao, L. R. (2014). Neutron depth profiling of Li-ion cell electrodes with a gas-controlled environment. *J. Power Sourc.* 248, 489–497. doi: 10.1016/j.jpowsour.2013.09.032

Nonaka, T., Okuda, C., Seno, Y., Nakano, H., Koumoto, K., and Ukyo, Y. (2006). *In situ* XAFS and micro-XAFS studies on LiNi0.8Co0.15Al0.05O2 cathode material for lithium-ion batteries. *J. Power Sourc.* 162, 1329–1335. doi: 10.1016/j.jpowsour.2006.09.003

Odziomek, M., Chaput, F., Rutkowska, A., Swierczek, K., Olszewska, D., Sitarz, M., et al. (2017). Hierarchically structured lithium titanate for ultrafast charging in long-life high capacity batteries. *Nat. Commun.* 8:15636. doi: 10.1038/ncomms15636

Oudenhoven, J. F. M., Labohm, F., Mulder, M., Niessen, R. A. H., Mulder, F., M., and Notten, P. H. L. (2011). *In situ* neutron depth profiling: a powerful method to probe lithium transport in micro-batteries. *Adv. Mater.* 23:4103. doi: 10.1002/adma.201101819

Parikh, N. R., Frey, E. C., Hofsäss, H. C., Swanson, M. L., Downing, R. G., et al. (1990). Neutron depth profiling by coincidence spectrometry. *Nucl. Instr. Methods Phys. Res. Sec. B* 45, 70–74. doi: 10.1016/0168-583X(90)90787-U

Singh, D. P., Mulder, F. M., Abdelkader, A. M., and Wagemaker, M. (2013a). Facile micro templating LiFePO4 electrodes for high performance Li-Ion batteries. *Adv. Energy Mater.* 3, 572–578. doi: 10.1002/aenm.201200704

Singh, D. P., Mulder, F. M., and Wagemaker, M. (2013b). Templated spinel Li4Ti5O12 Li-ion battery electrodes combining high rates with high energy density. *Electrochem. Commun.* 35, 124–127. doi: 10.1016/j.elecom.2013.08.014

Singh, M., Kaiser, J., and Hahn, H. (2015). Thick electrodes for high energy lithium ion batteries. *J. Electrochem. Soc.* 162, A1196–A1201. doi: 10.1149/2.0401507jes

Singh, M., Kaiser, J., and Hahn, H. (2016). Effect of porosity on the thick electrodes for high energy density lithium ion batteries for stationary applications. *Batteries* 2:35. doi: 10.3390/batteries2040035

Strobridge, F. C., Orvananos, B., Croft, M. H.,Yu, C., Robert, R., et al. (2015). Mapping the inhomogeneous electrochemical reaction through porous LiFePO4-electrodes in a standard coin cell battery. *Chem. Mater.* 27, 2374–2386. doi: 10.1021/cm504317a

Tang, Y., Yang, L., Fang, S., and Qiu, Z. (2009). Li4Ti5O12 hollow microspheres assembled by nanosheets as an anode material for high-rate lithium ion batteries. *Electrochim. Acta* 54, 6244–6249. doi: 10.1016/j.electacta.2009.05.092

Tanida, H., Yamashige, H., Orikasa, Y., Gogyo, Y., Arai, H., Uchimoto, Y., et al. (2016). Elucidating the driving force of relaxation of reaction distribution in LiCoO2and LiFePO4Electrodes using X-ray absorption spectroscopy. *J. Phys. Chem. C* 120, 4739–4743. doi: 10.1021/acs.jpcc.5b10210

Tomandl, I., Vacik, J., Mora Sierra, Y., Granja, C., and Kraus, V. (2017). High resolution imaging of 2D distribution of lithium in thin samples measured with multipixel detectors in sandwich geometry. *Rev. Sci. Instrum.* 88:023706. doi: 10.1063/1.4977217

Trask, S. E., Li, Y., Kubal, J. J., Bettge, M., Polzin, B. J., et al. (2014). From coin cells to 400 mAh pouch cells: enhancing performance of high-capacity lithium-ion cells via modifications in electrode constitution and fabrication. *J. Power Sourc.* 259, 233–244. doi: 10.1016/j.jpowsour.2014.02.077

Ünlü, K., Saglam, M., and Wehring, B. W. (1999). Helium-3 and boron-10 concentration and depth measurements in alloys and semiconductors using NDP. *Nucl. Instr. Methods Phys. Res. Sec. A* 422, 885–890. doi: 10.1016/S0168-9002(98)01036-5

Utsuro, M., and Ignatovich, V. K. (2010). Reflection, refraction, and transmission of unpolarized neutrons. *Handb. Neutron Optic.* 31–70. doi: 10.1002/9783527628780.ch2

Vasileiadis, A., de Klerk, N., Smith, R. B., Ganapathy, S. P., Harks, P., et al. (2018). Towards Optimal Performance and In-Depth Understanding of Spinel $Li_4Ti_5O_12$ Electrodes Through Phase Field Modeling. *Adv. Funct. Materials* 28:1705992. doi: 10.1002/adfm.201705992

Villevieille, C. (2015). "Electrochemical characterization of rechargeable lithium batteries," in *Rechargeable Lithium Batteries: From Fundamentals to Applications*, ed A. A. Franco (Woodhead Publishing), 183–232. doi: 10.1016/B978-1-78242-090-3.00007-9

Wang, C., and Hong, J. (2007). Ionic/electronic conducting characteristics of LiFePO4 cathode materials: the determining factors for high rate performance. *Electrochem. Solid-State Lett.* 10, A65–A69. doi: 10.1149/1.2409768

Wang, C., Gong, Y., Dai, J., Zhang, L., Xie, H., Pastel, G., et al. (2017). *In situ* neutron depth profiling of lithium metal–garnet interfaces for solid state batteries. *J. Am. Chem. Soc.* 139, 14257–14264. doi: 10.1021/jacs.7b07904

Wang, C., Wang, S., Tang, L., Y.-,He, B., Gan, L., et al. (2016). A robust strategy for crafting monodisperse Li4Ti5O12 nanospheres as superior rate anode for lithium ion batteries. *Nano Energy* 21, 133–144. doi: 10.1016/j.nanoen.2016.01.005

Wang, H., Downing, R. G., Dura, J. A., and Hussey, D. S. (2012). *In situ* neutron techniques for studying lithium ion batteries. *Polymers Energy Storage Deliv.* 1096, 91–106. doi: 10.1021/bk-2012-1096.ch006

Wang, J., Liu, D. X., Canova, M., Downing, R. G., Cao, L. R., and Co, A. C. (2014). Profiling lithium distribution in Sn anode for lithium-ion batteries with neutrons. *J. Radioanal. Nucl. Chem.* 301, 277–284. doi: 10.1007/s10967-014-3102-5

Wang, S., Quan, W., Zhu, Z., Yang, Y., Liu, Q., Ren, Y., et al. (2017). Lithium titanate hydrates with superfast and stable cycling in lithium ion batteries. *Nat. Commun.* 8:627. doi: 10.1038/s41467-017-00574-9

Whitney, S. M., Biegalski, S., R., F., and Downing, G. (2009). Benchmarking and analysis of 6Li neutron depth profiling of lithium ion cell electrodes. *J. Radioanal. Nucl. Chem.* 282:173. doi: 10.1007/s10967-009-0229-x

Wilson, W. D., Haggmark, L. G., and Biersack, J. P. (1977). Calculations of nuclear stopping, ranges, and straggling in the low-energy region. *Phys. Rev. B* 15, 2458–2468. doi: 10.1103/PhysRevB.15.2458

Yu, D. Y. W., Donoue, K., Inoue, T., Fujimoto, M., and Fujitani, S. (2006). Effect of electrode parameters on LiFePO4 cathodes. *J. Electrochem. Soc.* 153, A835–A839. doi: 10.1149/1.2179199

Yu, Y.-S., Kim, C., Shapiro, D. A., Farmand, M., Qian, D., et al. (2015). Dependence on crystal size of the nanoscale chemical phase distribution and fracture in LixFePO4. *Nano Lett.* 15, 4282–4288. doi: 10.1021/acs.nanolett.5b01314

Zhang, S. S. (2018). Problem, status, and possible solutions for lithium metal anode of rechargeable batteries. *ACS Appl. Energy Mater.* 1, 910–920. doi: 10.1021/acsaem.8b00055

Zhang, W., Zhuang, H. L., Fan, L., Gao, L., and Lu, Y. (2018). A cation-anion regulation synergistic anode host for dendrite-free lithium metal batteries. *Sci. Adv.* 4:2. doi: 10.1126/sciadv.aar4410

Zhang, X., van Hulzen, M., Singh, D. P., Brownrigg, A., Wright, J. P., et al. (2014). Rate-induced solubility and suppression of the first-order phase transition in olivine LiFePO4. *Nano Lett.* 14, 2279–2285. doi: 10.1021/nl404285y

Zhang, X., Verhallen, T. W., Labohm, F., and Wagemaker, M. (2015). Direct observation of Li-Ion transport in electrodes under nonequilibrium conditions using neutron depth profiling. *Adv. Energy Mater.* 5:1500498. doi: 10.1002/aenm.201500498

Ziegler, J. F. (1985). *The Stopping and Range of Ions in Matter*. Boston, MA: Springer.

Ziegler, J. F., Cole, G. W., and Baglin, J. E. (1972). Technique for determining concentration profiles of boron impurities in substrates. *J. Appl. Phys.* 43, 3809–3815. doi: 10.1063/1.1661816

Ziegler, J. F., Ziegler, M. D., and Biersack, J. P. (2010). SRIM - The stopping and range of ions in matter (2010). *Nucl. Instr. Methods Phys. Res. Sec. B* 268, 1818–1823. doi: 10.1016/j.nimb.2010.02.091

Zuo, X., Zhu, J., Müller-Buschbaum, P., and Cheng, J. (2017). Silicon based lithium-ion battery anodes: A chronicle perspective review. *Nano Energy* 31, 113–143. doi: 10.1016/j.nanoen.2016.11.013

Conflict of Interest Statement: The authors declare that the research was conducted in the absence of any commercial or financial relationships that could be construed as a potential conflict of interest.

frontiers in Energy Research

MINI REVIEW
published: 03 July 2018
doi: 10.3389/fenrg.2018.00056

In-Situ Transmission X-Ray Microscopy Probed by Synchrotron Radiation for Li-Ion Batteries

Nai-Hsuan Yang[1†], *Yen-Fang Song*[2*†] *and Ru-Shi Liu*[1,3*]

[1] Department of Chemistry, National Taiwan University, Taipei, Taiwan, [2] National Synchrotron Radiation Research Center, Hsinchu, Taiwan, [3] Department of Mechanical Engineering and Graduate Institute of Manufacturing Technology, National Taipei University of Technology, Taipei, Taiwan

Lithium-ion batteries are one of the main power sources for portable electronic devices and vehicles nowadays. However, the limitations of commercial cathode and anode materials cannot satisfy the increasing energy requirement of electronic devices. Therefore, investigating the chemistry and material changes during charge/discharge (lithiation/delithiation) is important to improve the properties of commercial LIBs. *In-situ* transmission X-ray microscopy has become one of the most important techniques for understanding the relationships between the electrode architecture and the cycling performance of electrode materials. In this mini review, we are focus on the theory of the synchrotron transmission X-ray microscopy and pick up one of the most important reports to discuss the electrode material investigation.

Keywords: battery, electrode, *in-situ*, in-operando, transmission X-ray microscopy

OPEN ACCESS

Edited by:
Verónica Palomares, University of the Basque Country (UPV/EHU), Spain

Reviewed by:
Manickam Minakshi, Murdoch University, Australia
Daniel Hernández-Cruz, Autonomous University of Chiapas, Mexico

***Correspondence:**
Yen-Fang Song
song@nsrrc.org.tw
Ru-Shi Liu
rsliu@ntu.edu.tw

[†]*These authors have contributed equally to this work.*

Specialty section:
This article was submitted to Energy Storage, a section of the journal Frontiers in Energy Research

Received: *27 February 2018*
Accepted: *04 June 2018*
Published: *03 July 2018*

Citation:
Yang NH, Song YF and Liu RS (2018) In-Situ Transmission X-Ray Microscopy Probed by Synchrotron Radiation for Li-Ion Batteries. Front. Energy Res. 6:56. doi: 10.3389/fenrg.2018.00056

INTRODUCTION

With the growth in portable electronic device, the development of advanced lithium-ion batteries (LIBs) becomes important, especially in determining new electrode materials. The present technologies, such as X-ray diffraction (XRD), scanning electron microscope (SEM), transmission electron microscope (TEM), Fourier transform infrared spectroscopy (FTIR), nuclear magnetic resonance (NMR), X-ray photoelectron spectroscopy (XPS), atomic force microscope (AFM), and Raman spectra are used for the investigation of LIBs. However, they can only show the morphology, structure, or surface function groups before and after the charge/discharge cycle process. *In-situ* synchrotron full field transmission X-ray microscopy (TXM) with 30–50 nm spatial resolution is a significant technique that can reveal the ultrafine variation for Li ions in and out of the electrode materials during the charge/discharge cycle process and help us to understand the mechanism and explore the effective new electrode materials (Wang et al., 2014; Chen et al., 2016; Wolf et al., 2017; Xu et al., 2017). In addition, synchrotron radiation X-ray tomographic microscopy (SRXTM) with 1 μm spatial resolution (Ebner et al., 2013) is also an important instrument for *in situ* mesoscale visualization in LIBs.

IMAGES OF LIB ELECTRODE MATERIALS BY USING *IN-SITU* TRANSMISSION X-RAY MICROSCOPY

Synchrotron TXM is an essential technique in the ion battery research. TXM provides 30–50 nm spatial resolution, 10 s temporal resolution and 20–50 μm probing depth by applying high flux

synchrotron radiation X-ray with tunable energy range of 5–12 keV as the source. Furthermore, TXM requires no vacuumed experimental environment; hence, the use of aqueous samples is feasible. The energy-resolved TXM elemental mapping can be performed with the complement of the X-ray absorption near-edge structure (XANES). Taking all of these advantages, TXM is a distinct technique to reveal in situ the working LIBs, sodium-ion batteries (NIBs), and all similar investigations. TXM applies the physical characteristics of absorption and phase contrasts of various materials within the specimen and explores the interior morphology. The sequential alteration of materials inside the anode, cathode, and electrolyte of LIBs during the charge/discharge cycle processes, including size (expansion/contraction), geometry shape, crack, fracture, pulverization, porous rate, and lithium dendrite, can be analyzed by *in-situ* TXM observation.

The layout of TXM beamline at the synchrotron radiation facility is shown in **Figure 1A.** The synchrotron radiation X-ray source passes through a vertical collimating mirror to the parallel beam to optimize the energy resolution (ΔE/E) of the double crystal monochromator (DCM). The monochromatized beam is focused by a horizontal focusing mirror (HFM) and a vertical focusing mirror (VFM) as the secondary source for the capillary condenser of the TXM end-station. The sketch and photograph of the TXM instrument are presented in **Figure 1B**. X-ray at the HFM and VFM focus is refocused by the capillary condenser to the sample position. This beam transmits the sample and subsequently passes through a zone plate, which is located at the downstream of the sample, to magnify the diffraction beam and apply the spatial resolution of 30–50 nm. Specimen with insufficient absorption contrast is equipped with a phase ring in the back focal plane of the zone plate to enhance phase contrast. A charge-coupled device (CCD) is installed at the end of the end-station for image acquisition. Prior to CCD installation, a scintillator is used to translate X-ray to visible light. A serious two dimensional (2D) images from −90° to 90° (181 images) are reconstructed as a three dimensional (3D) tomography.

The TXM applies the absorption and phase contrasts to reveal the internal morphology of the specimen (Schneider, 1998; Attwood, 1999; Born and Wolf, 1999; Mansuripur, 2002). The refraction index *n* of a material can be written as follows:

$$n = 1 - \delta - i\beta, \tag{1}$$

where δ and β are the real and image parts of the refraction index, respectively. The interaction in the X-ray electric field, which transmits a material with the thickness of *z*, can be illustrated as follows:

$$\mathrm{E(z)} = \mathrm{E_0 e^{(-ikn z)}}, \tag{2}$$

where $\mathrm{E_0}$ is the initial electric field of the X-ray, *k* is the wave number of the X-ray, $k = 2\pi/\lambda$, and λ is the wavelength of the X-ray. With the substitution of Equation (1) and $k = 2\pi/\lambda$ into Equation (2), E(z) can be expressed as follows:

$$\mathrm{E(z)} = \mathrm{E_0 e^{(-i2\pi z/\lambda)+(i2\pi\delta z/\lambda)-(2\pi\beta z/\lambda)}} \tag{3}$$

The electric field intensity is described as follows:

$$\mathrm{I(z)} = |\mathrm{E(z)}|^2 = \mathrm{I_0} e^{-4\pi\beta z/\lambda}, \tag{4}$$

where $\mathrm{I_0}$ is the initial intensity of the incident beam. Hence, the absorption contrast of various materials with different β values within the specimen can be expressed as follows:

$$\mu(z) = 4\pi\beta z/\lambda. \tag{5}$$

With regard to the specimen with insufficient absorption contrast, the Zernike phase contrast method can be applied to enhance the phase contrast of materials within the specimen. First, Abbe's theory of image formation in a microscope is introduced, with consideration of object imaging, which is illuminated by a plane wave, as shown in **Figure 1C** (Born and Wolf, 1999). The plane wave is diffracted by the grating-like object and develops a Fraunhofer diffraction pattern of the object in the back focal plane of the objective. The maximum intensity of continuous orders of this pattern is indicated by the following: …, S_{-2}, S_{-1}, S_0, S_1, S_2 … Each point on the focal plane can be treated as a center of a coherent secondary source. The waves that progress from these secondary sources interfere mutually and form an image of this object in the image plane. The Zernike phase contrast method locates a phase plate at the back focal plane of the objective. The zero-order phase of the diffraction pattern (S_0) is retarded (+) or advanced (–) with respect to the other diffraction spectra (S_1, S_{-1}, S_2, S_{-2}…) by π/2. This method can transform the phase term of the image to intensity, which can be recognized by a detector. To explain the principle of phase contrast method, the system is simplified to consider the phase term only by treating a one-dimensional transparent phase grating. The transmission function of this phase grating is as follows:

$$\mathrm{F(z)} = \exp(\mathrm{i}\Phi(z)), \tag{6}$$

where Φ (z) is a real periodic function. Compared with unity, if Φ is smaller, then F(z) can be expressed as follows:

$$\mathrm{F(z)} \cong 1 + \mathrm{i}\Phi(z). \tag{7}$$

When the S_0 phase is retarded or advanced with one quarter of period ($\pm\frac{\pi}{2}$), the according transmission function G(z) after calculation is as follows:

$$\mathrm{G(z)} = \pm\mathrm{i} + \mathrm{i}\Phi(z). \tag{8}$$

The positive and negative signs correspond to the phase of the 0th order, which is retarded and advanced, respectively. G(z) represents an assumed amplitude grating instead of a phase grating. The intensity in the image plane is as follows:

$$\mathrm{I(z)} = |G(z)|^2 = 1 \pm 2\Phi(z). \tag{9}$$

Moreover, the phase contrast for the transparent phase grating is expressed as follows:

$$\Phi(z) = 2\pi\delta z/\lambda. \tag{10}$$

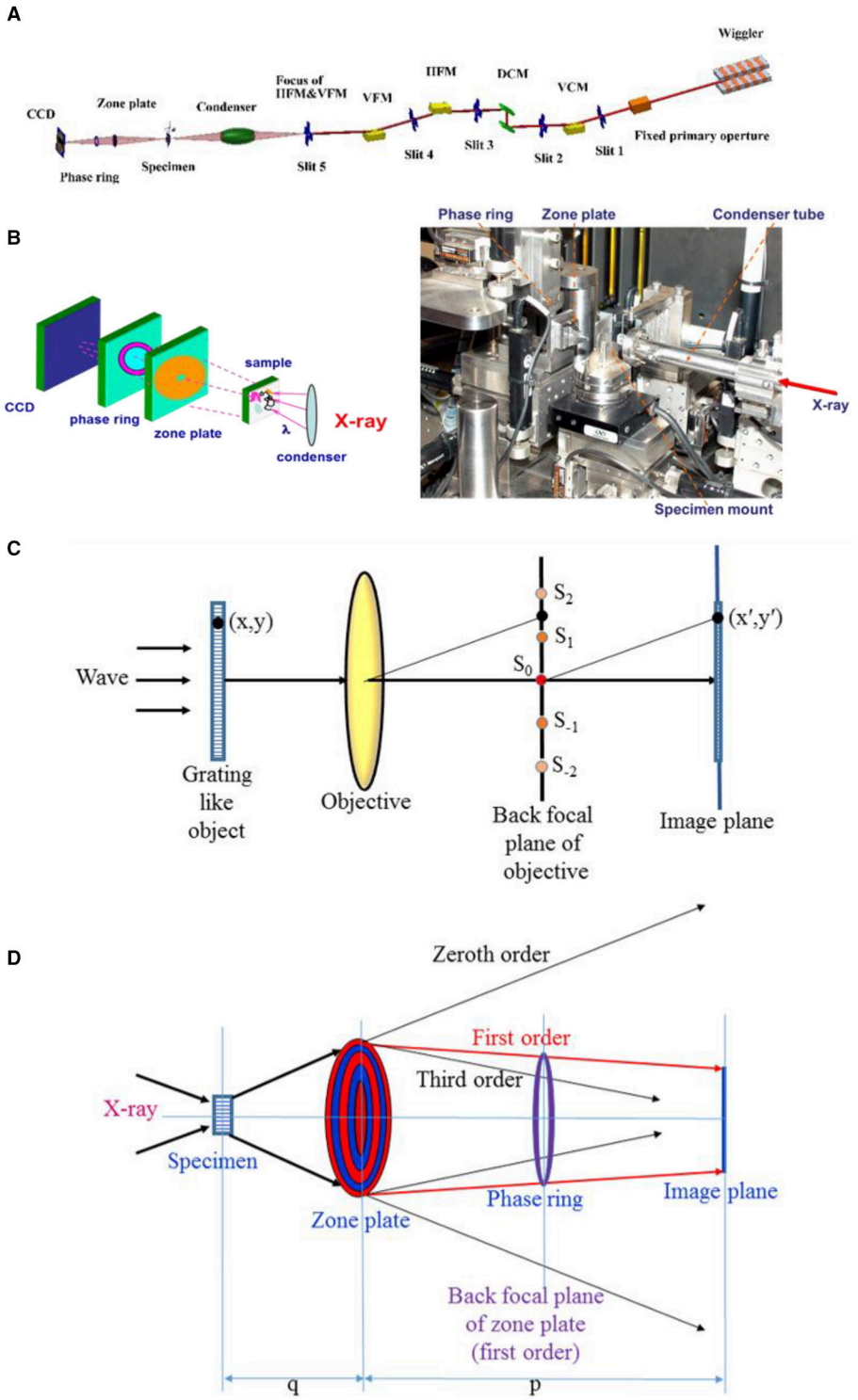

FIGURE 1 | (A) Layout of synchrotron radiation transmission X-ray microscopy (TXM) beamline. **(B)** Sketch (left) and photograph (right) of the TXM instrument. **(C)** Sketch of Abbe theory for image formation in a microscope. **(D)** Sketch of the zone plate and phase ring in the TXM instrument. The zone plate consists of concentric circle zones with Au (or other metal) (red circles) and Si_3N_4 (blue circles) replacements. The phase ring material is gold.

This relationship explains that the phase variation induced by the object is transformed to intensity variation by using Zernike phase contrast method. The image intensity is proportional to the phase of the corresponding element of the object.

Figure 1D shows the arrangement of the zone plate and phase ring in the TXM system. A phase ring is placed at the back focal plane of the zone plate to advance the S_0 phase of the specimen with $\frac{3\pi}{2}$. The thickness z of the phase ring can be estimated by considering the pure phase contrast image as $z = \frac{3\lambda}{4\delta}$. The Fresnel zone plate in the TXM system is the key component in providing spatial resolution. The zone plate structure, which consists of concentric circle zones with Au (or other metal) (red circles) and Si_3N_4 (blue circles) replacements, is shown in **Figure 1D**. X-ray passing through the zone plate will be focused, and it will induce diffraction phenomenon due to the optical path difference. The focal length of the zone plate is written as follows:

$$f_m = 2rdr_n/(m\lambda), \tag{11}$$

where r and dr_n are the radius and the outmost zone width of the zone plate, respectively, m is the diffraction order, and λ is the X-ray wavelength. For the synchrotron radiation TXM system, the monochromatized energy of the incident X-ray is selected by adopting the DCM in the beamline.

The spatial resolution (Δr_m) of the zone plate corresponding to the Rayleigh resolution limit for a circular aperture is determined by the following equation:

$$\Delta r_m = 0.610\lambda/(NA{\cdot}m); = 1.22dr_n/m; \tag{12}$$

where NA is the numerical aperture of the zone plate (NA = $\lambda/(2dr_n)$).

The theoretical diffraction efficiency of the zone plate can be calculated by using rigorous coupled-wave theory. Diffraction efficiency is related to the complex refractive index ($n = 1–\delta–i\beta$), thickness (aspect ratio) of the zone plate, wavelength, and X-ray incident divergence angle. Briefly, the result is proportional to $1/(\pi m)^2$. The practical measured value of the diffraction efficiency of the zone plate is commonly in the range of 10–30%. The zone width uniformity and zone plate thickness are crucial for diffraction efficiency, and they influence the signal-to-noise ratio of the image largely. When the numerical aperture of a zone plate is considerably small compared with the object distance q and image distance p, i.e., NA<<1, the zone plate can be treated as a lens. The object and image distances can be estimated by using the following formula:

$$1/q + 1/p = 1/f. \tag{13}$$

In addition, the magnification M of the zone plate is described as follows:

$$M = p/q. \tag{14}$$

Synchrotron radiation TXM is a distinct technique to reveal the *in-situ* internal morphological structure variation of the LIB material during charging, discharging, and idle processes.

This work used the case on the $xLi_2MnO_3(1\text{-}x)LiMO_2$ ($Li_{1+x}MO_2$, where M = Ni, Co, Mn) system to demonstrate the TXM 2D images in LIB investigations. The $xLi_2MnO_3(1\text{-}x)LiMO_2$ compounds consisting of Li_2MnO_3 and $LiMO_2$ is a promising cathode electrode with a high capacity of 250–300 mAh/g. Nonetheless, this material exhibits poor rate and cycling performance and a large hysteresis in the charge/discharge curves. To improve the capacity and cycling performance of

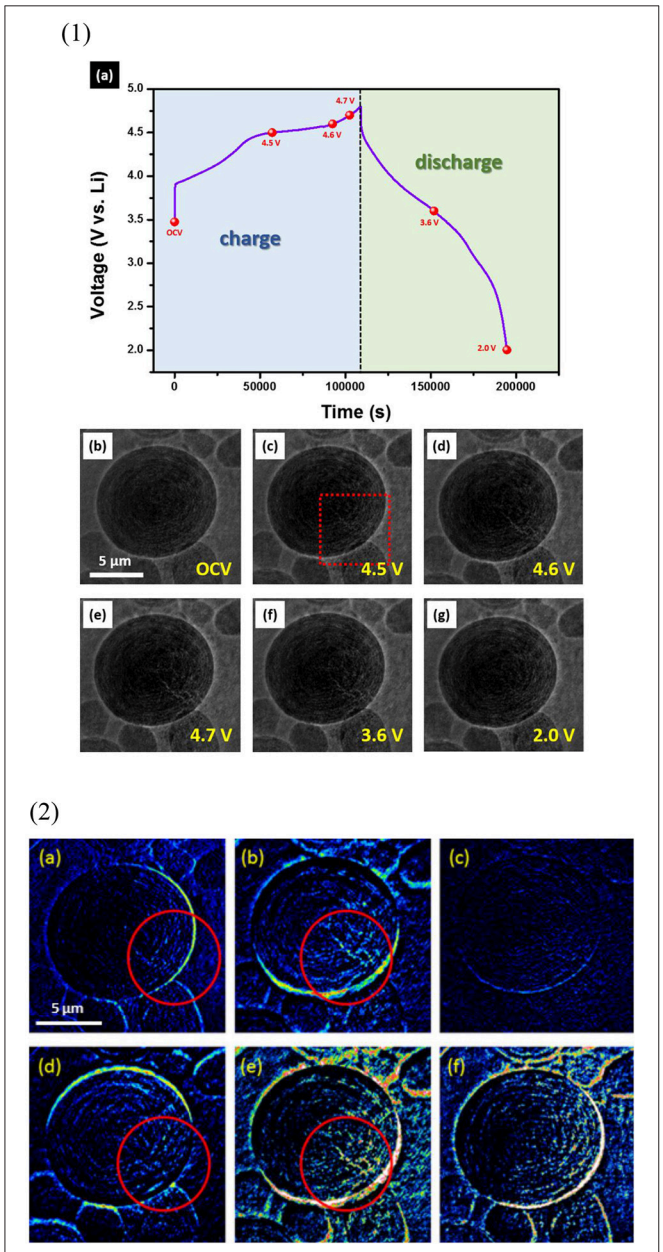

FIGURE 2 | TXM images of a working $Li_2MnO_3{\cdot}LiMO_2$ cathode particle. **(1) (a)** Voltage (V vs. Li^+/Li) vs. time curve during the first charge/discharge cycle. **(b–g)** are the corresponding snapshots of the marked numbers in **(a)**. **(2)** Variation in TXM images in (**1b–g**). (**2a–f**) represent the differences between 4.5 V and open-circuit voltage (OCV), 4.7 and 4.5 V, 3.6 and 4.7 V, 2.0 and 3.6 V, 4.7 V and OCV, and 2.0 V and OCV, respectively. Reprinted permission from Chen et al. (2016). Copyright 2016 American Chemical Society.

electrode materials, the structural evolution of $Li_2MnO_3{\cdot}LiMO_2$ cathode electrode with a high charge capacity (302 mAh/g) is investigated for the first time by combining operando TXM and operando neutron powder diffraction (NPD), which allows the correlation of morphological detail and atomic-scale crystallography to reveal electrode function (Chen et al., 2016). The TXM images of a working $Li_2MnO_3{\cdot}LiMO_2$ cathode particle are shown in **Figure 2-1. Figure 2-1a** presents the voltage (V vs. Li^+/Li) versus time curve during the first charge/discharge cycle, and the corresponding snapshots are shown in **Figures 2-1b–g**. The diameter of the approximately spherical $Li_2MnO_3{\cdot}LiMO_2$ particle at the OCV is 10.95 μm (**Figure 2-1b**). During charging to 4.5 V, cracks occur in $Li_2MnO_3{\cdot}LiMO_2$ particle (**Figure 2-1c**, red rectangular area), which further develop during charging to 4.7 V (**Figures 2-1d**,**e**). Upon discharge, the cracks fade (**f**), the particle almost heals, and the diameter is 10.78 μm at 2 V (**Figures 2-1g**). The variation of TXM images of $Li_2MnO_3{\cdot}LiMO_2$ particle in **Figure 2-1** is shown in **Figure 2-2. Figure 2-2a** displays the difference between 4.5 V and OCV. The cracks in $Li_2MnO_3{\cdot}LiMO_2$ particle are shown in red circle, and the volume reduction is about 2%. **Figure 2-2b** illustrates the variation in 4.7 and 4.5 V. The cracks develop with a volume reduction of 3%. The particle cracks and volume are almost unchanged during 4.7–3.6 V (**Figure 2-2c**). Notably, with further discharge from 3.6 to 2 V, the particle cracks are healed, with a volume expansion of 3% (**Figure 2-2d**). The overall cracks developed during charging (variation from OPC to 4.7 V) and healed during discharging (difference between 2 V and OPC) are illustrated in **Figures 2-2e**,**f**, respectively.

Operando NPD is used to investigate the $Li_2MnO_3{\cdot}LiMO_2$ phase and structure alternation in a complete cell containing a $Li_4Ti_5O_{12}$ (LTO) anode electrode during operation. Cracking in the $Li_2MnO_3{\cdot}LiMO_2$ electrode particle under *in-situ* TXM examination is induced by the solid-solution reaction of the $LiMO_2$ during charging to 4.55 V. The cracks are enhanced upon further charging to 4.7 V with the concurrent two-phase reaction of the $LiMO_2$ phase; this reaction is related to the largest lattice change in any phase and oxygen evolution from the Li_2MnO_3 phase. Crack healing is associated with the reverse solid-solution reaction of the $LiMO_2$ phase during discharge. Significantly, the phase separation during two-phase reaction of $LiMO_2$ phase hinders the complete healing of the electrode particle and results in pulverization over extended cycling. Consequently, the minimization of two-phase and oxygen evolution, which lead to phase separation, is a key strategy to improve the electrode capacity.

SUMMARY AND FUTURE PERSPECTIVES

In this mini review, we introduced the principle of the full field transmission X-ray microscopy and demonstrate one of the most important works that used this technique on the field of Li ion battery research. The full field transmission X-ray microscopy is a distinct and powerful technique for understanding the morphology changes and determining the mechanism of Li-ion insertion/extraction with the electrode materials during operation. Direct observation images provide significant information regarding the manufacture of Li ion batteries.

AUTHOR CONTRIBUTIONS

YFS and NHY wrote the manuscript. RSL conceived the idea and designed the writing content. All authors read and confirmed the paper before the submission.

ACKNOWLEDGMENTS

This work was supported by the Ministry of Science and Technology of Taiwan with contract no. MOST 104-2113-M-002-012-MY3 and Economic Affair of Taiwan with contract no. 107-EC-17-A-22-0497.

REFERENCES

Attwood, D. (1999). *Soft X-ray and Extreme Ultraviolet Radiation*. Cambridge: Cambridge University Press.

Born, M., and Wolf, E. (1999). *Principles of Optics*. Cambridge: Cambridge University Press.

Chen, C. J., Pang, W. K., Mori, T., Peterson, V. K., Sharma, N., Lee, P. H., et al. (2016). The origin of capacity fade in the $Li_2MnO_3{\cdot}LiMO_2$ (M = Li, Ni, Co, Mn) microsphere positive electrode: an operando neutron diffraction and transmission X-ray microscopy study. *J. Am. Chem. Soc.* 138, 8824–8833. doi: 10.1021/jacs.6b03932

Ebner, M., Marone, F., Stampanoni, M., and Wood, V. (2013). Visualization and quantification of electrochemical and mechanical degradation in Li ion batteries. *Science* 342, 716–720. doi: 10.1126/science.1241882

Mansuripur, M. (2002). *Classical Optics and Its Applications*. Cambridge: Cambridge University Press.

Schneider, G. (1998). Cryo x-ray microscopy with high spatial resolution in amplitude and phase contrast. *Ultramicroscopy* 75, 85–104. doi: 10.1016/S0304-3991(98)00054-0

Wang, J., Chen-Wiegart, Y. C., and Wang, J. (2014). In operando tracking phase transformation evolution of lithium iron phosphate with hard X-ray microscopy. *Nat. Commun.* 5:4570. doi: 10.1038/ncomms5570

Wolf, M., May, B. M., and Cabana, J. (2017). Visualization of electrochemical reactions in battery materials with X-ray microscopy and mapping. *Chem. Mater.* 29, 3347–3362. doi: 10.1021/acs.chemmater.6b05114

Xu, Y., Hu, E., Zhang, K., Wang, X., Borzenets, V., Sun, Z., et al. (2017). In situ visualization of state-of-charge heterogeneity within a $LiCoO_2$ particle that evolves upon cycling at different rates. *ACS Energy Lett.* 2, 1240–1245. doi: 10.1021/acsenergylett.7b00263

Conflict of Interest Statement: The authors declare that the research was conducted in the absence of any commercial or financial relationships that could be construed as a potential conflict of interest.

frontiers in Energy Research

HYPOTHESIS AND THEORY
published: 20 August 2018
doi: 10.3389/fenrg.2018.00082

In situ and *Operando* Raman Spectroscopy of Layered Transition Metal Oxides for Li-ion Battery Cathodes

Eibar Flores[1], *Petr Novák*[1] *and Erik J. Berg*[1,2]*

[1] *Electrochemistry Laboratory, Energy and Environment Research Division, Paul Scherrer Institute, Villigen, Switzerland,*
[2] *Department of Chemistry, Ångström Laboratory, Uppsala University, Uppsala, Sweden*

In situ and *operando* Raman spectroscopy is proposed to provide unique means for deeper fundamental understanding and further development of layered transition metal $LiMO_2$ (M = Ni, Co, Mn) oxides suitable for Li-ion battery applications. We compare several spectro-electrochemical cell designs and suggest key experimental parameters for obtaining optimum electrochemical performance and spectral quality. Studies of the most practically relevant $LiMO_2$ compositions are exemplified with particular focus on two experimental approaches: (1) lateral and axial Raman mapping of the electrode's (near-) surface to monitor inhomogeneous electrode reactions and (2) time-dependent single-particle spectra during cycling to analyze the Li_xMO_2 lattice dynamics as a function of lithium content. Raman Spectroscopy is claimed to provide a unique real-time probe of the M-O bonds, which are at the heart of the electrochemistry of $LiMO_2$ oxides and govern their stability. We highlight the need for further fundamental understanding of the relationships between the spectroscopic response and oxide lattice structure with particular emphasis on the development of a theoretical framework linking the position and intensity of the Raman bands to the local Li_xMO_2 lattice configuration. The use of complementary experimental techniques and model systems for validation also deserve further attention. Several novel $LiMO_2$ compositions are currently being explored, especially containing dopings and coatings, and Raman spectroscopy could offer a highly dynamic and convenient tool to guide the formulation of high specific charge and long cycle life $LiMO_2$ oxides for next-generation Li-ion battery cathodes.

Keywords: Raman spectroscopy, *operando*, *in situ*, $LiMO_2$, Li-ion batteries, cathodes

OPEN ACCESS

Edited by:
Neeraj Sharma,
University of New South Wales,
Australia

Reviewed by:
Montserrat Galceran Mestres,
CIC energigune, Spain
Liqiang Mai,
Wuhan University of Technology,
China

***Correspondence:**
Erik J. Berg
erik.berg@kemi.uu.se

Specialty section:
This article was submitted to Energy Storage, a section of the journal Frontiers in Energy Research

Received: *11 April 2018*
Accepted: *27 July 2018*
Published: *20 August 2018*

Citation:
Flores E, Novák P and Berg EJ (2018) In situ and Operando Raman Spectroscopy of Layered Transition Metal Oxides for Li-ion Battery Cathodes. Front. Energy Res. 6:82. doi: 10.3389/fenrg.2018.00082

INTRODUCTION

Lithium-ion batteries (LIBs) are the currently best performing electrochemical energy storage system on the market and are now helping to transform the transportation sector with hybrid and electric vehicles. Although the LIB performance is steadily improving, the demand for more energy (longer driving ranges), higher power output (stronger acceleration), improved dis-/charge efficiency, longer cycle lifetime, and higher safety continue to push the technology to its limits and sometimes beyond, as some accidents did show. It is therefore very important to fully understand the basics of LIBs (Berg et al., 2015; Nitta et al., 2015). Most research efforts today focus on the

positive electrode (commonly referred to as cathode) due to its decisive role in delimiting the overall LIB performance (Tarascon, 2010). During operation, Li^+ de-/intercalate from/into the cathode, which as a result may undergo several transformations in its atomic (lattice symmetries, internal coordinates, defects), electronic (band occupation, energy, overlap) and surface (reconstruction and reaction layers) configurations. The nature and extent of such transformations and particularly their reversibility define cathode performance and in extension its suitability for a given battery application.

The family of layered transition metal oxides $LiMO_2$ (M=Ni, Co, Mn) with α-$NaFeO_2$ structure are the most attractive positive electrodes for LIBs (Ellis et al., 2010). Their development was triggered after $LiCoO_2$ was found to reversibly react with Li^+ and successfully commercialized for portable electronics applications (Blomgren, 2017). Since then, several M substituted versions have been explored and higher capacity, higher operating voltage, longer lasting, and cheaper Li-ion cathodes have been achieved. Despite these continuous incremental increases in performance of $LiMO_2$ based cathodes during the past decade, there is still plenty of room for improvements, but progress is slow due to the lack of fundamental understanding of the adverse side reactions of this class of active materials. Particularly the underlying mechanisms governing irreversible structural phase transformations (induced by mechanical stress and cracking, cation site mixing, lattice oxygen release, and electrolyte decomposition) require further characterization and analysis in order to devise new design principles and guide further scientific and engineering efforts (Vetter et al., 2005; Ellis et al., 2010; Hausbrand et al., 2015; Hou et al., 2016; Mai et al., 2017).

Conventional characterization techniques typically monitor long-range atomic ordering (neutron and x-ray diffraction), bulk electronic and coordination structures (x-ray absorption/emission/scattering and nuclear magnetic resonance), composition and morphology (electron microscopies and spectroscopies) of the oxides, (Grey and Dupré, 2004; McBreen, 2009; Huang and Ikuhara, 2012; Balagurov et al., 2014; Shao, 2014; Qian et al., 2015; Sharma et al., 2015) which all in turn are correlated to their electrochemical performance (as probed by galvanostatic dis-/charge cycling, transient pulse tests and impedance spectroscopy). For commercial-like cells these techniques are however mostly or solely applied *ex situ*, that is, the oxides are analyzed before and/or after electrochemical cycling because of their inherent experimental restrictions (such as sample preparation procedure, high vacuum or confined geometries). Although *ex situ* measurements provide a first approach and often guide more specialized experiments, there are serious limitations: (i) most dynamic information is lost due to thermodynamic relaxation of the oxides during preparation for analysis, (ii) the risk of contamination and surface modification during transfer/washing, (iii) the voltage (or state of lithiation) interval between measurements is limited to how precise can be controlled the cycling stopping conditions on different electrodes, and (iv) the use of a different electrode for each measurement requires a highly controlled electrode preparation and composition with reproducible electrochemical data to compare with.

Raman spectroscopy is a highly versatile technique widely used to characterize electrode materials (Baddour-Hadjean and Pereira-Ramos, 2009). Briefly, a monochromatic light source with frequency ν_0 is shined upon the sample and the scattered light is collected, filtered, and decomposed into a frequency Raman spectrum by a dispersive element (e.g., a grating). Scattered light with frequencies $\lambda_i \pm \nu_0$ slightly deviating λ_i from the frequency of the irradiating light source ν_0 arise after interaction with the sample. The shifted frequencies λ_i are characteristic of its atomic vibrational modes [for a comprehensive tutorial on Raman Spectroscopy, we refer e.g. to the book by Ferraro et al. (2003)]. Since ν_0 usually is a frequency within the visible range of the electromagnetic spectrum, Raman spectroscopy possesses inherent advantages for *operando* characterization of electrode materials, including: (i) the light probe is potentially non-destructive, (ii) single oxide secondary particles in the composite electrode can be studied by using a microscope with a (sub-) micrometer lateral resolution, (iii) common window materials transparent to visible light can be implemented in the electrochemical cell for *operando* measurement, (iv) the spectrum acquisition time scales (in the order of seconds) available in standard instrumentation enable sufficient time resolution, and (v) strong infrared absorbers such as electrolyte solvents display moderate Raman signals and thus enable discerning vibrations from inorganic oxide particles.

The number, frequencies and intensities of the modes (or bands) in the Raman spectrum reveal fundamental lattice and bonding properties of the sample down to several hundreds of nanometers from its surface. A detailed analysis of the Raman spectra can infer lattice symmetry, coordination geometry, oxidation state, the coexistence of several phases, the presence of defects, impurities, strains and other phenomena relevant for the characterization of electrode materials for LIBs, as summarized in the comprehensive review from Baddour-Hadjean et al. (Baddour-Hadjean and Pereira-Ramos, 2009). Further reviews emphasize the effects of electrode interactions with electrolyte (Aurbach et al., 2007), the historical development of *in situ* experimental setups (Stancovski and Badilescu, 2014), and highlight results obtained by *in situ* electrode mapping (Shao, 2014). Raman spectroscopy applied on other battery chemistries such as lithium-oxygen (Gittleson et al., 2015) and lithium-sulfur (Tan et al., 2017) face similar challenges as in LIBs, therefore, they are also instructive. However, most measurements are performed *ex situ* due to the limitations outlined above. *In situ* and *operando* Raman measurements are on the contrary desired because the Raman spectrum is sensitive to particle size (Wang et al., 2002) and preferential crystallite orientations (Tornheim et al., 2017), which can vary from sample to sample and render an *ex situ* comparison difficult or impossible. In addition, spectral features from different particles at a given state of charge are inherently disperse due to lateral (Lei et al., 2005) and axial (Gilbert et al., 2018) (de)lithiation inhomogeneities.

Herein we propose that *in situ* and *operando* Raman spectroscopy provides unique means for deeper fundamental understanding and further development of layered transition

metal $LiMO_2$ (M = Ni,Co,Mn) oxides suitable for Li-ion battery applications. In order for us to argue for the future prospects of the technique we report on the past progress in the field and compare with our recent findings along with our interpretations. We start by comparing several spectro-electrochemical cell designs and discuss measurement parameters we consider crucial for obtaining optimum electrochemical performance and spectral quality. In the **second** part, we illustrate how the currently available experimental setups already permit *in situ* and *operando* measurements on $LiMO_2$ with high spectral and time resolutions. In particular, a comparison of our results on $LiCoO_2$, $LiNi_{0.8}Co_{0.15}Al_{0.05}O_2$, and $LiNi_{0.33}Co_{0.33}Mn_{0.33}O_2$ to previous experimental data reveal that each oxide displays an intrinsic Raman response to (de)lithiation, which we rationalize based on cycling-dependent changes of oxygen local environment and electronic structure. We conclude our report by proposing means of how *in situ/operando* Raman spectroscopy can be further developed beyond state-of-art to provide novel insights into $LiMO_2$ degradation processes, both on the electrode as well on the material level.

EXPERIMENTAL CONSIDERATIONS

The key challenge in the design of an *in situ*/*operando* cell for Raman spectroscopy is to incorporate an optically transparent window while keeping optimal electrochemical performance of the cell, a task full of compromises that have been historically approached with diverse cell designs (Stancovski and Badilescu, 2014). Examples of cell configurations are beaker (**Figure 1A**) (Inaba et al., 1995), Swagelok (Gross et al., 2013; Gross and Hess, 2014), pouch cell (**Figure 1B**) (Ghanty et al., 2015), coin-type (Singh et al., 2012; Huang et al., 2016), and custom-made cells (Novák et al., 2000) (**Figure 1C**). The beaker cell design can be easily assembled, customized and reused with different electrode chemistries; however both electrode geometry and excess electrolyte filling are very far from the specifications typically found for commercial LIB cells. The pouch-type design requires more effort in the assembly since most of the components are for single-time use and disposed after every measurement. Reproducing the exact electrode alignment and pressure may also prove difficult. Several coin-cell type designs employ reusable components and the electrode assembly is fitted within a cell frame machined to the exact dimensions of the electrodes, thus minimizing the risk of misalignment. Our work focused on the development of a custom-made coin-cell type configuration (**Figure 1C**) and we had identified many key parameters for achieving optimum performance:

Working Distance

The distance between the light source and the probed oxide sample should be minimized in order to maximize the solid angle of scattered light collection thereby improving the signal-to-noise ratio (Hendra, 2006). More importantly, minimizing the working distance also reduces the amount of electrolyte-filled space between the electrode and the optically transparent window, which reduces the strong Raman scattering from the electrolyte. To this point, the thickness of the optical window is already of importance and our choice fell on a thin microscope glass (thickness 100 μm).

Cell Sealing

Gas leaking into and electrolyte leaking from the cell result in poor electrochemical performance and higher risk of measuring artifacts associated with side reactions. Tight sealing is generally achieved by compression of rubber and/or plastic O-rings. Special care is however necessary to guarantee the chemical stability of the sealant in contact with the electrolyte. We have found both polytetrafluoroethylene (PTFE) and high density polyethylene (HDPE) O-rings to be chemically resistant toward typical Li-ion battery carbonate based electrolytes and effective in sealing the cell body toward leakage (cell part #6-7, **Figure 1C**).

Electrode Pressure

A strong mechanical compression of the electrode assembly is necessary to ensure the electrode integrity and reduce cell overpotentials (Poli et al., 2011). For instance, inappropriate electrical contact between the electrodes and their current collectors would lead to inhomogeneous electrode reactions and eventually misinterpretation of underlying cell (electro-)chemistry. A uniform and stable electrode compression is typically achieved by employing a spring and a hard window to resist fracture. In our studies the spring provides a pressure over the electrode stack of ca. 20 N/cm^2 (Lanz et al., 2013).

Electrode Size

Although only a few micrometer electrode surface is necessary for conventional Raman Spectroscopy based microscopes, small electrodes are difficult to handle and increase the risk of electrode misalignment and edge effects during electrochemical cycling. In addition, small electrodes require low currents that may approach the sensitivity limits of typical galvanostats.

Electrolyte Choice

Organic carbonate based electrolytes with $LiPF_6$ salt are almost exclusively used for commercial batteries. However, the $LiPF_6$ salt is prone to form fluorescent species, which result in high baselines that mask the Raman signals (Kostecki and McLarnon, 2004; Jarry et al., 2015). Many Raman spectroscopy studies therefore rather employ $LiClO_4$ salt for the electrolyte to reduce fluorescence masking and display comparable electrochemical performance in short term experiments (Xu et al., 2004).

Reactivity of Cell Components

All materials in contact with the electrodes and electrolyte (cell body, sealing parts, transparent window) should be chemically and electrochemically stable. For instance, polyetherketones (PEEK) belong to few plastics sufficiently stable in contact with metallic Li and thus often employed for *operando* cell designs. Construction materials including fluorine, especially Teflon, should preferably be avoided because of their reactivity with metallic Li.

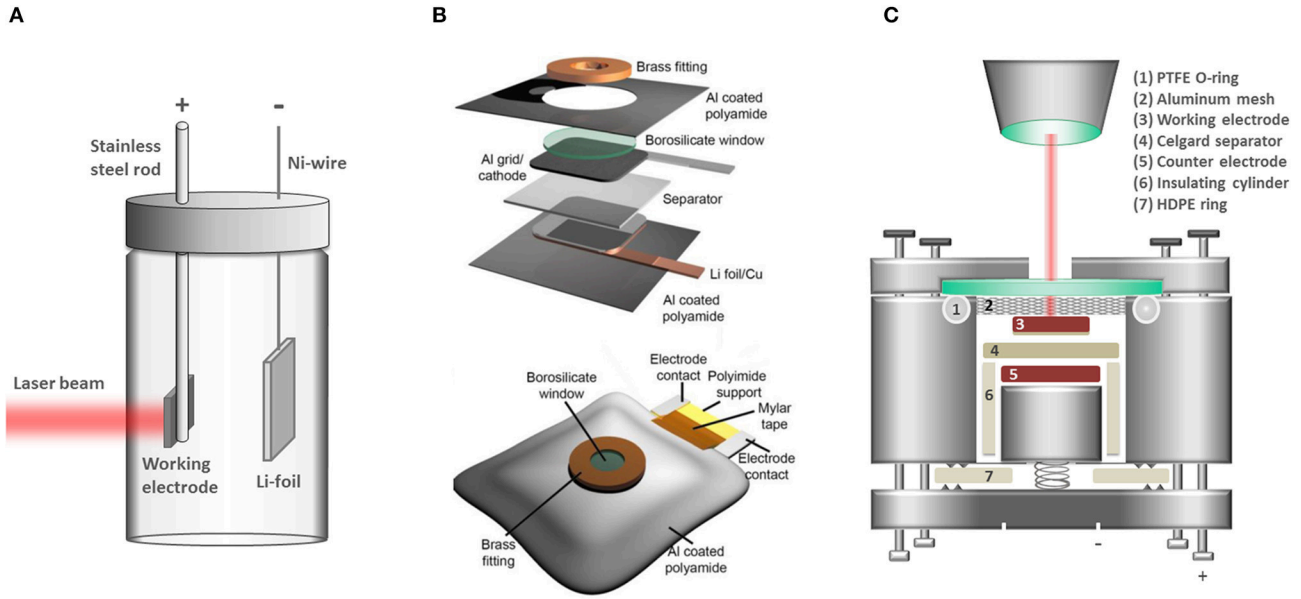

FIGURE 1 | Typical cell designs for *in situ*/*operando* Raman spectroscopy. **(A)** Beaker (pyrex) cell design used e.g., by Inaba et al. (1995). **(B)** Pouch cell from Ghanty et al. [reprinted from reference (Ghanty et al., 2015) with permission of John Wiley and Sons]. **(C)** Custom-made coin-cell type design developed in our group.

Laser Excitation Wavelength

The laser excitation wavelength can influence the Raman band intensity since the radiated power by an oscillating dipole is inversely proportional to the fourth power of the laser wavelength ($I \sim \lambda^{-4}$) (Keresztury, 2006), e.g., shifting from 514 nm to 633 nm excitation reduces the Raman scattering power by 43%. However, several layered materials are prone to electronic resonance (Ammundsen et al., 1999; Dokko et al., 2002; Julien, 2002; Gross and Hess, 2014), that is, the intensity of certain Raman bands is greatly enhanced if the excitation wavelength approaches or matches the energy of an electronic transition. The closer the laser photon energy is to the materials band-gap, the stronger the enhancement of the Raman cross-section (Clark and Dines, 1986). In this context, the resonance effect can be deliberately exploited for obtaining better signal to noise ratios. **Figures 2A,B** show an example from a study where a laser excitation of 633 nm (1.9 eV) was chosen to measure the Raman spectrum of $HNiO_2$ since this wavelength has the closest energy to the materials band gap of 1.8 eV (as estimated by UV-Vis measurements) and consequently results in greatly enhanced Raman signals (Chen et al., 2016). In addition, an appropriate choice of excitation wavelength can minimize fluorescence effects. The degree of fluorescent emission depends on how close the laser wavelength is to the absorption maxima of the fluorescent species, which generally is found toward the blue side of the visible spectra (Kostecki and McLarnon, 2004; Jarry et al., 2015). In summary, the laser excitation wavelength is a compromise between a high Raman scattering power ($I \sim \lambda^{-4}$, i.e., shorter wavelengths preferred) and the need for a low background signal (i.e., longer wavelengths preferred to reduce the fluorescence background) (Julien et al., 2006).

Laser Specific Power

The laser specific power should be sufficiently high to achieve reliable signal-to-noise ratios, but low enough to avoid laser-induced sample transformations. Most measurements reported herein couple the Raman spectrometer to an optical microscope in order to achieve sampling spot sizes down to 1 μm. Irradiating such small areas with high photon fluxes increases the risk of laser induced sample burning. Typical laser specific powers range from 0.01 to 1.0 mW/μm^2 (**Figure 2C**). Ruther et al. shows that a lithium-rich oxide is susceptible to laser-induced phase transformations generally above 1.0 mW/μm^2, but this limit can be lower for delithiated electrodes (Ruther et al., 2014) and even lower for *in situ*/*operando* conditions because of the presence of the organic electrolyte. An *in situ* stability test of the material at different laser powers for each type of experiment is recommended to avoid laser-induced sample transformations. Of course, electrolyte boiling with bubble formation must be avoided under any circumstances.

For the *operando* Raman spectroscopy measurements reported herein, the Raman spectra were acquired using a Labram HR800 Raman microscope (Horiba- Jobin Yvon) with a He–Ne excitation laser (632.8 nm). A grating was used as dispersion element with a groove density of 600 g/mm that attains a 2 cm^{-1} spectral resolution. The hole and slit of the confocal system were fixed at 1,000 μm and 100 μm, respectively. The laser was focused on the sample using a 50× (numerical aperture 0.55) objective, which produced a laser spot of ca. 4 μm diameter. The nominal laser power was filtered down 2 mW or 0.2 mW to avoid sample overheating. Every spectrum recorded results from the average of at least 5 acquisitions of more than 100 s each, depending on the intrinsic Raman scattering power

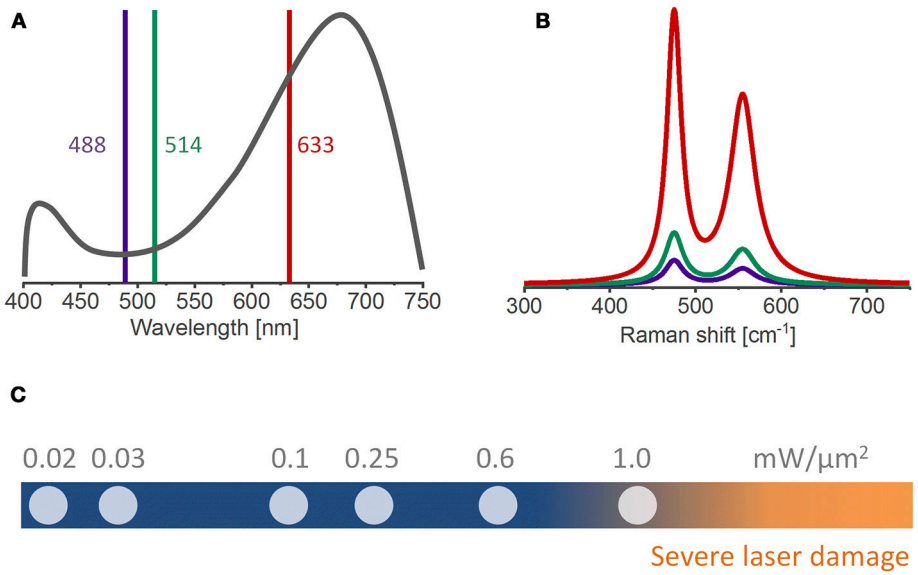

FIGURE 2 | (A) UV-Vis and **(B)** Raman spectra of $HNiO_2$ using different excitation wavelengths [adapted from reference (Chen et al., 2016)]. The 633 nm wavelength, closest to the absorption maxima of the material, yield enhanced Raman bands. **(C)** A range of laser specific powers commonly used in *ex situ* and *in situ* Raman measurements. The risk of laser-induced sample burning and/or structural changes increases for laser powers above 1 mW/μm^2.

of the active material. Composite electrodes were conventionally prepared by mixing oxide powders [$LiCoO_2$ (Alfa Aesar), $LiNi_{0.8}Co_{0.15}Al_{0.05}O_2$ (Toda), $LiNi_{0.33}Co_{0.33}Mn_{0.33}O_2$ (BASF)] with conductive carbon (Super C65, Imerys Graphite and Carbons) and PVdF binder (Solvay) in NMP, coating the formed slurry on top of Celgard 2400 separator (Celgard LLC) with a wet thickness of 100 μm, and letting it dry overnight at 80°C. The electrodes were punched (14 mm diameter), re-dried in dynamic vacuum (80°C for >12 h), and assembled in our custom-made Raman cell (**Figure 1C**), together with an electrolyte-wetted Celgard 2400 separator (16 mm diameter, Celgard LLC) and a lithium metal disk (0.2 mm thick, 12 mm diameter, Sigma-Aldrich). More details on electrode preparation are reported elsewhere (Streich et al., 2017) and the employed electrolyte is 1M $LiClO_4$ in 1:1 (w/w) ethylene carbonate(EC)/dimethyl carbonate (DMC). All *operando* experiments were performed at 10 mA/g rate between 3.0 and 4.3 V vs. Li^+/Li.

PROGRESS OF *IN SITU/OPERANDO* RAMAN SPECTROSCOPY ON $LiMO_2$ OXIDES

Background

Figure 3 shows a schematic representation of the $LiMO_2$ unit cell. Li, M (Ni, Co, Mn) and O atoms arrange into a rhombohedral layered structure with the $R\bar{3}m$ space group and consist of octahedrally coordinated cations within an oxygen cubic close-packed network based on ABCABC stacking (O3 phase) forming alternating LiO_6 and MO_6 slabs. M occupies the 3b Wyckoff sites while Li^+ resides at the 3a sites. In this context, the term stoichiometric refers to compounds with only one Li per formula unit, unlike the over-lithiated $Li_{1+y}M_{1-y}O_2$ oxides, which are not considered here. A factor group analysis based on the lattice symmetry predicts two Raman active modes for each transition metal in the unit cell: the E_g mode (**Figure 3**, orange arrows) involving an opposite motion of oxygens along adjacent O-layers and the A_{1g} mode where oxygens move symmetrically along the c-axis and is mostly stretching in character (**Figure 3**, purple arrows) (Julien, 2000). Stretching modes are typically stiffer than bending modes, so the higher wavenumber band is assigned to the A_{1g} mode whereas the lower wavenumber band is assigned to the E_g mode.

Figure 4 shows the Raman spectrum we have recorded of $LiCoO_2$ (top) and $LiNiO_2$ (bottom) pristine powders, along with several substitutional variants. Raman spectrum assignments are as discussed above generally based on the number of observed bands, their positions in wavenumbers and relative intensities. Assignment of $LiCoO_2$ spectrum is straightforward since it clearly displays only the two expected E_g and A_{1g} Raman active modes (Inaba et al., 1997). However, the substitution of further transition metals (M=Mn, Ni, etc.) results in complex spectral envelopes displaying more bands than the expected A_{1g}/E_g pair of modes, thus complicating interpretation. Several previous reports implicitly assume that a spectrum is uniquely determined only by the 1st coordination shell around M (i.e. individual MO_6 octahedra), which renders the spectral envelope of mixed $LiMO_2$ (M=Ni+Co+Mn) a simple combination of six bands: an E_g/A_{1g} pair from NiO_6, another from CoO_6, and a third pair from MnO_6, each at the same wavelength positions as expected for $LiNiO_2$, $LiCoO_2$ and α-$LiMnO_2$, respectively. Such an approach presumes that each pair contributes to the total intensity according to the particular M proportion and the result would

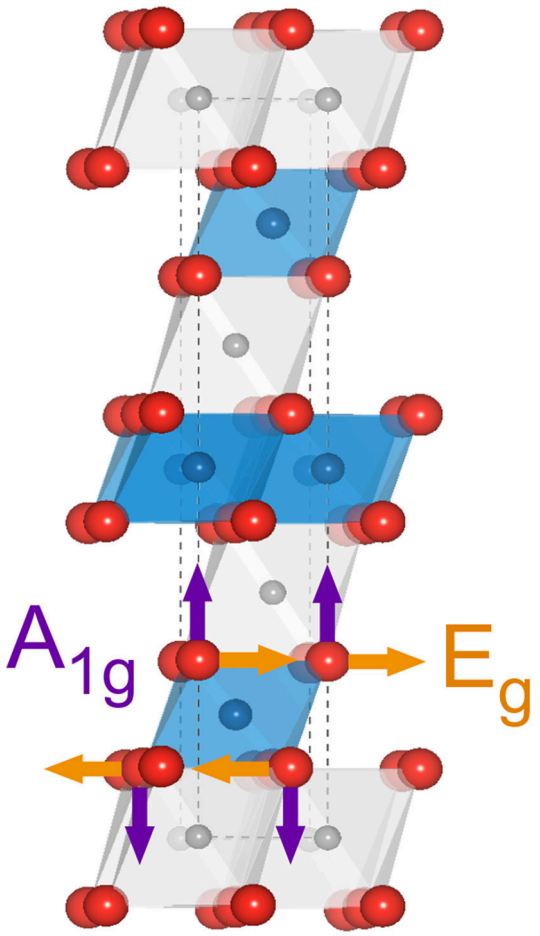

FIGURE 3 | Schematic representation of the $LiMO_2$ unit cell. The gray, blue and red spheres represent Li, M and O atoms, respectively. The atomic displacements from E_g and A_{1g} vibrational modes are shown in orange and purple arrows, respectively.

be equivalent to simply mixing $LiNiO_2$, $LiCoO_2$, and α-$LiMnO_2$ powders (Zhang et al., 2010; Ben-Kamel et al., 2012; Ruther et al., 2014; Ghanty et al., 2015). In an apparent support of this idea, the presence of Mn in the $LiMO_2$ lattice generally correlates to the existence of broad bands above 600 cm^{-1} (**Figures 4B–D**), which are absent in Mn-free oxides (**Figures 4A,E,F**) and grow in intensity together with the Mn proportion. The bands > 600 cm^{-1} can thus be tentatively assigned to A_{1g} modes of MnO_6 octahedra. However, increasing the Mn proportion also shifts those bands to higher wavenumbers (**Figures 4B–D**), suggesting a concomitant evolution of the Mn-O bonding strength. Our further analysis of **Figure 4** provides no clear relations between the spectral envelopes and the composition of the oxides. For instance, a simple sum of contributions does not capture the influence of Co substitution in $LiNiO_2$ (**Figures 4E,F**) since increasing Co proportion induces a general band broadening and a blue-shift of the A_{1g} mode (Julien, 2000) instead of resulting on independent Co and Ni A_{1g} bands, as expected given they are separated by 53 cm^{-1} in the pure compounds (**Figures 4A–F**). The previous example and several others (Koga et al., 2012; Ruther et al., 2014) illustrate the difficulty in assigning and interpreting the Raman spectra of $LiMO_2$ since the band positions, widths and intensities rather reflect strongly coupled local environments resulting from complex interactions between homogeneously distributed transition metals in the 3b Wyckoff sites. Furthermore, we stress that even comparisons of spectra from oxides of similar composition, particularly when measured at different setups under different experimental conditions, are a challenge and requires very mindful analysis of several effects introducing spectral variations. For instance, the oxide crystal size (Gouadec and Colomban, 2007), orientation (Inaba et al., 1997; Tornheim et al., 2017), purity (Gouadec and Colomban, 2007) and even internal stresses (Wang et al., 2005) within the oxide can significantly modulate the spectra. Experimental conditions, such as temperature, incident light polarization and wavelength, as well as sample exposure times also necessarily have to be taken into consideration, which is immediately seen in the comparison of measurements from different literature sources below. In the following examples we mainly focus on how spectra of several Li_xMO_2 oxides vary upon delithiation ($x < 1$) and how the change may be related to oxygen stacking order, lattice parameters, electronic band structure, bond characters and lengths.

$LiCoO_2$ (LCO)

Practical electrochemical delithiation of LCO is limited to a $x = 0.5–0.6$ (cutoff potential ~ 4.2 V vs. Li^+/Li, going up to ca. 4.3 V for more advanced industrial LCO cells). Above 4.2 V there is a risk of oxygen gliding (Lu et al., 2012) and oxidation (Ensling et al., 2014), which can quickly deteriorate the electrochemical performance unless the LCO is doped and surface coated. Pristine $LiCoO_2$ powder displays two Raman bands as expected, which are sharp and intense (**Figure 4A**). The intensity of the band at 596 cm^{-1} has a strong dependence on the polarization of the incident radiation so it has been assigned to the A_{1g} mode while the E_g mode is assigned to the band at 486 cm^{-1} (Inaba et al., 1997; Perkins et al., 1997; Liu et al., 2015a). Despite similar compositions, the spectra of LCO below illustrate that the experimentally measured position and relative intensity of the E_g and A_{1g} bands differ between literature reports, which is as discussed above related to slightly differing experimental condition during oxide synthesis, electrode preparation, and measurement configuration.

The evolution of the Raman bands upon delithiation had been vaguely interpreted in the literature, but we believe they are dominated by the insulator-metal transition of LCO. Delithiation ($1.0 > x > 0.95$) leads to a diluted concentration of lithium vacancies V_{Li} that bind to electron holes to form an impurity band in the electronic density of states (DOS), which renders the material an electric insulator (Marianetti et al., 2004). When the number of V_{Li} increases on further delithiation ($0.95 > x$) this particular hole configuration is disrupted and a new phase grows with metallic-like conduction (Ménétrier et al., 1999). The region $0.95 > x > 0.75$ is described as a two-phase transition between $Li_{0.95}CoO_2$ (Mott-insulator) and $Li_{0.75}CoO_2$ (metal). The latter phase is 3-orders of magnitude more conductive (Takahashi

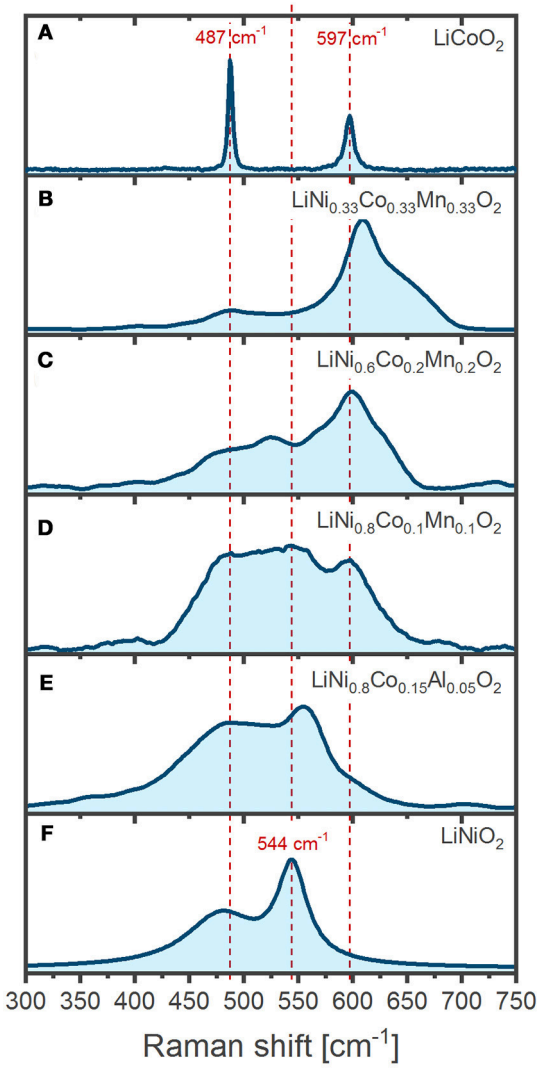

FIGURE 4 | Comparison of the Raman spectra from various isostructural $LiMO_2$: **(A)** $LiCoO_2$ (LCO) **(B)** $LiNi_{0.33}Co_{0.33}Mn_{0.33}O_2$ (NCM111) **(C)** $LiNi_{0.6}Co_{0.2}Mn_{0.2}O_2$ (NCM622) **(D)** $LiNi_{0.8}Co_{0.1}Mn_{0.1}O_2$ (NCM811) **(E)** $LiNi_{0.8}Co_{0.15}Al_{0.05}O_2$ (NCA) **(F)** $LiNiO_2$ (LNO).

et al., 2007) than $Li_{0.95}CoO_2$, thus drastically shallowing the penetration depth of the laser due to the so-called skin effect. Consequently, both Raman bands of LCO weaken in intensity as the $Li_{0.75}CoO_2$ phase grows. Although many reports evidence a drastic vanishing of the bands within the $0.95 > x > 0.75$ region (Itoh et al., 2000; Kuwata et al., 2012), several studies present spectra in which the band intensities survive past $0.75 > x$ and display weakened, broader and red shifted bands (**Figure 5A**, middle) (Heber et al., 2015; Otoyama et al., 2016a; Snyder et al., 2016; Park et al., 2017). Peak asymmetries (**Figure 5A**, top) possibly reveal the presence of the second phase $Li_{0.75}CoO_2$ with a larger c-lattice parameter (Inaba et al., 1997; Nishi et al., 2013). However, the origin of such disparate results between studies of LCO is unclear. Our *operando* measurements (**Figure 5A**, bottom) show that both Raman bands of LCO quickly fade as soon as delithiation starts with no remaining intensity once the lithium content drops below $x = 0.92$, thus indicating that the metallic phase appears from the very beginning of the delithiation process.

On relithiation the bands return to their initial positions (Kuwata et al., 2012), but with significantly weakened intensities [(Itoh et al., 1997, 2000) and our results] and sometimes overlap with new bands (Snyder et al., 2016). The lower intensities result from an incomplete relithiation and a persistence of the conducting $Li_{0.75}CoO_2$ phase. Long-term cycling has showed that the bands keep weakening and broadening when comparing spectra at the end of every lithiation (Snyder et al., 2016) until they entirely disappear > 300 cycles (Kuwata et al., 2012). The insulating phase $Li_{0.95}CO_2$ is no longer recovered due to Li-consuming electrolyte side reactions (Snyder et al., 2016) or Li^+ trapped in cracked (isolated) particles (Kuwata et al., 2012). The insulator-metallic transition of LCO can be further exploited for real-time monitoring of inhomogeneous electrode reactions. *In situ* electrode mapping (**Figure 5B**) by contrasting lithiated and delithiated particles has demonstrated that delithiation is spatially inhomogeneous: after charge around 6% of the particles remain lithiated, and after discharge ca. 10% of the particles remain delithiated. These observations illustrate severe SOC inhomogeneity within the composite electrode (Nishi et al., 2013).

$LiNiO_2$ (LNO)

$LiNiO_2$ (LNO) offers a higher specific charge at lower cost compared to LCO, but the partial presence of divalent Ni in lithium sites complicates the synthesis of the stoichiometric material and several detrimental phase transformations driven by lithium vacancy ordering result in rapid capacity fade during cycling (Delmas et al., 1999; Kalyani and Kalaiselvi, 2005). The Raman spectrum of LNO is barely reported in the literature and only *ex situ* spectra of its powder form have been presented (Julien, 2000; Zhang et al., 2005). The two main bands expected for the $R\bar{3}m$ space group are observed at 465 and 545 cm^{-1} and assigned to the E_g and A_{1g} phonon modes, respectively, in analogy to the LCO spectrum (Julien, 2002).

The Raman spectrum of the Li_xNiO_2 powder electrochemically delithiated to $x = 0.8$ has been reported to show broadened, weakened and red shifted bands compared to the pristine spectrum (**Figure 6**, top) proposedly resulting from either a reduction of the rhombohedral distortion and/or an increase in electronic conductivity as in the case of LCO. However, compared to LCO (Takahashi et al., 2007), the electronic conductivity of LNO barely changes upon delithiation (Molenda et al., 2002), and any influence thereof should be minor. Our *ex situ* experiments show that electrochemical delithiation of the powder ($LiNiO_2$, Aldrich) to $x = 0.4$ (**Figure 6**, bottom) results in sharper and stronger bands (along with a new shoulder at 572 cm^{-1}), which agrees with the observations for other Ni-rich $LiMO_2$ discussed below. However, the spectra from Julien et al. and ours were recorded at differing SOC ($x =$ 0.8 and 0.4, respectively) and one should again consider that the electrochemical response of $LiNiO_2$ might vary largely given its

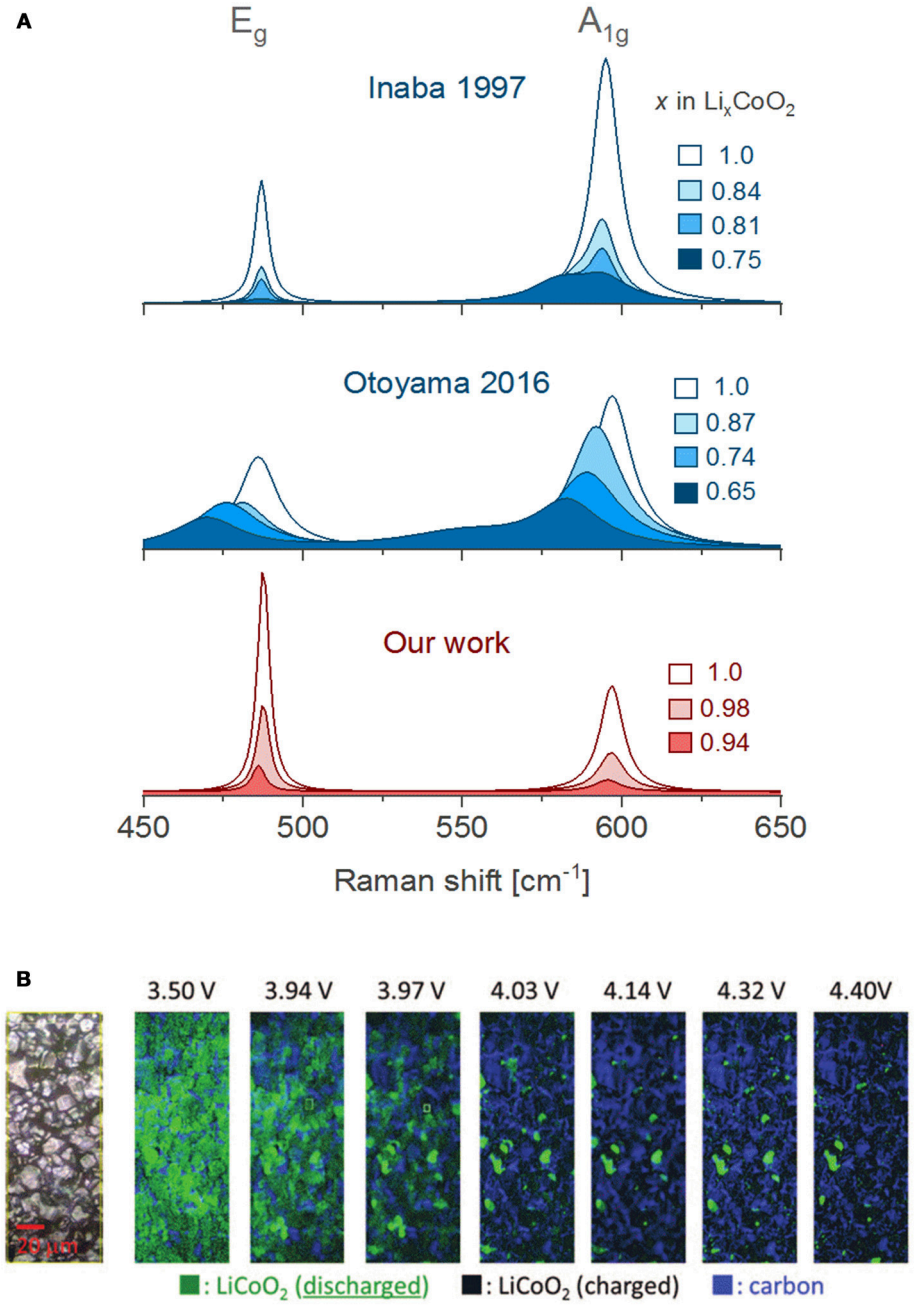

FIGURE 5 | (A) Comparison of *in situ*/*operando* Raman spectra obtained by Inaba et al. using a PC based liquid electrolyte (Inaba et al., 1997), Otoyama et al. in an all-solid-state cell (Otoyama et al., 2016a) and our results using an EC/DMC based liquid electrolyte. **(B)** *In situ* Raman mapping of a composite $LiCoO_2$ electrode during the first charge (reprinted from reference Nishi et al., 2013 with minor editions, with permission of the Electrochemical Society). All spectra were here adapted for clarity of comparison.

sensitivity to the synthesis conditions and electrode preparation procedure (causing inhomogeneous electrode reactions). In addition, Julien et al. employed a 476 nm laser excitation instead of a 632 nm used in our work. The latter wavelength probes the material near resonance conditions, assuming that the absorption maxima for $LiNiO_2$ is the same as reported for isostructural $HNiO_2$ (Clark and Dines, 1986; Chen et al., 2016). We nevertheless stress that there is a lack of data and further *in situ*/*operando* Raman measurements are necessary to elucidate the inherent behavior of these Raman bands and relate them to the known crystallographic transformations occurring during cycling; such links would be highly valuable to understand the redox activity of other Ni-rich layered oxides such as NCA and NCM811 as well.

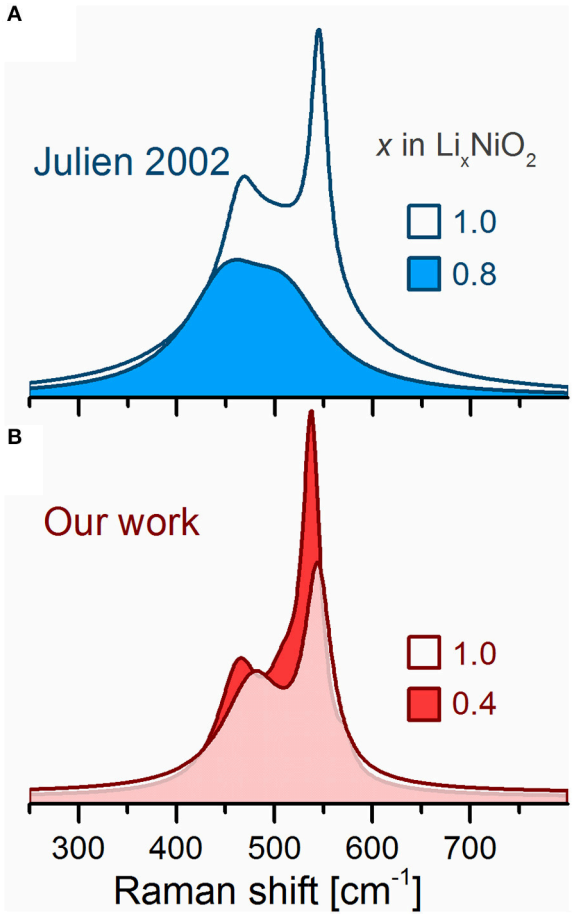

FIGURE 6 | *Ex situ* Raman spectra of electrochemically delithiated $LiNiO_2$. **(A)** Spectra adapted from Julien (2002). **(B)** Our results.

$LiNi_{0.8}Co_{0.15}Al_{0.05}O_2$ (NCA)

Co and Al substitution within $LiNiO_2$ improves significantly the structural stability and electrochemical performance of the oxide (Delmas and Croguennec, 2002; Chen et al., 2004), The optimized composition $LiNi_{0.8}Co_{0.15}Al_{0.05}O_2$ has been successfully commercialized for use in electric vehicles (e.g., Tesla Model X) (Blomgren, 2017). Pristine NCA displays two main Raman active bands, which again are assigned to the E_g (485 cm^{-1}) and the A_{1g} (560 cm^{-1}) modes (**Figure 7A**). Upon delithiation the bands intensify but at different rates. Although the origin of such behavior is unknown, the *x*-dependent E_g/A_{1g} intensity (or area) ratios have been used for *in situ* mapping of the SOC of the individual NCA particles in the composite electrodes (Lei et al., 2005). Compositional maps reveal the occurrence of inhomogeneous electrode reactions analogous to the observations for LCO described above (**Figure 5B**). For instance, several NCA particles were evidenced to remain lithiated during cycling while others reach undesirably high levels of delithiation (Nanda et al., 2011). These inhomogeneities seem to originate from a retreat of the conductive carbon additive upon cycling, equally observed by composition maps of the carbon Raman active bands. Carbon retreat leads to electronic disconnection of the NCA active particles, which thus experience non-uniform delithiation rates and state of charge throughout the electrode (Kostecki and McLarnon, 2004; Kostecki et al., 2006; Kerlau et al., 2007).

Recently, we recorded *operando* the spectral evolution of the Raman bands of NCA during three full dis-/charge cycles. In qualitative agreement with previous works, the bands display a general growth on delithiation (**Figure 7A**) (Lei et al., 2005). In addition, a set of new bands above 600 cm^{-1} are clearly resolved enabled by our improved signal-to-noise ratio. The spectral trends resemble those of $LiNiO_2$ (**Figure 6**, bottom) suggesting they are inherent to Ni-rich oxides. All band positions, intensities and widths were retrieved by deconvoluting the spectral envelope into Lorentz-type peak profiles at a comparably high time resolution (above 200 spectra per cycle). The band positions and heights during the first cycle (**Figure 7B**) show remarkable reversibility on dis-/charge and clearly correlate to the redox activity of NCA. The highly detailed shifts in band positions are found uncorrelated to the evolution of crystallographic (average) parameters, thus challenging the believed straightforward relation between lattice parameters and wavenumber shifts. The lack of correlation also emphasizes the dependence of band positions on local lattice features that cannot be resolved by conventional diffraction techniques. The Raman peak trends may be divided into stages indicating three different SOC-dependent processes. Early at $x \sim 0.8$ (Stage I), a step increase in band intensities occur, which coincides with the commonly reported dissolution of the native $-CO_3$ layer at the surface of NCA particles (observed $\sim$ 3.78 V vs. Li^+/Li). Later, at $x \sim 0.67$ (Stage II) the U-shaped trend of the E_g band positions reaches a minimum and the bands above 600 cm^{-1} appear and grow in intensity. DFT phonon calculations assign both phenomena to the formation of a local lithium vacancy ordering that coincides with the redox process at 3.73 V vs. Li^+/Li for NCA. Approaching the end of charge, at $x \sim 0.2$ (Stage III), the band intensities of both bands reach their maxima, which coincides with oxygen gas release from NCA. The evidence suggest that the redox process above 4.20 V vs. Li^+/Li originates from an $O^{2-} \rightarrow O^{-}/O$ oxidation involving electron depletion from M-O states and oxygen loss from the lattice. X-ray absorption spectroscopy further supports the hypothesis of bulk oxygen oxidation at high states of charge (Yoon et al., 2007; Kleiner et al., 2015). Our *operando* Raman spectroscopy measurements with high time resolution was demonstrated to provide further detailed insights into local structural evolution of NCA lattice upon electrochemical cycling (Flores et al., 2018).

$LiNi_aCo_bMn_{1-a-b}O_2$ (NCMs)

Although NCA based electrodes provide outstanding specific charge, a performance fade commonly associated with Ni-migration from the transition metal layer into the Li sites and the safety concerns due to highly exothermic reactions with electrolyte at high SOC motivate the further development of the $LiMO_2$ based oxides (Liu et al., 2015b). Partial substitution with Mn has been found to suppress Li/Ni exchange, improve

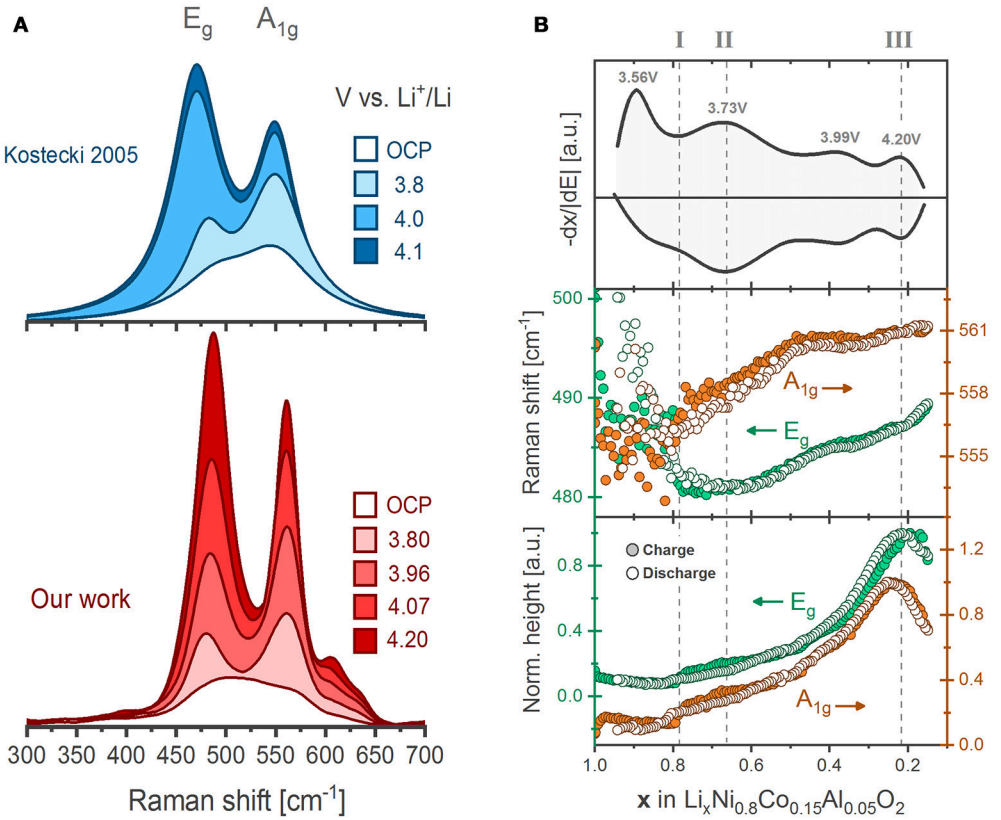

FIGURE 7 | (A) Comparison of the *in situ* evolution of NCA Raman spectrum as recorded by Kostecki et al. (Lei et al., 2005) and here adapted along with our results (Flores et al., 2018). **(B)** Differential charge plot of NCA together with the fitted peak positions and heights of the E_g and A_{1g} bands as a function of lithium content during the first galvanostatic cycle between 3.0 and 4.3 V vs. Li^+/Li (~C/20 rate). Each data point result from the deconvolution of a single spectrum.

cycling performance, and several Ni/Co/Mn based $LiMO_2$ oxides, commonly denoted NCMs, have been explored (Noh et al., 2013).

$LiNi_{0.33}Co_{0.33}Mn_{0.33}O_2$ (NCM111)

The Raman spectrum of pristine NCM111 is an envelope of highly overlapping bands (**Figure 4B**). There are at least three distinguishable bands, at 400 cm^{-1}, 485 cm^{-1} and 610 cm^{-1}, but a deconvolution of the E_g/A_{1g} pair of bands is not straightforward since the latter is partially overlapped by further bands above 620 cm^{-1}. The presence of more bands than the E_g/A_{1g} pair predicted for a $R\bar{3}m$ lattice [as confirmed by x-ray diffraction (Lanz et al., 2014)] indicates the existence of distinct, lower local symmetries likely resulting from a complex (Ni/Co/Mn)-O bonding (Sun and Zhao, 2017). *Ex situ* measurements have nevertheless revealed sufficient spectral differences between NCM111 particles at different SOC to permit for the collection of compositional maps of the composite electrode during cycling. As for LCO and NCA, spatially inhomogeneous electrode reactions also arise in NCM111 based electrodes (Kerlau et al., 2007).

Our *operando* Raman spectra of NCM111 (**Figure 8**) start (OCP) and end (4.3 V vs. Li^+/Li) with similar spectral envelopes as previously reported *ex situ* (Kerlau et al., 2007; Otoyama et al., 2016b). Unlike the case for NCA and LCO, the progressive evolution of the spectra upon de-/lithiation is hard to evaluate due to the difficulty of spectral deconvolution. The fitting solution space (goodness of fitting vs. fitting parameters) of the highly overlapping bands is likely to have multiple and virtually indistinguishable local minima, meaning that a unique solution to the fitting problem does not exist. In this sense, our attempts of fitting the bands of NCM111 result in arbitrary parameters likely not representative of the physical system. Meaningful information can however still be obtained by a visual description of the spectral envelopes without attempting deconvolution. Two cycling stages can be distinguished in **Figure 8** according to the spectral profiles. In the initial stage ($1.0 > x > 0.7$) the spectra (in blue) experience a general weakening on delithiation, possibly related to a 6-fold increase in the electronic conductivity (Qiu et al., 2012) of NCM111 due to a band gap narrowing (Hwang et al., 2003). In the second stage ($0.7 > x > 0.36$) the envelopes clearly transforms as the band at 485 cm^{-1} sharpens and a new band at 555 cm^{-1} appears. The cycling-dependent evolution of the spectra is fully consistent with the *in situ* behavior reported by Lanz et al. (2014). There is no crystallographic evidence of structural transitions with the formation of new phases in the $1.0 > x > 0.3$ range (Kim and Chung, 2004; Yin et al.,

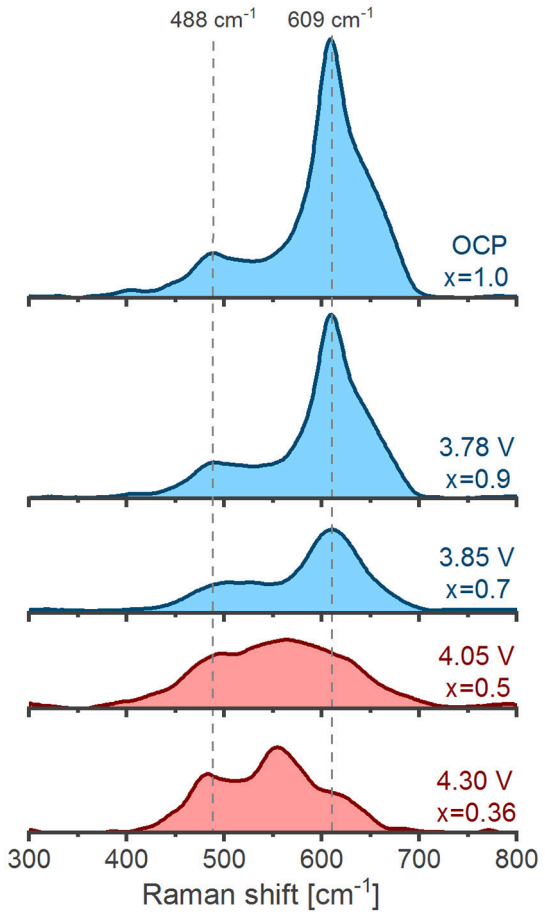

FIGURE 8 | *Operando* Raman spectra of NCM111 during charge. The evolution of the spectral envelopes is classified into an initial general weakening stage (blue) and a later envelope transformation stage (red).

2006). However, since the bands are similar to delithiated LNO (**Figure 6**) and NCA (**Figure 7**, left), they likely result from a $Ni^{IV}O_6$ – rich environment. The two-staged evolution of the spectral envelope of NCM111 appears to correlate to a stepwise oxidation (1) $Ni^{2+} \rightarrow Ni^{3+}$ and (2) $Ni^{3+} \rightarrow Ni^{4+}$ expected within the $1.0 > x > 0.33$ range (Hwang et al., 2003; Kim and Chung, 2004; Tsai et al., 2005), thus suggesting that Ni valence has a significant influence on the spectral profile of NCM111.

$LiNi_{0.5}Co_{0.2}Mn_{0.3}O_2$ (NCM523)

To the best of our knowledge neither *in situ* nor *operando* spectra of NCM523 has been reported in literature. *Ex situ* spectra of pristine NCM523 compare reasonably well to NCM111, as shown in reference (Ruther et al., 2014). Electrochemically delithiated NCM523 also displays a pair of bands (Nguyen et al., 2016), but at 500 and 617 cm^{-1}, considerably blue-shifted from the pair observed in NCM111 (485 and 555 cm^{-1}); the shifts might be a consequence of the different balance of Ni oxidation states in the two formulations (Dixit et al., 2017). *Ex situ* Raman spectroscopic electrode compositional mapping has shown that cracked particles (appearing after 30 cycles) feature broader and red-shifted Raman bands compared to undamaged particles, which was associated with a unit cell volume expansion preceding particle deterioration (Börner et al., 2016). The compositional maps of the electrode cross section clearly reveal the de-/lithiation inhomogeneity expected from electronic disconnections among the cracked NCM523 particles (Gilbert et al., 2018).

$LiNi_{0.8}Co_{0.1}Mn_{0.1}O_2$ (NCM811)

Ex situ Raman spectra (not shown) of pristine and electrochemically delithiated NCM811 composite electrodes are similar to NCA shown in **Figure 7**, which may be expected from their nearly identical composition. The initially broad envelope of two bands centered at 500 and 558 cm^{-1} grow, sharpen and red-shift on delithiation (Saavedra-Arias et al., 2009). Ghanty et al. identified several bands in their spectra for NCM811 and assigned an E_g/A_{1g} pair for each transition metal. Their *in situ* measured spectral bands displayed a general intensity increase on delithiation up to 4.3 V vs. Li^+/Li, involving as well non-monotonic band shifts and broadenings. The trends in fitted band parameters was rationalized in form of an evolution of the crystallographic lattice parameters, but due to the strong overlap of the fitted bands, further interpretations could not be made with sufficient certainty (Ghanty et al., 2015).

CONCLUDING REMARKS

In situ and *operando* Raman spectroscopic characterization of $LiMO_2$ oxides for Li-ion battery cathodes has mainly been explored for two purposes: (1) Compositional (near-) surface mapping to monitor inhomogeneous electrode reactions and (2) understanding of Li_xMO_2 lattice evolution during dis-/charge cycles. Raman spectro-electrochemical microscopy can provide micrometer-sized lateral resolution and thereby offers unique access to the de-/lithiation dynamics of individual oxide particles in the Li-ion composite cathodes. *Operando* mapping of reaction inhomogeneities could—despite the already numerous reports in the field (Kostecki and McLarnon, 2004; Lei et al., 2005; Kostecki et al., 2006; Kerlau et al., 2007; Nanda et al., 2011; Nishi et al., 2013)—be further developed to reveal the underlying causes of electric disconnection and cracking behavior of oxide particles in commercial-like electrodes under varying operating conditions (high current rates, elevated temperatures, etc.). The retrieved Raman spectra may furthermore not solely be employed to contrast individual particles, but in addition be analyzed to identify possible phase transformations and the course of the de-/lithiation processes within the single oxide particles and their aggregates. For that, however, further fundamental understanding of the Raman spectra of the Li_xMO_2 oxide family is a prerequisite. Raman spectroscopy probes the local lattice structure and its physicochemical parameters, such as atomic composition/coordination, crystal symmetry, bond character, length and strength, all contributing to the recorded spectrum. In order to determine the influence of each parameter and their complex interactions, two major challenges have to be overcome, namely: the spectra have to be confidently fitted and interpreted.

The spectral features are however often highly overlapped envelopes that cannot be deconvoluted with unique fitting parameters, thus the behavior of the bands cannot be followed individually during cycling. In order to modulate and optimize the spectral acquisition process, we propose that excitation lasers of different (or tunable) wavelengths should be employed, e.g., to take advantage of effects such as electronic resonance to enhance/suppress individual band intensities.

However, even if a reasonable fitting of band position and intensity succeeds, both need to be interpreted:

Band position: Molecular mechanics tells us that the band position (in units of cm^{-1} or in vibration frequency) of a given vibrational mode is proportional to the restoring force of any stretching or bending M-O bond motion, or more specifically to the square root of the spring constant of the corresponding bond configuration (Hotokka, 2006). Therefore, band position gauges the propensity of the vibrating atoms (i.e., the oxygens in $LiMO_2$) to remain in their equilibrium position. Both bond length and strength are here decisive and more refined models to justify their respective influence on the vibrational modes are desired.

Band intensity: Although the fading intensity of the Raman bands of LCO during charge can be confidently related to the skin effect, this case is more exception than rule. Particularly the Ni-rich $LiMO_2$ oxides experience no (or a very minor) increase in electronic conductivity during delithiation, yet the bands grow in intensity significantly. Besides the often used skin effect hypothesis, we had identified several plausible phenomena explaining the band intensity changes: (i) Li^+ de-/insertion affects the electron distribution around oxygen atoms, which effectively modulates the degree of polarizability of the associated M-O vibrations (Boulet-Roblin et al., 2016). (ii) Li_xMO_2 redox tunes the electronic band gap closer to the laser excitation wavelength and enhances the Raman cross-section by electronic resonance (Clark and Dines, 1986). (iii) Lattice strain build-up due to expansion/contraction of the oxide during cycling can also enhance Raman band intensities (Wang et al., 2005). (iv) A reduction of the rhombohedral distortion of $R\bar{3}m$ $LiMO_2$ would degenerate the A_{1g} and E_g modes into the inactive T_{2g} mode of the Fm3m cubic lattice (Julien and Massot, 2002; Julien et al., 2006). (v) The transition between Jahn-Teller active and inactive transition metals results in varying degrees of MO_6 distortions that can influence the Raman intensities due to change of site symmetry (Nakai et al., 1998; Balasubramanian et al., 2000).

Progress in the field will be slow (or completely arrest) unless more fundamental relationships between the $LiMO_2$ structure and its Raman spectroscopic response are established. As an inspiring example, graphitic materials are nowadays routinely characterized with Raman spectroscopy because such relationships are well known (Tuinstra and Koenig, 1970; Ferrari, 2007; Pimenta et al., 2007; Sole et al., 2014). Achieving a similar level of understanding of $LiMO_2$ will require multiple approaches, of which complementary techniques, model substrates and theoretical modeling deserve emphasis.

Several authors perform complementary structural characterization by x-ray diffraction (XRD) to describe the evolution of the Raman bands of Li_xMO_2 and relate them to crystallographic lattice parameters (Julien, 2000; Ben-Kamel et al., 2012; Ghanty et al., 2015). Intuitively, since the energetics of the lattice influences both the long-range atomic order and the vibration modes, XRD and Raman spectra should hence be much related. Indeed, the Raman spectra of $LiMO_2$ with different M substitution ratios and lithium contents show red/blue band shifts that generally correlate to the expansion/contraction of the lattice parameters (Julien et al., 1997; Julien, 2000, 2002). However, the techniques cannot always be paralleled because they probe fundamentally different ordering scales: XRD reflections indicate average interplanar spacings in a long-ranged atomic ordering while Raman bands originate from short-ranged local environments. The crystallographic lattice parameters and symmetry might remain invariant to the occurrence of highly local phenomena, such as non-cooperative Jahn Teller distortion (Rougier et al., 1995; Chen et al., 2011) and cation ordering (Reimers, 1992; Peres et al., 1999; Zeng et al., 2007), which are thermodynamically favored but invisible when solely investigating the long-range order (Dompablo et al., 2001; Zhecheva et al., 2002). Our recent study of NCA make particular emphasis on the lack of correlation between the lattice parameters and Raman band positions (Flores et al., 2018). Alternative techniques probing the local lattice structure, such as x-ray absorption and nuclear magnetic resonance spectroscopy, are therefore most suitable and further validation studies in the field are desired.

Model substrates could significantly facilitate characterization and band assignment. For instance, single crystals with sufficiently defect-free lattices generally yield sharp Raman bands distinguishable within otherwise broad and overlapping envelopes coming from multi-crystalline inhomogeneous environments. In addition, the dependence of the Raman bands on crystal size and orientation, temperature, light polarization and wavelength could be investigated and provide further insights into the symmetry of the modes and their interactions with electronic and magnetic properties of the oxides (Perkins et al., 1997; Liu et al., 2015a).

Although factor group analysis provides the expected number of Raman active vibrations and an approximate picture of the corresponding atomic displacements (Fateley et al., 1971), the prediction of band frequencies requires an explicit modeling of classical or quantum mechanical atomic interactions (i.e. bonding) (Hotokka, 2006; Matsuura and Yoshida, 2006). Electronic structure calculations are equally important to describe the band intensities, which depend on the effect that the atomic displacements have on the dielectric properties of the lattice (Keresztury, 2006; Maschio et al., 2013). Several modern *ab initio* software packages contain models to simulate the Raman spectrum of a wide range of materials, including the transition metal oxides. Despite the intensive research and modeling efforts dedicated to the $LiMO_2$ oxides in recent years, few theoretical studies of the Raman spectroscopic response of this important class of oxides have been reported so far.

Looking ahead, surface enhanced Raman spectroscopy (SERS) receives increasing attention in the field of Li-ion batteries and could provide unique insights into the local $LiMO_2$ structure, particularly at the interface to the electrolyte. Tornheim et al. demonstrated that the Raman intensity of NCM523 can be plasmon-enhanced by two orders of magnitude when the particles of active material are electroplated with sub-micron gold clusters (Tornheim et al., 2017); hence, the spectra recording times can be potentially reduced from fractions of hour to a few seconds. However, the highly reactive gold clusters are likely not stable in contact with the electrolyte at high anodic potentials. As a remedy, the plasmonic nanoparticles can be coated with a thin layer of an inert oxide in order to passivate the reactive surfaces (shell-isolated nanoparticle-enhanced Raman spectroscopy i.e. SHINERS) (Li et al., 2010). The approach had been used *in situ* to detect the formation of Li_2O at the surface of the Li-rich NCM, but the bands were barely above the noise level and the signals from the oxide were not detected (Hy et al., 2014). In general SHINERS have been seldom used on electrode materials because (i) the electrode surface is rough, heterogeneous and difficult to coat uniformly, and (ii) the challenging synthesis required to produce highly controlled shell isolated nanoparticles able to yield reproducible results (Lin et al., 2009). However, the promise of second and sub-second resolved electrode reactions justify further development of operando SERS.

In situ and *operando* Raman Spectroscopy provides a unique direct probe of the M-O bonding, which is at the heart of the electrochemistry of $LiMO_2$ oxides and govern their stability. Several novel $LiMO_2$ compositions are currently being explored with a particular focus on dopings and coatings. We propose that a further development of Raman Spectroscopy could in this context offer a highly dynamic and convenient tool to guide the formulation of high specific charge and long cycle life $LiMO_2$ oxides for next-generation Li-ion battery cathodes.

AUTHOR CONTRIBUTIONS

All authors listed have made a substantial, direct and intellectual contribution to the work, and approved it for publication.

ACKNOWLEDGMENTS

EF and EB acknowledges Swiss National Science Foundation (SNSF) under the Ambizione Energy funding scheme (Grant No. 160540).

REFERENCES

Ammundsen, B., Burns, G. R., Islam, S., Kanoh, H., and Rozière, J. (1999). Lattice dynamics and vibrational spectra of lithium manganese oxides: a computer simulation and spectroscopic Study. *J. Phys. Chem. B* 103, 5175–5180. doi: 10.1021/jp984398l

Aurbach, D., Markovsky, B., Salitra, G., Markevich, E., Talyossef, Y., Koltypin, M., et al. (2007). Review on electrode–electrolyte solution interactions, related to cathode materials for Li-ion batteries. *J. Power Sour.* 165, 491–499. doi: 10.1016/j.jpowsour.2006.10.025

Baddour-Hadjean, R., and Pereira-Ramos, J.-P. (2009). Raman microspectrometry applied to the study of electrode materials for lithium batteries. *Chem. Rev.* 110, 1278–1319. doi: 10.1021/cr800344k

Balagurov, A. M., Bobrikov, I. A., Samoylova, N. Y., Drozhzhin, O. A., and Antipov, E. V. (2014). Neutron scattering for analysis of processes in lithium-ion batteries. *Russ. Chem. Rev.* 83, 1120–1134. doi: 10.1070/RCR4473

Balasubramanian, M., Sun, X., Yang, X. Q., and McBreen, J. (2000). *In situ* X-Ray absorption studies of a high-rate LiNi0.85Co0.15O2 cathode material. *J. Electrochem. Soc.* 147, 2903–2909. doi: 10.1149/1.1393624

Ben-Kamel, K., Amdouni, N., Mauger, A., and Julien, C. M. (2012). Study of the local structure of LiNi0.33+δMn0.33+δCo0.33−2δO2 (0.025≤δ≤0.075) oxides. *J. Alloys Compd.* 528, 91–98. doi: 10.1016/j.jallcom.2012.03.018

Berg, E. J., Villevieille, C., Streich, D., Trabesinger, S., and Novák, P. (2015). Rechargeable batteries: grasping for the limits of chemistry. *J. Electrochem. Soc.* 162, A2468–A2475. doi: 10.1149/2.0081514jes

Blomgren, G. E. (2017). The development and future of lithium ion batteries. *J. Electrochem. Soc.* 164, A5019–A5025. doi: 10.1149/2.0251701jes

Börner, M., Horsthemke, F., Kollmer, F., Haseloff, S., Friesen, A., Niehoff, P., et al. (2016). Degradation effects on the surface of commercial LiNi0.5Co0.2Mn0.3O2 electrodes. *J. Power Sour.* 335, 45–55. doi: 10.1016/j.jpowsour.2016.09.071

Boulet-Roblin, L., Villevieille, C., Borel, P., Tessier, C., Novák, P., and Ben Yahia, M. (2016). Versatile approach combining theoretical and experimental aspects of raman spectroscopy to investigate battery materials: the case of the LiNi 0.5 Mn 1.5 O 4 Spinel. *J. Phys. Chem. C* 120, 16377–16382. doi: 10.1021/acs.jpcc.6b04155

Chen, C. H., Liu, J., Stoll, M. E., Henriksen, G., Vissers, D. R., and Amine, K. (2004). Aluminum-doped lithium nickel cobalt oxide electrodes for high-power lithium-ion batteries. *J. Power Sour.* 128, 278–285. doi: 10.1016/j.jpowsour.2003.10.009

Chen, D., Xiong, X., Zhao, B., Mahmoud, M. A., El-Sayed, M. A., and Liu, M. (2016). Probing structural evolution and charge storage mechanism of NiO2Hx electrode materials using in *operando* resonance raman spectroscopy. *Adv. Sci.* 3:1500433. doi: 10.1002/advs.201500433

Chen, H., Freeman, C. L., and Harding, J. H. (2011). Charge disproportionation and jahn-teller distortion in LiNiO2 and NaNiO2: a density functional theory study. *Phys. Rev. B* 84, 1–7. doi: 10.1103/PhysRevB.84.085108

Clark, R. J. H., and Dines, T. J. (1986). Resonance Raman spectroscopy, and its application to inorganic chemistry. new analytical methods (27). *Angew. Chemie Int. Edn. Engl.* 25, 131–158. doi: 10.1002/anie.198601311

Delmas, C., and Croguennec, L. (2002). Layered Li(Ni, M)O2 systems as the cathode material in lithium-ion batteries. *MRS Bull.* 27, 608–612. doi: 10.1557/mrs2002.196

Delmas, C., Menetrier, M., Croguennec, L., Levasseur, S., Peres, J. P., Pouillerie, C., et al. (1999). Lithium batteries: a new tool in solid state chemistry. *Int. J. Inorg. Mater.* 1, 11–19. doi: 10.1016/S1463-0176(99)00003-4

Dixit, M., Markovsky, B., Schipper, F., Aurbach, D., and Major, D. T. (2017). Origin of structural degradation during cycling and low thermal stability of Ni-rich layered transition metal-based electrode materials. *J. Phys. Chem. C* 121, 22628–22636. doi: 10.1021/acs.jpcc.7b06122

Dokko, K., Mohamedi, M., Anzue, N., Itoh, T., and Uchida, I. (2002). *In situ* raman spectroscopic studies of LiNi x Mn 2 – x O 4 thin film cathode materials for lithium ion secondary batteries. *J. Mater. Chem.* 12, 3688–3693. doi: 10.1039/B206764A

Dompablo, M. E. A., Marianetti, C., Van Der, V. A., and Ceder, G. (2001). Jahn-Teller mediated ordering in layered Li x M O 2 compounds. *Phys. Rev. B* 63:144107. doi: 10.1103/PhysRevB.63.144107

Ellis, B. L., Lee, K. T., and Nazar, L. F. (2010). Positive electrode materials for Li-Ion and Li-batteries. *Chem. Mater.* 22, 691–714. doi: 10.1021/cm902696j

Ensling, D., Cherkashinin, G., Schmid, S., Bhuvaneswari, S., Thissen, A., and Jaegermann, W. (2014). Nonrigid band behavior of the electronic structure of

$LiCoO_2$thin film during electrochemical li deintercalation. *Chem. Mater*. 26, 3948–3956. doi: 10.1021/cm501480b

Fateley, W. G., McDevitt, N. T., and Bentley, F. F. (1971). Infrared and raman selection rules for lattice vibrations: the correlation method. *Appl. Spectrosc*. 25, 155–173. doi: 10.1366/000370271779948600

Ferrari, A. C. (2007). Raman spectroscopy of graphene and graphite: disorder, electron-phonon coupling, doping and nonadiabatic effects. *Solid State Commun*. 143, 47–57. doi: 10.1016/j.ssc.2007.03.052

Ferraro, J. R., Nakamoto, K., and Brown, C. W. (2003). *Introductory Raman Spectroscopy, 2nd Edn*. California, CA: Academic press.

Flores, E., Vonrüti, N., Novák, P., Aschauer, U., and Berg, E. J. (2018). Elucidation of LixNi0.8Co0.15Al0.05O2 redox chemistry by *operando* raman spectroscopy. *Chem. Mater.* 30, 4694–4703. doi: 10.1021/acs.chemmater.8b01384

Ghanty, C., Markovsky, B., Erickson, E. M., Talianker, M., Haik, O., Tal-Yossef, Y., et al. (2015). Li^+ -Ion extraction/insertion of Ni-Rich $Li_{1+x}(Ni_yCo_zMn_z)_wO_2$ ($0.005< x <0.03$; $y : z =8:1$, $w \approx 1$) Electrodes: *in situ*, X. R. D., and Raman Spectroscopy Study. *ChemElectroChem* 2, 1479–1486. doi: 10.1002/celc.201500160

Gilbert, J. A., Maroni, V. A., Cui, Y., Gosztola, D. J., Miller, D. J., and Abraham, D. P. (2018). Composition and impedance heterogeneity in oxide electrode cross-sections detected by raman spectroscopy. *Adv. Mater. Interfaces* 5:1701447. doi: 10.1002/admi.201701447

Gittleson, F. S., Yao, K. P. C., Kwabi, D. G., Sayed, S. Y., Ryu, W. H., Shao-Horn, Y., et al. (2015). Raman spectroscopy in lithium-oxygen battery systems. *ChemElectroChem* 2, 1446–1457. doi: 10.1002/celc.201500218

Gouadec, G., and Colomban, P. (2007). Raman spectroscopy of nanomaterials: how spectra relate to disorder, particle size and mechanical properties. *Prog. Cryst. Growth Charact. Mater*. 53, 1–56. doi: 10.1016/j.pcrysgrow.2007.01.001

Grey, C. P., and Dupré, N. (2004). NMR studies of cathode materials for lithium-ion rechargeable batteries. *Chem. Rev*. 104, 4493–4512. doi: 10.1021/cr020734p

Gross, T., Giebeler, L., and Hess, C. (2013). Novel *in situ* cell for Raman diagnostics of lithium-ion batteries. *Rev. Sci. Instrum*. 84:073109. doi: 10.1063/1.4813263

Gross, T., and Hess, C. (2014). Raman diagnostics of $LiCoO_2$ electrodes for lithium-ion batteries. *J. Power Sour*. 256, 220–225. doi: 10.1016/j.jpowsour.2014.01.084

Hausbrand, R., Cherkashinin, G., Ehrenberg, H., Gröting, M., Albe, K., Hess, C., et al. (2015). Fundamental degradation mechanisms of layered oxide Li-ion battery cathode materials: methodology, insights and novel approaches. *Mater. Sci. Eng. B* 192, 3–25. doi: 10.1016/j.mseb.2014.11.014

Heber, M., Schilling, C., Gross, T., and Hess, C. (2015). *In situ* Raman and UV-Vis spectroscopic analysis of lithium-ion batteries. *Mater. Res. Soc. Symp. Proc*. 1773, 33–40. doi: 10.1557/opl.2015.634

Hendra, P. J. (2006). "Sampling considerations for raman spectroscopy," in *Handbook of Vibrational Spectroscopy,* ed J. M. Chalmers (Chichester: John Wiley and Sons, Ltd).

Hotokka, M. (2006). "Calculation of vibrational frequencies by molecular mechanics," in *Handbook of Vibrational Spectroscopy*, ed J. M. Chalmers (Chichester: John Wiley and Sons, Ltd), 216–234.

Hou, P., Chu, G., Gao, J., Zhang, Y., and Zhang, L. (2016). Li-ion batteries: phase transition. *Chinese Phys. B* 25:016104. doi: 10.1088/1674-1056/25/1/016104

Huang, J.-X., Li, B., Liu, B., Liu, B.-J., Zhao, J.-B., and Ren, B. (2016). Structural evolution of NM (Ni and Mn) lithium-rich layered material revealed by *in-situ* electrochemical Raman spectroscopic study. *J. Power Sources* 310, 85–90. doi: 10.1016/j.jpowsour.2016.01.065

Huang, R., and Ikuhara, Y. (2012). STEM characterization for lithium-ion battery cathode materials. *Curr. Opin. Solid State Mater. Sci*. 16, 31–38. doi: 10.1016/j.cossms.2011.08.002

Hwang, B. J., Tsai, Y. W., Carlier, D., and Ceder, G. (2003). A combined computational/experimental study on $LiNi_{1/3}Co_{1/3}Mn_{1/3}O_2$. *Chem. Mater*. 15, 3676–3682. doi: 10.1021/cm030299v

Hy, S., Felix, F., Rick, J., Su, W.-N., and Hwang, B. J. (2014). Direct *in situ* observation of Li_2O evolution on li-rich high-capacity cathode material, $Li[NixLi_{(1-2x)}/3Mn_{(2-x)/3}]O_2$ ($0 \leq x \leq 0.5$). *J. Am. Chem. Soc*. 136, 999–1007. doi: 10.1021/ja410137s

Inaba, M., Iriyama, Y., Ogumi, Z., Todzuka, Y., and Tasaka, A. (1997). Raman study of layered rock-salt $LiCoO_2$ and its electrochemical lithium deintercalation. *J. Raman Spectrosc*. 28, 613–617.

Inaba, M., Yoshida, H., Ogumi, Z., Abe, T., Mizutani, Y., and Asano, M. (1995). *In situ* Raman study on electrochemical li intercalation into graphite. *J. Electrochem. Soc*. 142, 20–26. doi: 10.1149/1.2043869

Itoh, T., Anzue, N., Mohamedi, M., Hisamitsu, Y., Umeda, M., and Uchida, I. (2000). Spectroelectrochemical studies on highly polarized $LiCoO_2$ electrode in organic solutions. *Electrochem. Commun*. 2, 743–748. doi: 10.1016/S1388-2481(00)00112-0

Itoh, T., Sato, H., Nishina, T., Matue, T., and Uchida, I. (1997). *In situ* Raman spectroscopic study of $LixCoO_2$ electrodes in propylene carbonate solvent systems. *J. Power Sour*. 68, 333–337. doi: 10.1016/S0378-7753(97)02539-1

Jarry, A., Gottis, S., Yu, Y. S., Roque-Rosell, J., Kim, C., Cabana, J. et al. (2015). The formation mechanism of fluorescent metal complexes at the $Li_xNi_{i0.5}M_{n1.5}O_{4-\delta}$/carbonate ester electrolyte interface. *J. Am. Chem. Soc*. 137, 3533–3539. doi: 10.1021/ja5116698

Julien, C. M. (2000). Local cationic environment in lithium nickel-cobalt oxides used as cathode materials for lithium batteries. *Solid State Ionics* 136–137, 887–896. doi: 10.1016/S0167-2738(00)00503-8

Julien, C. M. (2002). Raman scattering of LiNi1–yAlyO2. *Solid State Ionics* 148, 53–59. doi: 10.1016/S0167-2738(02)00117-0

Julien, C. M., and Massot, M. (2002). Spectroscopic studies of the local structure in positive electrodes for lithium batteries. *Phys. Chem. Chem. Phys*. 4, 4226–4235. doi: 10.1039/b203361e

Julien, C. M., Massot, M., Perez-Vicente, C., Haro-Poniatowski, E., Nazri, G. A., and Rougier, A. (1997). Vibrational spectroscopic studies of the local environment in 4-Volt cathode materials. *MRS Proc.* 496:415. doi: 10.1557/PROC-496-415

Julien, C. M., Massot, M., and Ramana, C. V. (2006). "Structure of electrode materials for Li-ion batteries : the Raman spectroscopy investigations," in *Portable and Emergency Energy Sources*, eds Z. Stoynov and D. Vladikova (Sofia: Martin Drinov Academic Publishing House), 37–70.

Kalyani, P., and Kalaiselvi, N. (2005). Various aspects of LiNiO 2 chemistry: a review. *Sci. Technol. Adv. Mater*. 6, 689–703. doi: 10.1016/j.stam.2005.06.001

Keresztury, G. (2006). Raman spectroscopy : theory. *Handb. Vib. Spectrosc*. 1, 71–87. doi: 10.1002/0470027320.s0109

Kerlau, M., Marcinek, M., Srinivasan, V., and Kostecki, R. (2007). Reprint of "Studies of local degradation phenomena in composite cathodes for lithium-ion batteries." *Electrochim. Acta* 53, 1386–1393.doi: 10.1016/j.electacta.2007.10.009

Kim, J. M., and Chung, H. T. (2004). The first cycle characteristics of Li[Ni1/3Co1/3Mn1/3]O2charged up to 4.7 V. *Electrochim. Acta* 49, 937–944. doi: 10.1016/j.electacta.2003.10.005

Kleiner, K., Melke, J., Merz, M., Jakes, P., Nagel, P., Schuppler, S., et al. (2015). Unraveling the degradation process of LiNi0.8Co0.15Al0.05O2 electrodes in commercial lithium ion batteries by electronic structure investigations. *ACS Appl. Mater. Interfaces* 7, 19589–19600. doi: 10.1021/acsami.5b03191

Koga, H., Croguennec, L., Mannessiez, P., Ménétrier, M., Weill, F., Bourgeois, L., et al. (2012). $Li_{1.20}Mn_{0.54}Co_{0.13}Ni_{0.13}O_2$ with different particle sizes as attractive positive electrode materials for lithium-ion batteries: insights into their structure. *J. Phys. Chem. C* 116, 13497–13506. doi: 10.1021/jp301879x

Kostecki, R., Lei, J., McLarnon, F., Shim, J., and Striebel, K. (2006). Diagnostic evaluation of detrimental phenomena in high-power lithium-ion batteries. *J. Electrochem. Soc*. 153:A669. doi: 10.1149/1.2170551

Kostecki, R., and McLarnon, F. (2004). Local-probe studies of degradation of composite $LiNi_{0.8}Co_{0.15}Al_{0.05}O_2$ cathodes in high-power lithium-ion cells. *Electrochem. Solid-State Lett*. 7, A380–A383. doi: 10.1149/1.1793771

Kuwata, N., Ise, K., Matsuda, Y., Kawamura, J., Tsurui, T., and Kamishima, O. (2012). "Detection of degradation in 2 thin films by *in situ* micro raman microscopy," in *Solid State Ionics*, eds B. V. R. Chowdari, J. Kawamura, J. Mizusaki, and K. Amezawa (Singapore), 138–143.

Lanz, P., Villevieille, C., and Novák, P. (2013). Electrochemical activation of Li2MnO3 at elevated temperature investigated by *in situ* Raman microscopy. *Electrochim. Acta* 109, 426–432. doi: 10.1016/j.electacta.2013.07.130

Lanz, P., Villevieille, C., and Novák, P. (2014). *Ex situ* and *in situ* Raman microscopic investigation of the differences between stoichiometric Li_xMO_2

and high-energy $xLi_2MnO_3 \cdot (1–x)$ Li_xMO_2 (M = Ni, Co, Mn). *Electrochim. Acta* 130, 206–212. doi: 10.1016/j.electacta.2014.03.004

Lei, J., McLarnon, F., and Kostecki, R. (2005). *In situ* Raman microscopy of individual $LiNi_{0.8}Co_{0.15}Al_{0.05}O_2$ particles in a Li-Ion battery composite cathode. *J. Phys. Chem. B* 109, 952–957. doi: 10.1021/jp046027c

Li, J. F., Huang, Y. F., Ding, Y., Yang, Z. L., Li, S. B., Zhou, X. S. et al. (2010). Shell-isolated nanoparticle-enhanced Raman spectroscopy. *Nature* 464, 392–395. doi: 10.1038/nature08907

Lin, X. M., Cui, Y., Xu, Y. H., Ren, B., and Tian, Z. Q. (2009). Surface-enhanced raman spectroscopy: substrate-related issues. *Anal. Bioanal. Chem.* 394, 1729–1745. doi: 10.1007/s00216-009-2761-5

Liu, H. L., Ou-Yang, T. Y., Tsai, H. H., Lin, P. A., Jeng, H. T., Shu, G. J., et al. (2015a). Electronic structure and lattice dynamics of $LixCoO_2$ single crystals. *New J. Phys.* 17:103004. doi: 10.1088/1367-2630/17/10/103004

Liu, W., Oh, P., Liu, X., Lee, M.-J., Cho, W., Chae, S., et al. (2015b). Nickel-rich layered lithium transition-metal oxide for high-energy lithium-ion batteries. *Angew. Chemie Int. Ed. Engl.* 54, 4440–4457. doi: 10.1002/anie.201409262

Lu, X., Sun, Y., Jian, Z., He, X., Gu, L., Hu, Y.-S., et al. (2012). New insight into the atomic structure of electrochemically delithiated O_3-$Li_{(1-x)}CoO_2$ ($0 \leq x \leq 0.5$) nanoparticles. *Nano Lett.* 12, 6192–6197. doi: 10.1021/nl303036e

Mai, L., Yan, M., and Zhao, Y. (2017). Track batteries degrading in real time. *Nature* 546, 469–470. doi: 10.1038/546469a

Marianetti, C. A., Kotliar, G., and Ceder, G. (2004). A first-order Mott transition in LixCoO2. *Nat. Mater.* 3, 627–631. doi: 10.1038/nmat1178

Maschio, L., Kirtman, B., Rérat, M., Orlando, R., and Dovesi, R. (2013). *Ab initio* analytical Raman intensities for periodic systems through a coupled perturbed Hartree-Fock/Kohn-Sham method in an atomic orbital basis. II. Validation and comparison with experiments. *J. Chem. Phys.* 139:164101. doi: 10.1063/1.4824442

Matsuura, H., and Yoshida, H. (2006). "Calculation of vibrational frequencies by hartree-fock-based and density functional theory," in *Handbook of Vibrational Spectroscopy*, ed J. M. Chalmers (Chichester: John Wiley and Sons, Ltd), 216–234.

McBreen, J. (2009). The application of synchrotron techniques to the study of lithium-ion batteries. *J. Solid State Electrochem.* 13, 1051–1061. doi: 10.1007/s10008-008-0685-1

Ménétrier, M., Saadoune, I., Levasseur, S., and Delmas, C. (1999). The insulator-metal transition upon lithium deintercalation from $LiCoO_2$: electronic properties and 7Li NMR study. *J. Mater. Chem.* 9, 1135–1140. doi: 10.1039/a900016j

Molenda, J., Wilk, P., and Marzec, J. (2002). Structural, electrical and electrochemical properties of $LiNiO_2$. *Solid State Iconics* 146, 73–79. doi: 10.1016/S0167-2738(01)00992-4

Nakai, I., Takahashi, K., Shiraishi, Y., Nakagome, T., and Nishikawa, F. (1998). Study of the jahn–teller distortion in $LiNiO_2$, a cathode material in a rechargeable lithium battery, by *in situ* x-ray absorption fine structure analysis. *J. Solid State Chem.* 140, 145–148. doi: 10.1006/jssc.1998.7943

Nanda, J., Remillard, J., O'Neill, A., Bernardi, D., Ro, T., Nietering, K. E., et al. (2011). Local state-of-charge mapping of Lithium-ion battery electrodes. *Adv. Funct. Mater.* 21, 3282–3290.doi: 10.1002/adfm.201100157

Nguyen, D.-T., Kang, J., Nam, K.-M., Paik, Y., and Song, S.-W. (2016). Understanding interfacial chemistry and stability for performance improvement and fade of high-energy Li-ion battery of $LiNi_{0.5}Co_{0.2}Mn_{0.3}O_2$ //silicon-graphite. *J. Power Sources* 303, 150–158. doi: 10.1016/j.jpowsour.2015.10.089

Nishi, T., Nakai, H., and Kita, A. (2013). Visualization of the state-of-charge distribution in a $LiCoO_2$ cathode by *in situ* raman imaging. *J. Electrochem. Soc.* 160, A1785–A1788. doi: 10.1149/2.061310jes

Nitta, N., Wu, F., Lee, J. T., and Yushin, G. (2015). Li-ion battery materials: present and future. *Mater. Today* 18, 252–264. doi: 10.1016/j.mattod.2014.10.040

Noh, H. J., Youn, S., Yoon, C. S., and Sun, Y. K. (2013). Comparison of the structural and electrochemical properties of layered Li[NixCoyMnz]O2 (x = 1/3, 0.5, 0.6, 0.7, 0.8 and 0.85) cathode material for lithium-ion batteries. *J. Power Sources* 233, 121–130. doi: 10.1016/j.jpowsour.2013.01.063

Novák, P., Panitz, J. C., Joho, F., Lanz, M., Imhof, R., and Coluccia, M. (2000). Advanced *in situ* methods for the characterization of practical electrodes in lithium-ion batteries. *J. Power Sources* 90, 52–58. doi: 10.1016/S0378-7753(00)00447-X

Otoyama, M., Ito, Y., Hayashi, A., and Tatsumisago, M. (2016a). Raman imaging for $LiCoO_2$ composite positive electrodes in all-solid-state lithium batteries using Li_2 S–P_2 S_5 solid electrolytes. *J. Power Sources* 302, 419–425. doi: 10.1016/j.jpowsour.2015.10.040

Otoyama, M., Ito, Y., Hayashi, A., and Tatsumisago, M. (2016b). Raman Spectroscopy for LiNi1/3Mn1/3Co1/3o2 composite positive electrodes in all-solid-state lithium batteries. *Electrochemistry* 84, 812–814. doi: 10.5796/electrochemistry.84.812

Park, Y., Kim, Y., Kim, S. M., Jin, S., Han, I. K., Lee, S. M., et al. (2017). Reaction at the electrolyte-electrode interface in a li-ion battery studied by *in situ* raman spectroscopy. *Bull. Korean Chem. Soc.* 38, 511–513. doi: 10.1002/bkcs.11117

Peres, J. P., Weill, F., and Delmas, C. (1999). Lithium/vacancy ordering in the monoclinic Li_xNiO_2 (0. 50 $\leq$ x $\leq$ 0. 75) solid solution. *Solid State Ionics* 116, 19–27. doi: 10.1016/S0167-2738(98)00239-2

Perkins, J. D., Fu, M. L., Trickett, D. M., McGraw, J. M., Ciszek, T. F., Pariila, P. A. et al. (1997). Raman scattering in $LiCoO_2$ single crystals and thin films. *MRS Proc.* 496:329. doi: 10.1557/PROC-496-329

Pimenta, M. A., Dresselhaus, G., Dresselhaus, M. S., Cançado, L. G., Jorio, A., and Saito, R. (2007). Studying disorder in graphite-based systems by Raman spectroscopy. *Phys. Chem. Chem. Phys.* 9, 1276–1291. doi: 10.1039/B613962K

Poli, F., Kshetrimayum, J. S., Monconduit, L., and Letellier, M. (2011). New cell design for *in-situ* NMR studies of lithium-ion batteries. *Electrochem. Commun.* 13, 1293–1295. doi: 10.1016/j.elecom.2011.07.019

Qian, D., Ma, C., More, K. L., Meng, Y. S., and Chi, M. (2015). Advanced analytical electron microscopy for lithium-ion batteries. *NPG Asia Mater.* 7:e193. doi: 10.1038/am.2015.50

Qiu, X.-Y., Zhuang, Q.-C., Zhang, Q.-Q., Cao, R., Qiang, Y.-H., Ying, P.-Z. et al. (2012). Investigation of layered $LiNi_{1/3}Co_{1/3}Mn_{1/3}O_2$ cathode of lithium ion battery by electrochemical impedance spectroscopy. *J. Electroanal. Chem.* 687, 35–44. doi: 10.1016/j.jelechem.2012.09.027

Reimers, J. N. (1992). Electrochemical and *in situ* X-ray diffraction studies of lithium intercalation in Li_xCoO_2. *J. Electrochem. Soc.* 139, 2091–29097. doi: 10.1149/1.2221184

Rougier, A., Delmas, C., and Chadwick, A. V. (1995). Non-cooperative jahn-teller effect in LiNiO2: an EXAFS study. *Solid State Commun.* 94, 123–127. doi: 10.1016/0038-1098(95)00020-8

Ruther, R. E., Callender, A. F., Zhou, H., Martha, S. K., and Nanda, J. (2014). Raman microscopy of Lithium-manganese-rich transition metal oxide cathodes. *J. Electrochem. Soc.* 162, A98–A102. doi: 10.1149/2.0361501jes

Saavedra-Arias, J. J., Thomas, R., Karan, N. K., Ishikawa, Y., and Katiyar, R. S. (2009). First principles computations studies: structural and electrochemical behavior of layered cathode materials. *ECS Trans.* 16, 9–18. doi: 10.1149/1.3115303

Shao, M. (2014). *In situ* microscopic studies on the structural and chemical behaviors of lithium-ion battery materials. *J. Power Sour.* 270, 475–486. doi: 10.1016/j.jpowsour.2014.07.123

Sharma, N., Pang, W. K., Guo, Z., and Peterson, V. K. (2015). *In situ* powder diffraction studies of electrode materials in rechargeable batteries. *ChemSusChem* 8, 2826–2853. doi: 10.1002/cssc.201500152

Singh, G., West, W. C., Soler, J., and Katiyar, R. S. (2012). *In situ* Raman spectroscopy of layered solid solution Li2MnO3– Li_xMO_2 (M = Ni, Mn, Co). *J. Power Sour.* 218, 34–38. doi: 10.1016/j.jpowsour.2012.06.083

Snyder, C., Apblett, C., Grillet, A., Beechem, T., and Duquette, D. (2016). Measuring Li+ inventory losses in $LiCoO_2$ /graphite cells using raman microscopy. *J. Electrochem. Soc.* 163, A1036–A1041. doi: 10.1149/2.1111606jes

Sole, C., Drewett, N. E., and Hardwick, L. J. (2014). *In situ* Raman study of lithium-ion intercalation into microcrystalline graphite. *Faraday Discuss.* 172, 223–237. doi: 10.1039/C4FD00079J

Stancovski, V., and Badilescu, S. (2014). *In situ* Raman spectroscopic–electrochemical studies of lithium-ion battery materials: a historical overview. *J. Appl. Electrochem.* 44, 23–43. doi: 10.1007/s10800-013-0628-0

Streich, D., Erk, C., Guéguen, A., Mu, P., Chesneau, F., and Berg, E. J. (2017). *Operando* monitoring of early Ni-mediated surface reconstruction in layered lithiated Ni – Co – Mn oxides. *J. Phys. Chem. C* 121, 13481–13486. doi: 10.1021/acs.jpcc.7b02303

Sun, H., and Zhao, K. (2017). Electronic structure and comparative properties of LiNixMnyCozO2 cathode materials. *J. Phys. Chem. C* 121, 6002–6010. doi: 10.1021/acs.jpcc.7b00810

Takahashi, Y., Kijima, N., Tokiwa, K., Watanabe, T., and Akimoto, J. (2007). Single-crystal synthesis, structure refinement and electrical properties of $Li_{0.5}CoO_2$. *J. Phys.* 19:436202. doi: 10.1088/0953-8984/19/43/436202

Tan, J., Liu, D., Xu, X., and Mai, L. (2017). *In situ*/*operando* characterization techniques for rechargeable lithium-sulfur batteries: a review. *Nanoscale* 9, 19001–19016. doi: 10.1039/C7NR06819K

Tarascon, J.-M. (2010). Key challenges in future Li-battery research. *Philos. Trans. A Math. Phys. Eng. Sci.* 368, 3227–3241. doi: 10.1098/rsta.2010.0112

Tornheim, A., Maroni, V. A., He, M., Gosztola, D. J., and Zhang, Z. (2017). Enhanced raman scattering from ncm523 cathodes coated with electrochemically deposited gold. *J. Electrochem. Soc.* 164, A3000–A3005. doi: 10.1149/2.0461713jes

Tsai, Y. W., Hwang, B. J., Ceder, G., Sheu, H. S., Liu, D. G., and Lee, J. F. (2005). *In-situ* X-ray absorption spectroscopic study on variation of electronic transitions and local structure of $LiNi_{1/3}Co_{1/3}Mn_{1/3}O_2$ cathode material during electrochemical cycling. *Chem. Mater.* 17, 3191–3199. doi: 10.1021/cm048027v

Tuinstra, F., and Koenig, J. L. (1970). Raman spectrum of graphite. *J. Chem. Phys.* 53, 1126–1130. doi: 10.1063/1.1674108

Vetter, J., Novák, P., Wagner, M. R., Veit, C., Möller, K. C., Besenhard, J. O., et al. (2005). Ageing mechanisms in lithium-ion batteries. *J. Power Sour.* 147, 269–281. doi: 10.1016/j.jpowsour.2005.01.006

Wang, H., Mann, C. K., and Vickers, T. J. (2002). Effect of powder properties on the intensity of raman scattering by crystalline solids. *Appl. Spectrosc.* 56, 1538–1544. doi: 10.1366/000370202321115779

Wang, X., Loa, I., Kunc, K., Syassen, K., and Amboage, M. (2005). Effect of pressure on the structural properties and Raman modes of $LiCoO_2$. *Phys. Rev. B Condens. Matter.* 72:224102. doi: 10.1103/PhysRevB.72.224102

Xu, K., About, M., and Article, T. (2004). Nonaqueous liquid electrolytes for lithium-based rechargeable batteries nonaqueous liquid electrolytes for lithium-based rechargeable batteries. *Chem. Rev.* 104, 4303–4418. doi: 10.1021/cr030203g

Yin, S.-C., Rho, Y.-H., Swainson, I., and Nazar, L. F. (2006). X-ray/neutron diffraction and electrochemical studies of lithium de/re-intercalation in Li1-xCo1/3Ni1/3Mn1/3O2 (x = 0 → 1). *Chem. Mater.* 18, 1901–1910. doi: 10.1021/cm0511769

Yoon, W. S., Chung, K. Y., McBreen, J., Fischer, D. A., and Yang, X. Q. (2007). Electronic structural changes of the electrochemically Li-ion deintercalated LiNi0.8Co0.15Al0.05O2 cathode material investigated by X-ray absorption spectroscopy. *J. Power Sour.* 174, 1015–1020. doi: 10.1016/j.jpowsour.2007.06.214

Zeng, D., Cabana, J., Bréger, J., Yoon, W. S., and Grey, C. P. (2007). Cation ordering in $Li[Ni_xMn_xCo_{(1-2x)}]O_2$ -layered cathode materials: a nuclear magnetic resonance (NMR), pair distribution function, X-ray absorption spectroscopy, and electrochemical study. *Chem. Mater.* 19, 6277–6289. doi: 10.1021/cm702241a

Zhang, L., Takada, K., Ohta, N., Fukuda, K., Osada, M., Wang, L., et al. (2005). Layered $(1–x–y)LiNi_{1/2}Mn_{1/2}O_2 \cdot xLi[Li_{1/3}Mn_{2/3}]$ $O_2 \cdot yLiCoO_2$ ($0 \leq x=y \leq 0.3$ and $x+y=0.5$) cathode materials. *J. Electrochem. Soc.* 152, A171–A178. doi: 10.1149/1.1829416

Zhang, X., Mauger, A., Lu, Q., Groult, H., Perrigaud, L., Gendron, F., et al. (2010). Synthesis and characterization of $LiNi_{1/3}Mn_{1/3}Co_{1/3}O_2$ by wet-chemical method. *Electrochim. Acta* 55, 6440–6449. doi: 10.1016/j.electacta.2010.06.040

Zhecheva, E., Stoyanova, R., Alcantara, R., Lavela, P., and Tirado, J. L. (2002). Cation order/disorder in lithium transition-metal oxides as insertion electrodes for lithium-ion batteries. *Pure Appl. Chem.* 74, 1885–1894. doi: 10.1351/pac200274101885

Conflict of Interest Statement: The authors declare that the research was conducted in the absence of any commercial or financial relationships that could be construed as a potential conflict of interest.

frontiers in Energy Research

REVIEW
published: 31 July 2018
doi: 10.3389/fenrg.2018.00066

Application of Operando X-ray Diffraction and Raman Spectroscopies in Elucidating the Behavior of Cathode in Lithium-Ion Batteries

Wen Zhu[1], *Dongqiang Liu*[2], *Andrea Paolella*[2], *Catherine Gagnon*[2], *Vincent Gariépy*[2], *Ashok Vijh*[1] *and Karim Zaghib*[2]*

[1] IREQ-Hydro Québec, Varennes, QC, Canada, [2] Centre d'Excellence en Électrification des Transports et Stockage d'Énergie, Varennes, QC, Canada

With the advances in characterization techniques, various operando/in-situ methods were applied in studying rechargeable batteries in order to improve the electrochemical properties of electrode materials, prolonging the battery life and developing new battery materials. In the present review, we focus on the characterization of electrode materials with operando/in-situ X-ray diffraction and Raman spectroscopies. By correlating the results obtained via these two techniques in different electrode chemistry: (a) intercalation materials, such as layered metal oxides and (b) conversion materials, such as elemental sulfur. We demonstrate the importance of using operando/in-situ techniques in examining the microstructural changes of the electrodes under various operating conditions, in both macro and micro-scales. These techniques also reveal the working and the degradation mechanisms of the electrodes and the possible side reactions involved. The comprehension of these mechanisms is fundamental for ameliorating the electrode materials, enhancing the battery performance and lengthening its cycling life.

Keywords: operando/in-situ XRD, operando/in-situ Raman, lithium-sulfur, layered metal oxide, $LiFePO_4$, spinel oxide

OPEN ACCESS

Edited by:
Verónica Palomares, University of the Basque Country (UPV/EHU), Spain

Reviewed by:
Zhixiang Shi, Southeast University, China
Xifei Li, Xi'an University of Technology, China

***Correspondence:**
Karim Zaghib
zaghib.karim@ireq.ca

Specialty section:
This article was submitted to Energy Storage, a section of the journal Frontiers in Energy Research

Received: *28 February 2018*
Accepted: *19 June 2018*
Published: *31 July 2018*

Citation:
Zhu W, Liu D, Paolella A, Gagnon C, Gariépy V, Vijh A and Zaghib K (2018) Application of Operando X-ray Diffraction and Raman Spectroscopies in Elucidating the Behavior of Cathode in Lithium-Ion Batteries. Front. Energy Res. 6:66. doi: 10.3389/fenrg.2018.00066

INTRODUCTION

Rechargeable batteries are the main energy source for electric vehicles (EV), consumer electronics, and promising candidates for renewable energy storage, owing to their relative high energy and power densities, light weight, long cycle life and environmental acceptability (Tarascon and Armand, 2001; Palacín, 2009; Dunn et al., 2011; Budde-Meiwes et al., 2013). For the large-scale commercialization of EVs and the utilization of renewable energy, the energy storage capacity, cycle life, rate capacity and safety of most commercial batteries still need to be improved (Armand and Tarascon, 2008; Etacheri et al., 2011; Wen et al., 2012). To achieve these goals, the scientific community is devoting a major effort to improve the existing materials and identify new ones to meet these requirements.

Among the many rechargeable battery materials, the layered oxide family of $LiMeO_2$ (Me = Ni, Co, Mn, and their mixtures) has been widely studied. These oxides yield high specific

energy and/or power, and structural and thermal stability, as well as long cycling life (Hwang et al., 2003; Hu et al., 2009; Huang et al., 2011; Park et al., 2012; Liao et al., 2016; Berckmans et al., 2017), but they still suffer from poor rate capability, especially at high C-rates (Chen et al., 2016b). Spinel $Li(Mn,Ni)_2O_4$ (LMN) is of great interest due to its high working voltage and high energy density, relatively low cost and environmentally benign. However, its fast capacity fade at elevated temperatures makes it unsuitable for practical applications (Amine et al., 1996; Ohzuku et al., 1999; Goodenough and Kim, 2010; Yang et al., 2013; Julien et al., 2014). Olivine structured $LiFePO_4$ (LFP) is another promising cathode with reasonable high capacity, superior cycle life, structural and thermal stability, low cost, high safety and non-toxicity. However, its low operating voltage and low conductivity limit its wide applications (MacNeil et al., 2002; Sarkar and Mitra, 2014; Zhao et al., 2016). In addition to the Li-ion families mentioned above, Li-sulfur and Li-air batteries are also being intensively investigated owing to their high theoretical capacities, low cost and environmentally benign. Unfortunately, the present performance of both Li-S and Li-air batteries, such as energy density, rate capability, cyclability, Li-metal fading and safety, are unable to satisfy the requirements of commercial applications (Girishkumar et al., 2010; Ji and Nazar, 2010; Mikhaylik et al., 2010; Kraytsberg and Ein-Eli, 2011; Manthiram et al., 2013; Yang et al., 2018).

To further improve the performance of the batteries already present in the market, such as those based on $LiCoO_2$ (LCO), $Li(Ni,Co,Mn)O_2$, and LFP cathodes, it is essential to have a clear picture of the working and failure mechanisms of these batteries. Various ex-situ materials characterization techniques, such as X-Ray Diffraction (XRD), X-ray Absorption Spectroscopy (XAS), X-ray computed tomography (micro CT) (Carter et al., 2018), neutron diffraction, neutron magnetic resonance (NMR) (Ogata et al., 2014), Raman spectroscopy, Fourier-Transform Infrared (FTIR), Ultraviolet and Visible (UV-Vis) spectroscopy, Scanning and Transmission Electron Microscopies (SEM, TEM) etc. are employed to investigate the pristine and cycled electrodes at both macro and atomic scales. However, these ex-situ analyses cannot provide real-time information of the electrodes during cycling, which is crucial for understanding the working and degradation mechanisms of the batteries. In recent years, operando and in-situ (operando and in-situ will be used interchangeably hereafter) characterization techniques have been advanced and widely applied in following the real-time situation of electrodes in batteries under various operating conditions. Operando XRD is used to investigate the phase transformation and crystal structure changes of electrodes during cycling (Yang et al., 2002; Yang and Nam, 2010; Sun et al., 2013; Zhang et al., 2014; Zhu et al., 2014; Wang and Wang, 2016). Neutron diffraction is also applied to study the structure and phase developments in cycling cells (Wang et al., 2012; Bobrikov et al., 2014, 2017; Dolotko et al., 2014; Li et al., 2015) because it is more sensitive to the light elements (such as lithium) as compared to XRD, an important issue in understanding the behavior of lithium in Li-ion batteries. Operando XAS is employed to probe the changes in the local environment of a cation and its electronic structure in relation to the electrochemical processes happening on electrode surfaces (Chan et al., 2006; Dominko et al., 2009; Giorgetti, 2013; Menzel et al., 2013; Fehse et al., 2014; Giuliana et al., 2017). The absorption spectrum is divided into the X-ray Absorption Near-Edge Structure (XANES) region and the Extended X-ray Absorption Fine Structure (EXAFS) region; the former examines the oxidation state, coordination number, electronic configuration and site symmetry, whereas the latter provides information on average interatomic distances. Raman spectroscopy is also used to explore the variation in the local structure and oxidation state, as well as the thermal stability of electrode surfaces or electrode-electrolyte interfaces during charge-discharge and heat treatment (Dokko et al., 2002; Hardwick et al., 2008; Membreno et al., 2013; Stancovski and Badilescu, 2013; Wu et al., 2013); FTIR is another effective tool for studying the surface and evolution of electrode-electrolyte interfaces under cell operating conditions (Aurbach and Chusid, 1997; Chusid et al., 2001; Cheng et al., 2007; Ye et al., 2016). In addition to these spectroscopic techniques, operando SEM (Miller et al., 2013; Hovington et al., 2014; Marceau et al., 2016) and TEM (Liu, S. et al., 2014; Janish and Carter, 2015; Wang, 2015; Chen et al., 2016a; Xu et al., 2016) show the evolution of direct images of cycling electrode at the micro- and nano-scales. By combining the images with energy dispersive X-ray spectroscopy, electron energy loss spectroscopy and electron diffraction, the information on particle morphology, crystal structure, phase transformation, multi-phase interface behavior, element distribution and element positions are obtained as a function of the electrochemical process. In short, operando measurements or multi-operando measurements reveal indispensable information on how the electrodes behave and how their structures change under working conditions. These insights enable researchers to correlate the electrochemical process with the crystal structure, composition, oxidation state of ions and stresses etc. at both macro- and micro-scales, which are essential to understand the operation and failure mechanisms of batteries. The outcome of this effort is to identify new solutions being able to improve the performance of electrodes to meet the requirements for electric vehicles and storage of renewable electrical energy. Ideally the best operando techniques must be non-invasive and performed under real battery cycling. Among all the possibilities, operando X-ray diffraction is the most widely used due to the instrument availability, simple cell design, examining "bulk" material and most importantly, revealing the information on crystal structure, phase transformation as well as stresses, etc.; whereas operando TEM involves complicated cell design; testing conditions are far from real operating conditions; damage of the analyzed materials and decomposition of the liquid electrolyte are often induced due to intense electron beam used, but the technique provides information on the structural morphological changes in nano-scale. On the other hand, operando XAS and Raman techniques are also used to study the local structure of the electrode materials, but unfortunately the former need to be performed with synchrotron radiation source which is not accessible to many researchers whereas Raman spectrometer is widely available in many research facilities. In the present work, we focus on the applications of XRD and Raman to

four types of electrodes, i.e., LCO, LMN, LFP and elemental sulfur. We demonstrate the contribution of these techniques to the fundamental comprehension of electrode behavior under operating conditions that are critical for raising the capacity and life span of the batteries from the current state.

METHODS

The Operando X-ray Diffraction

The operando XRD, both reflection and transmission modes are used to monitor crystal structure and phase changes of electrodes during battery cycling. Different in-situ cell configurations were designed (Li et al., 1993; Leriche et al., 2010; Zhu W. et al., 2013; Roberts et al., 2014; Bleith et al., 2015) with an x-ray transparent window, such as a beryllium disk (Reimers and Dahn, 1992; Ma et al., 2013; Cañas et al., 2017), polymer films (Kapton, Mylar) (Mohanty et al., 2013; Sun et al., 2013) and aluminum foil (Zhu W. et al., 2013; Roberts et al., 2014). A beryllium window has the advantages of maintaining contact between cell components and is nearly 100% x-ray transparent due to disk rigidity and low x-ray absorption. However, beryllium corrosion was observed, especially at high voltage >4.2 V (Reimers and Dahn, 1992; Morcrette et al., 2002). In addition, beryllium is toxic and expensive compared to many other materials. Kapton, Mylar and aluminum are stable, low cost and non-toxic. They also allow X-rays to pass through with certain absorption, but it is difficult to keep cell pressurized with a large area window due to their flexibility. Aluminum foil is used as a current collector in many cases; the same aluminum foil is also used as an x-ray window to reduce undesired diffraction peaks in the spectra. While synchrotron based high-energy X-rays are used, the transmission mode can be applied (Leriche et al., 2010; He et al., 2013; Harks et al., 2015) to follow the evolution of both cathode and anode simultaneously. **Figure 1A** is a schematic diagram of the principle of X-ray diffraction analysis; (**Figure 1a1**) in situ XRD cell design; (**Figure 1a2**) the X-rays diffracted by the atoms on a (hkl) crystal plane satisfying the Bragg's law; (**Figure 1a3**) The information collected by the detector can be expressed as a plot of Intensity vs. d-spacing or 2θ; (**Figure 1a4**) Determination of the crystal structure from the spectrum; the unit cell size and symmetry can be obtained from peak positions whereas the number of atoms and their positions in the cell depend on the peak intensities.

The Operando Raman Spectroscopy

Raman spectroscopy is a technique used to obtain unique structural information at the atomic scale, and it can analyze both solids and liquids. Raman spectroscopy is sensitive to the ion oxidation state and local structure of the material, thus it is useful in monitoring valence and bond change, as well as the corresponding phase transformation of the electrode under operating conditions. The operando Raman cell has a laser-transparent glass window. The cell components can be arranged in different configurations, depending on the components to be examined. Various cell components are amenable to analysis, for example, the changes in the electrodes, the species in the electrolyte on both sides of the separator or changes to the separator surface (Zhu et al., 2017). **Figures 1b1,b2** show the schematic diagrams of the in-situ Raman cells for analyzing the electrode surface (**Figure 1b1**) and electrolyte on the lithium metal side or separator surface (**Figure 1b2**); (**Figure 1b3**) after filtering the elastic scattered radiation out, the inelastic Raman scattering signal is collected (**Figure 1b3**) and expressed in (**Figure 1b4**) from where the local structure, such as chemical bonds and symmetry, oxidation state of the ions can be obtained (**Figure 1b5**).

THE OPERANDO STUDIES ON CATHODES

$LiCoO_2$

Layered oxide compounds are the most widely used cathodes for lithium-ion batteries. To achieve high capacity and long life, major effort is focused on understanding the crystal structure change at different stages of charge-discharge, with operando XRD studies making significant contributions in revealing various phase transformations in different cathode materials (Lu and Dahn, 2002; Godbole et al., 2011; Mohanty et al., 2013), especially in the $LiCoO_2$ family. The operando XRD investigations showed the complicated phase transitions involved in the delithiation of Li_xCoO_2 ($0 \leq x \leq 1$). **Figure 2A** plots the XRD spectra collected during the first charge at rate of C/4.5 in which phases H1, H2, O1a and O1 are observed as a function of cell voltage, where H1 is the fully lithiated phase at $x = 1$ and O1 is the completely delithiated phase at $x = 0$, the others are partially delithiated with $0<x<1$. The phase-transformation steps are: H1→H2→O1a→O1 (Sun et al., 2001; Chung et al., 2006, 2007). The H1 and H2 have hexagonal lattice in space group (S.G.) $R\bar{3}m$, with similar lattice parameter *a*, but different in *c*, $c_{H1} = 14.089$ A, $c_{H2} = 14.370$A respectively (Yang et al., 2000), therefore, the (003) peak shifted to the lower 2θ direction as lattice parameter *c* increased during the H1 to H2 phase transition; on the other hand, the positions of (101) and (102) are almost unchanged. As the charge voltage reached ∼ 4.6 V, (100) and (101) peaks of O1a phase (hexagonal lattice, S.G. $R\bar{3}m$, $a = 2.823$ A, $c = 27.07$ A, Chen et al., 2002) appeared and their intensities increased thereafter at the expense of H2 phase. H2 phase completely disappeared as O1 phase started to form, finally, all the O1a phase transformed to O1 phase (hexagonal lattice, $a = 2.83$ A, $c = 4.24$ A, S.G.: $P\bar{3}m1$; Amatucci et al., 1996; Yang et al., 2000). A monoclinic phase formed near $x = 0.5$ and other transitional phase, such as H2a, were also detected via operando XRD in different studies under various experimental conditions (Reimers and Dahn, 1992; Ohzuku and Ueda, 1994; Morcrette et al., 2002; Chen and Dahn, 2004). **Figure 2E** is the spectra recorded during the 5th charge to 4.8 V at C/4.5 (Chung et al., 2006). The spectra show no O1 phase formation at the end of charge, instead, the existing phases are O1a and H2 suggesting a delayed phase transformation, which indicates the loss of capacity in the previous cycles. The electrode was further cycled to 8.35 V at C/4.5 during the 12th cycle (not shown here) (Chung et al., 2007). At 4.8 V, the major phases are H1 and H2, O1a was first observed at 5.04 V, and O1a to O1 phase transition completed ∼ 6.05 V, which demonstrates the further delayed phase transformation compare to the 5th cycle. After

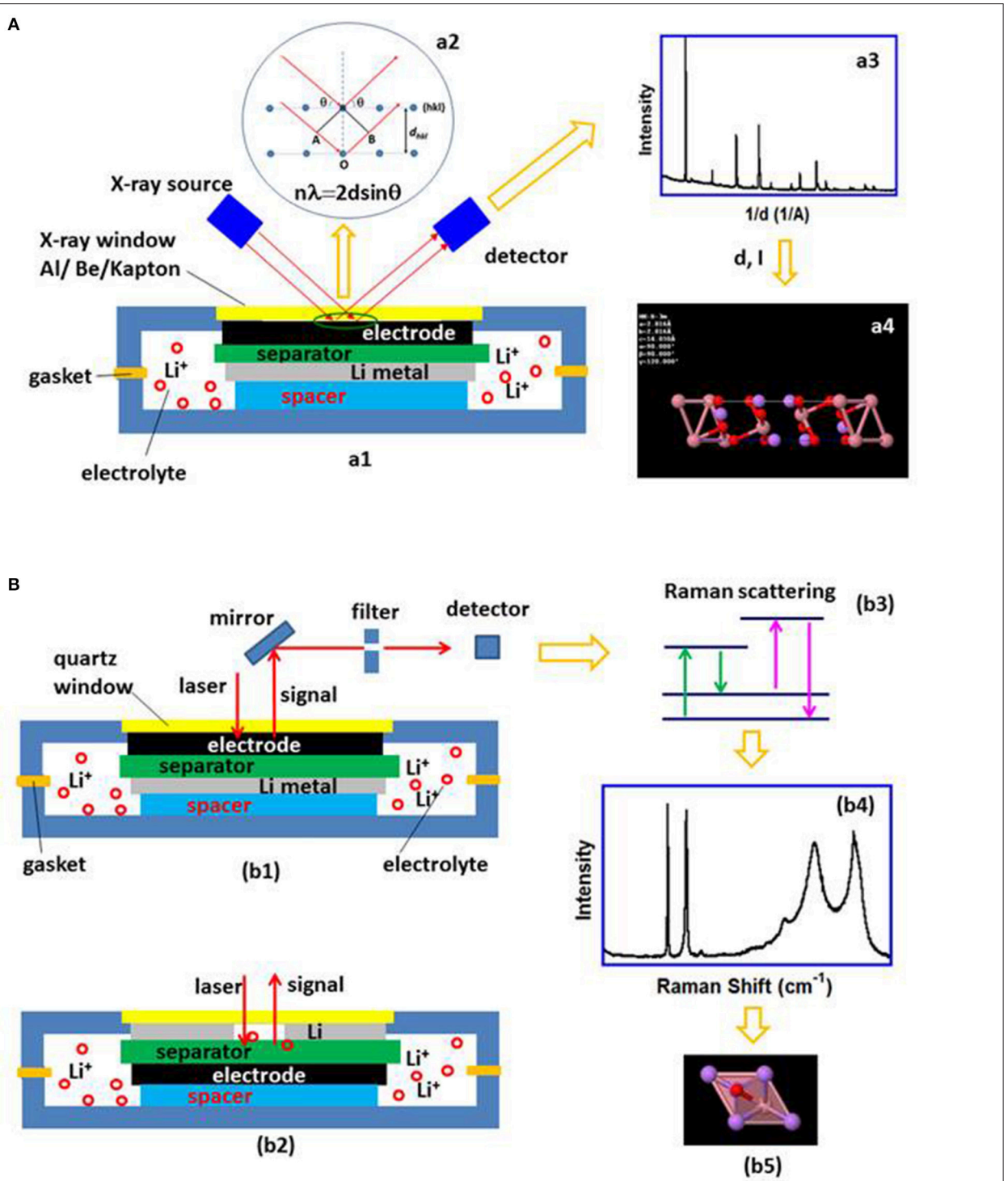

FIGURE 1 | (A) A schematic diagram of the principle of X-ray diffraction analysis; **(a1)** in situ XRD cell design; **(a2)** The incident X-ray satisfying Bragg's law is diffracted; **(a3)** The diffracted X-ray is plotted as a function of Intensity vs. d-spacing or 2θ; **(a4)** Determination of the crystal structure from the spectrum. Schematic diagrams of the in-situ Raman cells for analyzing the electrode surface and electrolyte on the lithium metal side or separator surface are plotted in **(b1,b2)** respectively; **(b3)** shows the Raman signal is collected after filtering the other radiation out and expressed as a function of Intensity and Raman shift **(b4)** from which the local structure information can be obtained **(b5)**.

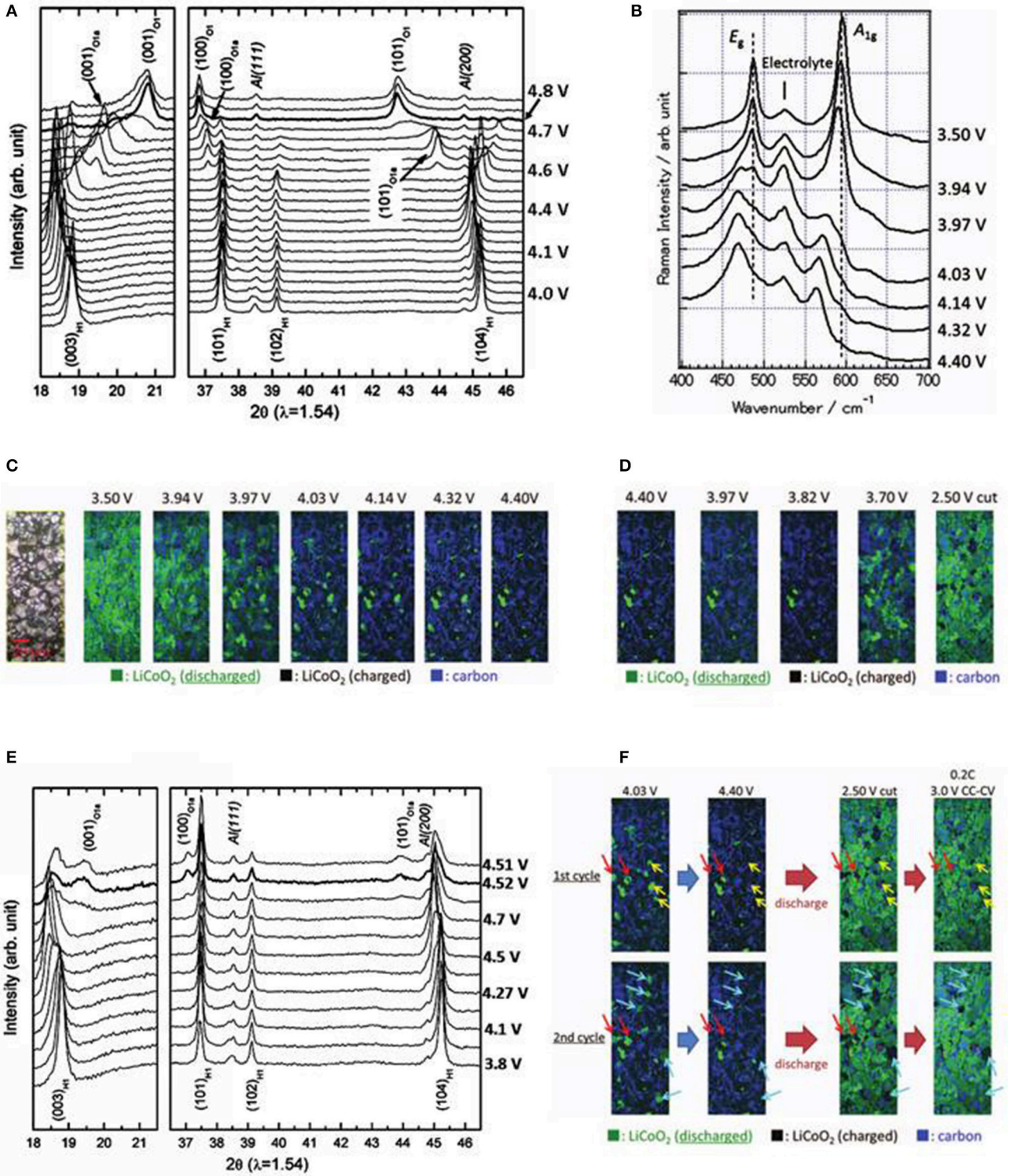

FIGURE 2 | Operando XRD and Raman measurements on $LiCoO_2$ electrodes; **(A)** XRD spectra during the first charge to 4.8 V at C/4.5, demonstrating a complete phase transformation from H1 to O1. (Chung et al., 2006); **(B)** Raman spectra from first charge, 3.5–4.4 V at C/2.5 rate (Nishi et al., 2013); **(C)** In situ Raman images at various potentials during first charge to 4.4 V at C/2.5 rate with corresponding optical graph at the left (Nishi et al., 2013); **(D)** In situ Raman images at various potential during first discharge, 4.4–2.5 V at 1C rate (Nishi et al., 2013); **(E)** XRD spectra from 5th charge to 4.8 V at C/4.5, showing an incomplete phase transition between H1 and O1. (Chung et al., 2006); **(F)** In situ Raman images collected from 1st and 2nd cycles; after galvanostatic discharge to 2.5 V at 1C, the cell voltage was relaxed from 2.5 to 3.7 V, the cell was then discharged to 3 V at C/5 followed by holding at 3 V for 3 h which reduced the delithiated particles (Nishi et al., 2013);

(Continued)

FIGURE 2 | Legends: Red arrows, particles charged and discharged at a slower rate during both cycles; yellow arrows, particles charged at a slower rate in the 1st charge and could not be discharged in the following cycle; blue arrows, particles charged and discharged at a slower rate during the 2nd cycle. Green, black and blue colors in the image represent the discharged $LiCoO_2$, charged $LiCoO_2$ and carbon; Panels **(A, E)** with permission from Elsevier. Panels **(B–D, F)** with permission from ECS.

the transformation to O1 is completed at 6.05 V, no new phase was found even up to 8.35 V, indicating all Li ions or almost all Li ions are removed from the structure. The charging curves show that the first voltage plateaus are ∼4.0, 4.1, and >4.7 V for the 1st, 5th, and 12th cycles respectively, indicating the cell polarization increase caused by the impedance augmentation due to the electrolyte decomposition at high voltage.

The phase transformation mechanism is well-described with the operando XRD results, but the origin of the electrode degradation is still unclear. Therefore, Raman spectroscopy is used to probe the local structure (∼ μm scale) changes of $LiCoO_2$ (Inaba et al., 1997; Itoh et al., 1997; Nishi et al., 2013; Gross and Hess, 2014) in order to understand the causes of capacity loss. Factorial group analysis indicates that $LiCoO_2$ has two Raman active modes, A_{1g} and E_g; the former originates from two adjacent oxygen layers moving against each other and parallel to the c-axis, whereas the latter is from the atomic displacements perpendicular to the c-axis (Baddour-Hadjean and Pereira-Ramos, 2010). The E_g and A_{1g} vibration modes were observed experimentally at 486 and 596 cm^{-1} (Inaba et al., 1997). **Figure 2B** plots the development of Raman spectra of a $LiCoO_2$ cathode as the voltage increased from 3.5 to 4.4 V during the first charge. The spectra show: (1) the broadening of E_g and A_{1g} bands due to the formation of shoulder peaks; (2) the shifts of E_g and A_{1g} to the low wave number direction; and (3) the decrease of the band intensities. The appearance of the shoulder peaks on the low wave number side is due to the formation of H2 phase with larger *c*-axis that causes the downward shifts of both bands. At 4.4 V, the E_g and A_{1g} bands contain mainly H2 phase component with a very small H1 phase shoulder, which agrees with the in-situ XRD results. The voltage difference for the first detection of the H2 phase in XRD and Raman measurements reflects the difference between the average particles and individual particle. The band intensity decrease is attributed to the reduced optical skin depth of the incident laser beam due to increasing conductivity from the semiconducting H1 phase transforming to metallic H2 (Inaba et al., 1997). **Figures 2C,D** are the evolutions of Raman images, measured over 180 × 70 μm^2 with 400 × 150 Raman spectra, during the first charge and discharge respectively, which were constructed using the intensity distributions of the A_{1g} mode of $LiCoO_2$ and the carbon G band at ∼1,600 cm^{-1}. Starting with fully lithiated LCO (green) at 3.5 V, delithiated LCO (black) formed and grew during charge, eventually reached 94% of the total measured area at 4.4 V, and holding the cell at 4.4 V for an additional 16 h did not delithiate LCO completely (∼2.5% of total measured area remained green), **Figure 1C**. The images show a reversed change, the lithiated areas (green) increase to 90% at 2.5 V when the electrode is discharged at 1C rate (**Figure 1D**). These images illustrate that both charge and discharge rates are significantly different from particle to particle. **Figure 2F** is a comparison of the Raman images of the 1st and 2nd cycles. Most of the particles were charged and discharged normally, but the behavior of two types of particles directly contributes to the capacity loss: (1) particles were charged at a slower rate in the 1st charge process and could not be discharged in the following cycle (yellow arrows); (2) particles were charged and discharged at a slower rate during the 2nd cycle (blue arrows) resulted in an accumulated delithiated particles of 16% at the end of the 2nd discharge which is more than that of the 1st cycle (10%). The degradation of the electrode with cycling is consistent with the delayed and incomplete phase transformation in comparison of the operando XRD spectra of 1st and 5th cycles (**Figures 2A,E**). After stopping the discharge at 2.5 V, the cell voltage relaxed back to 3.7 V, then was discharged again to 3 V at C/5 and held for 3 h, the delithiated particles were reduced from 10 to 2% for the first cycle (no data was reported for the 2nd cycle). The existence of these "slow" particles is mainly due to the poor local conductivities (Nishi et al., 2013). The operando Raman measurements expose the cause of degradation, i.e., the inhomogeneity of carbon distribution on micrometer scale which makes some particles "slow." This situation will be aggravated at high cycling rate and after more cycles (Kostecki and McLarnon, 2004). Operando XRD measurements show that phase transformation proceeds progressively, whereas Raman analysis adds details to this progressive transition which is mainly attributed to the reaction speed difference of individual particles caused by local conductivity difference.

$LiMn_{1.5}Ni_{0.5}O_4$

$LiMn_{1.5}Ni_{0.5}O_4$ is a high-voltage cathode material with high energy density and low cost, but its cycling stability at high rates needs to be improved for use in practical applications. $LiMn_{1.5}Ni_{0.5}O_4$ has two different structures, disordered and order, based on the Ni and Mn cation distributions in the LMN. The disordered LMN has a cubic spinel structure with space group $Fd\bar{3}m$, where the Ni and Mn ions are randomly distributed at the octahedral 16d sites. In contrast, the ordered LMN has the $P4_332$ space group, in which the Ni and Mn ions are located in an orderly fashion at the split 4a and 12d sites (Kim et al., 2004; Takahashi et al., 2004; Amdouni et al., 2006). The disordered LMN has better rate capacity because of its higher electric conductivity (Kunduraci et al., 2006) and lithium ions diffusivity (Minami et al., 2005).

The phase evolution during lithium de-intercalation/intercalation of these two structures was studied using in-situ XRD (Kunduraci and Amatucci, 2006; Rhodes et al., 2011; Wang et al., 2011; Hugues et al., 2014; Zhu et al., 2014; Komatsu et al., 2015; Saravanan et al., 2015; Samarasingha et al., 2016) and in situ Raman (Dokko et al., 2002, 2004; Zhu et al., 2015). **Figure 3A** displays the development of the XRD spectra of a $Li_xMn_{1.45}Ni_{0.45}Cr_{0.1}O_4$ (Cr-LMN) cathode cycled at C/24 with expanded views of peaks (311) and (511) in **Figure 3B**. The initial

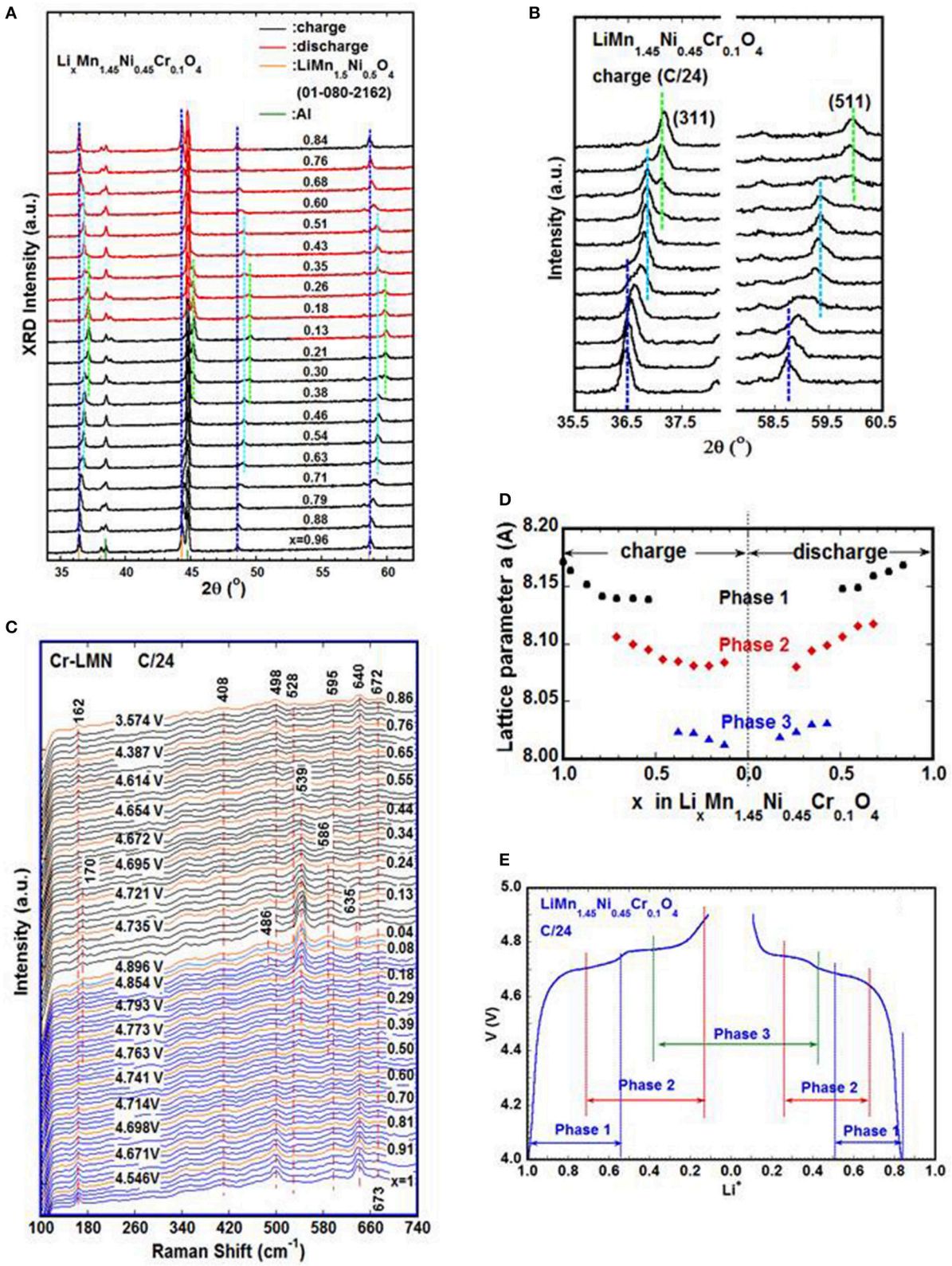

FIGURE 3 | Operando XRD (Zhu W. et al., 2013) and Raman (Zhu et al., 2015) measurements on $Li_xMn_{1.45}Ni_{0.45}Cr_{0.1}O_4$ cathodes during galvanostatic cycle at C/24; **(A)** Evolution of XRD patterns as a function of lithium concentration; **(B)** XRD patterns focused on (311) and (511) peaks which clearly show the three different phases present during charge; **(C)** Development of Raman spectra during cycle, the appearance of new bands at 170 and 539 cm^{-1} toward the end of charge

(Continued)

FIGURE 3 | attributed to the vibration modes of Ni^{4+}-O bond; the two bands are initially observed at ∼4.76 V corresponding to Phase-3 formation detected by operando XRD. Blue: charge; black: discharge; voltage and x values of orange spectra are labeled; **(D)** Variation of the lattice parameters of different cubic phases in Cr-LMN as a function of Li concentration; **(E)** Relation of cell voltage, lithium concentration and phases determined via operando XRD.

phase is cubic spinel (S.G. $Fd\bar{3}m$) with $a = 8.177$ A (Phase-1). All the diffraction peaks shift to higher 2θ angles as the lithium ions are continuously removed from the host structure and two more phases (Phase-2 and Phase-3) form during charge. Upon discharge, the evolution of the spectra changes reversibly. The analysis of the XRD patterns shows that all the phases in the spectra are cubic spinel (S.G. $Fd\bar{3}m$), and the lattice parameters for each phase as a function of lithium content (x) are obtained from Rietveld refinement of the spectra and plotted in **Figure 3D**. **Figure 3E** shows the variation of the cell voltage with x and the corresponding phases. As charge proceeds from x = 1, a solid solution is in the range of $1 \leq x \leq 0.72$; the decrease in Li results only in the decrease of the lattice parameter of the cubic Phase-1. A new cubic spinel phase (Phase-2) starts to emerge and the system entered in a two-phase domain, $0.72 \leq x \leq 0.54$, in which the Phase-2 grows at the expense of the Phase-1 and Phase-1 eventually disappears at x = 0.54. Below this concentration, $0.54 \leq x \leq 0.37$, the Cr-LMN is again a solid solution of the Phase-2 only. The system re-enters a two-phase region in the range $0.37 < x < 0.13$ with the coexistence of Phase-2 and a new phase (Phase-3) that grows at the expense of Phase-2. Finally, a solid solution with Phase-3 only is observed in the range $x \leq 0.13$. There is a difference between charge and discharge curves in **Figure 3E** that suggest the thermodynamic equilibrium is not reached even at a slow rate of C/24. The off-equilibrium effects evidenced by hysteresis in the structure and electrochemical properties between charge and discharge as a function of x are also linked to its cation disorder (Zhu W. et al., 2013).

While the phase-lithium content relation is determined by operando XRD, the oxidation state of Ni ions is investigated via operando Raman. The vibration modes of Cr-LMN are experimentally detected at 162(T_{2g}(T)), 408(E_g(Ni^{2+}/Mn^{4+})), 498(T_{2g}(Ni^{2+})), 528 (T_{2g}(Ni^{2+})), 593(A_{1g}(Mn^{4+})), 613(A_{1g}(Ni^{2+})), 639 (A_{1g}(Mn^{3+}/ Ni^{2+})), 672 cm^{-1}(T_{2g}(Cr^{3+})) (Zhu et al., 2015). The evolution of the Raman spectra of a Cr-LMN electrode cycled at C/24 is shown in **Figure 3C** and has the following characteristics:

(1) Near the end of charge, the intensity of the 162 cm^{-1} band decreases and finally disappears, accompanied by the formation and growth of a new band at 170 cm^{-1} which is first observed at ∼4.76 V (x∼0.39), and assigned to the translation mode of the lattice vibration, T_{2g}(T). This 4.76 V is close to the potential of the 2nd anodic peak in the plot of dQ/dV vs. V (Zhu et al., 2015) which is related to the oxidation of Ni^{3+} to Ni^{4+}. Compared to the phase diagram in **Figure 3E**, it is reasonable to assume that the appearance of the 170 cm^{-1} band corresponds to the presence of Phase-3 with less lithium. The lattice parameter of Phase-3 is ∼2% smaller than that of Phase-1 leading to the up shift of this vibration mode from 162 to 170 cm^{-1}.

(2) A new band at ∼539 cm^{-1} is observed at the same time as the 170 cm^{-1} band and reaches its maximum as the voltage approaches 4.9 V, it is identified as the symmetric vibration of the Ni^{4+}-O bond, T_{2g}(Ni^{4+}); simultaneously, the band at 528 cm^{-1} (T_{2g}(Ni^{2+})) fades away. The initial broadening of the 528 cm^{-1} band is attributed to the formation of the Ni^{3+}-O bond, and its disappearance indicates the Ni^{2+}/Ni^{3+} are oxidized to Ni^{4+}.

(3) A small band is detected at ∼586 cm^{-1} as the voltage approaches 4.9 V and is attributed to the asymmetric vibration of the Ni^{4+}-O bond, which evolved from A_{1g}(Ni^{2+}-O) at 613 cm^{-1}.

(4) The broadening of the 498 cm^{-1} band is seen near 4.9 V, leading to the presence of a small new band at ∼486 cm^{-1} at ∼ 4.9 V (x ∼ 0.12), which is ascribed to a stretching mode of Ni^{4+}-O.

(5) During discharge, the evolution of the Raman bands proceeds reversely, all the new bands formed during charge fade away and the bands in the pristine cathode reappear.

In summary, the operando Raman spectroscopy study of Cr-LMN establishes the relation of oxidation state of Ni ion and the corresponding phases, i.e., Phase-2 is associated to the phase where all Ni^{2+} are converted to Ni^{3+}, i.e., $Li_{0.55}Mn_{1.45}Ni_{0.45}Cr_{0.1}O_4$. Similarly, $Li_{0.1}Mn_{1.45}Ni_{0.45}Cr_{0.1}O_4$ is Phase-3 at equilibrium, corresponds to the state where all of the nickel ions are converted to Ni^{4+}.

$LiFePO_4$

Lithium iron phosphate is one of the most investigated cathode material for lithium-ion batteries due to its high theoretical capacity (170 mAh/g), long cycle life, good thermal stability, high reversibility, low cost, non-toxicity and high safety characteristics (Joachin et al., 2009; Ramana et al., 2009; Dong et al., 2017). $LiFePO_4$ and $FePO_4$ (FP) have similar crystal structure described by space group *Pnma*, but different lattice parameters. When the $LiFePO_4$ cathode is charged and discharged, the Li^+ ions are de-intercalated and intercalated, respectively, along a channel in the [010] direction (Islam et al., 2005; Li et al., 2018). Several models, such as Shrinking core model (Padhi et al., 1997), Domino cascade model (Delmas et al., 2008) describe the phase transformation between $LiFePO_4$ and $FePO_4$, but the mechanism is still in debate. As a result, several operando techniques were applied to understand the process (Perea et al., 2012; Orikasa et al., 2013; Ouvrard et al., 2013; Dong et al., 2017), especially using operando XRD (Shin et al., 2008; Roberts et al., 2014) and operando Raman (Wu et al., 2013; Siddique et al., 2015). The LFP↔FP transition is generally considered as a two-phase reaction (Chen et al., 2006; Laffont et al., 2006; Zhu Y. et al., 2013), also confirmed by XRD measurements conducted on slow cycled cells (Andersson et al., 2000; Shin et al., 2011; Siddique et al., 2015). **Figure 4A** shows the diffraction patterns (top) and corresponding cycling curve (bottom) at rate of 1C. The transformation of LFP to FP was first observed at Li = 0.62 at 1C, the same authors also reported the beginning of FP formation at Li = 0.80 at slower rate of C/5. The content of FP increases at the

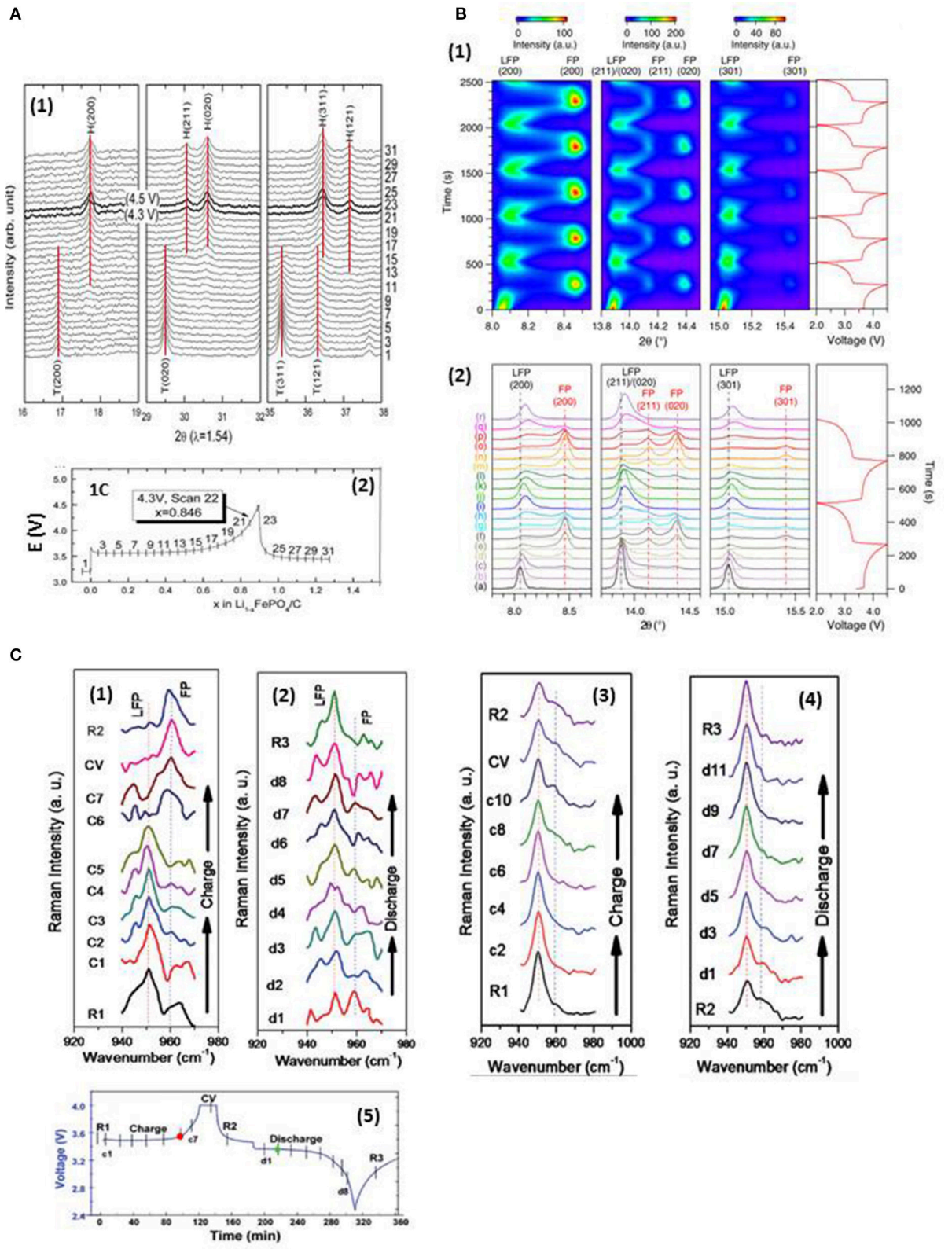

FIGURE 4 | (A) C-coated $LiFePO_4$ charged at 1C rate **(A1)** Evolution of XRD spectra shows that the FP is first detected at Li = 0.62, and the LFP disappears completely at 4.3 V; (**A2)** corresponding charge-discharge curve (Shin et al., 2011 with permission from Elsevier); **(B)** LFP cycled at a rate of 10C (Liu, H. et al., 2014); **(B1)** image plot of diffraction patterns for (200), (211), (020), and (301) reflections during first five cycles; the scale bars of diffraction intensity are shown on top.

(Continued)

FIGURE 4 | The corresponding voltage curve is plotted to the right. **(B2)** diffraction patterns from first two cycles stacked against the voltage profile; black vertical lines mark the positions of LFP peaks at the start of reaction; red vertical lines mark the position of FP peaks formed during the first cycle; with permission from AAAS. **(C)** Raman spectra collected on LFP electrode surface at a cycling rate of 0.3C (Siddique et al., 2015); **(C1)** carbon-rich spot A during charge; **(C2)** spot A during discharge; **(C3)** carbon-poor spot B during charge; **(C4)** spot B during discharge; **(C5)** corresponding electrochemical cell performance curve with vertical lines indicating the moment when the Raman spectra were taken; with permission from Wiley-VCH Verlag GmbH&Co. KGaA, Weinheim.

expense of LFP as charge proceeds, LFP disappeared completely after voltage reached 4.3 V; and the development of the phase reverses during discharge. The diffraction patterns show that the peak positions of the two phases are unchanged, suggesting a two phase reaction mechanism at the cycling rate of 1C or slower. The same technique is also used to explore the behavior of LFP nano-particles cycled at high rate. **Figure 4B** shows diffraction patterns (bottom) and the image plot of diffraction patterns (top) for (200), (211), (020), and (311) lines obtained on a LFP cathode cycled at 10C rate by using synchrotron X-ray ($\lambda = 0.7272$A). Authors indexed all the peaks observed to either the Li-rich $Li_{1-\alpha}FePO_4$ or the Li-poor $Li_{\beta}FePO_4$ in the space group Pnma. As expected in the cycling at slow rate, $Li_{1-\alpha}FePO_4$ peaks disappear on charge and are restored on discharge; $Li_{\beta}FePO_4$ peaks start to form and grow on charge and disappear on discharge. Unlike in the case of slow cycling, there are appreciable positive intensities within the 8.15° (LPF(200)) to 8.4° (FP(200)), 13.95° (LFP (211)/(020)) to 14.1° (FP(211)), and 15.15° (LFP(301)) to 15.4° (FP(301)) 2θ ranges, which indicate the existence of phases with lattice parameters that deviate from those of $LiFePO_4$ and $FePO_4$ under equilibrium (the corresponding (hkl) of LFP/FP are labeled in the parentheses). The phenomenon is more pronounced at 20C (not shown here). **Figure 4B2** shows that all the peaks are symmetrical at the onset of the first charge, the LFP(200) and (301) started to broaden asymmetrically toward higher angles as charge proceeded. The most severe asymmetrical broadening is around beginning of discharge in both 1st and 2nd cycles. Neither the peak position nor the peak shape of LFP is restored to that of the original state at the end of the discharge, indicating a solid solution of $Li_{1-\alpha}FePO_4$ was formed, which has smaller unit cell and more disordered structure compare to the pristine LFP. These results reveal a different mechanism at high cycling rate, i.e., LFP transforms to FP through a non-equilibrium solid solution instead of two-phase reaction. Capacity fading mechanism in a 18,650 commercial battery was also explored by in situ XRD; the authors observed a different mechanism in LFP/FP conversion after long cycling by formation of a single $Li_{1-x}FePO_4$ phase (Liu et al., 2018). These operando XRD investigations indicate that the working mechanism of the electrode materials may vary with the operating conditions, which may also shed the light on the failure mechanisms under different conditions.

The operando XRD examines the collective behavior of LFP particles on a centimeter scale, whereas Raman spectroscopy explores the local-phase transformation in the micrometer region. The conductivity of LFP is enhanced by adding carbon to the electrode. **Figure 4C** presents the Raman spectra collected from carbon-rich (**Figures 4C1,2**) and carbon-poor (**Figures 4C3,4**) regions of the electrodes during cycling at 0.3C. The bands at ∼950 and 960 cm^{-1} are attributed to the symmetric stretching mode of PO_4^{3-} in LFP and FP. During charge (**Figure 4C1**), the spectra show little change to the end of the 3.5 V plateau, then the 950 cm^{-1} band vanishes and 960 cm^{-1} band appears suddenly (red dot in **Figure 4C5**); the reverse change during discharge (**Figure 4C2**) is observed after the beginning of the discharge plateau (green dot in **Figure 4C5**). The evolution of the spectra demonstrates that the phase transformation between the LFP and FP particles is fast in the carbon-rich environment. A different phenomenon is seen in the carbon-poor area, where no abrupt phase change is detected during charge and discharge, (**Figures 4C3,4**); the main part of LFP does not participate in the reaction, which indicates that less carbon in the area reduces the local conductivity between the LFP particles, thus decreasing electrochemical charge transfer in the active material and leading to capacity loss. These results point out that the problem of capacity loss can be mitigated by converting the non-active regions of the electrode to active regions via homogenizing carbon distribution on a nano-scale. It is clear from both XRD and Raman that the progressive phase transformation observed via XRD is mainly attributed to the increase in the number of completely transformed particles.

Sulfur Cathode

Lithium–sulfur batteries have a high theoretical capacity of 1,675 $mAhg^{-1}$ and utilize low-cost materials. The discharge mechanism of the sulfur electrode is a complex and controversial issue, which was investigated by various *in situ* techniques (Nelson et al., 2012; Cañas et al., 2013; Cui et al., 2013; Cuisinier et al., 2013; Hagen et al., 2013; Patel et al., 2013; Gorlin et al., 2015; Marceau et al., 2016; Paolella et al., 2016). These studies indicate that elemental sulfur discharge is a multi-step process involving different intermediate species that are sensitive to the electrolyte and the operating conditions.

Operando XRD is used to study the battery working mechanism, but it cannot recognize the intermediate poly-sulfides (PSs) due to their non-crystalline nature. The phases which can be identified are the initial phase of α-S_8 (orthorhombic, $a = 10.465$, $b = 12.866$, $c = 24.486$, S.G.: Fddd), the end product of discharge Li_2S(a = 5.72 A, S.G.: $Fm\bar{3}m$), and end product of charge, β-S_8 (monoclinic, $a = 10.926$, $b = 10.855$, $c = 10.790$ A, $\beta = 95.92$, S.G.: P21/c) (Walus et al., 2013; Lowe et al., 2014), as shown in **Figure 5b** (Walus et al., 2013). To study this problem, fused silica is added to the electrolyte because it reacts with the intermediate species and leads to specific absorption of long chain poly-sulfides to form an organized layer (Lay et al., 2003; Hwang et al., 2016) from which the finger prints of the absorbed poly-sulfides are detected via XRD. **Figure 5a** (Conder et al., 2017) shows the evolution of the XRD spectra from the cell with fused silica during the first cycle (left), the corresponding contour plot (right), and the galvanostatic curve (center). The starting red pattern is from

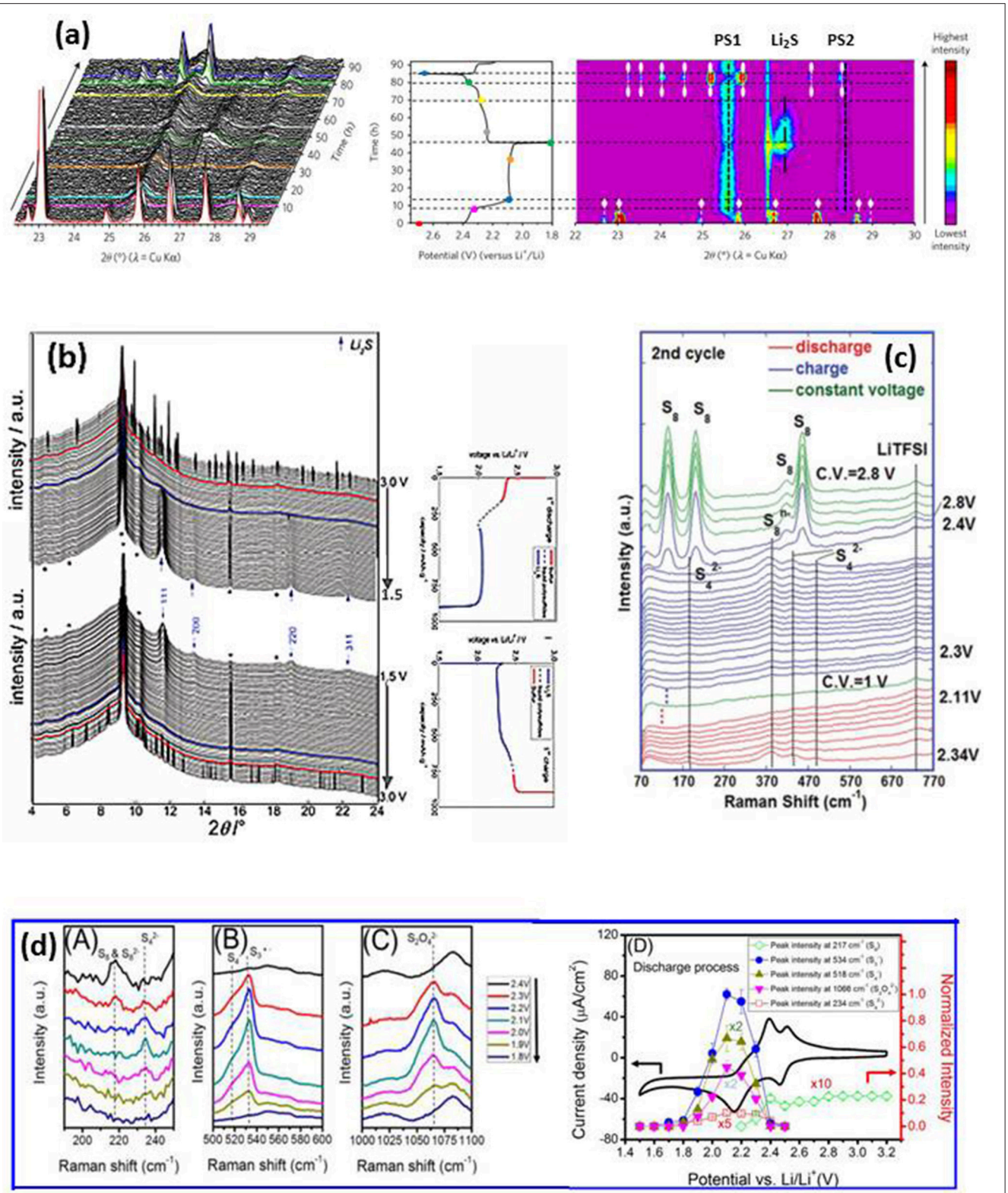

FIGURE 5 | (a) Development of XRD patterns of a Li-S cell with fused silica additive during first cycle (left), corresponding galvanostatic curve at C/50 (center) and XRD image plot (right). The colored patterns (left) correspond to colored dots on the cycling curve (center). α-S_8 and β-S_8 are represented by white lines with diamond and oval symbols, respectively (right). PS1 and PS2 are attributed to the PSs–SiO_2 interactions (vertical black dashed lines). Li_2S is symbolized by a dashed-dotted black vertical line; * is from cell package (Conder et al., 2017); with permission from Springer Nature; **(b)** XRD patterns of a cell during 1st cycle with corresponding

(Continued)

FIGURE 5 | electrochemical plot; arrow, Li_2S; *, cell package; bold lines indicate initial appearance of solid phase and subsequent disappearance (Walus et al., 2013); with permission from RSC; **(c)** Raman spectra from 1 M LiTFSI–DOL–DME electrolyte on the lithium side during first cycle; * separator (Zhu et al., 2017). **(dA-C)** Raman spectra of sulfur cathode during discharge; **(dD)** Cyclic voltammetry of as-prepared sulfur-carbon cathode and potential dependence of the peak intensities (Wu et al., 2015); with permission from ACS.

α-S_8. It disappears quickly as discharge begins, and two broad peaks are observed at 25.56° and 28.32° immediately (labeled PS1 and PS2 respectively). At this early stage of lithiation, the peaks may be related only to the long-chain PSs, the authors attributed them to Li_2S_8, or toLi_2S_6. These two peaks reach a maximum at the end of the first discharge plateau on which the lithiation corresponds to a liquid-liquid equilibrium and Li_2S_8 is reduced to Li_2S_6, then to Li_2S_4. Near the end of discharge, a new peak at ∼27° is detected (orange pattern) that is ascribed to cubic Li_2S. Meanwhile PS1 and PS2 decrease toward the end of the discharge, but do not disappear completely, indicating the incomplete reduction of PS1/PS2. During charge, the phase evolution process is reversed, except the final product is monoclinic β-S_8 (green) instead of α-S_8.

The nature of the non-crystalline intermediate PSs formed during cycling makes the XRD analysis difficult, even with the above-mentioned method. On the other hand, Raman spectroscopy can clearly detect different species formed in the cathode and dissolved in the electrolyte (Yeon et al., 2012; Hannauer et al., 2015; Paolella et al., 2018). **Figure 5c** (Zhu et al., 2017) displays the development of Raman spectra of the electrolyte (1M LiTFSI-DME-DOL) near the lithium anode during the 2nd cycle. It is interesting to note that elemental sulfur is observed at the end of charge near lithium anode; this sulfur is β-S_8 according to operando XRD, which cannot be distinguished from α-S_8 by Raman spectra in the measured region. The loss of active material near the lithium anode reduces the local conductivity and corrodes the lithium, which has a negative effect on battery capacity and cycle life. The effect of the electrolyte on the discharge mechanism was also studied in the same work. The species detected in the 1M LiTFSI-DME-DOL electrolyte near the Li electrode of an as made cell are S_8^{n-} and S_4^{2-}, indicating a rapid self-discharge in this widely used liquid electrolyte. In contrast, self-discharge is much slower in an ionic liquid, where elemental S_8 began to appear on the lithium side at the middle of the high-voltage plateau, and remains until the end of the plateau where S_8^{n-} and S_4^{2-} are observed. The mechanism and kinetics of sulfur reduction in LiTFSI-TEGDME-DIOX electrolyte was investigated by operando Raman, and the results are shown in **Figure 5d** (Wu et al., 2015). S_8/S_8^{2-}, S_4^{2-}, S_4^- and $S_3^{\cdot-}$ are detected at different stages of discharge, and the process is summarized as (1) the formation of long chain PSs as S_8 ring opens at ∼2.4 V; (2) the short chain PSs start to form at ∼2.3 V and they decompose again at 1.6 V. The rate constants of different species are obtained from the evolution of the spectra by fitting the appearance and disappearance of bands to a pseudo first order reaction. Compared to the PSs observed in LiTFSI-DME-DOL, an additional specie $S_3^{\cdot-}$ is detected in LiTFSI-TEGDME-DIOX, indicating that the intermediate PSs are sensitive to the electrolyte used, thus the different discharge mechanisms may vary with the electrolyte chosen. The insights gained from operando Raman analysis provide an explanation for one of the causes of capacity fade, and may be a helpful guide in the selection of a more appropriate electrolyte.

CONCLUSIONS

We reviewed the application of operando X-ray diffraction and operando Raman techniques to characterize operating batteries along with the importance of these techniques to help researchers to understand how the rechargeable batteries work, why they behave in their specific ways, how and why they fail. Operando XRD provides information on the average crystal structural changes of electrodes during cycling. Operando Raman probes the structure of individual particle on the electrode surface, the electrode-electrolyte interface and the electrolyte as well as the species in it to reveal information related to the oxidation state of ions and the interatomic bond length, etc. Raman maps constructed from the information collected describe the behavior of individual electrode particles under operating condition and their influence on the kinetics of phase transformation that is directly related to the battery rate capacity and cycle life. The information obtained by both in situ XRD and Raman methods leads to an atomic level understanding of the variations of structure and its stability, the development of surface and interface structures, which are critical to the battery performance. But for the improvement of the existing electrode materials, the design of new high performance materials, we need more advanced in-situ techniques to reveal the working and degradation mechanisms of different materials. For this purpose, the present operando techniques have to be ameliorated and developed in the directions of (1) multi-functioning, to allow collecting different types of information simultaneously; (2) capability of obtaining 3D morphology information of electrode which is important for improving electrode quality; (3) rapid measurement/fast data collection, to monitor the non-equilibrium state and the rate effect on the materials; (4) ability of measuring the desired materials in the same environment and conditions as the battery in practical applications.

AUTHOR CONTRIBUTIONS

WZ wrote the draft. All authors contributed to the writing, discussion and revision of the final version.

FUNDING

Centre d'excellence en électrification des transports et stockage d'énergie, Québec, Canada.

REFERENCES

Amatucci, G. G., Tarascon, J. M., and Klein, C. (1996). CoO2 the end member of the LiCoO2 solid solution. *J. Electrochem. Soc.* 143, 1114–1123. doi: 10.1149/1.1836594

Amdouni, N., Zaghib, K., Gendron, F., Mauger, A., and Julien, C. M. (2006). Structure and insertion properties of disordered and ordered LiNi0.5Mn1.5O4 spinels prepared by wet chemistry. *Ionics (Kiel).* 12, 117–126. doi: 10.1007/s11581-006-0021-7

Amine, K., Tukamoto, H., Yasuda, H., and Fuiita, Y. (1996). A new three-volt spinel Li1+Mn1.5Ni0.5O4 for secondary lithium batteries. *J. Electrochern. Soc.* 143, 1607–1613. doi: 10.1149/1.1836686

Andersson, A. S., Kalska, B., Häggström, L., and Thomas, J. O. (2000). Lithium extraction/insertion in LiFePO4: an X-ray diffraction and Mössbauer spectroscopy study. *Solid State Ionics* 130, 41–52. doi: 10.1016/S0167-2738(00)00311-8

Armand, M., and Tarascon, J.-M. (2008). Building better batteries. *Nature* 451, 652–657. doi: 10.1038/451652a

Aurbach, D., and Chusid, O. (1997). The use of in situ Fourier-transform infrared spectroscopy for the study of surface phenomena on electrodes in selected lithium battery electrolyte solutions. *J. Power Sour.* 68, 463–470. doi: 10.1016/S0378-7753(97)02622-0

Baddour-Hadjean, R., and Pereira-Ramos, J.-P. (2010). Raman microspectrometry applied to the study of electrode materials for lithium batteries. *Chem. Rev.* 110, 1278–1319. doi: 10.1021/cr800344k

Berckmans, G., Messagie, M., Smekens, J., Omar, N., Vanhaverbeke, L., and Mierlo, J. V. (2017). Cost Projection of state of the art lithium-ion batteries for electric vehicles up to 2030. *Energies* 10:1314. doi: 10.3390/en10091314

Bleith, P., Kaiser, H., Novák, P., and Villevieille, C. (2015). *In situ* X-ray diffraction characterisation of Fe0.5TiOPO4 and Cu0.5TiOPO4 as electrode material for sodium-ion batteries. *Electrochim. Acta* 176, 18–21. doi: 10.1016/j.electacta.2015.06.105

Bobrikov, I. A., Balagurov, A. M., Hu, C.-W., Lee, C.-H., Chen, T.-Y., Deleg, S., et al. (2014). Structural evolution in LiFePO4-based battery materials: in-situ and ex-situ time-of-flight neutron diffraction study. *J. Power Sour.* 258, 356–364. doi: 10.1016/j.jpowsour.2014.02.060

Bobrikov, I. A., Samoylova, N. Y., Sumnikov, S. V., Ivanshina, O. Y., Vasin, R. N., Beskrovnyi, A. I., et al. (2017). *In-situ* time-of-flight neutron diffraction study of the structure evolution of electrode materials in a commercial battery with LiNi0.8Co0.15Al0.05O2 cathode. *J. Power Sour.* 372, 74–81. doi: 10.1016/j.jpowsour.2017.10.052

Budde-Meiwes, H., Drillkens, J., Lunz, B., Muennix, J., Rothgang, S., Kowal, J., et al. (2013). A review of current automotive battery technology and future prospects *Proc. Inst. Mech. Eng. Part D J. Automob. Eng.* 227, 761–776. doi: 10.1177/0954407013485567

Cañas, N. A., Einsiedel, P., Freitag, O. T., Heim, C., Steinhauer, M., Park, D.-W., et al. (2017). Operando X-ray diffraction during battery cycling at elevated temperatures: a quantitative analysis of lithium-graphite intercalation compounds. *Carbon* 116, 255–263. doi: 10.1016/j.carbon.2017.02.002

Cañas, N. A., Wolf, S., Wagner, N., and Friedrich, K. A. (2013). *In-situ* X-ray diffraction studies of lithium–sulfur batteries. *J. Power Sour.* 226, 313–319. doi: 10.1016/j.jpowsour.2012.10.092

Carter, R., Huhman, B., Love, C. T., and Zenyuk, I. V. (2018). X-ray computed tomography comparison of individual and parallel assembled commercial lithium iron phosphate batteries at end of life after high rate cycling. *J. Power Sour.* 381, 46–55. doi: 10.1016/j.jpowsour.2018.01.087

Chan, H.-W., Duh, J.-G., and Lee, J.-F. (2006). Valence change by in situ XAS in surface modified LiMn2O4 for Li-ion battery. *Electrochem. Commun.* 8, 1731–1736. doi: 10.1016/j.elecom.2006.07.038

Chen, G., Song, X., and Richardson, T. J. (2006). Electron microscopy study of the LiFePO4 to FePO4 phase transition. *Electrochem. Solid State Lett.* 9, A295–A298. doi: 10.1149/1.2192695

Chen, K., Cao, K., Xing, C., Hu, Y., Liu, J., He, Y., et al. (2016a). *In-situ* TEM study of the lithiation and delithiation of FeS nanosheets. *J. Alloys Comp.* 688, 946–952. doi: 10.1016/j.jallcom.2016.07.008

Chen, Z., and Dahn, J. R. (2004). Methods to obtain excellent capacity retention in LiCoO2 cycled to 4.5 V. *Electrochim. Acta* 49, 1079–1090. doi: 10.1016/j.electacta.2003.10.019

Chen, Z., Lu, Z., and Dahn, J. R. (2002). Staging phase transitions in Li[sub x]CoO[sub 2]. *J. Electrochem. Soc.* 149, A1604–A1609. doi: 10.1149/1.1519850

Chen, Z., Wang, J., Chao, D., Baikie, T., Bai, L., Chen, S., et al. and Shen, Z. (2016b). Hierarchical porous LiNi1/3Co1/3Mn1/3O2 Nano-/micro spherical cathode material: minimized cation mixing and improved Li+ mobility for enhanced electrochemical performance. *Sci. Rep.* 6:25771. doi: 10.1038/srep25771

Cheng, H., Zhu, C. B., Lu, M., and Yang, Y. (2007). *In situ* micro-FTIR study of the solid–solid interface between lithium electrode and polymer electrolytes. *J. Power Sour.* 174, 1027–1031. doi: 10.1016/j.jpowsour.2007.06.213

Chung, K. Y., Yoon, W.-S., Lee, H. S., McBreen, J., Yang, X.-Q., Oh, S. H., et al. (2006). *In situ* XRD studies of the structural changes of ZrO2-coated LiCoO2 during cycling and their effects on capacity retention in lithium batteries. *J. Power Sour.* 163, 185–190. doi: 10.1016/j.jpowsour.2005.12.063

Chung, K. Y., Yoon, W.-S., Mcbreen, J., Yang, X. Q., Oh, S. Y., Shin, H. C., et al. (2007). *In situ* X-ray diffraction studies on the mechanism of capacity retention improvement by coating at the surface of LiCoO2. *J. Power Sour.* 174, 619–623. doi: 10.1016/j.jpowsour.2007.06.242

Chusid, O., Gofer, Y., Aurbach, D., Watanabe, M., Momma, T., and Osaka, T. (2001). Studies of the interface between lithium electrodes and polymeric electrolyte systems using in situ FTIR spectroscopy. *J. Power Sour.* 97–98, 632–636. doi: 10.1016/S0378-7753(01)00643-7

Conder, J., Bouchet, R., Trabesinger, S., Marino, C., Gubler, L., and Villevieille, C. (2017). Direct observation of lithium polysulfides in lithium–sulfur batteries using operando X-ray diffraction. *Nat. Energy* 2:17069. doi: 10.1038/nenergy.2017.69

Cui, Y., Abouimrane, A., Lu, J., Bolin, T., Ren, Y., Weng, W., et al. (2013). (De)Lithiation Mechanism of Li/SeSx (x =0–7) batteries determined by in situ synchrotron X-ray diffraction and X-ray absorption spectroscopy. *J. Am. Chem. Soc.* 135, 8047–8056. doi: 10.1021/ja402597g

Cuisinier, M., Cabelguen, P.-E., Evers, S., He, G., Kolbeck, M., Garsuch, A., et al. (2013). Sulfur speciation in Li–S batteries determined by operando X-ray absorption spectroscopy. *J. Phys. Chem. Lett.* 4, 3227–3232. doi: 10.1021/jz401763d

Delmas, C., Maccario, M., Croguennec, L., Le Cras, F., and Weill, F. (2008). Lithium deintercalation in LiFePO4 nanoparticles via a domino-cascade model. *Nat. Mater.* 7, 665–671. doi: 10.1038/nmat2230

Dokko, K., Anzue, N., Mohamedi, M., Itoh, T., and Uchida, I. (2004). Raman spectro-electrochemistry of LiCoxMn2–xO4 thin film electrodes for 5 V lithium batteries. *Electrochem. Commun.* 6, 384–388. doi: 10.1016/j.elecom.2004.02.005

Dokko, K., Mohamedi, M., Anzue, N., Itoh, T., and Uchida, I. (2002). In situ Raman spectroscopic studies of LiNixMn2 – xO4thin film cathode materials for lithium ion secondary batteries. *J. Mater. Chem.* 12, 3688–3693. doi: 10.1039/B206764A

Dolotko, O., Senyshyn, A., Mühlbauer, M. J., Nikolowski, K., and Ehrenberg, H. (2014). Understanding structural changes in NMC Li-ion cells by in situ neutron diffraction. *J. Power Sour.* 255, 197–203. doi: 10.1016/j.jpowsour.2014.01.010

Dominko, R., Arčon, I., Kodre, A., HanŽel, D., and Gaberšček, M. (2009). In-situ XAS study on Li2MnSiO4 and Li2FeSiO4 cathode materials. *J. Power Sour.* 189, 51–58. doi: 10.1016/j.jpowsour.2008.11.077

Dong, H., Guo, H., He, Y., Chen, D., Li, H., Gao, J., et al. (2017). Structural stability and Li-ion transport property of LiFePO4 under high-pressure. *Solid State Ionics* 301, 133–137. doi: 10.1016/j.ssi.2017.01.026

Dunn, B., Kamath, H., and Tarascon, J.-M. (2011). Electrical energy storage for the grid: a battery of choices. *Science* 334, 928–935. doi: 10.1126/science.1212741

Etacheri, V., Marom, R., Elazari, R., Salitraa, G., and Aurbach, D. (2011). Challenges in the development of advanced Li-ion batteries: a review *Energy Environ. Sci.* 4, 3243–3262. doi: 10.1039/C1EE01598B

Fehse, M., Monconduit, L., Fischer, F., Tessier, C., and Stievano, L. (2014). Study of the insertion mechanism of lithium into anatase by operando X-ray diffraction and absorption spectroscopy. *Solid State Ionics* 268, 252–255. doi: 10.1016/j.ssi.2014.09.018

Giorgetti, M. (2013). A review on the structural studies of batteries and host materials by X-Ray absorption spectroscopy. *ISRN Mater. Sci.* 2013, 1–22. doi: 10.1155/2013/938625

Girishkumar, G., Mccloskey, B., Luntz, A. C., Swanson, S., and Wilcke, W. (2010). Lithium-Air battery: promise and challenges. *J. Phys. Chem. Lett.* 1, 2193–2203. doi: 10.1021/jz1005384

Giuliana, A., Marco, G., Robert, D., Lorenzo, S., Iztok, A., Nicola, N., et al. (2017). Operando characterization of batteries using x-ray absorption spectroscopy: advances at the beamline XAFS at synchrotron elettra. *J. Phys. D Appl. Phys.* 50:074001. doi: 10.1088/1361-6463/aa519a

Godbole, V. A., Colin, J.-F., and Nováka, A. P. (2011). Study of Overcharge behavior of Li11x(Ni1/3Mn1/3Co1/3)1-xO2 using in situ and ex situ X-ray synchrotron diffraction. *J. Electrochem. Soc.* 158, A1005–A1010. doi: 10.1149/1.3607982

Goodenough, J. B., and Kim, Y. (2010). Challenges for rechargeable Li Batteries. *Chem. Mater.* 22, 587–603. doi: 10.1021/cm901452z

Gorlin, Y., Siebel, A., Piana, M., Huthwelker, T., Jha, H., Monsch, G., et al. (2015). Operando Characterization of Intermediates produced in a Lithium-Sulfur Battery. *J. Electrochem. Soc.* 162, A1146–A1155. doi: 10.1149/2.0081507jes

Gross, T., and Hess, C. (2014). Raman diagnostics of LiCoO2 electrodes for lithium-ion batteries. *J. Power Sour.* 256, 220–225. doi: 10.1016/j.jpowsour.2014.01.084

Hagen, M., Schiffels, P., Hammer, M., Dorfler, S., Tubke, J., Hoffmann, M. J., et al. (2013). *In-Situ* raman investigation of polysulfide formation in Li-S cells. *J. Electrochem. Soc.* 160, A1205–A1214. doi: 10.1149/2.045308jes

Hannauer, J., Scheers, J., Fullenwarth, J., Fraisse, B., Stievano, L., and Johansson, P. (2015). The quest for polysulfides in Lithium-Sulfur battery electrolytes: an operando confocal raman spectroscopy study. *Chemphyschem* 16, 2755–2759. doi: 10.1002/cphc.201500448

Hardwick, L. J., Ruch, P. W., Hahn, M., Scheifele, W., Kötz, R., and Novák, P. (2008). *In situ* raman spectroscopy of insertion electrodes for lithium-ion batteries and supercapacitors: first cycle effects. *J. Phys. Chem. Solids* 69, 1232–1237. doi: 10.1016/j.jpcs.2007.10.017

Harks, P. P. R. M. L., Mulder, F. M., and Notten, P. H. L. (2015). *In situ* methods for Li-ion battery research: a review of recent developments. *J. Power Sour.* 288, 92–105. doi: 10.1016/j.jpowsour.2015.04.084

He, H., Huang, C., Luo, C.-W., Liu, J.-J., and Chao, Z.-S. (2013). Dynamic study of Li intercalation into graphite by in situ high energy synchrotron XRD. *Electrochim. Acta* 92, 148–152. doi: 10.1016/j.electacta.2012.12.135

Hovington, P., Dontigny, M., Guerfi, A., Trottier, J., Lagacé, M., Mauger, A., et al. (2014). *In situ* Scanning electron microscope study and microstructural evolution of nano silicon anode for high energy Li-ion batteries. *J. Power Sour.* 248, 457–464. doi: 10.1016/j.jpowsour.2013.09.069

Hu, S.-K., Cheng, G.-H., Cheng, M.-Y., Hwang, B.-J., and Santhanam, R. (2009). Cycle life improvement of ZrO2-coated spherical LiNi1/3Co1/3Mn1/3O2 cathode material for lithium ion batteries. *J. Power Sour.* 188, 564–569. doi: 10.1016/j.jpowsour.2008.11.113

Huang, Z. D., Liu, X. M., Oh, S. W., Zhang, B., Maa, P. C., and Kim, J. K. (2011). Microscopically porous, interconnected single crystal LiNi1/3Co1/3Mn1/3O2 cathode material for Lithium ion batteries *J. Mater. Chem.* 21, 10777–10784. doi: 10.1039/C1JM00059D

Hugues, D., Hai, B., Leskes, M., Grey, C. P., and Chen, G. (2014). Relationships between Mn3+ content, structural ordering, phase transformation, and kinetic properties in LiNixMn2–xO4 cathode materials. *Chem. Mater.* 26, 5374–5382. doi: 10.1021/cm502607v

Hwang, B. J., Tsai, Y. W., Carlier, D., and Ceder, G. (2003). A combined computational/experimental study on LiNi1/3Co1/3Mn1/3O2. *Chem. Mater.* 15, 3676–3682. doi: 10.1021/cm030299v

Hwang, J. Y., Kim, C. M., Lee, S. K., Lee, J. H., Abouimrane, A., Mo Khaleel, M. A., et al. (2016). Lithium-Sulfur batteries: high-energy, high-rate, lithium–sulfur batteries: synergetic effect of hollow TiO2-webbed carbon nanotubes and a dual functional carbon-paper interlayer. *Adv. EnergyMater.* 6:1501480 doi: 10.1002/aenm.201501480

Inaba, M., Iriyama, Y., Ogumi, Z., Todzuka, Y., and Tasaka, A. (1997). Raman study of layered rock-salt LiCoO2 and its electrochemical lithium deintercalation. *J. Raman Spectrosc.* 28, 613–617. doi: 10.1002/(SICI)1097-4555(199708)28:8<613::AID-JRS138>3.0.CO;2-T

Islam, M. S., Driscoll, D. J., Fisher, C. A. J., and Slater, P. R. (2005). Atomic-scale investigation of defects, dopants, and lithium transport in the LiFePO4 olivine-type battery material. *Chem. Mater.* 17, 5085–5092. doi: 10.1021/cm050999v

Itoh, T., Sato, H., Nishina, T., Matue, T., and Uchida, I. (1997). *In situ* Raman spectroscopic study of LixCoO2 electrodes in propylene carbonate solvent systems. *J. Power Sour.* 68, 333–337. doi: 10.1016/S0378-7753(97)02539-1

Janish, M. T., and Carter, C. B. (2015). *In situ* TEM observations of the lithiation of molybdenum disulfide. *Scr. Mater.* 107, 22–25. doi: 10.1016/j.scriptamat.2015.05.011

Ji, X., and Nazar, L. F. (2010). Advances in Li–S batteries. *J. Mater. Chem.* 20, 9821–9826. doi: 10.1039/b925751a

Joachin, H., Kaun, T. D., Zaghib, K., and Prakasha, J. (2009). electrochemical and thermal studies of carbon-coated LiFePO4 cathode. *J. Electrochem. Soc.* 156, A401–A406. doi: 10.1149/1.3106121

Julien, C. M., Mauger, A., Zaghib, K., and Groult, H. (2014). Comparative issues of cathode materials for Li-Ion batteries. *Inorganics* 2, 132–154. doi: 10.3390/inorganics2010132

Kim, J.-H., Myung, S.-T., Yoon, C. S., Kang, S. G., and Sun, Y.-K. (2004). Comparative study of LiNi0.5Mn1.5O4-ä and LiNi0.5Mn1.5O4 cathodes having two crystallographic structures: Fd3hm and P4332. *Chem. Mater.* 16, 906–914. doi: 10.1021/cm035050s

Komatsu, H., Arai, H., Koyama, Y., Sato, K., Kato, T., Yoshida, R., et al. (2015). Solid solution domains at phase transition front of LixNi0.5Mn1.5O4. *Adv. Energy Mater.* 5:1500638. doi: 10.1002/aenm.201500638

Kostecki, R., and McLarnon, F. (2004). Local-Probe studies of degradation of composite LiNi0.8Co0.15Al0.05O2 cathodes in high-power lithium-ion cells. *Electrochem. Solid-State Lett.* 7, A380–A383. doi: 10.1149/1.1793771

Kraytsberg, A., and Ein-Eli, Y. (2011). Review on Li–air batteries—opportunities, limitations and perspective. *J. Power Sour.* 196, 886–893. doi: 10.1016/j.jpowsour.2010.09.031

Kunduraci, M., Al-Sharab, J. F., and Amatucci, G. G. (2006). High-Power nanostructured LiMn2-xNixO4 high-voltage lithium-ion battery electrode materials: electrochemical impact of electronic conductivity and morphology. *Chem. Mater.* 18, 3585–3592. doi: 10.1021/cm060729s

Kunduraci, M., and Amatucci, G. G. (2006). Synthesis and characterization of nanostructured 4.7 V Li[sub x]Mn[sub 1.5]Ni[sub 0.5]O[sub 4] spinels for high-power lithium-ion batteries. *J. Electrochem. Soc.* 153, A1345–A1352. doi: 10.1149/1.2198110

Laffont, L., Delacourt, C., Gibot, P., Wu, M. Y., Kooyman, P., Masquelier, C., et al. (2006). Study of the LiFePO4/FePO4 two-phase system by high-resolution electron energy loss spectroscopy. *Chem. Mater.* 18, 5520–5529. doi: 10.1021/cm0617182

Lay, M. D., Varazo, K., and Stickney, J. L. (2003). Formation of sulfur atomic layers on gold from aqueous solutions of sulfide and thiosulfate: studies using EC-STM, UHV-EC, and TLEC. *Langmuir* 19, 8416–8427. doi: 10.1021/la034474y

Leriche, J. B., Hamelet, S., Shu, J., Morcrette, M., Masquelier, C., Ouvrard, G., et al. (2010). An electrochemical cell for operando study of lithium batteries using synchrotron radiation. *J. Electrochem. Soc.* 157, A606–A610. doi: 10.1149/1.3355977

Li, J., Petibon, R., Glazier, S., Sharma, N., Pang, W. K., Peterson, V. K., et al. (2015). *In-situ* neutron diffraction study of a high voltage Li(Ni0.42Mn0.42Co0.16)O2/graphite pouch cell. *Electrochim. Acta* 180, 234–240. doi: 10.1016/j.electacta.2015.08.122

Li, W., Reimers, J. N., and Dahn, J. R. (1993). *In situ* X-ray diffraction and electrochemical studies of Lil -xNiO2. *Solid State Ionics* 67, 123–130. doi: 10.1016/0167-2738(93)90317-V

Li, Z., Yang, J., Li, C., Wang, S., Zhang, L., Zhu, K., et al. (2018). Orientation-dependent lithium miscibility gap in LiFePO4. *Chem. Mater.* 30, 874–878. doi: 10.1021/acs.chemmater.7b04463

Liao, X., Sun, P., Xu, M., Xing, L., Liao, Y., Zhang, Y., et al. (2016). Application of tris(trimethylsilyl)borate to suppress self-discharge of layered nickel cobalt manganese oxide for high energy battery. *Appl. Energy* 175, 505–511. doi: 10.1016/j.apenergy.2016.03.114

Liu, H., Strobridge, F. C., Borkiewicz, O. J., Wiaderek, K. M., Chapman, K. W., Chupas, P. J., et al. (2014). Capturing metastable structures during high-rate cycling of LiFePO4 nanoparticle electrodes. *Science* 344:1252817. doi: 10.1126/science.1252817

Liu, Q., Liu, Y., Yang, F., He, H., Xiao, X., Ren, Y., et al. (2018). Capacity fading mechanism of the commercial 18650 LiFePO4-based lithium-ion batteries: an *in situ* time-resolved high-energy synchrotron XRD study. *ACS Appl. Mater. Interfaces* 10, 4622–4629. doi: 10.1021/acsami.7b13060

Liu, S., Xie, J., Su, Q., Du, G., Zhang, S., Cao, G., et al. (2014). Understanding Li-storage mechanism and performance of MnFe2O4 by in situ TEM observation

on its electrochemical process in nano lithium battery. *Nano Energy* 8, 84–94. doi: 10.1016/j.nanoen.2014.06.001

Lowe, M. A., Gao, J., and Abruña, H. D. (2014). Mechanistic insights into operational lithium–sulfur batteries by in situ X-ray diffraction and absorption spectroscopy. *RSC Adv.* 4:18347. doi: 10.1039/c4ra01388c

Lu, Z., and Dahn, J. R. (2002). Understanding the anomalous capacity of Li/Li[Ni[sub x]Li[sub (1/3–2x/3)]Mn[sub (2/3–x/3)]]O[sub 2] cells using *In Situ* X-Ray diffraction and electrochemical studies. *J. Electrochem. Soc.* 149, A815–A822. doi: 10.1149/1.1480014

Ma, R., Shao, L., Wu, K., Shui, M., Wang, D., Pan, J., et al. (2013). Comparison of LiVPO4F to Li4Ti5O12 as anode materials for lithium-ion batteries. *ACS Appl. Mater. Interfaces* 5, 8615–8627. doi: 10.1021/am402132u

MacNeil, D. D., Lu, Z., Chen, Z., and Dahn, J. R. (2002). A comparison of the electrode/electrolyte reaction at elevated temperatures for various Li-ion battery cathodes. *J. Power Sour.* 108, 8–14. doi: 10.1016/S0378-7753(01)01013-8

Manthiram, A., Fu, Y., and Su, A. S. (2013). Challenges and prospects of lithium-sulfur batteries. *Acc. Chem. Res.* 46, 1125–1134. doi: 10.1021/ar300179v

Marceau, H., Kim, C.-S., Paolella, A., Ladouceur, S., Lagacé, M., Chaker, M., et al. (2016). In operando scanning electron microscopy and ultraviolet–visible spectroscopy studies of lithium/sulfur cells using all solid-state polymer electrolyte. *J. Power Sour.* 319, 247–254. doi: 10.1016/j.jpowsour.2016.03.093

Membreno, N., Xiao, P., Park, K. S., Goodenough, J. B., Henkelman, G., and Stevenso, K. J. (2013). *In Situ* raman study of phase stability of α-Li3V2(PO4)3 upon thermal and laser heating. *J. Phys. Chem. C* 117, 11994–12002. doi: 10.1021/jp403282a

Menzel, M., Schlifke, A., Falk, M., Janek, J., Fröba, M., and Fittschen, U. E. A. (2013). Surface and in-depth characterization of lithium-ion battery cathodes at different cycle states using confocal micro-X-ray fluorescence-X-ray absorption near edge structure analysis. *Spectrochim. Acta Part B Atomic Spectrosc.* 85, 62–70. doi: 10.1016/j.sab.2013.04.001

Mikhaylik, Y., Kovalev, I., Schock, R., Kumaresan, K., Xu, J., and Affinito, J. (2010). High energy rechargeable Li-S cells for ev application. *Status Remain. Probl. Solut. ECS Trans.* 25, 23–34. doi: 10.1149/1.3414001

Miller, D. J., Proff, C., Wen, J. G., Abraham, D. P., and Bareño, J. (2013). Observation of microstructural evolution in Li battery cathode oxide particles by *In Situ* electron microscopy. *Adv. Energy Mater.* 3, 1098–1103. doi: 10.1002/aenm.201300015

Minami, T., Tatsumisago, M., Wakihara, M., Iwakura, C., Kohjiya, S., and Tanaka, I. (eds.). (2005). *Recent Development of Electrode Materials in Lithium Ion Batteries*. Tokyo: Springer.

Mohanty, D., Kalnaus, S., Meisner, R. A., Rhodes, K. J., Li, J., Payzant, E. A., et al. (2013). Structural transformation of a lithium-rich Li1.2Co0.1Mn0.55Ni0.15O2 cathode during high voltage cycling resolved by in situ X-ray diffraction. *J. Power Sour.* 229, 239–248. doi: 10.1016/j.jpowsour.2012.11.144

Morcrette, M., Chabre, Y., Vaughan, G., Amatucci, G., Leriche, J. B., Patoux, S., et al. (2002). *In situ* X-ray diffraction techniques as a powerful tool to study battery electrode materials. *Electrochim. Acta* 47, 3137–3149. doi: 10.1016/S0013-4686(02)00233-5

Nelson, J., Misra, S., Yang, Y., Jackson, A., Liu, Y., Wang, H., et al. (2012). In operando X-ray diffraction and transmission X-ray microscopy of lithium sulfur batteries. *J. Am. Chem. Soc.* 134, 6337–6343. doi: 10.1021/ja2121926

Nishi, T., Nakai, H., and Kita, A. (2013). Visualization of the state-of-charge distribution in a LiCoO2 cathode by *in situ* raman imaging. *J. Electrochem. Soc.* 160, A1785–A1788. doi: 10.1149/2.061310jes

Ogata, K., Salager, E., Kerr, C. J., Fraser, A. E., Ducati, C., Morris, A. J., et al. (2014). Revealing lithium–silicide phase transformations in nano-structured silicon-based lithium ion batteries via *in situ* NMR spectroscopy. *Nat. Commun.* 5:3217. doi: 10.1038/ncomms4217

Ohzuku, T., Takeda, S., and Iwanaga, M. (1999). Solid-state redox potentials for Li[Me1/2Mn3/2]O4 (Me: 3d-transition metal) having spinel-framework structures: a series of 5 volt materials for advanced lithium-ion batteries. *J. Power Sour.* 81-82, 90–94. doi: 10.1016/S0378-7753(99)00246-3

Ohzuku, T., and Ueda, A. (1994). Solid-State redox reactions of LiCoO (R3m) for 4 volt secondary lithium cells. *J. Electrochem. Soc.* 141, 2972–2977. doi: 10.1149/1.2059267

Orikasa, A. Y., Maeda, T., Koyama, B. Y., Minato, T., Murayama, H., Fukuda, K., et al. and Ogumi, Z. (2013). Phase transition analysis between LiFePO4 and FePO4 by *In-Situ* time-resolved X-ray absorption and X-ray diffraction. *J. Electrochem. Soc.* 160, A3061–A3065 doi: 10.1149/2.012305jes

Ouvrard, G., Zerrouki, M., Soudan, P., Lestriez, B., Masquelier, C., Morcrette, M., et al. (2013). Heterogeneous behaviour of the lithium battery composite electrode LiFePO4. *J. Power Sour.* 229, 16–21. doi: 10.1016/j.jpowsour.2012.11.057

Padhi, A. K., Nanjundaswamy, K. S., and Goodenough, J. B. (1997). Phospho-olivines as positive-electrode materials for rechargeable lithium batteries. *J. Electrochem. Soc.* 144, 1188–1194. doi: 10.1149/1.1837571

Palacín, M. R. (2009). Recent advances in rechargeable battery materials: a chemist's perspective. *Chem. Soc. Rev.* 38, 2565–2575. doi: 10.1039/b820555h

Paolella, A., Laul, D., Timoshevskii, V., Zhu, W., Marras, S., Bertoni, G., et al. (2018). The role of metal disulfide interlayer in Li–S batteries. *J. Phys. Chem. C* 122, 1014–1023. doi: 10.1021/acs.jpcc.7b08719

Paolella, A., Zhu, W., Marceau, H., Kim, C.-S., Feng, Z., Liu, D., et al. (2016). Transient existence of crystalline lithium disulfide Li2S2 in a lithium-sulfur battery. *J. Power Sour.* 325, 641–645. doi: 10.1016/j.jpowsour.2016.06.086

Park, J. H., Cho, J. H., Kim, S. B., Kim, W. S., Lee, S. Y., and Lee, S. Y. (2012). A novel ion-conductive protection skin based on polyimide gel polymer electrolyte: application to nanoscale coating layer of high voltage LiNi1/3Co1/3Mn1/3O2 cathode materials for lithium-ion batteries *J. Mater. Chem.* 22, 12574–12581. doi: 10.1039/c2jm16799a

Patel, M. U., Demir-Cakan, R., Morcrette, M., Tarascon, J. M., Gaberscek, M., and Dominko, R. (2013). Li-S battery analyzed by UV/Vis in operando mode. *ChemSusChem* 6, 1177–1181. doi: 10.1002/cssc.201300142

Perea, A., Sougrati, M. T., Ionica-Bousquet, C. M., Fraisse, B., Tessier, C., Aldon, L., et al. (2012). Operando57Fe Mössbauer and XRD investigation of LixMnyFe1-yPO4/C composites (y = 0.50; 0.75). *RSC Adv.* 2, 9517–9524. doi: 10.1039/C2RA20949G

Ramana, C. V., Mauger, A., Gendron, F., Julien, C. M., and Zaghib, K. (2009). Study of the Li-insertion/extraction process in LiFePO4/FePO4. *J. Power Sour.* 187, 555–564. doi: 10.1016/j.jpowsour.2008.11.042

Reimers, J. N., and Dahn, J. R. (1992). Electrochemical and *In Situ* X-Ray diffraction studies of lithium intercalation in LixCo02. *J. Electrochem. Soc.* 139, 2091–2097. doi: 10.1149/1.2221184

Rhodes, K., Meisner, R., Kim, Y., Dudney, N., and Daniela, C. (2011). Evolution of phase transformation behavior in Li(Mn1.5Ni0.5)O4m cathodes studied by *In Situ*, X. R. D. *J. Electrochem. Soc.* 158, A890–A897. doi: 10.1149/1.3596376

Roberts, M. R., Madsen, A., Nicklin, C., Rawle, J., Palmer, M. G., Owen, J. R., et al. (2014). Direct observation of active material concentration gradients and crystallinity breakdown in LiFePO4 electrodes during charge/discharge cycling of lithium batteries. *J. Phys. Chem. C* 118, 6548–6557. doi: 10.1021/jp411152s

Samarasingha, P., Sottmanna, J., Margadonna, S., and Fjellvåga, H. (2016). *In situ* synchrotron study of ordered and disordered LiMn1.5Ni0.5O4 as lithium ion battery positive electrode. *Acta Mater.* 116, 290–297. doi: 10.1016/j.actamat.2016.06.040

Saravanan, K., Jarry, A., Kostecki, R., and Chen, G. (2015). A study of room-temperature LixMn1.5Ni0.5O4 solid solutions. *Sci. Rep.* 5:8027. doi: 10.1038/srep08027

Sarkar, S., and Mitra, S. (2014). Carbon coated submicron sized-LiFePO4: improved high rate performance lithium battery cathode. *Energy Proc.* 54, 718–724. doi: 10.1016/j.egypro.2014.07.312

Shin, H. C., Chung, K. Y., Min, W. S., Byun, D. J., Jang, H., and Cho, B. W. (2008). Asymmetry between charge and discharge during high rate cycling in LiFePO4 – *in situ* X-ray diffraction study. *Electrochem. Commun.* 10, 536–540. doi: 10.1016/j.elecom.2008.02.002

Shin, H. C., Nam, K. W., Chang, W. Y., Cho, B. W., Yoon, W.-S., Yang, X.-Q., et al. (2011). Comparative studies on C-coated and uncoated LiFePO4 cycling at various rates and temperatures using synchrotron based in situ X-ray diffraction. *Electrochim. Acta* 56, 1182–1189. doi: 10.1016/j.electacta.2010.10.087

Siddique, N. A., Salehi, A., Wei, Z., Liu, D., Sajjad, S., and Liu, F. (2015). Length-Scale-Dependent Phase transformation of LiFePO4 an *In situ* and operando study using Micro-Raman spectroscopy and XRD. *Chemphyschem* 16, 2383–2388. doi: 10.1002/cphc.201500299

Stancovski, V., and Badilescu, S. (2013). *In situ* Raman spectroscopic–electrochemical studies of lithium-ion battery materials: a historical overview. *J. Appl. Electrochem.* 44, 23–43. doi: 10.1007/s10800-013-0628-0

Sun, X., Yang, X. Q., Mcbreen, J., Gao, Y., Yakovleva, M. V., Xing, X. K., et al. (2001). New phases and phase transitions observed in over-charged states of LiCoO2-based cathode materials. *J. Power Sour.* 97–98, 274–276. doi: 10.1016/S0378-7753(01)00512-2

Sun, Y., Zhao, L., Pan, H., Lu, X., Gu, L., Hu, Y. S., et al. (2013). Direct atomic-scale confirmation of three-phase storage mechanism in Li4Ti5O12 anodes for room-temperature sodium-ion batteries. *Nat. Commun.* 4:1870. doi: 10.1038/ncomms2878

Takahashi, K., Saitoh, M., Sano, M., Fujita, M., and Kifunec, K. (2004). Electrochemical and structural properties of a 4.7 V-Class LiNi0.5Mn1.5O4 positive electrode material prepared with a self-reaction method. *J. Electrochem. Soc.* 151, A173–A177. doi: 10.1149/1.1633267

Tarascon, J. M., and Armand, M. (2001). Issues and challenges facing rechargeable lithium batteries. *Nature* 414, 359–367. doi: 10.1038/35104644

Waluś, S., Barchasz, C., Colin, J. F., Martin, J. F., Elkaïm, E., Leprêtre, J. C., et al. (2013). New insight into the working mechanism of lithium-sulfur batteries: in situ and operando X-ray diffraction characterization. *Chem. Commun. (Camb).* 49, 7899–7901. doi: 10.1039/c3cc43766c

Wang, C. M. (2015). *In situ* transmission electron microscopy and spectroscopy studies of rechargeable batteries under dynamic operating conditions: a retrospective and perspective view. *J. Mater. Res.* 30, 326–339. doi: 10.1557/jmr.2014.281

Wang, H., and Wang, F. (2016). *In situ*, operando measurements of rechargeable batteries. *Curr. Opin. Chem. Eng.* 13, 170–178. doi: 10.1016/j.coche.2016.09.002

Wang, L., Li, H., Huang, X., and Baudrin, E. (2011). A comparative study of Fd-3m and P4332 "LiNi0.5Mn1.5O4". *Solid State Ionics* 193, 32–38. doi: 10.1016/j.ssi.2011.04.007

Wang, X. L., An, K., Cai, L., Feng, Z., Nagler, S. E., Daniel, C., et al. (2012). Visualizing the chemistry and structure dynamics in lithium-ion batteries by *in-situ* neutron diffraction. *Sci. Rep.* 2:747. doi: 10.1038/srep00747

Wen, J., Yu, Y., and Chen, C. (2012). A review on lithium-ion batteries safety issues: existing problems and possible solutions. *Mater. Express* 2, 197–212. doi: 10.1166/mex.2012.1075

Wu, H. L., Huff, L. A., and Gewirth, A. A. (2015). *In situ* Raman spectroscopy of sulfur speciation in lithium-sulfur batteries. *ACS Appl. Mater. Interfaces* 7, 1709–1719. doi: 10.1021/am5072942

Wu, J., Dathar, G. K., Sun, C., Theivanayagam, M. G., Applestone, D., Dylla, A. G., et al. (2013). *In situ* Raman spectroscopy of LiFePO4: size and morphology dependence during charge and self-discharge. *Nanotechnology* 24:9. doi: 10.1088/0957-4484/24/42/424009

Xu, Z.-L., Cao, K., Abouali, S., Akbari Garakani, M., Huang, J., Huang, J.-Q., et al. (2016). Study of lithiation mechanisms of high performance carbon-coated Si anodes by in-situ microscopy. *Energy Storage Mater.* 3, 45–54. doi: 10.1016/j.ensm.2016.01.003

Yang, J., Han, X., Zhang, X., Cheng, F., and Chen, J. (2013). Spinel LiNi0.5Mn1.5O4 cathode for rechargeable lithiumion batteries: nano vs micro, ordered phase (P4332) vs disordered phase (Fd3-m). *Nano Res.* 6, 679–687. doi: 10.1007/s12274-013-0343-5

Yang, S., He, P., and Zhou, H. (2018). Research progresses on materials and electrode design towards key challenges of Li-air batteries. *Energy Storage Mater.* 13, 29–48. doi: 10.1016/j.ensm.2017.12.020

Yang, X. Q., Mcbreen, J., Yoon, W.-W., and Grey, C. P. (2002). Crystal structure changes of LiMn0:5Ni0:5O2 cathode materials during charge and discharge studied by synchrotron based in situ XRD. *Electrochem. Commun.* 4, 649–654. doi: 10.1016/S1388-2481(02)00406-X

Yang, X. Q., and Nam, K. W. (2010). *In situ Characterizations of New Battery Materials and the Studies of High Energy Density Li-Air Batteries*. PPT.

Yang, X. Q., Sun, X., and Mcbreen, J. (2000). New phases and phase transitions observed in Li1–xCoO2 during charge: *in situ* synchrotron X-ray diffraction studies. *Electrochem. Commun.* 2, 100–103. doi: 10.1016/S1388-2481(99)00155-1

Ye, J.-Y., Jiang, Y.-X., Sheng, T., and Sun, S.-G. (2016). *In-situ* FTIR spectroscopic studies of electrocatalytic reactions and processes. *Nano Energy* 29, 414–427. doi: 10.1016/j.nanoen.2016.06.023

Yeon, J. T., Jang, J. Y., Han, J. G., Cho, J., Lee, K. T., and Choi, N. S. (2012). Raman spectroscopic and X-ray diffraction studies of sulfur composite electrodes during discharge and charge. *J. Electrochem. Soc.* 159, A1308–A1314. doi: 10.1149/2.080208jes

Zhang, X., Kuhnel, R.-S., Schroeder, M., and Balducci, A. (2014). Revisiting Li3V2(PO4)3 as an anode – an outstanding negative electrode for high power energy storage devices. *J. Mater. Chem. Phys.* 2, 17906–17913. doi: 10.1039/C4TA03845B

Zhao, N., Li, Y., Zhi, X., Wang, L., Zhao, X., Wang, Y., et al. (2016). Effect of Ce3+ doping on the properties of LiFePO4 cathode material. *J. Rare Earths* 34, 174–180. doi: 10.1016/S1002-0721(16)60011-X

Zhu, W., Liu, D., Trottier, J., Gagnon, C., Guerfi, A., Julien, C. M., et al. (2014). Comparative studies of the phase evolution in M-doped LixMn1.5Ni0.5O4 (M = Co, Al, Cu and Mg) by *in-situ* X-ray diffraction. *J. Power Sour.* 264, 290–298. doi: 10.1016/j.jpowsour.2014.03.122

Zhu, W., Liu, D., Trottier, J., Gagnon, C., Howe, J., Mauger, A., et al. (2015). *In-situ* Raman spectroscopic investigation of LiMn1.45Ni0.45M0.1O4 (M = Cr, Co) 5 V cathode materials. *J. Power Sour.* 298, 341–348. doi: 10.1016/j.jpowsour.2015.07.083

Zhu, W., Liu, D., Trottier, J., Gagnon, C., Mauger, A., Julien, C. M., et al. (2013). *In-situ* X-ray diffraction study of the phase evolution in undoped and Cr-doped LixMn1.5Ni0.5O4 ($0.1 < x < 1.0$) 5-V cathode materials. *J. Power Sources* 242, 236–243. doi: 10.1016/j.jpowsour.2013.05.021

Zhu, W., Paolella, A., Kim, C.-S., Liu, D., Feng, Z., Gagnon, G., et al. (2017). Investigation of the reaction mechanism of lithium sulfur batteries in different electrolyte systems by *in situ* Raman spectroscopy and in situ X-ray diffraction. *Sustain. Energy Fuels* 1, 737–747. doi: 10.1039/C6SE00104A

Zhu, Y., Wang, J. W., Liu, Y., Liu, X., Kushima, A., Liu, Y., et al. (2013). *In Situ* atomic-scale imaging of phase boundary migration in fepo 4 microparticles during electrochemical lithiation. *Adv. Mater. Weinheim.* 25, 5461–5466. doi: 10.1002/adma.201301374

Conflict of Interest Statement: The authors declare that the research was conducted in the absence of any commercial or financial relationships that could be construed as a potential conflict of interest.

frontiers in Energy Research

ORIGINAL RESEARCH
published: 04 July 2018
doi: 10.3389/fenrg.2018.00059

Revealing Operando Transformation Dynamics in Individual Li-ion Electrode Crystallites Using X-Ray Microbeam Diffraction

*Martijn van Hulzen[1], Frans G. B. Ooms[1], Jonathan P. Wright[2] and Marnix Wagemaker[1]**

[1] Department of Radiation Science and Technology, Delft University of Technology, Delft, Netherlands, [2] ID11 - Materials Science Beamline, European Synchrotron Radiation Facility, Grenoble, France

For the development of next-generation batteries it is important to understand the structural changes in electrodes under realistic non-equilibrium conditions. With microbeam X-ray diffraction it is possible to probe many individual electrode grains concurrently under non-equilibrium conditions in realistic battery systems. This makes it possible to capture phase transformation behavior that is difficult or even impossible with powder diffraction. By decreasing the X-ray beam size, the diffraction powder rings fall apart in the (hkl) reflections belonging to individual electrode crystallites. Monitoring these reflections during (dis)charging provides direct insight in the transformation mechanism and kinetics of individual crystallite grains. Here operando microbeam diffraction is applied on two different cathode materials, $LiFePO_4$ (LFP) displaying a first-order phase transformation and $LiNi_{1/3}Co_{1/3}Mn_{1/3}O_2$ (NCM) displaying a solid solution transformation. For LFP four different phase transformation mechanisms are distinguished within a single crystallite: (1) A first-order phase transformation without phase coexistence, (2) with phase coexistence, (3) a homogeneous solid solution phase transformation and (4) an inhomogeneous solid solution crystal transformation, whereas for NCM only type (3) is observed. From the phase transformation times of individual crystallites, the local current density is determined as well as the active particle fractions during (dis)charge. For LFP the active particle fraction increases with higher cycling rates. At low cycling rates the active particle fraction in NCM is much larger compared to LFP which appears to be related to the nature of the phase transition. In particular for LFP the grains are observed to rotate during (dis)charging, which can be quantified by microbeam diffraction. It brings forward the mechanical working of the electrodes due to the volumetric changes of the electrode material possibly affecting electronic contacts to the carbon black conducting matrix. These results demonstrate the structural information that can be obtained under realistic non-equilibrium conditions, combining local information on single electrode crystallites, as well as global information through the observation in many crystallites concurrently. This provides new and complementary possibilities in operando battery research, which can contribute to fundamental understanding as well as the development of electrodes and electrode materials.

Keywords: microbeam X-ray diffraction, operando, transformation kinetics, Li-ion, X-ray diffraction, electrodes, phase transitions

OPEN ACCESS

Edited by:
Neeraj Sharma,
University of New South Wales, Australia

Reviewed by:
Matthew Ryan Rowles,
Curtin University, Australia
Jianping Huang,
Stony Brook University, United States
Wesley M. Dose,
Argonne National Laboratory (DOE), United States

***Correspondence:**
Marnix Wagemaker
m.wagemaker@tudelft.nl

Specialty section:
This article was submitted to Energy Storage, a section of the journal Frontiers in Energy Research

Received: *04 April 2018*
Accepted: *05 June 2018*
Published: *04 July 2018*

Citation:
van Hulzen M, Ooms FGB, Wright JP and Wagemaker M (2018) Revealing Operando Transformation Dynamics in Individual Li-ion Electrode Crystallites Using X-Ray Microbeam Diffraction. Front. Energy Res. 6:59. doi: 10.3389/fenrg.2018.00059

1. INTRODUCTION

Li-ion batteries have driven the development of today's portable electronics and electrical vehicles. More generally, next-generation electrochemical storage is expected to be a key technology for our renewable energy future, including large scale introduction of electrical mobility and lifting the difference between supply and demand of renewable energy sources. This puts significant pressure on the development of battery chemistries, which requires comprehensive atomic scale understanding of electrochemical processes. A crucial aspect for many battery chemistries is the formation, decomposition and transformation of electrochemically active crystalline phases, which typically determine a battery's cycle life, practical capacity and kinetic performance. To understand these structural processes, powder diffraction experiments are applied intensively (Harks et al., 2015; Ma et al., 2016). With *ex-situ* experiments non-equilibrium states and processes are not captured, and often the reactivity of the components during the process toward *ex-situ* measurements hinder the observation of the true equilibrium state. As a consequence there is a strong demand to do operando structural investigations, that is to perform diffraction during battery charging and discharging.

1.1. Operando Investigations

Operando powder diffraction, both neutron and X-ray (Harks et al., 2015; Ma et al., 2016; Lin et al., 2017; Peterson et al., 2017; Tan et al., 2017) have contributed to the understanding of the solid state reactions taking place in batteries. Powder diffraction provides average structural properties over a large ensemble of electrode crystallites present in realistic electrodes. This inevitably obscures the transformation mechanism of individual electrode crystallites and how these collectively contribute to the macroscopic phase transition, which is key information for thoroughly understanding the relation between materials properties and the performance of battery electrodes. The potentially (dis)charge rate dependent transformation mechanisms of individual crystallites provides insight in the electrode material cycle life and what limits the (dis)charge rate of the material. The collective behavior of many individual electrode particles provides insight in how the total battery current is distributed over the individual grains, potentially creating detrimental hotspots. An inhomogeneous current distribution enhances local electrolyte decomposition and overcharge behavior, making the lifetime shorter and the safety lower (Kerlau et al., 2007; Maire et al., 2008; Katayama et al., 2014; Taminato et al., 2016; Tanida et al., 2016).

1.2. Operando X-Ray Microbeam Diffraction

Recently, operando microbeam diffraction has been introduced, which is able to probe the phase transformation of many individual electrode grains in realistic battery systems under non-equilibrium battery conditions (Zhang et al., 2015; Ganapathy et al., 2016; Niwa et al., 2017). By reducing the X-ray beam size to micron scale, fewer crystallites will be in Bragg condition and as a result diffract. As a consequence, the powder diffraction rings fall apart in single crystal reflections, each originating from a single electrode crystallite. Along operando experiments on two types of electrodes, (1) $LiFePO_4$ and (2) $LiNi_{1/3}Co_{1/3}Mn_{1/3}O_2$, we demonstrate the principle, data analysis and interpretation, and hence the information that can be extracted from operando microbeam diffraction. These experiments reveal various crystal transformation mechanisms as well as the transformation times of individual crystallites, occurring concurrently in the many crystallites that are monitored. In addition this brings forward the active particle fraction and also the mechanically induced rotations of the electrode crystallites in the electrode matrix providing new insights in the working of electrodes. The non-invasive nature of these operando microbeam experiments, provides the ability to obtain more understanding of the structural transformations in realistic battery electrodes, that will help understanding the fundamental processes that determine the performance of batteries.

2. MATERIALS AND METHODS

2.1. Cathode Preparations

The starting material is carbon coated $LiFePO_4$ from Phostech with an average particle size of 140 nm. Regular $LiFePO_4$ cathodes were prepared through mixing a slurry of $LiFePO_4$, Carbon Black (Super P), PVDF, (polyvinylidene fluoride, Solvay) in NMP (N-methylpyrrolidone), with a mass ratio of the active material ($LiFePO_4$), carbon black (SuperP) and binder (PVDF) of 75:15:10. In addition carbonate template electrodes were prepared to reach high capacities at high rates as reported recently (Singh et al., 2013). For the electrodes, 40 wt% $NaHCO_3$ (Aldrich) is added to the electrode slurry mixing, a large part of which is lost by dissolution in the solvent. The final slurry was casted on carbon coated Aluminium current collectors by doctor blading. The coatings were dried on a heater plate under air at approximately 155°C overnight followed by drying under vacuum at around 60°C for more than 24h. The resulting coatings were pressed using a roller hand press to enhance the electronic contact. After mechanical compaction the $NaHCO_3$ templated electrodes were washed in demineralized water that reacts with the $NaHCO_3$ to form NaOH and gaseous CO_2, resulting in a an electrode where the interconnectivity of the porosity in the electrodes is improved as demonstrated previously (Singh et al., 2013). Finally, the electrodes are dried for at least 3h under vacuum at 100°C. The results are reported on electrodes with loading density between 2 and 4 mg/cm^2 and with a thickness of approximately 10–20 μm. For preparing the $LiNi_{1/3}Co_{1/3}Mn_{1/3}O_2$ cathodes the same method with ratio, 80:10:10, of active material, Carbon Black and PVDF were used. No templating was applied.

2.2. Pouch Cell Preparation and Testing

The electrodes were assembled in coffee-bag type cells all assembled under argon atmosphere ($<$ 0.1 ppm O_2/H_2O). The electrodes were separated by glass microfiber filters (Whatman) with a few droplets of 1 mol/liter $LiPF_6$ (EC:DMC 1:1, Novolyte) electrolyte.

2.3. X-Ray Microdiffraction Experiment

At the European Synchrotron Radiation Facility in Grenoble, France the operando microbeam X-ray experiments were conducted at beamline ID11. For the $LiFePO_4$ experiments using a combination of beryllium and aluminum mirrors a monochromatic X-ray microbeam with an energy of 45 keV (wavelength 0.27552 Å) and a beam size of $\sim 2x3\mu m$ was configured. For NCM an energy of 42 keV (wavelength 0.29519 Å) and a beam-size of $\sim 8x8\mu m$ was used (NCM crystallites are $\sim 1-2\ \mu m$ in size). **Figure 2** shows a schematic experiment setup where the X-ray beam transmits through two layers of Al, the cathode material of interest, the solipor separator soaked in EC/DMC electrolyte, a disc of Li-metal and two layers of Cu. All the electrochemical tests were performed galvanostatically within a voltage window of 4.3 and 2.5 V vs. Li/Li+ for the $LiFePO_4$ electrodes and of 4.3 and 3.0 V vs. Li/Li+ for the NCM electrodes using an Autolab PGSTAT302N potentiostat/galvanostat.

With microbeam X-ray diffraction it is possible to follow reflections of individual grains over time. Initial beam exposure tests were conducted to make sure that the material, electrode and electrolyte do not decompose/degrade. As an additional measure the sample was moved between two points after each omega scan, to spread the beam exposure. In **Table 1** an overview of the experiment details is provided. For the LFP 1C experiment, with C/n denoting the rate at which a full charge or discharge takes n hours, an omega scan from –2.5 to 2.5 degrees was performed, hence the sample was rotated along the z-axis in ten steps of each half a degree (see **Figure 1** for the experiment geometry). Each rotation step of half a degree takes 5 s, which is also the frame exposure time. As a result the average temporal resolution for individual omega scans is 13.5 s and for a complete omega

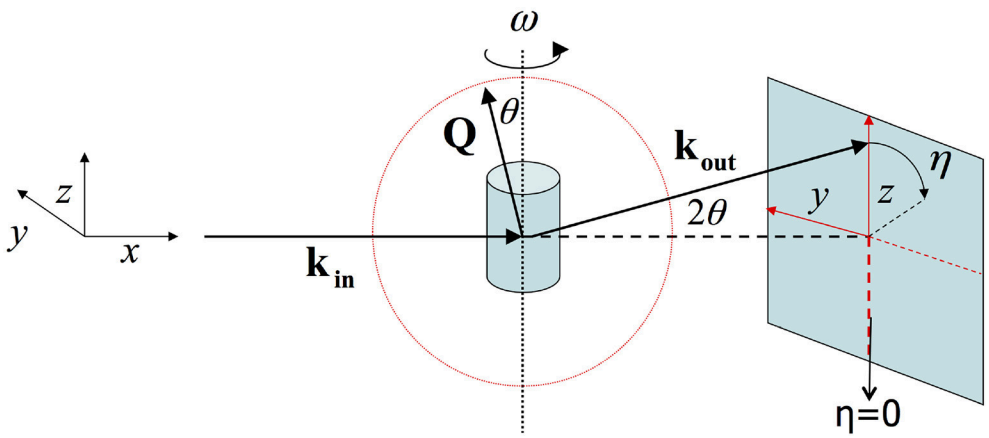

FIGURE 1 | In the geometry of 2D X-ray diffraction the X-ray beam lies along the x-axis. ω reflects the angle with which the sample is rotated along the z-axis. And η is the angle along the diffraction ring.

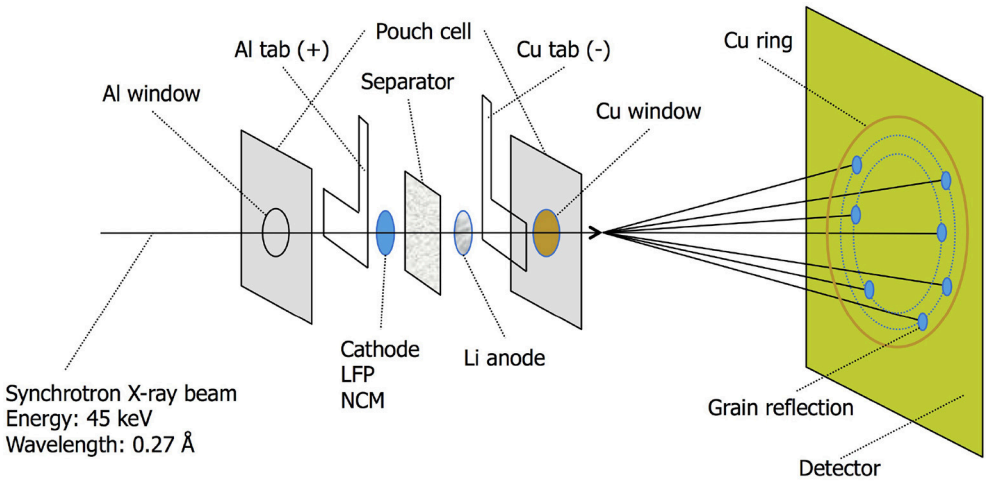

FIGURE 2 | ID11 X-ray synchrotron beamline passing through the various layers of the pouch cell. The microbeam causes the diffraction ring to break up in spots originating from single electrode grains.

TABLE 1 | Experiment execution details.

Material	Rate	ω angle range (step)	Nr of ω steps	Nr of frames (compounded)	Exposure time	Full cycle duration	Beam size
LFP	1C	-2.5–2.5 (0.5)	10	1560 (156)	5 s	2 h	2 × 3 μm
LFP	5C	-0.5–0.5 (1)	1	400	5 s	24 mins	2 × 3 μm
LFP	10C	-0.5–0.5 (1)	1	417	3 s	12 mins	2 ×3 μm
NCM	C/4	-3–3 (0.5)	12	4656 (387)	5 s	9 h	8 ×8 μm

For each cycling rate a different combination of exposure time and angle range was used. In the LFP 1C a 10 step ω scan over 5° was performed with an exposure time of 5 s per step. For the 5C and 10C experiment only one rotation step of a full degree was used to be able to capture the faster dynamics. For the short cycles in the 10C experiment only a frame exposure of 3 s was used. The NCM experiment used a 12 step ω scan over six degrees with 5 s exposure per step.

scan 135 s. By monitoring the intensity of the reflection during the omega scan, it is possible to derive the direction and speed of the grain rotation, and when the omega scan completely crosses the reflection of the individual grain, its grain volume can be determined, see supplement of Zhang et al. (2015).

2.4. Data Processing

Each reflection is indexed based on its 2Θ angle and its position on the diffraction ring, defined by its η angle along this ring. In addition the size and the total intensity of each reflection is determined. **Figure 3** shows an EDF (ESRF Data Format) frame that was collected during the experiment. It records the intensity of each of the 2,048 × 2,048 pixels of the detector. The X-ray beam is small enough for the diffraction rings to break up in individual grain reflections. The Al and Cu layers show up as strong rings in the corners. In Table S1 the reflections of a few grains and their properties are listed. To identify and follow grain reflections over time Matlab® was used to process the experiment data consisting of the collected EDF frames for each experiment. Three steps were followed: (1) finding grain reflections per frame, (2) labeling grain reflections in different frames and (3) add meta data which includes the number of reflections, initial, minimum and maximum 2Θ values. The reflections gathered in step (1) make it possible to break down the reflections according to hkl index. In Figure S1 the average number of reflections per frame per hkl is shown. Connecting the reflections occurring in different frames, step (2), is the most challenging to automate. Here the approach was chosen to start with a reflection from the first frame and to look for reflections in subsequent frames that have the same hkl and fall within a certain η range (a certain section of the diffraction ring). This process is repeated until all reflections are labeled. The last step is to add meta data including number of reflections, min/max 2Θ, η and ω angles. In Table S2 a few labels and their meta data are shown. The integrated intensity of a reflection can be used to derive the crystal volume (Zhang et al., 2015). After determining the incident flux of photons Φ_0 from the intensity of a powder ring of your material of interest it is possible to directly calculate the crystal volume from the observed reflection intensity, see Zhang et al. (2015) supplement note 3 for a detailed explanation.

3. RESULTS AND DISCUSSION

Reduction of the X-ray beam size toward micron size makes that fewer crystallites are in Bragg condition. As a consequence, the powder diffraction rings fall apart in single crystal reflections, each originating from a single electrode crystallite. By performing microbeam X-ray diffraction during battery operation it is possible to track many individual reflections concurrently during a charge/discharge cycle. In **Figure 4** the number of $LiFePO_4$ (LFP) and $FePO_4$ (FP) crystallites are shown as a function of time during a full 1C charge discharge cycle. The decreasing amount of observed LFP domains, and increasing FP domains during charge, and vice versa during discharge reflects the expected first-order phase transition of this material upon lithium extraction and insertion. However, to gain insight how this proceeds within single grains we can monitor individual reflections. Here we discuss experiment data obtained from three LFP experiments with C-rates 1C, 5C and 10C, and one NCM C/4 experiment. Details on the charge/discharge regime as well as material loading and Coulombic efficiency for of each of these experiments are given in Table S3.

3.1. Transformation Mechanics

In presenting the results it is useful to first look at compounded data where frames belonging to the same ω scan are added up and averaged (see frame numbers in brackets in **Table 1**). In **Figure 5A** the (200) reflection of an LFP grain is shown at various states of charge. During charge both LFP and FP phases are visible between t = 18–55 min. A first observation is the stretched shape of the reflection along the diffraction ring. Where broadening in the 2Θ directions relates to the crystallite domains size and strain, in this case perpendicular to the (200) lattice plain direction, the distribution of intensity over η suggests mosaicity in the a-lattice direction for both the LFP and FP domains. The intensity of the LFP phase reflection decreases while at the same time that of the FP phase is growing, clearly representing the well-known phase transition, but in this case monitored operando for an individual crystallite electrode particle. During this 1C experiment the LFP-FP phase transition in this specific grain takes around 37 min, 62% of total charging time. From the intensity of the reflections it is possible to approximate the volume of the grain (see 2.4), and thereby the phase-volume transition-rate. This allows us to calculate the current this individual grain is contributing, and hence the local current density. After the complete transformation from LFP to FP during charging, discharging is initiated at t = 95 min. As expected the intensity of the FP reflection weakens, but also moves along the η angle. After t = 146 min the reflection completely disappears, and the LFP reflection does not reappear.

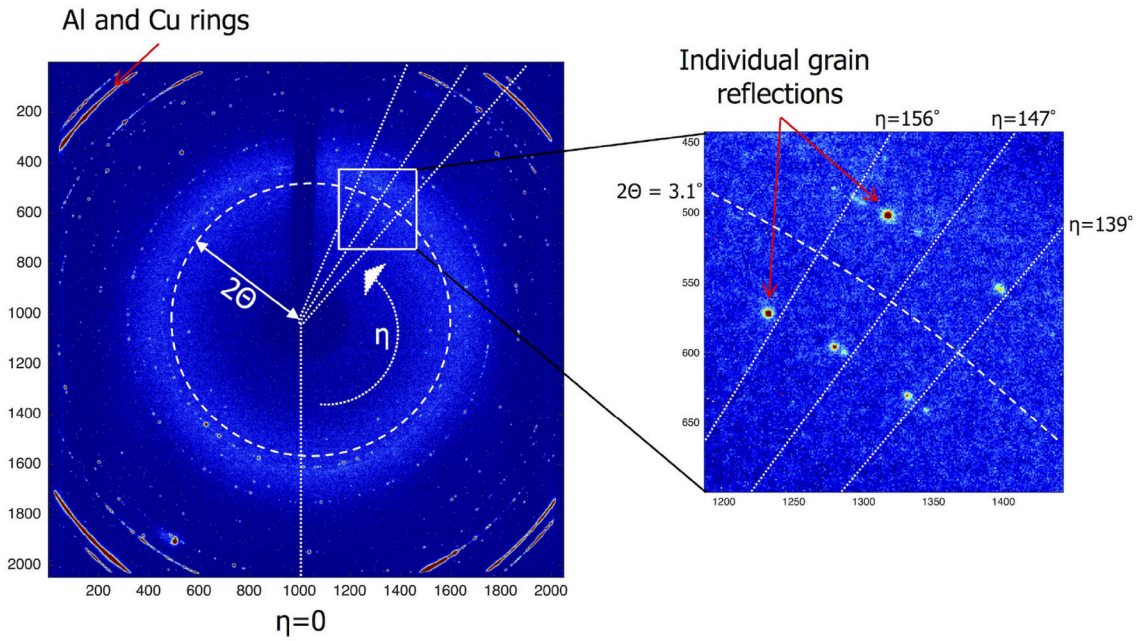

FIGURE 3 | Sample of an EDF Frame which is a read-out of the detectors 2,048 × 2,048 pixels. The location of each grain reflection is a unique combination of the polar coordinates η and 2Θ. Using the 2Θ angle the miller index can be derived. The η angle can be used to find reflections of the same grain in subsequent frames.

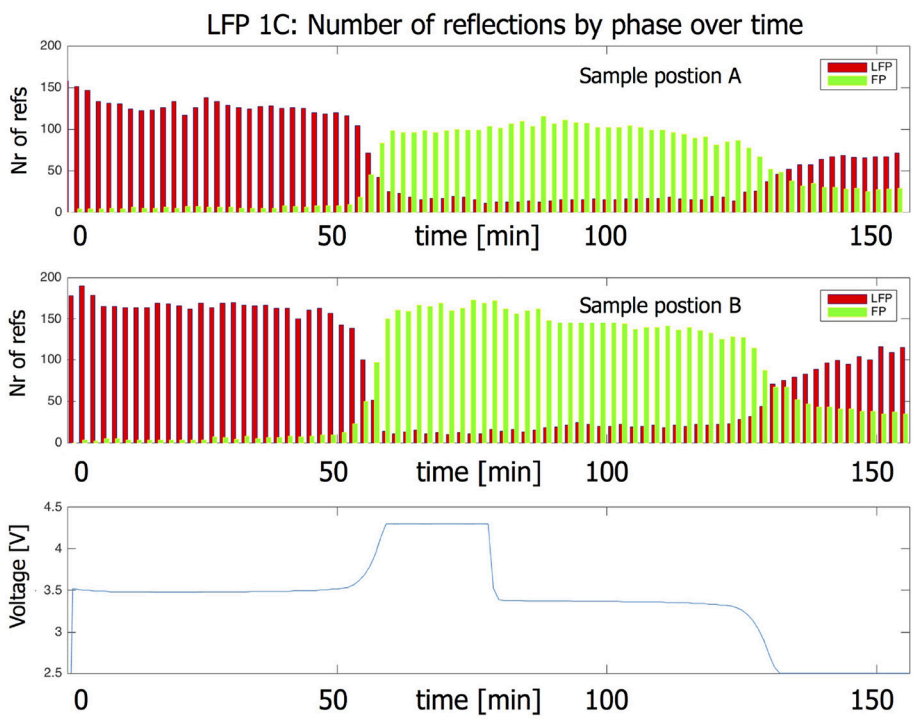

FIGURE 4 | Number of LFP and FP reflections of individual grains during a 1C charge/discharge cycle.

In Figure S3, which shows the omega sensitive data for this reflection, we can see that the FP domain remains within the visible omega range. This makes it reasonable to assume that the FP domain is shrinking but at the same that the LFP domain that is forming is not in Bragg condition (perhaps the phase transition to LFP causes a rotational shift) and therefore not visible. At

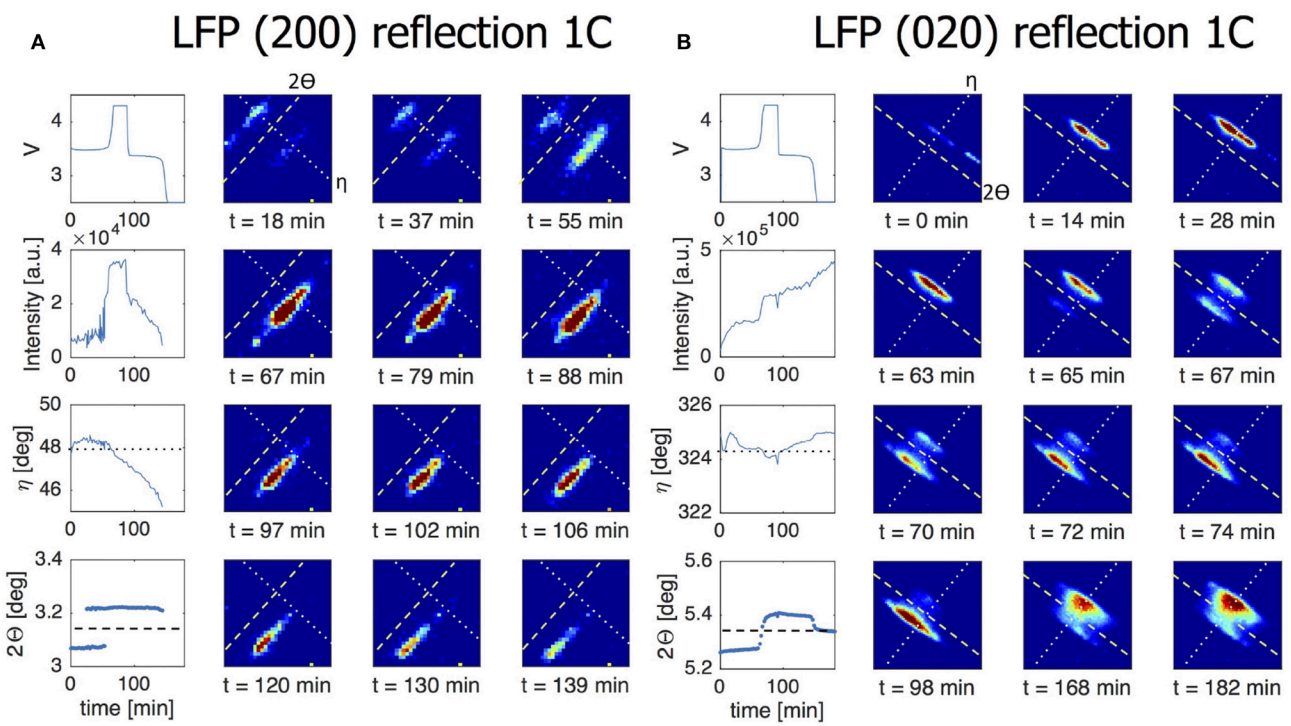

FIGURE 5 | The line charts in the left most column of both figures show from top to bottom the voltage of the battery, the intensity of the grain reflection, the change in the η angle and the change in the 2Θ angle for this particular grain reflection. All for a 1C charge/discharge cycle. The dotted line in the η graph corresponds to the dotted line shown in the 2D plots. The dashed line in the 2Θ graph corresponds to the dashed line in the 2D plots. **(A)** Direct view on a (200) reflection of an LFP grain during a 1C constant-current experiment. At t = 18 min both LFP and FP phases are visible, indicating phase coexistence occurs in this particular grain. The LFP phase is is visible from t = 0 – 55 min and the FP phase is visible from t = 18 – 146 min. **(B)** Here a (020) grain reflection is tracked during a 1C experiment. The phase transition from LFP to FP at the end of charge is not complete as some intensity is still visible for LFP. At the end of discharge clear solid solution behavior is on display where this grain never fully transitions back to LFP.

first η slightly increases from 47.5 to 48.5 deg (indicating a counter clockwise rotation along the x-axis). At t = 60 min, at the end of constant-current charge, η steadily decreases to 45 deg, evidence of a clockwise rotation. In reality the effective rotation of this grain is a combination of rotations along all three axis. Especially rotation along the y-axis will bring the grain out of Bragg condition resulting in decreasing intensity, which is what seems to happen for this particular grain after t = 60 min. These observations imply that $LiFePO_4$ grains embedded in the electrode matrix are rotating during (dis)charging, as will be quantified and discussed below. In **Figure 5B** a (020) reflection is shown, representing another LFP grain, again during a 1C charge/discharge cycle. This grain displays only very limited rotation along the x-axis ($<1^\circ$ in variation for the η angle). However, the steadily increasing intensity suggests that it rotates along the y-axis into the Bragg condition. The transformation toward FP takes only 9 min, between t = 65 – 74 min (15% of total charging time) and is not complete as at t = 74 min the LFP phase remains vaguely visible. Upon discharge, starting at t = 98 min, the transformation back from FP to LFP is very different because in this case significant intensity appears between the reflections that represent the FP and LFP end-member phases. This implies that the individual grain upon discharge has a distribution of b-lattice parameters, most likely indicating that part of the material has an intermediate Li composition as has been observed for the average behavior under high rate conditions (Orikasa et al., 2013; Zhang et al., 2014; Li et al., 2017) and in individual crystallites by microbeam diffraction previously (Zhang et al., 2015). Surprisingly however, is that this is observed at 1C rate, where the rate induced solid solution behavior has not been observed, and that it occurs on discharge (lithiation) and not on charge. This non-symmetric behavior is in line with the composition dependence of the charge transfer rate constants, and lithiation/delithiation behavior of large individual crystallites investigated with STXM nano-imaging (Bai et al., 2016). Such behavior will not be observed with powder diffraction experiments, as the deviating behavior of a few grains will be masked by the bulk of the transformation. Surprisingly, even 30 min after constant-current discharge is succeeded by constant-voltage discharge (V = 2.5 V), the intensity profile has barely changed, indicating that part of this crystallite is stuck in this solid solution state, which typically relaxes away quickly when no current is applied (Orikasa et al., 2013; Zhang et al., 2014; Li et al., 2017). The average 2Θ angle of the reflection at and after t = 150 min is around 5.35°, well above the equilibrium value of 5.25° for the LFP (020) reflection. Currently there appears

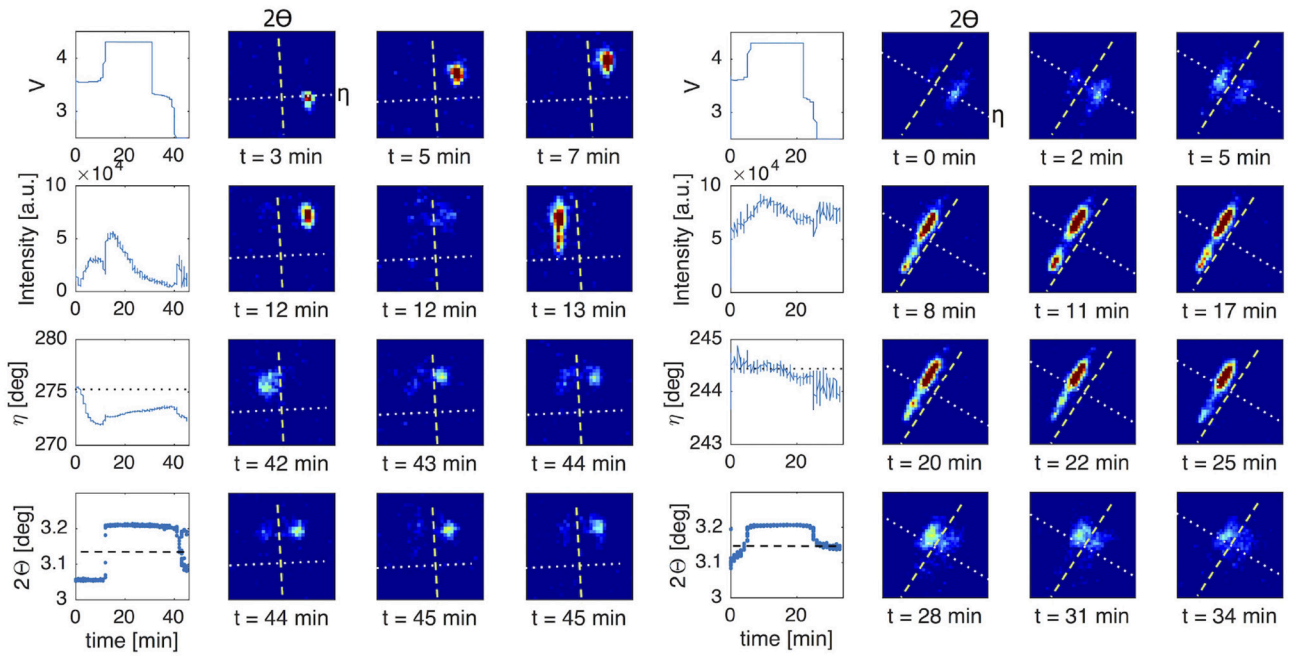

FIGURE 6 | The line charts in the left most column of both figures show from top to bottom the voltage of the battery, the intensity of the grain reflection, the change in the η angle and the change in the 2Θ angle for this particular grain reflection. All for a 5C/10C charge/discharge cycle. The dotted line in the η graph corresponds to the dotted line shown in the 2D plots. The dashed line in the 2Θ graph corresponds to the dashed line in the 2D plots. **(A)** The (200) reflection in this 5C experiment shows significant η movement at the beginning of charge. This continues until LFP-FP phase transition takes place without phase coexistence and within 2 min. During the transition back from FP to LFP the a-lattice is changing in a homogeneous way although a part of the crystallite remains in the FP phase. The observed decrease in integrated intensity during the upper voltage hold is likely caused by the grain rotating out of Bragg condition. Since this reflection is seen around the equator (η = 90 or η = 270) a rotation along the z-axis will remove the Bragg condition. **(B)** In a 10C experiment we are following a (200) reflection. At t = 5 min there is clear phase coexistence during the LFP-FP phase transition. At the FP-LFP phase transition the intensity is spread and this grain remains inhomogeneous for the a-lattice well after discharging has stopped.

no framework to understand this condition, unless the present solid solution phase observed represents an extensive diffuse interface between the end-member phases. Detailed analysis of these observations is outside the scope of this work and will be the subject of follow-up publications. In the 5C and 10C experiments in **Figure 6** the 2Θ profile at the end of discharge also indicates a rate induced solid solution transformation. In the 5C experiment however, the FP-LFP crystal transformation (during discharge) is more homogeneous showing no significant intensity of the end-member reflections, which points to a more homogeneous change in the a-lattice parameter within this single crystallite. In line with earlier findings, this demonstrates that rate induced solid solution transformation takes place in individual grains (Zhang et al., 2015). Where the integrated intensity of the 10C grain is rather constant during the charge discharge cycle, the integrated intensity of the reflection followed in the 5C experiment shows a significant drop at the end of charge during the constant-voltage regime (V = 4.2). This reflection is observed at η = 275°, which is around the equator (η = 90 or η = 270°). Reflections observed around the equator will move out of Bragg condition when they rotate along ω (the z-axis). In this 5C experiment the sample is only rotated for one degree ω. If a larger ω rotation was used it would have been possible to record similar integrated intensities for neighboring omegas. The small omega range chosen here is a trade-off against better capturing the transformation dynamics of grain reflections that do stay in Bragg condition.

Where $LiFePO_4$ is known to display a first-order phase transition upon charge and discharge which is driven toward a complex solid solution reaction a larger currents, $LiNi_{1/3}Co_{1/3}Mn_{1/3}O_2$ (NCM) displays a solid solution transformation even near equilibrium conditions. In **Figure 7A** the (108) reflection of an individual NCM grain is monitored during C/4 charge/discharge experiment. The gradual change in battery voltage during charge and discharge, reflects the well-known solid solution reaction of NCM. Consistently, the (108) reflection gradually shifts, representing a gradual change in d-spacing of the (108) plane within a single grain. 2Θ is decreasing in line with the increase in c-lattice parameter upon charging (delithiation) (Yin et al., 2006). Upon discharge, the reflection moves reversibly back toward the position associated with the lithiated state. The observed solid solution transformation within a single NCM grain takes the complete charge and discharge time. This is the case for all transforming grains (see Figure S2),

signifying that the current is distributed equally over all grains for this material during the course of the complete cycle. This in contrast to the LiFePO4 grains that (de)intercalate for only part of the cycle, indicating more localized transformations. In **Figure 7B** the (110) reflection of another NCM grain consistently shows the gradual shift, in this case toward larger 2Θ angles upon charging (delithiations), a consequence of the decreasing a and b lattice parameters. Both the intensity and the η angle are stable throughout the cycle which implies that this particular grain does not rotate along the y and x-axis, respectively.

These results demonstrate that microbeam X-ray diffraction can be used to distinguish different phase transformation mechanisms taking place in an individual crystallites. $LiFePO_4$ grains display four different mechanisms, and only one type is observed in NCM grains: (1) A phase transition without phase coexistence, LFP-FP in **Figure 6A**, (2) A phase transition with phase coexistence, LFP-FP in both **Figures 5A,B**, (3) solid solution phase transition where the grain remains homogeneous in structure, **Figure 7** and (4) solid solution phase transition with an inhomogeneous crystal lattice, FP-LFP in **Figure 5B**. With X-ray powder diffraction, it is hard to deconvolute the contribution of the different phase transition types to the observed intensity between the end member states, as noted in Liu et al. (2014). Microbeam diffraction enables this distinction through the ability to monitor individual grains, which compared to microscopic techniques has the advantage that this can be done for many crystallites at the same time under realistic battery conditions.

3.2. Transformation Kinetics

By following the individual reflections during (dis)charge, as shown in **Figures 5**–**7**, of the $LiFePO_4$ and NCM individual crystallites, their phase transformation rates can be determined. From the intensity it is possible to approximate the volume of the observed domains, which, in combination with the transformation rate, results in the local current exposed to a single electrode grain. Through the average transformation times of many individual grains the active grain fractions can be determined, as well as the average local current density over the actively transforming grains.

This is hard to determine by other techniques, in particular under operando conditions, and has previously been performed *ex-situ* at for instance 50% state of charge (Li et al., 2014; Bai et al., 2016). Using microbeam diffraction this was recently reported as a function of charge rate for $LiFePO_4$ (Zhang et al., 2015), as shown in **Figure 8**. As observed, at low charging rates the active particle fraction is low. The increasing current, associated with the increasing charge rate, is realized by increasing the active particle fraction, and to a lesser extent by increasing the average local current density at individual electrode grains. For LFP we determined the active particle fraction for 1C, 5C, and 10C rate experiments by assessing which fraction of the observed particles was active. This resulted in active particle fractions of approximately 24, 29, and 36% for 1C, 5C, and 10C during the constant-current regime, respectively, in good agreement with the results shown in **Figure 8**. For the NCM C/4 charging/discharging experiment shown in **Figure 7** the average transformation time during charge is $\sim$ 232 min and during discharge is $\sim$199 min, resulting in an overall active particle fraction of $\sim$80%, which is much larger than observed for $LiFePO_4$ at similar (and even higher) charging rates. In the first place charge transport of both electrons and Li-ions is expected to determine the active particle fraction (and hence the inhomogeneity of the reactions) in an electrode. The charge transport depends on many factors including the electrode configuration, porosity, thickness, amount and distribution of conductive additive and the current rate (Kerlau et al., 2007; Maire et al., 2008; Liu et al., 2010; Fleckenstein et al., 2011; Mima et al., 2012; Nishi et al., 2013; Katayama et al., 2014; Taminato et al., 2016). However, another interesting factor is the nature of the phase transition, either being solid solution, as occurring in NCM, or a first-order phase transition, such as occurring in LFP at low rates. Compositional differences in electrodes that display a solid solution reaction should be expected to be leveled based on the difference in electrochemical potential, whereas there is no electrochemical driving force to level the difference in local state of (dis)charge in first-order phase transition electrodes, as observed experimentally (Tanida et al., 2016). As a consequence solid solution materials are expected to result in more homogeneous reactions throughout the electrodes, and therefore also in a larger active particle fraction as compared to first-order phase transition electrode materials. This may provide a rational for the larger active particle fraction observed for NCM as compared to LFP at low charging rates, where charge transport induced inhomogeneities are less likely to be dominant.

3.3. Electrode Grain Rotation

In 3.1 we used compounded data where grain data of a complete omega scan is averaged. When looking at the omega sensitive data it is possible to detect grain rotation along the z-axis. **Figure 9A** shows the intensity of the LFP (020) reflection as function of time and omega. The shift in $\omega = -2.25$ to 0.25 implies that this grain is turning around its z-axis by about 2.5° in total. Also taking into account the change in η the total grain rotation can be calculated, the result of which is shown in **Figure 9B**. (See equation S1 in the Supplement for details on how the total grain rotation is estimated). The ability of microbeam diffraction to monitor the crystallite rotations during (dis)charging provides the opportunity to consider the mechanical working in electrodes, most likely induced by the volumetric changes of the grains itself upon lithium insertion and extraction. It has been shown that the local electron transport between the electrode particles and the carbon black network can be rate limiting, strongly depending on the electronic percolation, homogeneity of the electronic network and the electrode particle size (Awarke et al., 2011; Li et al., 2014). The observed rotations may introduce another factor in the electronic transport, as it may lead to fluctuations in the electronic contact with the carbon black matrix. The observed grain rotation can not be attributed to the experiment set up (e.g., beam energy transfer) as it is not observed when the battery is only exposed to the X-ray beam and no current is applied. Furthermore, not all observed grains rotate during the charge/discharge regime. At this stage very little knowledge exists on these phenomena, where microbeam diffraction may play an important role in the future.

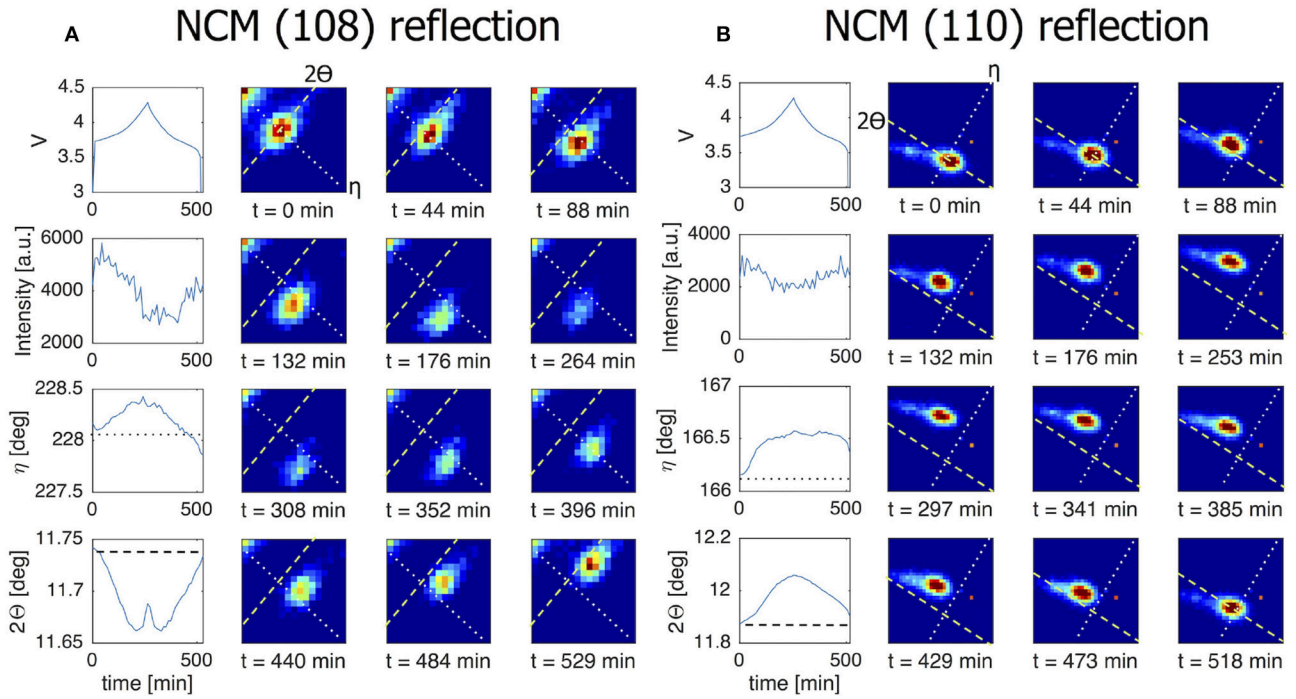

FIGURE 7 | The line charts in the left most column of both figures show from top to bottom the voltage of the battery, the intensity of the grain reflection, the change in the η angle and the change in the 2Θ angle for this particular grain reflection. All for a C/4 charge/discharge cycle. The dotted line in the η graph corresponds to the dotted line shown in the 2D plots. The dashed line in the 2Θ graph corresponds to the dashed line in the 2D plots. **(A)** NCM (108) reflection that is active throughout the charge/discharge cycle. Here the 2Θ profile reveals the solid solution nature of the material. **(B)** This (110) reflection also perfectly follows the electrochemistry. The intensity practically does not change throughout the cycle pointing to a constant crystal volume.

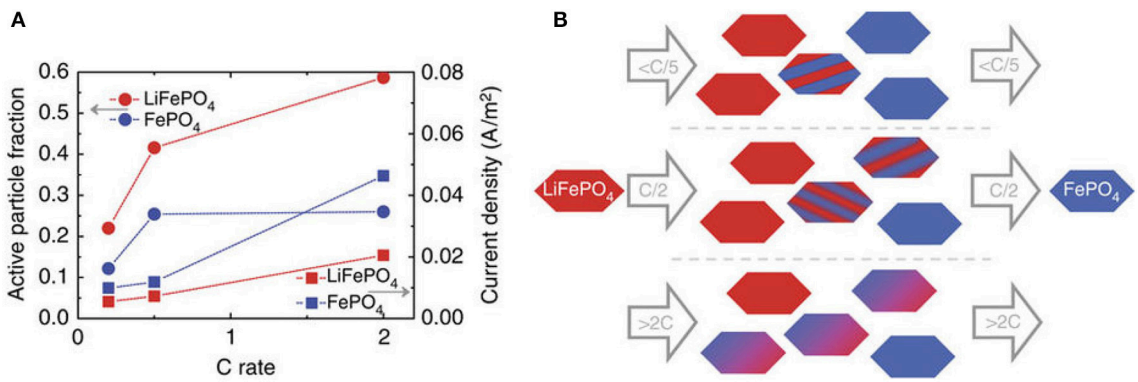

FIGURE 8 | (A) Active fraction and current density of the particles resulting from the average transformation times. **(B)**: Sketch of the rate-dependent transformation upon charge as follows from the microbeam diffraction experiments (similar upon discharge only with a smaller active particle fraction, see **A**). This figure is reproduced from (Zhang et al., 2015) and licensed by CC-BY.

4. CONCLUSION

With microbeam diffraction it is possible to investigate the transformation behavior of individual electrode grains while they are being cycled in a realistic battery system. For $LiFePO_4$, a first-order phase transition material, this is demonstrated by four different transformation mechanisms from $LiFePO_4$ to $FePO_4$ and vice versa. Tracking individual $LiNi_{1/3}Co_{1/3}Mn_{1/3}O_2$ crystallites displays the expected solid solution transformation mechanism, revealing that almost all grains actively participate during the charge/discharge cycle. In comparison with LFP where a much smaller part of the grains is active, this indicates a relation between the homogeneity of the reaction and the phase transformation mechanism. The more localized transformations in LFP electrodes also result in considerable rotations of the grain, most likely due to the local volumetric changes, which may influence the local electronic contact of the grains. Microbeam diffraction makes it possible to directly monitor changes in the

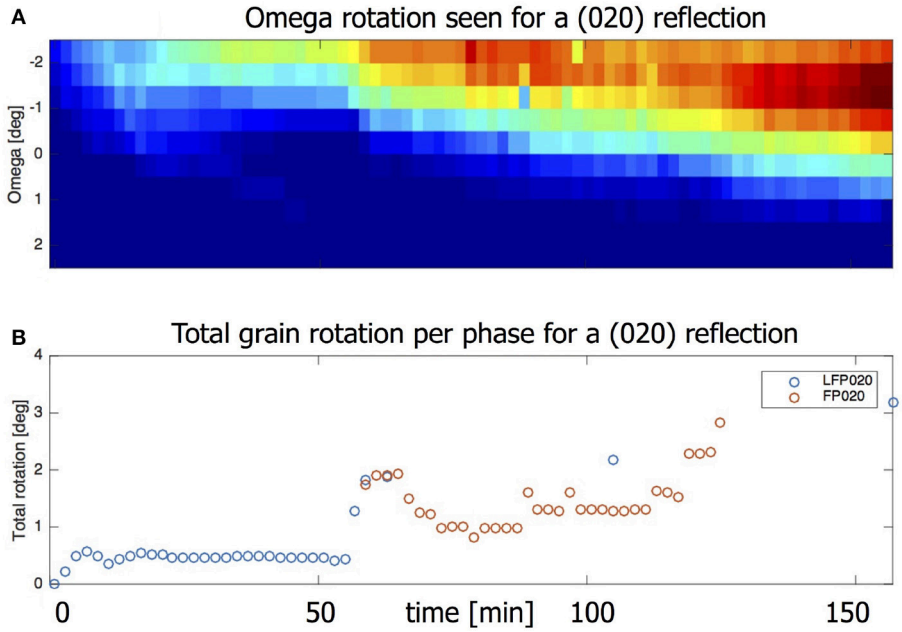

FIGURE 9 | (A) Heat map showing the omegas for which this is reflection is visible. Intensity first appears for $\omega = -2.5$. At the end intensity is strongest for $\omega = -1$ but is visible all the way to $\omega = 0.5$. **(B)** The omega rotation taken together with the eta movement gives the total grain rotation.

crystal phase volume, derived from the reflection intensity, which quantifies the local current. This provides insight in how the total current is distributed over the electrodes depending on the (dis)charging conditions, which is an important parameter that determines the cycle life. Microbeam diffraction is a non-invasive technique, allowing to monitor up to a few hundred grains concurrently with a temporal resolution of a few seconds. Thereby it offers the possibility to obtain better understanding on the transformation mechanics and kinetics in Li-ion electrodes and battery electrodes in general.

DATA AVAILABILITY STATEMENT

The dataset generated while analyzing the grain diffraction data can be found in the 4TU. Centre for Research Data with this link. Here you will find the complete dataset as presented in Tables S1 and S2. The grain diffraction data itself, collected during the ESRF experiments, is not included in this dataset.

AUTHOR CONTRIBUTIONS

MvH and MW wrote the manuscript, MvH processed and analyzed the data, MvH and FO prepared the electrodes and the pouch cell batteries, MvH, FO, MW, and JW performed the experiments at the ESRF beamline.

FUNDING

The research leading to these results has received funding from the European Research Council under the European Union's Seventh Framework Programme (FP/2007–2013)/ERC Grant Agreement n. [307161] of MW.

ACKNOWLEDGMENTS

We acknowledge the European Synchrotron Radiation Facility for provision of synchrotron radiation facilities and thank the beamline staff for assistance in using beamline ID11.

SUPPLEMENTARY MATERIAL

The Supplementary Material for this article can be found online at: https://www.frontiersin.org/articles/10.3389/fenrg.2018.00059/full#supplementary-material

REFERENCES

Awarke, A., Lauer, S., Pischinger, S., and Wittler, M. (2011). Percolation–tunneling modeling for the study of the electric conductivity in $LiFePO_4$ based Li-ion battery cathodes. *J. Power Sources* 196, 405–411. doi: 10.1016/j.jpowsour.2010.07.048

Bai, P., Cogswell, D. A., Liu, X., Jin, N., Yu, Y.-s., Tyliszczak, T., et al. (2016). Origin and hysteresis of lithium compositional spatiodynamics within battery primary particles. *Science* 353, 566–571. doi: 10.1126/science.aaf4914

Fleckenstein, M., Bohlen, O., Roscher, M. A., and Bäker, B. (2011). Current density and state of charge inhomogeneities in Li-ion battery cells with $LiFePO_4$ as cathode material due to temperature gradients. *J. Power Sources* 196, 4769–4778. doi: 10.1016/j.jpowsour.2011.01.043

Ganapathy, S., Heringa, J. R., Anastasaki, M. S., Adams, B. D., van Hulzen, M., Basak, S., et al. (2016). Operando Nano-beam Diffraction to Follow the

Decomposition of Individual Li_2O_2 Grains in a Non-aqueous Li-O_2 Battery. *J. Phys. Chem. Lett.* 7, 3388–3394. doi: 10.1021/acs.jpclett.6b01368

Harks, P. P., Mulder, F. M., and Notten, P. H. (2015). *In situ* methods for Li-ion battery research: a review of recent developments. *J. Power Sources* 288, 92–105. doi: 10.1016/j.jpowsour.2015.04.084

Katayama, M., Sumiwaka, K., Miyahara, R., Yamashige, H., and Arai, H. (2014). X-ray absorption fine structure imaging of inhomogeneous electrode reaction in $LiFePO_4$ lithium-ion battery cathode. *J. Power Sources* 269, 994–999. doi: 10.1016/j.jpowsour.2014.03.066

Kerlau, M., Marcinek, M., Srinivasan, V., and Kostecki, R. M. (2007). Studies of local degradation phenomena in composite cathodes for lithium-ion batteries. *Electrochim. Acta* 52, 5422–5429. doi: 10.1016/j.electacta.2007.02.085

Li, Y., Gabaly, F. E., Ferguson, T. R., Smith, R. B., Bartelt, N. C., Sugar, J. D., et al. (2014). Current-induced transition from particle-by-particle to concurrent intercalation in phase-separating battery electrodes. *Nat. Mater.* 13, 1149–1156. doi: 10.1038/nmat4084

Li, Y., Li, Y., Pei, A., Yan, K., Sun, Y., Wu, C. L., et al. (2017). Atomic structure of sensitive battery materials and interfaces revealed by cryoelectron microscopy. *Science* 358, 506–510. doi: 10.1126/science.aam6014

Lin, F., Liu, Y., Yu, X., Cheng, L., Singer, A., Shpyrko, O. G., et al. (2017). Synchrotron X-ray analytical techniques for studying materials electrochemistry in rechargeable batteries. *Chem. Rev.* 117, 13123–13186. doi: 10.1021/acs.chemrev.7b00007

Liu, H., Strobridge, F. C., Borkiewicz, O. J., Wiaderek, K. M., Chapman, K. W., Chupas, P. J., et al. (2014). Capturing metastable structures during high-rate cycling of $LiFePO_4$ nanoparticle electrodes. *Science* 344, 1451–1452. doi: 10.1126/science.1252817

Liu, J., Kunz, M., Chen, K., Tamura, N., and Richardson, T. J. (2010). Visualization of charge distribution in a lithium battery electrode. *J. Phys. Chem. Lett.* 1, 2120–2123. doi: 10.1021/jz100634n

Ma, X., Luo, W., Yan, M., He, L., and Mai, L. (2016). *In situ* characterization of electrochemical processes in one dimensional nanomaterials for energy storages devices. *Nano Energy* 24, 165–188. doi: 10.1016/j.nanoen.2016.03.023

Maire, P., Evans, A., Kaiser, H., Scheifele, W., and Novák, P. (2008). Colorimetric determination of lithium content in electrodes of lithium-ion batteries. *J. Electrochem. Soc.* 155, 862–865. doi: 10.1149/1.2979696

Mima, K., Azuma, H., Yamazaki, A., Okuda, C., Ukyo, Y., Sawada, H., et al. (2012). Li distribution characterization in Li-ion batteries positive electrodes containing $Li_xNi_{0.8}Co_{0.15}Al_{0.05}O_2$ secondary particles ($0.75 \leq x \leq 1.0$). *Nuclear Inst. Methods Phys. Res. B* 290, 79–84. doi: 10.1016/j.nimb.2012.08.016

Nishi, T., Nakai, H., and Kita, A. (2013). Visualization of the state-of-charge distribution in a $LiCoO_2$ cathode by *in situ* Raman imaging. *J. Am. Chem. Soc.* 160, 1785–1788. doi: 10.1149/2.061310jes

Niwa, H., Shibata, T., Imai, Y., Kimura, S., and Moritomo, Y. (2017). Domain size of phase-separated Na_xCoO_2 as investigated by X-ray microdiffraction. *Batteries* 3, 5. doi: 10.3390/batteries3010005

Orikasa, Y., Maeda, T., Koyama, Y., Murayama, H., Fukuda, K., Tanida, H., et al. (2013). Direct observation of a metastable crystal phase of Li_xFePO_4 under electrochemical phase transition. *J. Am. Chem. Soc.* 135, 5497–5500. doi: 10.1021/ja312527x

Peterson, V. K., Auckett, J. E., and Pang, W.-K. (2017). Real-time powder diffraction studies of energy materials under non-equilibrium conditions. *IUCrJ* 4, 540–554. doi: 10.1107/S2052252517010363

Singh, D. P., Mulder, F. M., Abdelkader, A. M., and Wagemaker, M. (2013). Facile micro templating $LiFePO_4$ electrodes for high performance Li-ion batteries. *Adv. Energy Mater.* 3, 572–578. doi: 10.1002/aenm.201200704

Taminato, S., Yonemura, M., Shiotani, S., Kamiyama, T., and Torii, S. (2016). Real-time observations of lithium battery reactions–operando neutron diffraction analysis during practical operation. *Nat. Pub. Group* 6:28843. doi: 10.1038/srep28843

Tan, J., Liu, D., Xu, X., and Mai, L. (2017). In situ/operando characterization techniques for rechargeable lithium-sulfur batteries: a review. *Nanoscale* 9, 19001–19016. doi: 10.1039/C7NR06819K

Tanida, H., Yamashige, H., Orikasa, Y., Gogyo, Y., Arai, H., Uchimoto, Y., et al. (2016). Elucidating the Driving Force of Relaxation of Reaction Distribution in $LiCoO_2$ and $LiFePO_4$ Electrodes Using X-ray Absorption Spectroscopy. *J. Phys. Chem. C* 120, 4739–4743. doi: 10.1021/acs.jpcc.5b10210

Yin, S.-C., Rho, Y.-H., Swainson, I., and Nazar, L. F. (2006). X-ray/neutron diffraction and electrochemical studies of lithium. *Chem. Mater.* 2, 1901–1910. doi: 10.1021/cm0511769

Zhang, X., Van Hulzen, M., Singh, D. P., Brownrigg, A., Wright, J. P., Van Dijk, N. H., et al. (2014). Rate-induced solubility and suppression of the first-order phase transition in olivine $LiFePO_4$. *Nano Lett.* 14, 2279–2285. doi: 10.1021/nl404285y

Zhang, X., van Hulzen, M., Singh, D. P., Brownrigg, A., Wright, J. P., van Dijk, N. H., et al. (2015). Direct view on the phase evolution in individual $LiFePO_4$ nanoparticles during Li-ion battery cycling. *Nat. Commun.* 6:8333. doi: 10.1038/ncomms9333

Conflict of Interest Statement: The authors declare that the research was conducted in the absence of any commercial or financial relationships that could be construed as a potential conflict of interest.

frontiers in Energy Research

ORIGINAL RESEARCH
published: 08 August 2018
doi: 10.3389/fenrg.2018.00076

A Cylindrical Cell for *Operando* Neutron Diffraction of Li-Ion Battery Electrode Materials

Laura Vitoux[1,2†], Martin Reichardt[1†], Sébastien Sallard[1‡], Petr Novák[1], Denis Sheptyakov[2] and Claire Villevieille[1*]*

[1] Electrochemisty Laboratory, Paul Scherrer Institute, Villigen, Switzerland, [2] Laboratory for Neutron Scattering and Imaging, Paul Scherrer Institute, Villigen, Switzerland

OPEN ACCESS

Edited by:
Neeraj Sharma,
University of New South Wales,
Australia

Reviewed by:
Wei Kong Pang,
University of Wollongong, Australia
Stephen Hull,
Science and Technology Facilities
Council, United Kingdom

***Correspondence:**
Denis Sheptyakov
denis.cheptiakov@psi.ch
Claire Villevieille
claire.villevieille@psi.ch

[†]These authors have contributed
equally to this work

[‡]**Present Address:**
Sébastien Sallard,
Flemish Institute for Technological
Research (VITO), Mol, Belgium

Specialty section:
This article was submitted to
Energy Storage,
a section of the journal
Frontiers in Energy Research

Received: 27 March 2018
Accepted: 17 July 2018
Published: 08 August 2018

Citation:
Vitoux L, Reichardt M, Sallard S,
Novák P, Sheptyakov D and
Villevieille C (2018) A Cylindrical Cell
for Operando Neutron Diffraction of
Li-Ion Battery Electrode Materials.
Front. Energy Res. 6:76.
doi: 10.3389/fenrg.2018.00076

Neutron diffraction is a powerful technique to localize and quantify lithium in battery electrode materials. However, obtaining high-quality *operando* neutron diffraction data is challenging because it requires achieving good electrochemical performance while cycling a large amount of active material to ensure optimal signal-to-noise ratio. We have developed a cylindrical cell specifically suited for *operando* neutron diffraction studies, and used it to investigate the structural changes in the Ni-rich $LiNi_{0.6}Co_{0.2}Mn_{0.2}O_2$ cathode material during cycling between 2.5 and 4.3 V vs. Li^+/Li. The cell demonstrates reliable electrochemical performance, even after long-term cycling, and the important crystal structure parameters of the active material, including Li occupancy, could be successfully refined with the Rietveld method using neutron diffraction data collected in *operando* after appropriate background subtraction.

Keywords: *operando* neutron diffraction, Li-ion batteries, $LiNi_{0.6}Co_{0.2}Mn_{0.2}O_2$, cylindrical cell, long-term cycling, Rietveld refinement

INTRODUCTION

With their high energy density and high power, lithium-ion batteries are nowadays the leading technology used in portable devices and have started to enter the market for electric vehicles with success (Tarascon and Armand, 2010; Croguennec and Palacin, 2015). In particular, $LiNi_{1-x-y}Co_xMn_yO_2$, referred to as NCM (or NMC) in the literature, is one of the most promising cathode materials used to enhance battery performance (Robert et al., 2014). NCM combines the advantages of the three transition metals: nickel contributes to the high reversible specific charge, cobalt improves the rate capability, and manganese enhances the structural and thermal stability, particularly at high degrees of delithiation. The electrochemical properties are strongly influenced by the chemical composition of the NCM material (Noh et al., 2013). $LiNi_{1/3}Co_{1/3}Mn_{1/3}O_2$ (NCM111) and $LiNi_{0.5}Co_{0.2}Mn_{0.3}O_2$ (NCM523) have already been implemented in commercial batteries, and research is moving toward Ni-rich and Li-rich materials, which provide high specific charge but still suffer from low cycling stability (Liu et al., 2015; Rozier and Tarascon, 2015; Manthiram et al., 2017; Schipper et al., 2017). To develop these technologies further, we must understand the reaction mechanisms in the cell both at the anode and cathode. *In situ/operando* powder diffraction is a powerful tool for the identification and to some extent, for quantification of the crystallographic changes occurring in the battery materials during operation; these changes are often the origin of the losses in electrochemical performance (Sharma et al., 2015; Peterson et al., 2017). Neutron powder diffraction, in particular, presents several

advantages for the study of Li-ion batteries. First, neutron scattering lengths are not correlated to the atomic numbers of the elements. Compared to X-ray powder diffraction, neutron powder diffraction is, thus, more sensitive to light elements in presence of heavier elements, such as transition metals, and enables the localization and quantification of lithium ions in the structure. Moreover, it also facilitates the differentiation of elements with similar atomic numbers, such as the transition metals (for example, Ni, Mn, Co, and Fe) that usually make up the cathode materials. Finally, neutrons have high penetration depth, which enables the study of the crystallographic changes in the bulk structure of the sample. Unfortunately, a large amount of active material must be exposed to the neutron beam to obtain a sufficiently intense diffraction pattern in a reasonable measurement time. The increase in the amount of active material in an electrochemical cell is often detrimental to its electrochemical performance. Moreover, in *in situ/operando* measurements, every cell component is exposed to the neutron beam and contributes to the diffraction pattern. In particular, both the separator and the electrolyte usually contain hydrogen, which generates a high background because of its high incoherent scattering cross section, hindering thorough data analysis. The challenge in cell design for *operando* neutron diffraction is, thus, to obtain high-quality diffraction pattern to enable structural refinements while achieving electrochemical performance similar to that in coin-cell configuration. Commercial 18650-type batteries present excellent electrochemical performance, but the poor signal-to-noise ratio in the diffraction pattern, mainly because of the contributions from the hydrogenated electrolyte and separators, limits the structural information retrievable from Rietveld refinements. Moreover, it narrows the range of study to commercialized batteries, such as $LiFePO_4$ (Rodriguez et al., 2010; Sharma et al., 2010, 2017), $LiCoO_2$ (Dolotko et al., 2012; Senyshyn et al., 2014), and $LiNi_{1/3}Mn_{1/3}Co_{1/3}O_2$ (Alam et al., 2014; Dolotko et al., 2014; Pang et al., 2015; Taminato et al., 2016).

A reasonable alternative, and thus an approach pursued by many, is to design custom-made cells for *operando* neutron diffraction experiments that mimic the electrochemistry obtained with commercial batteries while allowing advanced materials' investigation. Since the pioneering reports of a custom-made cell for *in situ* neutron diffraction (Bergström et al., 1998; Berg, 2001), several cell designs have been developed to meet the requirements of the neutron diffraction experiments. They can be divided into three categories: coin-type cells, cylindrical roll-over cells, and pouch-type cells.

In coin-type cells, a large amount of loose active material powder is encased in a compartment, which is the only part exposed to the neutron beam. In the first designs, polyetheretherketone (PEEK) polymer (Rosciano et al., 2008; Colin et al., 2010) and aluminum/titanium (Godbole et al., 2013) were used to manufacture the compartment, but these prevented conclusive refinements during cell operation because of high background and strong overlap of the diffraction peaks of the compartment with those of the electroactive materials. Structural information was obtained from diffraction patterns collected *in situ* at a constant voltage for several hours. High-quality structural refinements based on the diffraction patterns acquired *operando* during battery operation were achieved with a similar cell using a Ti–Zr alloy, which is transparent to neutrons (Bianchini et al., 2013, 2015). However, the large amount of loose powder was detrimental to the electrochemical performance and resulted in significant polarization, limiting the study to the first few cycles at low rate.

To improve the electrochemical performance, Sharma et al. introduced a roll-over design mimicking the cylindrical 18650-type cell, in which the positive electrode, separators, and lithium foil used as the negative electrode are rolled together, put inside a vanadium tube, and sealed with wax (Sharma et al., 2011). The quality of the diffraction patterns compared to those collected using commercial batteries was significantly improved by the use of deuterated electrolytes and vanadium casing, which produces almost no coherent diffraction of neutrons. The structural evolution of several cathode ($LiFePO_4$) and anode (MoS_2, $Li_4Ti_5O_{12}$) materials was then investigated using this approach, but only the unit cell parameters and phase fraction could be refined using the Rietveld method on the neutron diffraction patterns (Du et al., 2011; Sharma et al., 2011, 2012; Brant et al., 2014). This design was later adapted by closing a cylindrical cell (quartz or aluminum casing) with Swagelok-type metallic current collectors (Roberts et al., 2013; Brant et al., 2016). High cycling rates could successfully be achieved, but structural refinements required long measurement times. Unit cell parameters and atomic coordinates for $LiFePO_4$ and $Li_{0.18}Sr_{0.66}Ti_{0.5}Nb_{0.5}O_3$ were then refined for the diffraction patterns collected *in situ* at a constant voltage at specific states of charge. A modified 18650-type battery, adapted with a screw to add the deuterated electrolyte, was later proposed. This design improvement allowed, for the first time, the study of $LiNi_{0.5}Mn_{1.5}O_4$ vs. graphite after long-term cycling. This cell showed reliable electrochemical performance at high rates, up to 1C, using a highly loaded cathode (4 g of materials). Rietveld refinement on the diffraction patterns obtained in the charge and discharge states was possible (Boulet-Roblin et al., 2016, 2017). Owing to this design, Boulet-Roblin et al. successfully determined the amount of Li consumed by surface reactions after 100 cycles by performing Rietveld refinement.

The pouch-cell is the latest design developed for *operando* neutron diffraction experiments (Liu et al., 2013; Pang and Peterson, 2015) and is increasingly in use thanks to its "easy" construction and flexibility regarding the choice of components (separators and electrodes). As in their commercial equivalents, the cathode, anode, and separators are stacked and wrapped in a propylene-coated aluminum pouch, which is heat-sealed after the addition of the electrolyte. Although they provide relatively good electrochemical performance with higher cycling rates, the polymer-coating of the aluminum pouch generates significant background in the diffraction pattern. The quality of refinements is also affected by the anisotropic absorption of the diffracted beam caused by the non-radial geometry of the cell. To minimize such effects, an annular sample can be simulated by probing a stack with equal width and thickness, or the whole setup can be rotated or oscillated in a sufficiently large range of angles

normal to the scattering plane, thus averaging out the effects of anisotropy (Pang and Peterson, 2015). Using the first method, the refinement of the cell parameters, lithium content, and oxygen positional parameters with Rietveld method could be carried out for $Li_{1+x}Mn_2O_4$ (Sharma et al., 2013), $Li_4Ti_5O_{12}$ (Pang et al., 2014b), $LiNi_{0.5}Mn_{1.5}O_4$ (Pang et al., 2014c), and $Li(Ni_{1/3}Mn_{1/3}Fe_{1/3})O_2$ (Pang et al., 2014a).

Based on these previous studies, we opted for a home-made cylindrical cell with optimized design to ensure long-term cycling with reliable electrochemistry and low absorption from the undesirable components located in the beam path (such as the electrolyte, separator, and casing). As a proof of concept, we used *operando* neutron diffraction to investigate $Li_x(Ni_{0.6}Co_{0.2}Mn_{0.2})O_2$ as a cathode material cycled vs. lithium metal (Li^+/Li). We follow the evolution of the refined unit cell, as well as of the internal crystal structure parameters, including the atomic coordinates and site occupation for the charge carrier (lithium), during the first charge–discharge cycle of the battery. Additionally, we demonstrate that the cell can achieve long-term cycling stability, and post-mortem scanning electron microscopy (SEM) analysis was carried out on the cathode material, the lithium metal anode, and the separator to reveal a possible cell failure mechanism.

MATERIALS AND METHODS

Ex Situ and *Operando* Neutron Diffraction Experiments

All neutron diffraction experiments were carried out at the HRPT high-resolution powder diffractometer at the SINQ spallation source (PSI) using the high intensity mode with a wavelength of 1.494 Å obtained from the (533) reflection of a Ge vertically focusing monochromator (Fischer et al., 2000) and determined using Si powder standard sample (NIST standard reference material 640d). The instrument is featuring a position-sensitive detector covering a scattering angles range of 160°, and a total solid angle of ∼0.1 sr. Rietveld refinements were carried out using the Fullprof suite (Rodríguez-Carvajal, 1993).

For the *ex situ* neutron diffraction experiments, pristine $Li(Ni_{0.6}Co_{0.2}Mn_{0.2})O_2$ powder (NCM622, MTI) (>1 g), separator foils, and liquid electrolytes (2 mL) were measured inside vanadium cylindrical containers (Ø 6 mm) sealed with indium wire. Separator foils, polyvinylidene fluoride (PVDF) film (Goodfellow), PVDF Inmmobilion-P membrane (Merck), polyethylene (Goodfellow), Celgard 2400 (Celgard), and Celgard 2500 (Celgard) were dried prior to the measurement at 60°C to remove the water adsorbed at the surface. The standard electrolyte was LP30 (1 M $LiPF_6$ in ethylene carbonate (EC) : dimethyl carbonate (DMC) 50 : 50 wt.%), and the deuterated electrolyte had the following composition: 1 M in $LiPF_6$ in d-EC:d-DMC (30 : 70 wt.%).

For the *operando* neutron diffraction experiments, the electrochemical cell NCM622 : SuperC65 : PVDF (80:10:10 in wt.%)|1 M $LiPF_6$ in d-EC : d-DMC (50:50)|Li metal was assembled in the cylindrical cell configuration in an argon-filled glovebox. The lithium foil used as the counter electrode (3 × 13 cm) was calendered to 170 μm to ensure easy introduction of the stack into the cylindrical cell. For the positive electrode, a mixture of 80 wt.% of active material (NCM622, MTI), 10 wt.% of Super C65 (Imerys) as a conducting additive, and 10 wt.% polyvinylidene fluoride (PVDF, Arkema) as a binder was mixed in *N*-methyl-2-pyrrolidinone (NMP) solvent using a mechanical turbo stirrer and, then, cast with the doctor blade technique onto an aluminum foil, which was used as the current collector. The quantity of active material in the neutron beam was maximized by using double-side coated electrode. The cast slurry was first dried at 80°C under vacuum overnight to remove the NMP solvent. The electrode (3 × 14 cm) was calendered to a final thickness of 120 μm and achieved a loading of ca. 700 mg of active material. The electrode was finally dried overnight at 120°C under vacuum prior to its insertion in an argon-filled glovebox. Two Celgard 2500 foils (3 × 16 cm) were used as separators and dried overnight at 60°C to remove absorbed water before the cell assembly.

To collect neutron diffraction data during cell cycling, the cell was fixed vertically on a dedicated sample holder in the middle of the sample table, which enabled the center of the cylindrical cell to be matched to the optimal beam height. Horizontal and vertical beam reductions were used to avoid unwanted scattering, such as from the parts made of PEEK. The cell was connected directly to a VMP-300 potentiostat (Bio-Logic) and galvanostatically cycled using 8.5 mA/g as specific current (1 Li reaction in 20 h using a practical specific charge of 170 mAh/g) between 2.5 and 4.3 V vs. Li^+/Li at room temperature. The cell voltage was held constant for 3 and 5 h at 4.3 V vs. Li^+/Li and 2.5 V vs. Li^+/Li, respectively. Neutron diffraction patterns were collected in *operando* mode, i.e., during cell operation, without any relaxation period. One scan was collected over a period of just less than 2 min, and 32 scans were merged into one pattern, corresponding to ca. 1 h of counting time, in order to obtain a good signal-to-noise ratio enabling reliable Rietveld refinement. This way, it is possible to control that no significant lattice or phase evolution during the resulting counting time. The applied cycling rate and merging procedure should be optimized for each new experiment. At both cut-off voltages, the scans were merged over the whole duration of the potentiostatic step (3 h for 4.3 V vs. Li^+/Li and 5 h for 2.5 V vs. Li^+/Li). Subtraction of the substantial background scattering is a rather critical step for successful data treatment and was performed prior to Rietveld analysis. By using normalization on the well isolated broad peaks at low scattering angles, the unwanted scattering from the Celgard could be effectively removed. These diffraction peaks, which do not appear for dry Celgard, are thought to originate from the adsorption of water molecules at the surface of the separator following their wetting with electrolyte. Normalization was done using diffraction data from non-dried Celgard in vanadium can with an air atmosphere. Additionally, the parasitic scattering from the deuterated electrolyte, which yields a few intense broad maxima originating from short-range correlations in the liquid, could be eliminated. Sequential refinements on all 46 diffraction patterns collected during cell operation were done using the Fullprof Suite (Rodríguez-Carvajal, 1993).

Electrochemical Tests

For the long-term cycling experiments, the same cylindrical cell configuration as for the neutron diffraction measurements was used, but with standard LP30 electrolyte instead of the deuterated electrolyte. Galvanostatic cycling was undertaken using a 8.5 mA/g specific current (C/20 rate using a practical specific charge of 170 mAh/g) between 2.5 and 4.3 V vs. Li^+/Li with a 1 h potentiostatic step at both cut-off voltages.

The electrodes used in the cylindrical cell were also tested vs. lithium metal using the same cycling protocol in a standard type coin-type cell with the standard LP30 electrolyte and glass fiber separators.

Post-mortem Experiments

SEM measurements were performed with a Carl Zeiss Ultra 55 scanning electron microscope, using the secondary electron detector to emphasize the surface morphology. The images were taken at an acceleration voltage of 3 kV and a working distance of ca. 3 mm to ensure limited damage of the species formed upon cycling, particularly the polymeric species formed by electrolyte decomposition.

RESULTS AND DISCUSSION

Cylindrical Cell Design

The designed cylindrical cell for *operando* neutron diffraction experiment is presented in **Figure 1**.

The design is inspired by the 18650 commercial cells and should reduce the number of unwanted components in the beam path or, if this is not possible, allow the use of materials with low neutron scattering and absorption. In this regard, aluminum has been chosen because of its relatively low cost, ease of machining, and its relatively low neutron absorption, even though coherent diffraction on the aluminum of the cell housing cannot be avoided.

The stack, comprising separator/positive electrode/separator/negative electrode, was rolled around an inner hollow mandrel made of aluminum (Ø 6 mm) and inserted into the cylindrical aluminum outer casing (Ø 10 mm). The electrolyte (ca. 1 mL) was added on top of the rolled layers before the cell was sealed with a PEEK cap. One separator foil acts as insulator by shielding the roll from the cylindrical outer casing, and the second prevents short circuits by separating the two electrodes. The positive connector is the central part of the mandrel made of aluminum (in agreement with the casing to avoid an additional undesired phase in the beam), while the negative connector, located at the other end of the cylinder, is made of titanium. Both connectors are insulated from each other with PEEK.

All components were tuned to reduce the background in the diffraction pattern **(Figure 2)**. The standard electrolyte LP30 with its high hydrogen content generates a large amount of incoherent scattering, producing a considerable background signal. As highlighted in **Figure 2A**, using deuterated electrolytes reduces the background by almost a factor of three and is therefore essential for significantly improving the signal-to-noise ratio in *operando* neutron diffraction experiments using home-made cell designs. The separators are the next source of significant background signal. Several separators were tested, as shown in **Figure 2B**. PVDF foils and PVDF membrane, as well as polyethylene, have been reported to be better alternatives to the state-of-art Celgard (Brant et al., 2014; Pang and Peterson, 2015). Although in the literature the intensities of the diffraction peaks are normalized per gram of material, we found it more suitable to normalize them according to the actual amounts (in mm^2) inserted in the neutron diffraction cell. Using this approach, the Celgard foils were found to generate the least background on the neutron diffraction pattern, whereas PVDF foil and membrane produced similarly high backgrounds. Moreover, the PVDF foils and membrane are thicker than Celgard, which limits the number of coils around the mandrel and, thus, the quantity of active material in the beam. Thus, Celgard 2500 was selected as the separator foil for *operando* neutron diffraction experiments. Kapton tape, which is used as an adhesive to fix the positive electrode and separator foils to the mandrel and maintain the tightness of the electrodes in the roll, was also analyzed. Its background is rather low compared to that produced by the liquid electrolyte and Celgard foil, but the amount should still be kept to a minimum.

The acquisition of neutron diffraction patterns with high signal-to-noise ratio in a relatively short time for structural refinements is, thus, possible with this design.

Operando Neutron Diffraction Experiment

Structure of the Pristine Material

Initially, the crystal structure of the NCM622 pristine material was assessed by *ex situ* neutron powder diffraction. The result of the Rietveld refinement is presented in **Figure 3** and the refined structural parameters are summarized in **Table 1**.

As described in the literature for $Li(Ni_xCo_yMn_z)O_2$ compounds (Yabuuchi and Ohzuku, 2003), the pristine material has an α-$NaFeO_2$-type layered structure (space group *R*-3*m*, N°166), in which the transition metals (TM) form with oxygen layers of edge-sharing TMO_6 octahedra that are stacked along the *c*-axis (**Figure 4**). Lithium ions intercalate into the octahedral sites between these slabs. In addition, an exchange of lithium and nickel ions between the crystallographic sites *3a* and *3b* may occur because of the similar ionic radii of Li^+ (0.76 Å) and Ni^{2+} (0.69 Å) ions (Shannon, 1976). This phenomenon, usually referred to as cation mixing in the literature, is particularly common for Ni-rich materials ($x_{Ni} \geq 0.5$). According to the literature, this Li/Ni exchange depends on the cationic ratio in $Li(Ni_xCo_yMn_z)O_2$, as well as on the synthetic route, and strongly affects the cycling stability (Noh et al., 2013; Yu et al., 2014; Zhao et al., 2017). Based on reasonable assumptions, i.e., the stability of the Mn, Co, and O stoichiometry, neutron diffraction appears to be the most reliable experimental technique to investigate and quantify the cation mixing arising from the difference between the coherent scattering lengths of lithium (−1.90 fm) and nickel (10.3 fm) (Sears, 1992). In the pristine material, 3.5% of lithium ions have been estimated to be exchanged with nickel ions, which is in agreement with previous reports for this compound (Lee et al., 2007) and similar to the values reported for NCM materials with various cationic ratios (Yin et al., 2006; Noh et al., 2013; Yu et al., 2014; Zhao et al., 2017).

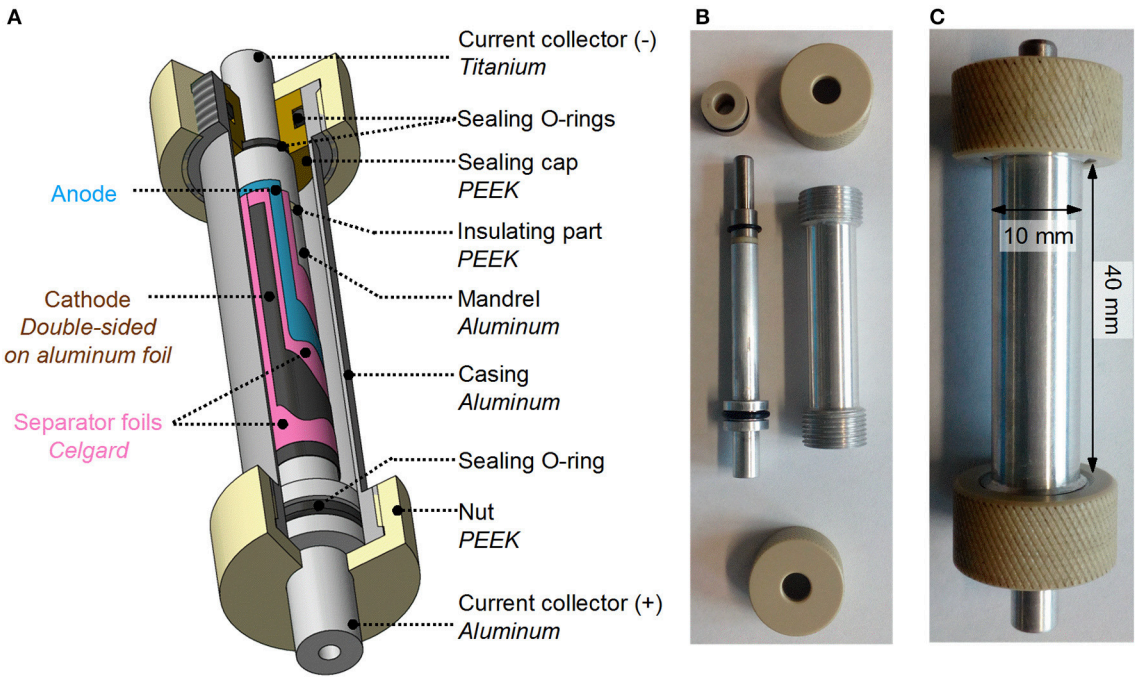

FIGURE 1 | (A) Cylindrical cell design for *operando* neutron diffraction experiments. **(B)** Photograph of a dismantled cylindrical cell. **(C)** Photograph of an assembled cylindrical cell.

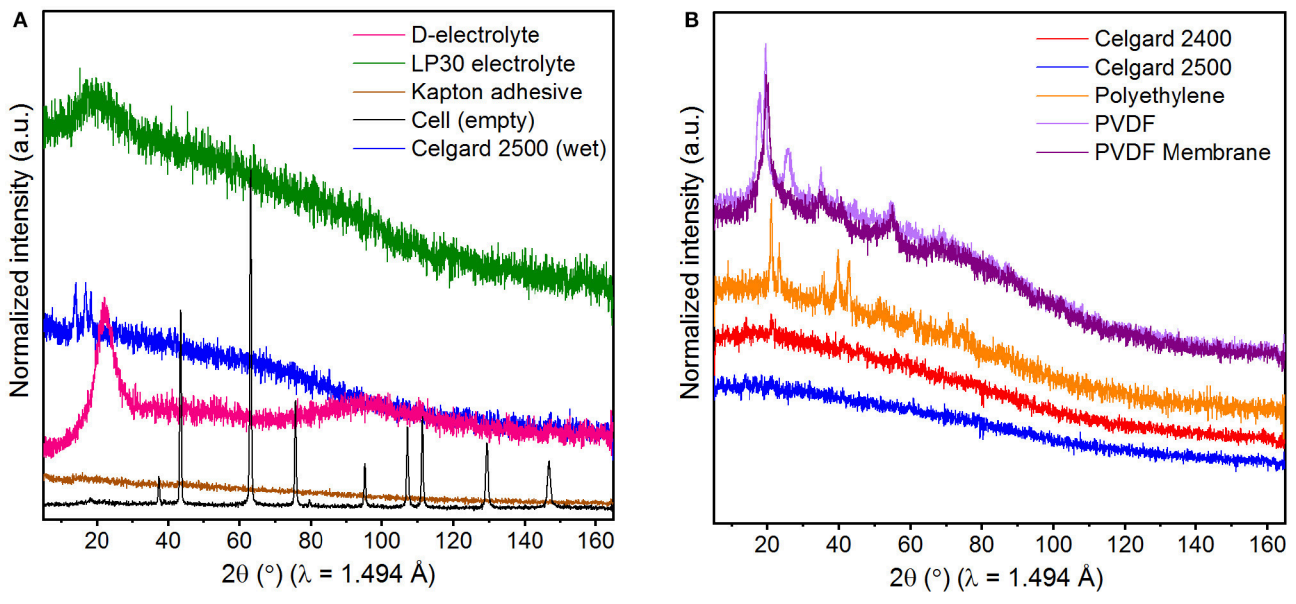

FIGURE 2 | (A) Neutron diffraction patterns of all components of the cylindrical cell (other than cathode and anode). **(B)** Neutron diffraction patterns of several dry polymeric foils as a possible separator. The intensities are normalized for two separator foils used in the cylindrical cell.

Data Treatment and Refinement Protocol

The structural evolution of NCM622 during the first cycle was investigated by *operando* neutron diffraction using the cylindrical cell.

A neutron diffraction pattern measured for 1 h at ca. 3.7 V vs. Li^+/Li during charging is presented as an example in **Figure 5A**. The achieved signal-to-noise ratio is sufficient to allow the diffraction peaks of the layered material to stand out

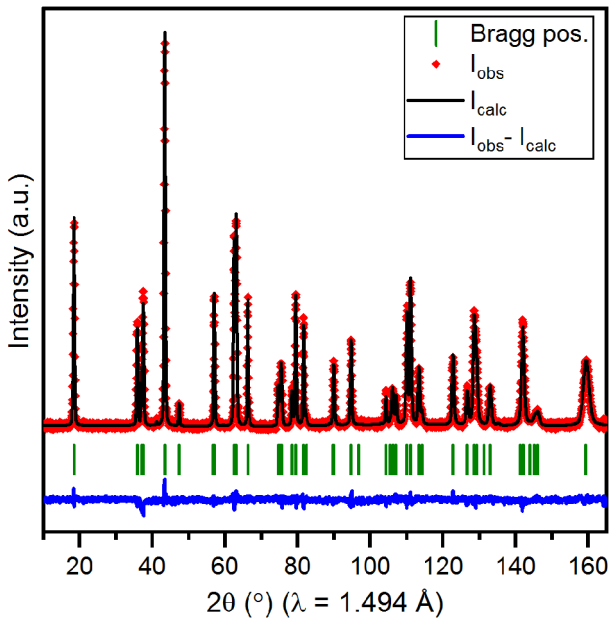

FIGURE 3 | Rietveld refinement profile obtained using the *ex situ* neutron diffraction pattern of the NCM622 pristine powder. The calculated profile (black) is superimposed on the experimental profile (red diamonds) and the difference curve is drawn in blue. The calculated Bragg positions of the diffraction peaks are indicated by green ticks.

TABLE 1 | Crystallographic data obtained from the Rietveld refinement using the NCM622 pristine powder neutron diffraction data.

$Li(Ni_{0.6}Mn_{0.2}Co_{0.2})O_2$			
R-3*m* (no. 166) (*Z* = 3)		*a* = 2.86793 (4)Å *c* = 14.2209 (2) Å *V* = 101.297 (2) Å^3	
Atomic parameters			
Atoms	**Fractional site occupancy**		**B_{iso} (Å^2)**
Wyckoff position 3b (0, 0, 1/2)			
Li Ni (exchanged)	0.965 (1)** 0.035 (1)**		0.69 (6)
Wyckoff position 3a (0, 0, 0)			
Li (exchanged) Ni Mn Co	0.035 (1)** 0.565 (1)** 0.2* 0.2*		0.34 (2)
Wyckoff position 6c (0, 0, z)			
O *z* = 0.25885 (5)	1.0*		0.75 (2)
Interatomic distances (Å)			
TM – O	1.9656 (5)	Li-O	2.1119 (5)
Agreement factors			
R_{Bragg} = 3.78%	R_f = 2.65%		χ^2 = 1.36

Fixed parameters are indicated by "", and restrained parameters by "**" ($OccNi_{3a}$ + $OccNi_{3b}$ = 0.6, $OccLi_{3a}$ + $OccLi_{3b}$ = 1, $OccLi_{3a}$ = $OccNi_{3b}$).*

and enables to follow the evolution of the Bragg reflections during lithiation/delithiation. However, the high background generated by the separators and deuterated electrolyte prevented the conclusive refinement of the structural parameters based on the raw data. Both these contributions, which were previously singled out (**Figure 2A**), were mathematically subtracted from the background of every neutron diffraction pattern. Rietveld refinements could then be successfully carried out. To illustrate the quality of this background subtraction procedure, a corrected pattern collected at ca. 3.7 V vs. Li^+/Li during charge is compared to the raw diffraction pattern in **Figure 5A** and the Rietveld refinement profile based on this data is presented in **Figure 5B**.

Three phases were needed to index all Bragg reflections in the background-corrected patterns: NCM622, aluminum (space group *Fm*-3*m*, $a \approx 4.052$ Å), and lithium metal (space group *Im*-3*m*, $a \approx 3.512$ Å). Special care is required for the treatment of the contribution of aluminum from the cell casing because many of the diffraction peaks arising from aluminum overlap with those of NCM622. Thus, data acquisition was carried out on the empty cell (**Figure 2**) and the diffraction pattern from this machined piece shows severe preferred orientation effects that are challenging to handle quantitatively given the limited number of diffraction peaks in the pattern with the wavelength $\lambda = 1.494$ Å. To take into account the contribution of the strongly textured Al casing without compromising the precision of the refinement of the main phase of interest, the profile matching mode with constant relative intensities, as implemented in the Fullprof program (Rodríguez-Carvajal, 1993), was used. With this method, the relative peak intensities were calculated during the refinement based on the powder diffraction pattern of the empty Al-casing using the profile matching mode. They were then fixed from the Rietveld refinement using the *operando* neutron diffraction data and only the scale factor was varied for the aluminum phase. This approach showed limitations in two regions of the patterns ($2\theta \approx 63°$ and $2\theta \approx 129°$), where peaks arising from the Al casing coincided with those of both Li metal and NCM622 material. These two regions were, thus, excluded from the sequential refinements. Note that profile matching refinement alone is not a suitable method for treating the empty cell contribution because the peak overlap with the peaks of the NCM622 material is significant throughout the whole diffraction pattern. For the NCM622 layered material, the structural model of the pristine material (**Table 1**) was used and the following parameters were refined: cell parameters (*a*,*c*), two profile peak broadening parameters to account for the microstructure variations of the NCM material, and structural parameters (lithium content in the interslab space (site *3b*) and the oxygen *z*-coordinate). The quantity of Li/Ni exchange and atomic displacement parameters B_{iso} were fixed to the reasonable refined values from the high-quality neutron diffraction data of the pristine powder. Values for instrumental parameters, cell and profile parameters for aluminum and

lithium, and Gaussian profile parameters for NCM622 were determined during the simultaneous refinement of NCM622 structure at 4.3 V vs. Li^+/Li (measured for 3 h) and at 2.5 V vs. Li^+/Li (measured for 5 h) using the Rietveld method. For this combined refinement, every parameter was refined except for the atomic displacement parameters (B_{iso}) and the extent of Li/Ni exchange, which were fixed to the values of the pristine material.

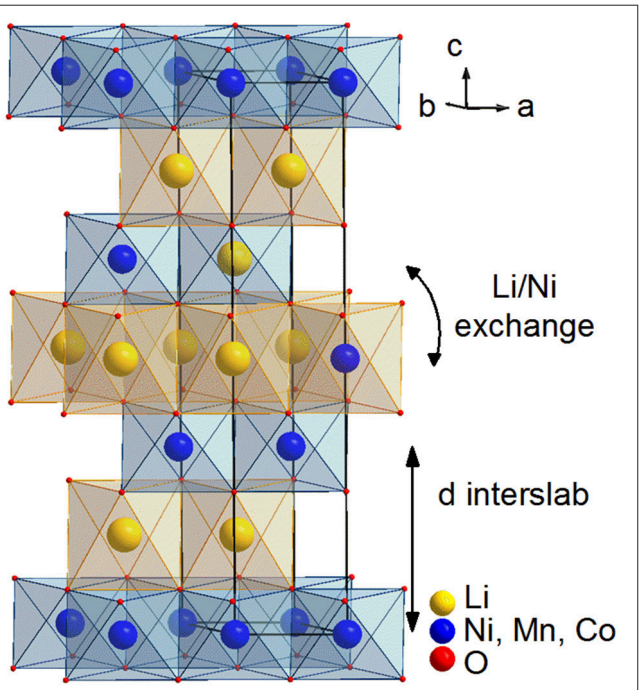

FIGURE 4 | Layered structure of the $Li(Ni_{0.6}Mn_{0.2}Co_{0.2})O_2$ pristine material.

Evolution of the Crystal Structure Upon Cycling

A contour plot of the *operando* neutron diffraction data is presented alongside the electrochemical profile in **Figure 6A**. Significant crystallographic changes are indicated by the shifting of the NCM622 diffraction lines in the 5–165° 2θ range. Enlargements between 17–19° and 55.5–69° in 2θ are shown in **Figure 6B**, following, respectively, the evolution of the (003) and (110) reflections. In layered oxides with an α-$NaFeO_2$ structure, the positions of the (00*l*) lines are linked to the *c*-axis, i.e. the distance between the transition metal (TM) layers, also known as the interslab distance ($d_{interslab} = c/3$). The position of the (110) reflection is correlated to the value of the *a*-axis parameter and corresponds to the distance between the transition metals (d_{TM-TM}) **(Figure 4)**.

In addition, the evolution of the unit cell and atomic parameters refined using the Rietveld method during the sequential refinement of *operando* neutron diffraction data is represented in **Figure 7**. The R-Bragg factor attests to the reliability of the refinement for each pattern.

The gradual shifting of the diffraction lines reveals a solid solution process during the delithiation and lithiation of the active material and is consistent with the evolution of the refined structural parameters (**Figure 7**).

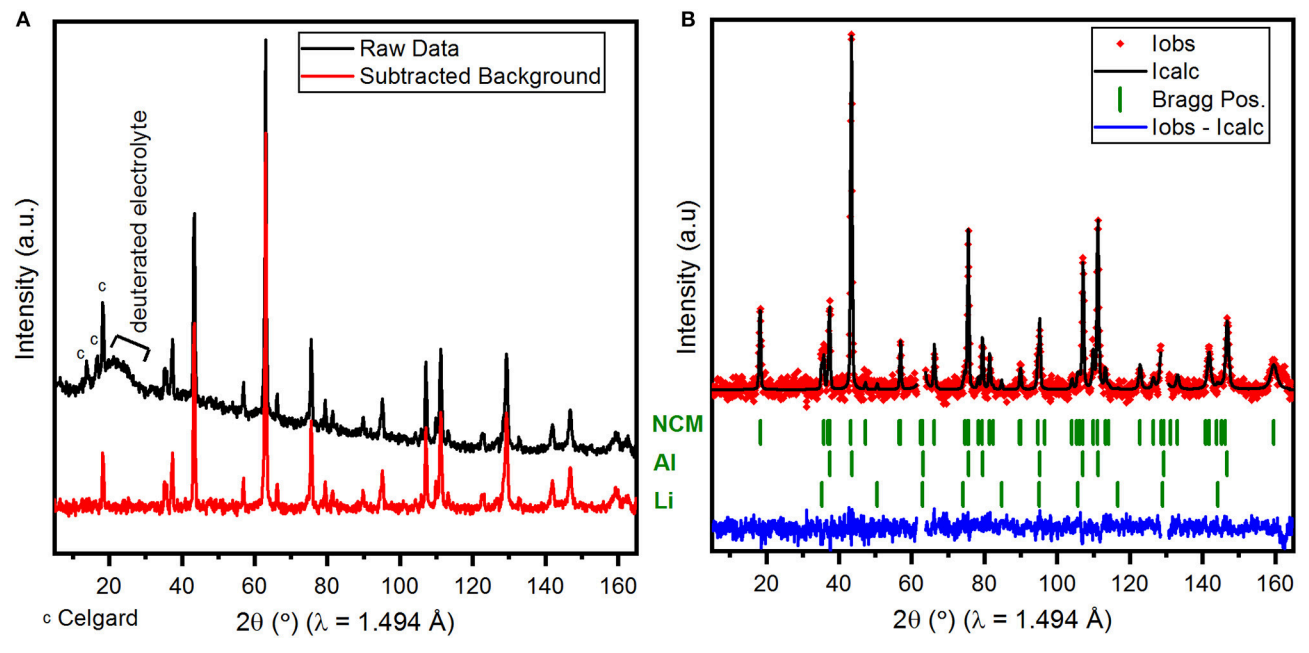

FIGURE 5 | (A) Comparison of a neutron diffraction pattern as collected during the *operando* experiments (ca. 3.7 V vs. Li^+/Li during charge) (black) and after subtraction of the background contributions of the Celgard and deuterated electrolyte (red). **(B)** Rietveld refinement profile based on this background-subtracted diffraction pattern.

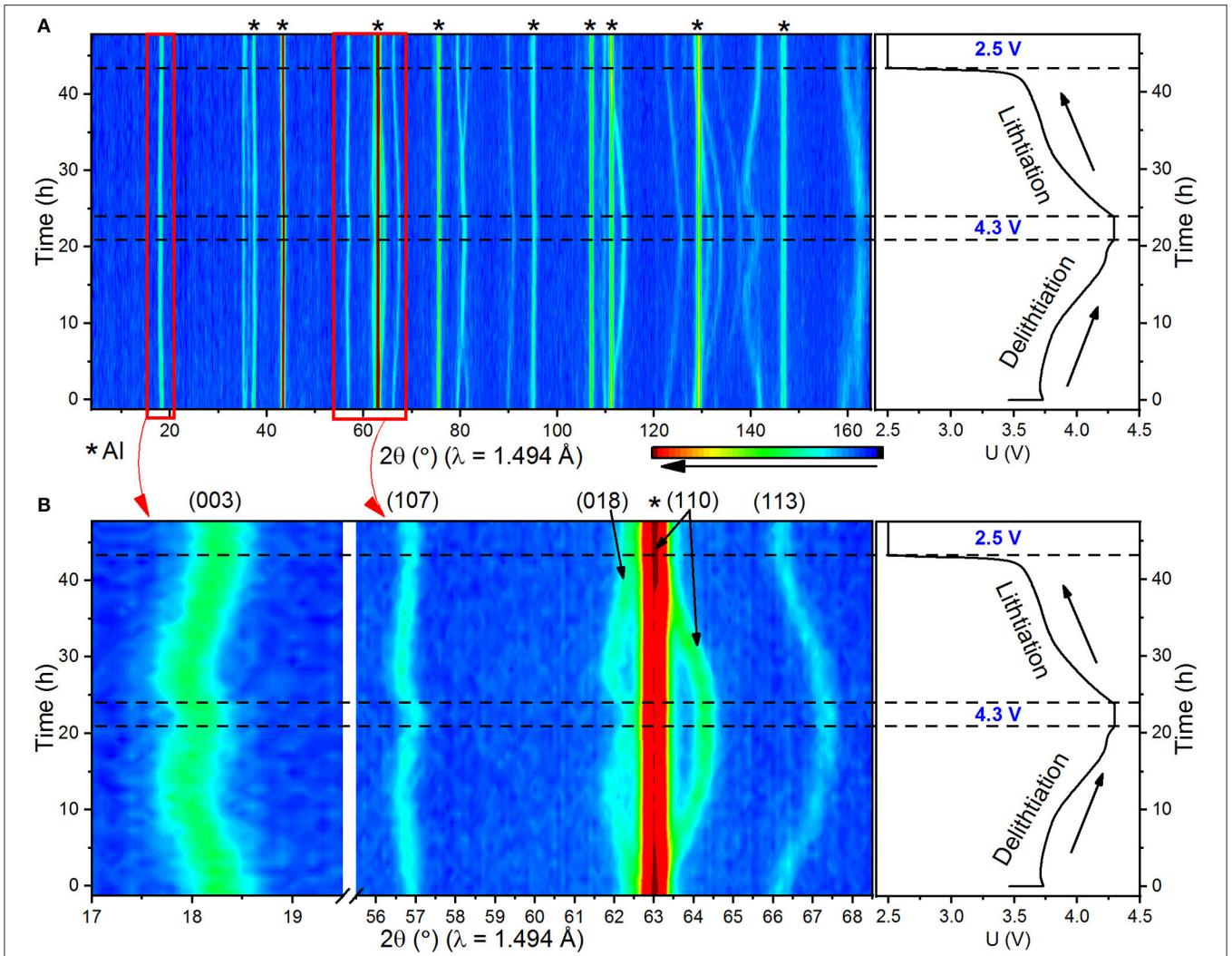

FIGURE 6 | (A) Contour plot representation of the *operando* neutron diffraction data alongside the electrochemical curve obtained during the cycling of the cylindrical cell with NCM622 as the active material. **(B)** Enlargements of the contour plot highlight the evolution of *(003)* and *(110)* reflections of the active material.

The shifting of the (110) diffraction line toward higher angles is continuous until the cut-off potential, 4.3 V vs. Li^+/Li. This highlights the reduction in the *a*-axis and, thus, of the in-plane TM-TM distance, from 2.8680(2) to 2.8154(3) Å. This 1.8% shrinkage is the result of the oxidation of the Ni^{2+}/Ni^{3+} ions to Ni^{4+}, which has a smaller ionic radius. At the same time, the bond between transition metal and oxygen becomes more covalent, as suggested by the decrease of the interatomic distance between the transition metals and oxygen (d_{TM-O}) from 1.964(4) to 1.880(5) Å.

Meanwhile, the shifting of the *(003)* diffraction line is less straightforward to understand. It first shifts toward lower 2θ angles indicating an increase in the *c* cell parameter and, thus, of the interslab distance, starting with $c = 14.2208(11)$ Å ($d_{interslab} \sim 4.740$ Å) at 3.7 V vs. Li^+/Li. The latter results from increasing electrostatic repulsion forces between the oxygenated layers when lithium ions are removed from the interslab space (Van der Ven et al., 1998). However, the highest value for the *c* cell parameter [$c = 14.502(3)$ Å, $d_{interslab} \sim 4.836$ Å] was reached at $x_{Li} = 0.40(11)$ at ca. 4.0 V vs. Li^+/Li. Pursuing delithiation, the (003) diffraction line, as well as all other peaks with the *l* index dominating in their (*hkl*) Miller indices, shifts slightly back to higher 2θ angles, and the *c* cell parameter decreases, reaching 14.383(2) Å ($d_{interslab} \sim 4.794$ Å) for $x_{Li} \approx 0.10(10)$ at 4.3 V vs. Li^+/Li. This behavior has been reported for layered Li_xNiO_2 (Li et al., 1993), Li_xCoO_2 (Ohzuku and Ueda, 1994; Amatucci et al., 1996), and $Li_x(Ni,Co,Mn)O_2$ materials (Alam et al., 2014; Ishidzu et al., 2016; Kondrakov et al., 2017b) and its origin is still under debate. A theoretical investigation of the $LiCoO_2$ phase diagram (Van der Ven et al., 1998) suggested that a strong overlap of the *2p* orbitals of oxygen and the partially filled e_g orbitals of the transition metal would lead to charge transfer, resulting in the depletion of the oxygen charge. The decrease in electrostatic repulsions between oxygenated

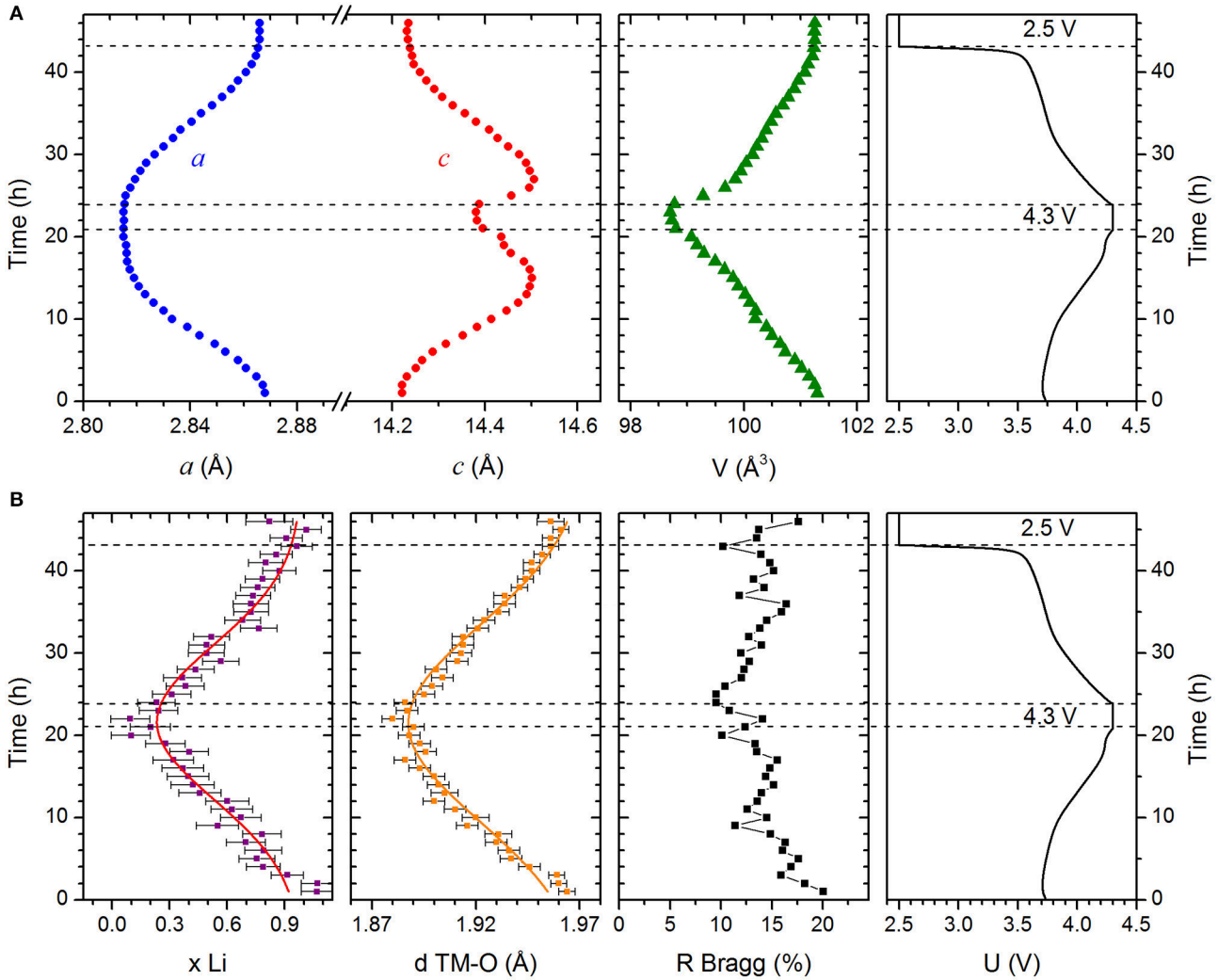

FIGURE 7 | Evolution of the structural parameters of NCM622 determined from the sequential refinement using neutron diffraction data collected during the *operando* experiments. **(A)** Unit cell parameters and volume. The errors on these values are smaller than the symbol sizes. **(B)** Lithium content and the interatomic distance between oxygen and transition metal atoms (d_{TM-O}). Solid lines in these panels are guides to eye. The reliability factor, R-Bragg, is indicated for each refinement. The standard deviations of the refined parameters for the refinements done on the background-subtracted data have been corrected to account for the artificial underestimation of the errors, see text for details.

layers would then lead to the collapse of the interlayer space. This model was experimentally and theoretically confirmed for $Li_xNi_{0.8}Co_{0.1}Mn_{0.1}O_2$ (Kondrakov et al., 2017a). According to *in situ* X-ray powder diffraction experiments (Yoon et al., 2006; Ghanty et al., 2015), it could also be linked to the formation of a second hexagonal phase at high voltage, as it has been shown for $LiNiO_2$ (Li et al., 1993). This second phase is isostructural with the pristine material but has a shorter *a*-axis, longer *c*-axis, and significantly lower lithium content. This mechanism would induce a splitting or broadening of the diffraction peaks, which is not observed in our experiment. The hypothesis of variations in the coulombic repulsion between oxygenated layers with lithium content is, thus, favorable in our case.

The evolution of the *a* and *c* cell parameters results in a continuous shrinkage of the unit cell volume upon delithiation, from 101.299(11) Å^3 at 3.7 V vs. Li^+/Li to 98.73(2) Å^3 at 4.3 V vs. Li^+/Li. This volume variation (2.5%) is in agreement with the literature values (Kondrakov et al., 2017a). It has been shown to vary linearly with the nickel content in NCM materials and result in the degradation of the Ni-rich cathode material (Noh et al., 2013; Ishidzu et al., 2016; Kim et al., 2016; Kondrakov et al., 2017b).

Operando neutron diffraction was performed consecutively during the discharge of the cell, i.e., lithiation of the NCM622 material, and shows that the structural changes previously described for delithiation are reversible. Indeed, the intercalation of lithium between the layers first leads to an increase in the

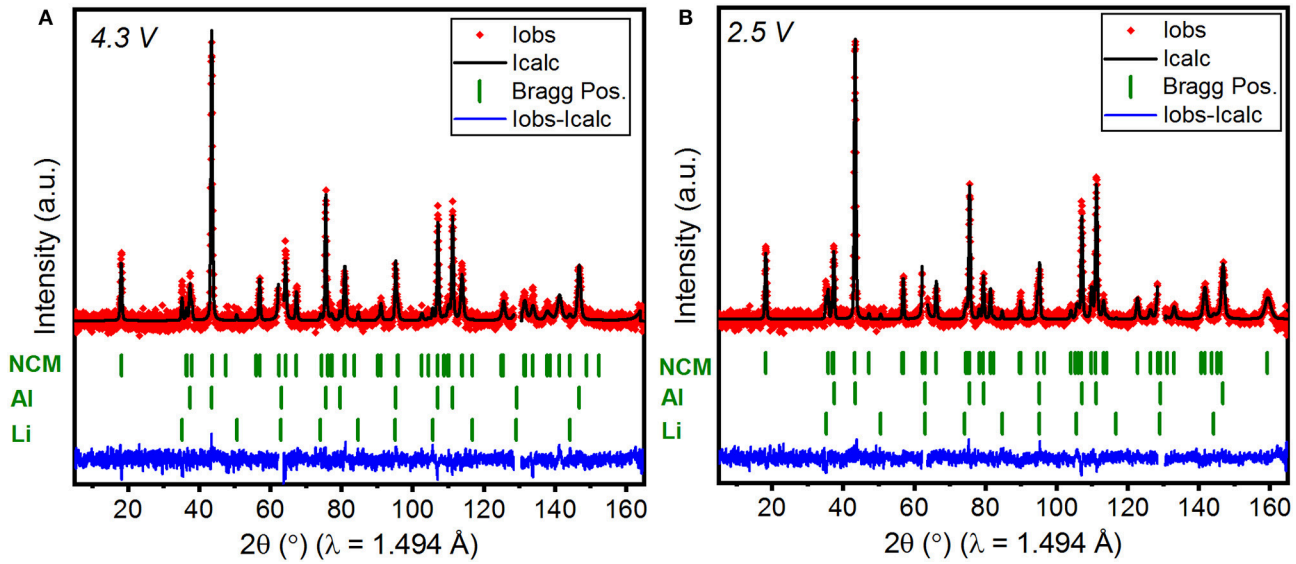

FIGURE 8 | Rietveld refinements profiles obtained using neutron diffraction data collected at constant voltage. **(A)** At 4.3 V for 3 h and **(B)** at 2.5 V for 5 h. Both refinements feature two excluded regions, as discussed in the text.

TABLE 2 | Refined crystal structure parameters obtained from the Rietveld refinement using the background-corrected neutron diffraction data collected at constant voltage (CV), in *operando* (O), and for the pristine powder (values taken from **Table 1**).

	4.3 V (CV)	**4.3 V (O)**	**2.5 V (CV)**	**2.5 V (O)**	**Pristine**
a (Å)	2.8151 (3)	2.8154 (2)	2.8656 (3)	2.8661 (2)	2.86793 (4)
c (Å)	14.376 (2)	14.383 (2)	14.2364 (12)	14.232 (1)	14.2209 (2)
V (Å^3)	98.66 (2)	98.73 (2)	101.245 (15)	101.25 (2)	101.297 (2)
x_{Li}	0.09 (10)	0.09 (10)	0.96 (6)	1.01 (8)	0.965 (1)
z_O	0. 2671 (8)	0.2676 (8)	0.2596 (4)	0.2593 (5)	0.25885 (5)
d_{TM-O} (Å)	1.884 (5)	1.880 (5)	1.959 (3)	1.961 (4)	1.9656 (5)
d_{Li-O} (Å)	2.173 (8)	2.179 (8)	2.118 (4)	2.117 (5)	2.1119 (5)
R_{Bragg} (%)	10.8	14.13	11.6	13.7	3.78
χ^2	1.07	0.84	1.07	0.82	1.36

The standard deviations of the refined parameters for the refinements done on the background-corrected data have been corrected to account for the artificial underestimation of the errors, see text for details.

c cell parameter, which then continuously decreases until 2.5 V vs. Li^+/Li because of the screening effect of the lithium ions on the electrostatic repulsion forces between the oxygenated layers. As expected the *a* cell parameter increases because of the increase of TM-TM distance induced by the larger ionic radii of nickel ions in a reduced state; in addition, the interatomic distance, d_{TM-O}, increases. Moreover, the structure of NCM622 at 2.5 V vs. Li^+/Li after the first cycle is very close to the structure of the material at 3.7 V vs. Li^+/Li at the beginning of cycling.

To complete the study, the voltage was held constant for 3 and 5 h at cut-off potentials of 4.3 and 2.5 V vs. Li^+/Li, respectively. The corresponding Rietveld refinement profiles are presented **Figure 8.** The refined structural parameters are summarized in **Table 2** and compared to the structural parameters obtained from the Rietveld refinements on neutron diffraction data collected in *operando* and for the pristine powder. The results of refinements from the datasets collected in the cell, at constant voltage (CV), and in *operando* (O), were in fact obtained on the background-corrected data: the contributions from the Celgard separator and from the deuterated electrolyte were subtracted prior to the refinements. This subtraction procedure inevitably led to substantially higher variances of the background-subtracted data. This, in turn, has led to the smaller weights of the point-by-point calculated squared differences between the "experimental" and the calculated intensities, entering the calculation of χ^2, and thus, to unrealistically low values of the χ^2 values. In this respect, these unusually low χ^2 values are a consequence of the higher intensity variances than these would be expected for the directly measured intensities of the same magnitudes. The exact absolute χ^2 values in **Table 2** are therefore irrelevant characteristics of the refinement quality, and should be considered as relative refinement quality indicators only. On the other hand, special care needs to be taken of the errors of the refined parameters, when statistics of the data used for the refinements is modified during data reduction, as it is the case with our operando data. Rietveld refinement code of Fullprof uses the value of the reduced chi-squared $\chi^2_\upsilon = \frac{\chi^2}{n-p}$, where *n-p* is the number of degrees of freedom of the refinement problem (Rodríguez-Carvajal, 1993), to additionally correct the standard deviations of the refined parameters, in a way that the estimated standard deviations are multiplied by the $\sqrt{\chi^2_\upsilon}$. This is why, in the refinements of our operando data characterized by the unusually low χ^2 values because of the background subtraction done in advance, the directly output standard deviations of the

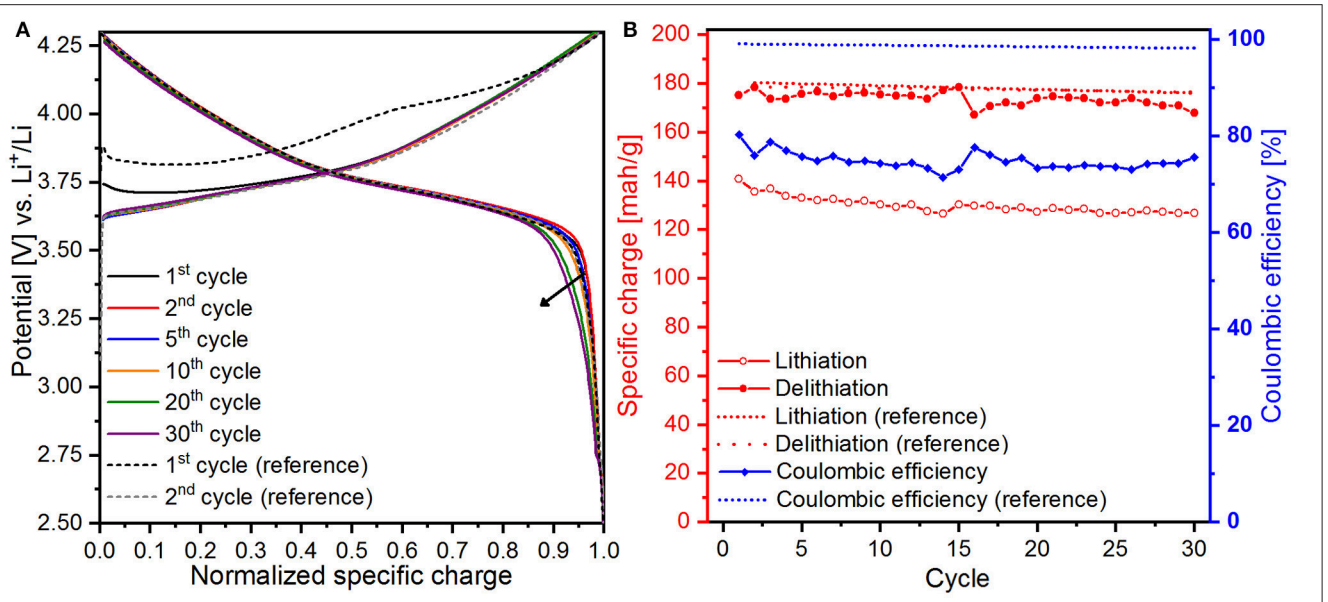

FIGURE 9 | (A) Normalized galvanostatic curves and **(B)** evolution of the specific charge and coulombic efficiency from the cycling of NCM622 in the cylindrical cell and in standard-type coin cell (reference) for 65 cycles. For clarity, only the linear fit of the reference set of data is represented.

refined parameters would all be underestimated by a factor $\sqrt{\frac{\chi^2_{our}}{\chi^2_{hypoth}}}$, χ^2_{our} and χ^2_{hypoth} being the chi-squared values for "our" refinement on the background-subtracted data, and for the "hypothetical" refinement with exactly the same model on the data with original, unperturbed counting statistics. In order to evaluate this underestimation factor for the standard deviations of the refined parameters from our operando data, and to correspondingly correct for it, we consider the exact formulation for calculation of the χ^2 values used in Fullprof: $\chi^2 = \sum_{i=1}^{n} w_i \{y_{i,\exp} - y_{i,calc}\}^2$, with the point-by-point calculated weights of the profile points' contributions $w_i = \frac{1}{\sigma_i^2}$. It is thus logical to estimate the artificial reduction factor for errors of refined parameter as $\sqrt{\sum_{i=1}^{n} \frac{1}{\sigma^2_{i,our}} \Big/ \sum_{i=1}^{n} \frac{1}{\sigma^2_{i,orig}}}$, with $\sigma^2_{i,our}$ and $\sigma^2_{i,orig}$ being the point-by-point variances of "our", background-corrected, and of the "original", measured data. We have calculated these underestimation factors, and these amount for the 46 patterns we were refining between $\sqrt{1/1.42}$ and $\sqrt{1/1.44}$. Thus, the strongest underestimation of the errors of the refined parameters as provided directly by the refinement program is most probably by a factor of 1.2. In order to stay on the safe side, we have decided to "back-correct" these output errors for the refinements done on the background-corrected data (*operando*) by multiplying them all by a more conservative value of 1.3.

Refinement of the structure using the neutron diffraction data collected for 3 h at 4.3 V vs. Li^+/Li confirms that the delithiation of the layered phase is almost complete at 4.3 V vs. Li^+/Li with the Li content estimated to be 0.09(10) at the *3b* site, in good agreement with the value deduced from electrochemical measurements ($x \approx 0.08$). After the discharge of the cell to 2.5 V vs. Li^+/Li, NCM622 is again fully lithiated according to the refinement on the neutron diffraction data collected at a constant voltage. Moreover, the structural parameters of the material NCM622 at this voltage are similar to those of the pristine material, which attests to the reversibility of the delithiation process.

Notably, the values for unit cell parameters and atomic parameters obtained from the refinement on neutron diffraction data acquired in *operando* mode and at a constant voltage at both cut-off voltages are very similar. The difference lies in the reliability of the refinement, as shown by the R-Bragg and R-f factors, which are, as expected, better for refinements using neutron data collected for longer periods at a constant voltage. This suggests, nevertheless, that longer acquisitions (>1 h) are not essential for the monitoring of the crystallographic changes upon lithiation and delithiation with this cylindrical cell design, given adequate data treatment. Moreover, the reasonable evolution of the structural parameters upon cycling (**Figure 7**) and the similar values obtained for *operando* and *ex situ* (pristine) measurements attest to the validity of the Rietveld refinement using *operando* neutron diffraction data. However, quantitative results concerning the atomic parameters and, in particular, the exact Li occupation should be considered with care because several parameters were fixed during the Rietveld refinement, including the atomic displacement parameters (B_{iso}) and the Li/Ni mixing ratio, which can evolve during delithiation and lithiation. For precise structural determination, *operando* experiments should, as far as possible, be complemented with *ex situ* neutron diffraction at different states of charge.

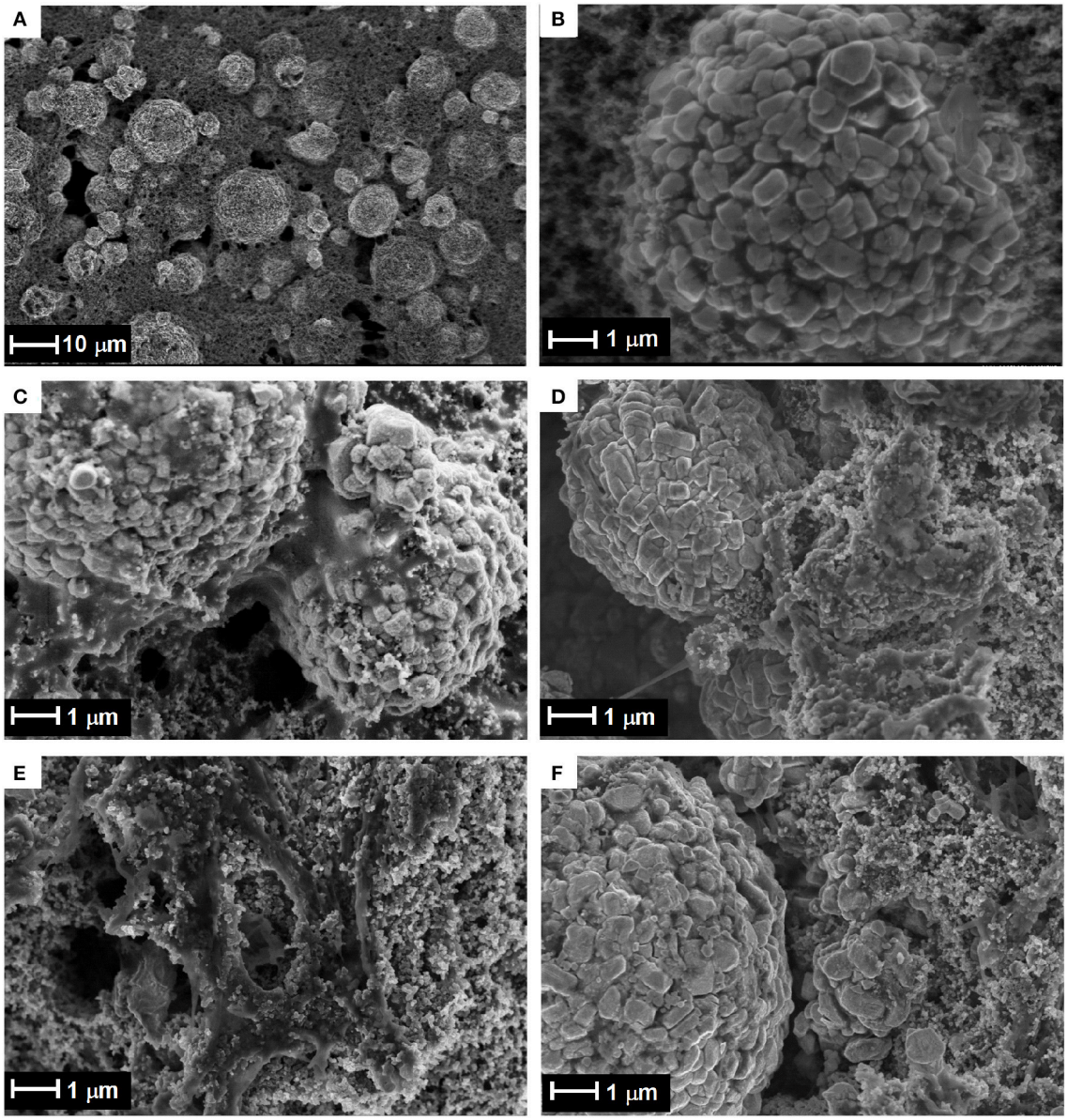

FIGURE 10 | Scanning electron microscopy images of **(A)** pristine material and **(B)** a sample taken from the center of the electrode after 65 cycles, **(C)** unwashed electrode and **(D)** washed electrode with DMC, and a sample taken from the edge of the electrode, **(E)** unwashed and **(F)** washed with DMC.

Electrochemical Performance

An added value of the designed cell is that it can deliver reliable electrochemical performance upon long-term cycling. The electrochemical performance obtained in the cylindrical cell was compared to the reference values deduced from the cycling under identical conditions of the same material in a standard coin-type cell (**Figure 9**).

The normalized galvanostatic curves obtained in the cylindrical cell are presented in **Figure 9A** and compared to the 1st and 2nd normalized galvanostatic curves from the cycling of NCM622 in a standard coin-type cell. The similar shape of the galvanostatic curves from both designs confirms that the same electrochemical behavior occurs. Starting from the 20th cycle, small polarization effects appear at the end of the lithiation from 0.9 to 1.0 in normalized specific charge. There are several sources of this phenomenon, such as irregular current density distribution on the electrode surface or the formation of a thick surface layer on the cathode/separator, which increases the apparent internal resistance of the cell and reduces the diffusion. It could also be linked to the degradation of the NCM622 cathode, as previously reported (Liu et al., 2015; Choi and Aurbach, 2016).

The evolution of the specific charge and the coulombic efficiency is presented in **Figure 9B**. A high cycling stability

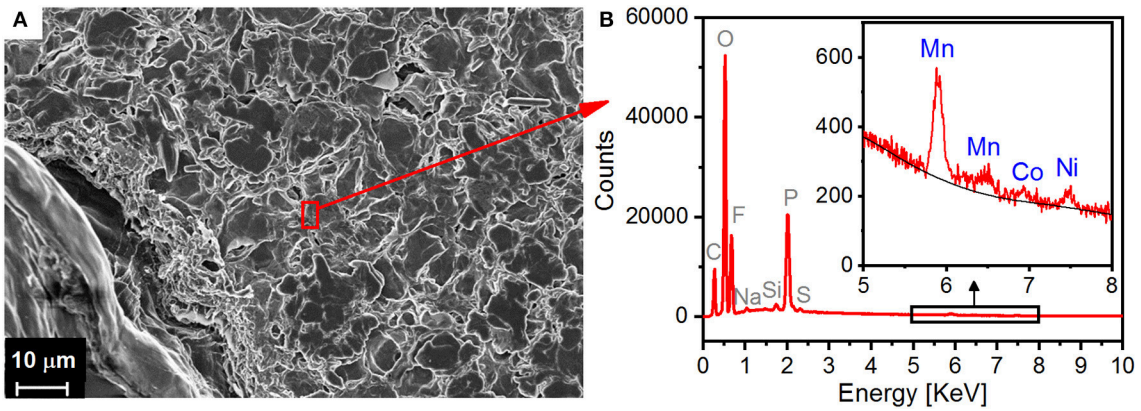

FIGURE 11 | (A) SEM image of cycled lithium anode (center) from the cylindrical cell and **(B)** EDX spectrum of the surface of the lithium anode after 65 cycles.

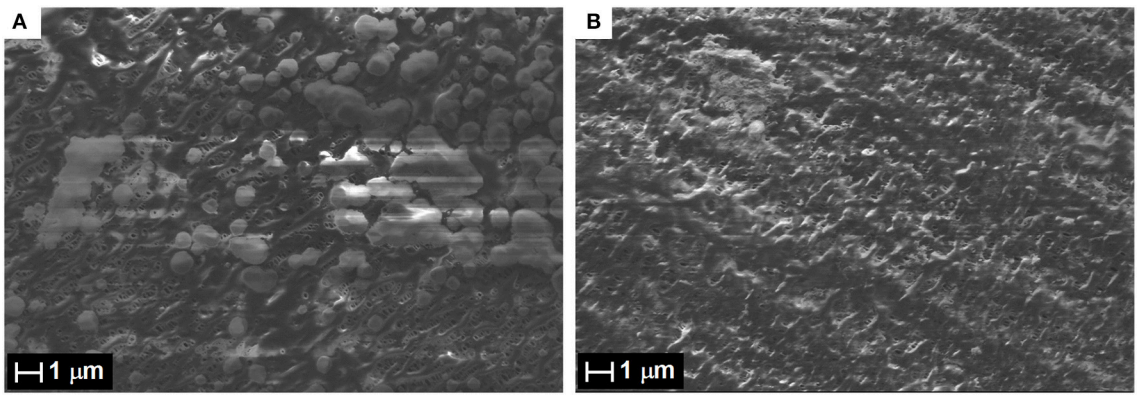

FIGURE 12 | SEM image of the cycled Celgard separators (facing the cathode) of the cylindrical neutron powder diffraction Li-ion cell after 65 cycles: **(A)** unwashed foil and **(B)** foil washed with DMC.

was achieved in the standard cell, having a specific charge of ca. 180 mAh/g after the first cycle (195 mAh/g) and a stable coulombic efficiency close to 98–99%. The specific charge values obtained from cycling in the cylindrical cell during the delithiation process are very close to the reference values, approximately 175 mAh/g for the first 30 cycles. Lower specific charge values were obtained during the lithiation, from 140 mAh/g at the first cycle to 127 mAh/g at the 30th cycle. This results in a coulombic efficiency fluctuating around 80%. After 30 cycles, the specific charge values during delithiation dropped, whereas they remained relatively constant during lithiation, resulting in an increase in the coulombic efficiency. These fluctuations are thought to originate from the assembly of the cylindrical cell. First, the inner pressure inside the cell, as well as the quality of electrical contacts with the current collectors, depends on the tightness of the roll, which can be difficult to control because the rolling is manual. Secondly, the inhomogeneous wettability of the electrodes and separators, along with the irregular inner pressure between the electrodes, could cause an irregular current density distribution over the electrode surface, as mentioned previously. In light of these observations, further optimization of the design would increase the tightness between the electrodes during the hand-rolling. The homogeneity of the wettability of the separators and electrodes could possibly be improved by adding electrolyte during rolling or by using pre-wetted separators, even though it would increase the risk of short-circuits during the assembly of the cell. Also, higher charge on delithiation could be a signature of enhanced electrolyte decomposition or, more generally, of parasitic oxidative processes.

Post-mortem Analysis

Post-mortem analysis using scanning electron microscopy (SEM) coupled with energy-dispersive X-ray spectroscopy (EDX) was performed after long-term cycling (65 cycles) on the cathode, anode and Celgard. Samples were taken from different areas of the electrodes (edges or center) to check possible inhomogeneous reactions and/or gradients. As shown in **Figures 10A,B**, there were no significant microscale changes in the shape and morphology of the electrode after long-term cycling, which is in agreement with the small volume change estimated from the Rietveld refinement. However, a polymeric-like film,

attributed to the solid permeable interphase (i.e., electrolyte decomposition products; Edström et al., 2004), was detected at the surface of the unwashed electrode and, especially, at the grain boundaries **(Figure 10C)**. It can be noted that this layer is more pronounced for samples taken from the edge of the electrode **(Figure 10E)**. This inhomogeneity supports the hypothesis discussed above of an irregular current density distribution and parasitic oxidation reactions, which could explain the fluctuating coulombic efficiency and the appearance of polarization effects in the galvanostatic curves after 20 cycles **(Figure 9)**. Additionally, the surface of the aged NCM622 primary particles appears rougher with a small amount of chipping at the edges **(Figures 10D–F)**, which could be attributed to surface degradation associated with the transition metal dissolution. This hypothesis is supported by the detection at the surface of the lithium metal anode of manganese, as well as, to a lesser extent, nickel and cobalt (**Figure 11**). Transition metal dissolution is detrimental to the electrochemical performance (Choi and Manthiram, 2006; Zheng et al., 2012) because it enhances the development of the solid electrolyte interphase (SEI) at the surface of the negative electrode (here, Li metal), resulting in an increased resistance that hinders the lithium diffusion. The same effect can be generated by the clogging of the separators pores caused by side-products of the electrolyte decomposition (Sharabi et al., 2012). It can indeed be seen in **Figure 12** that a polymer-like film, as well as small agglomerates, covers the surface of the Celgard separator after cycling. A higher resistance arising from the electrolyte decomposition coupled to the transition metal dissolution and clogging of the separator pores could explain the overall decrease of the specific charge in delithiation that is observed during the cycling in the cylindrical cell (**Figure 9**). However, it is important to note that such effects explain the deviation of the observed electrochemical data in the cell designed for neutron diffraction but do not diminish the quality of the structural refinement.

CONCLUSION

The design of the cylindrical cell developed for *operando* neutron diffraction has been validated by monitoring the changes in the crystal structure parameters of $Li_x(Ni_{0.6}Mn_{0.2}Co_{0.2})O_2$, which were found to be in good agreement with the literature values. A good signal-to-noise ratio in the diffraction patterns was achieved, enhanced by appropriate background subtraction; thus, the refinement of the unit cell, as well as atomic parameters (with reasonable constraints), was successfully carried out on the neutron diffraction data acquired in *operando* mode. However, the reliability of the Rietveld refinement based solely on the *operando* data may not always be sufficient to extract precise quantitative results because of the limited statistics and assumptions used for the constraints. It is, therefore, recommended to complement the *operando* measurements with *in situ* experiments (keeping the cell at a certain voltage for the acquisition of better statistics, as presented in this study) or by *ex situ* experiments on extracted materials at key points of the galvanostatic curve. Electrochemical tests proved that this cylindrical cell is suitable for the investigation of the structural changes in the active material after long-term cycling. Post-mortem analysis contributed to our understanding of ways to improve the cell assembly. However, some further design optimization is required to guarantee uniform and strong contact between the electrodes and separator and the wetting of the separator with electrolyte.

AUTHOR CONTRIBUTIONS

CV and MR designed the cell for the neutron experiments with the help of DS. MR and LV collected, respectively, the *operando* and *pristine* neutron diffraction data with DS and the help of CV and SS. LV and DS carried out the structural analysis and discussed the results. MR conducted the electrochemical characterization and post-mortem analyses with the help of SS and CV. MR, CV, and SS discussed the experiments and the results. MR, LV, CV, and DS wrote the manuscript, and all authors approved the final manuscript.

FUNDING

The authors are grateful to the PSI CROSS initiative for financial support.

ACKNOWLEDGMENTS

The authors thank H. Kaiser for his valuable help in the design of the cell. This work is partly based on experiments performed at the Swiss spallation neutron source, SINQ, Paul Scherrer Institute, Villigen, Switzerland.

REFERENCES

Alam, M., Hanley, T., Pang, W. K., Peterson, V. K., and Sharma, N. (2014). Comparison of the so-called CGR and NCR cathodes in commercial lithium-ion batteries using *in situ* neutron powder diffraction. *Powder Diffr.* 29, S35–S39. doi: 10.1017/S088571561400102X

Amatucci, G. G., Tarascon, J. M., and Klein, L. C. (1996). CoO_2, the end member of the Li_xCoO_2 solid solution. *J. Electrochem. Soc.* 143, 1114–1123. doi: 10.1149/1.1836594

Berg, H. (2001). The LiMn2O4 to λ-MnO2 phase transition studied by *in situ* neutron diffraction. *Solid State Ion* 144, 65–69. doi: 10.1016/S0167-2738(01)00894-3

Bergstöm, Ö., Andersson, A. M., Edström, K., and Gustafsson, T. (1998). A neutron diffraction cell for studying lithium-insertion processes in electrode materials. *J. Appl. Crystallogr.* 31, 823–825. doi: 10.1107/S002188989800538X

Bianchini, M., Fauth, F., Suard, E., Leriche, J. B., Masquelier, C., and Croguennec, L. (2015). Spinel materials for Li-ion batteries: new insights obtained by *operando* neutron and synchrotron X-ray diffraction. *Acta Crystallogr. Sect. B Struct. Sci. Cryst. Eng. Mater.* 71, 688–701. doi: 10.1107/S2052520615017199

Bianchini, M., Leriche, J.-B., Laborier, J.-L., Gendrin, L., Suard, E., Croguennec, L., et al. (2013). A new null matrix electrochemical cell for Rietveld refinements of *in-situ* or operando neutron powder diffraction data. *J. Electrochem. Soc.* 160, A2176–A2183. doi: 10.1149/2.076311jes

Boulet-Roblin, L., Borel, P., Sheptyakov, D., Tessier, C., Novák, P., and Villevieille, C. (2016). Operando neutron powder diffraction using cylindrical cell design: the case of LiNi $_{0.5}$ Mn $_{1.5}$ O $_4$ vs. graphite. *J. Phys. Chem. C* 120, 17268–17273. doi: 10.1021/acs.jpcc.6b05777

Boulet-Roblin, L., Sheptyakov, D., Borel, P., Tessier, C., Novák, P., and Villevieille, C. (2017). Crystal structure evolution *via* operando neutron diffraction during long-term cycling of a customized 5 V full Li-ion cylindrical cell LiNi $_{0.5}$ Mn $_{1.5}$ O $_4$ vs. graphite. *J. Mater. Chem. A* 5, 25574–25582. doi: 10.1039/C7TA07917F

Brant, W. R., Roberts, M., Gustafsson, T., Biendicho, J. J., Hull, S., Ehrenberg, H., et al. (2016). A large format in operando wound cell for analysing the structural dynamics of lithium insertion materials. *J. Power Sour.* 336, 279–285. doi: 10.1016/j.jpowsour.2016.10.071

Brant, W. R., Schmid, S., Du, G., Brand, H. E. A., Pang, W. K., Peterson, V. K., et al. (2014). *In situ* neutron powder diffraction using custom-made Lithium-ion batteries. *J. Vis. Exp.* 10:e52284. doi: 10.3791/52284

Choi, J. W., and Aurbach, D. (2016). Promise and reality of post-lithium-ion batteries with high energy densities. *Nat. Rev. Mater.* 1:16013. doi: 10.1038/natrevmats.2016.13

Choi, W., and Manthiram, A. (2006). Comparison of Metal Ion Dissolutions from Lithium Ion Battery Cathodes. *J. Electrochem. Soc.* 153:A1760. doi: 10.1149/1.2219710

Colin, J. F., Godbole, V., and Novák, P. (2010). *In situ* neutron diffraction study of Li insertion in Li4Ti5O12. *Electrochem. Commun.* 12, 804–807. doi: 10.1016/j.elecom.2010.03.038

Croguennec, L., and Palacin, M. R. (2015). Recent Achievements on inorganic electrode materials for Lithium-ion batteries. *J. Am. Chem. Soc.* 137, 3140–3156. doi: 10.1021/ja507828x

Dolotko, O., Senyshyn, A., Mühlbauer, M. J., Nikolowski, K., and Ehrenberg, H. (2014). Understanding structural changes in NMC Li-ion cells by *in situ* neutron diffraction. *J. Power Sour.* 255, 197–203. doi: 10.1016/j.jpowsour.2014.01.010

Dolotko, O., Senyshyn, A., Mühlbauer, M. J., Nikolowski, K., Scheiba, F., and Ehrenberg, H. (2012). Fatigue process in Li-ion Cells: an *in situ* combined neutron diffraction and electrochemical study. *J. Electrochem. Soc.* 159, A2082–A2088. doi: 10.1149/2.080212jes

Du, G., Sharma, N., Peterson, V. K., Kimpton, J. A., Jia, D., and Guo, Z. (2011). Br-Doped Li4Ti5O12 and composite TiO2 anodes for Li-ion batteries: synchrotron X-ray and *in situ* Neutron Diffraction Studies. *Adv. Funct. Mater.* 21, 3990–3997. doi: 10.1002/adfm.201100846

Edström, K., Gustafsson, T., and Thomas, J. O. (2004). The cathode–electrolyte interface in the Li-ion battery. *Electrochim. Acta* 50, 397–403. doi: 10.1016/j.electacta.2004.03.049

Fischer, P., Frey, G., Koch, M., Könnecke, M., Pomjakushin, V., Schefer, J., et al. (2000). High-resolution powder diffractometer HRPT for thermal neutrons at SINQ. *Phys. B Condens. Matter* 276, 146–147. doi: 10.1016/S0921-4526(99)01399-X

Ghanty, C., Markovsky, B., Erickson, E. M., Talianker, M., Haik, O., Tal-Yossef, Y., et al. (2015). Li^+ -Ion extraction/insertion of Ni-Rich $Li_{1+x}(Ni_yCo_z Mn_z)_wO_2$ ($0.005< x <0.03$; $y : z =8:1$, $w \approx 1$) electrodes: *in situ*, X. R. D., and Raman Spectroscopy study. *ChemElectroChem* 2, 1479–1486. doi: 10.1002/celc.201500160

Godbole, V. A., Heß, M., Villevieille, C., Kaiser, H., Colin, J.-F., and Novák, P. (2013). Circular *in situ* neutron powder diffraction cell for study of reaction mechanism in electrode materials for Li-ion batteries. *RSC Adv.* 3, 757–763. doi: 10.1039/C2RA21526H

Ishidzu, K., Oka, Y., and Nakamura, T. (2016). Lattice volume change during charge/discharge reaction and cycle performance of Li[Ni x Co y Mn z]O 2. *Solid State Ion* 288, 176–179. doi: 10.1016/j.ssi.2016.01.009

Kim, N. Y., Yim, T., Song, J. H., Yu, J. S., and Lee, Z. (2016). Microstructural study on degradation mechanism of layered LiNi 0.6 Co 0.2 Mn 0.2 O 2 cathode materials by analytical transmission electron microscopy. *J. Power Sour.* 307, 641–648. doi: 10.1016/j.jpowsour.2016.01.023

Kondrakov, A. O., Geßwein, H., Galdina, K., de Biasi, L., Meded, V., Filatova, E. O., et al. (2017a). Charge-transfer-induced lattice collapse in Ni-rich NCM cathode materials during delithiation. *J. Phys. Chem. C* 121, 24381–24388. doi: 10.1021/acs.jpcc.7b06598

Kondrakov, A. O., Schmidt, A., Xu, J., Geßwein, H., Mönig, R., Hartmann, P., et al. (2017b). Anisotropic lattice strain and mechanical degradation of high- and low-nickel NCM cathode materials for li-ion batteries. *J. Phys. Chem. C* 121, 3286–3294. doi: 10.1021/acs.jpcc.6b12885

Lee, K. S., Myung, S. T., Amine, K., Yashiro, H., and Sun, Y. K. (2007). Structural and electrochemical properties of layered $Li[Ni_{1-2x}Co_xMn_x]O_2$ (x=0.1–0.3) positive electrode materials for Li-ion batteries. *J. Electrochem. Soc.* 154, A971–A977, doi: 10.1149/1.2769831

Li, W., Reimers, J., and Dahn, J. (1993). *In situ* x-ray diffraction and electrochemical studies of Li1–xNiO2. *Solid State Ion* 67, 123–130. doi: 10.1016/0167-2738(93)90317-V

Liu, H., Fell, C. R., An, K., Cai, L., and Meng, Y. S. (2013). *In-situ* neutron diffraction study of the xLi2MnO3·(1 – x)LiMO2 (x = 0, 0.5; M = Ni, Mn, Co) layered oxide compounds during electrochemical cycling. *J. Power Sour.* 240, 772–778. doi: 10.1016/j.jpowsour.2013.04.149

Liu, W., Oh, P., Liu, X., Lee, M. J., Cho, W., Chae, S., et al. (2015). Nickel-rich layered lithium transition-metal oxide for high-energy lithium-ion batteries. *Angew. Chem. Int. Ed.* 54, 4440–4457. doi: 10.1002/anie.201409262

Manthiram, A., Song, B., and Li, W. (2017). A perspective on nickel-rich layered oxide cathodes for lithium-ion batteries. *Energy Storage Mater.* 6, 125–139. doi: 10.1016/j.ensm.2016.10.007

Noh, H. J., Youn, S., Yoon, C. S., and Sun, Y. K. (2013). Comparison of the structural and electrochemical properties of layered Li[NixCoyMnz]O2 (x = 1/3, 0.5, 0.6, 0.7, 0.8 and 0.85) cathode material for lithium-ion batteries. *J. Power Sour.* 233, 121–130. doi: 10.1016/j.jpowsour.2013.01.063

Ohzuku, T., and Ueda, A. (1994). Solid-state redox reactions of licoo2 ($R\bar{3}m$) for 4 volt secondary lithium cells. *J. Electrochem. Soc.* 141, 2972–2977. doi: 10.1149/1.2059267

Pang, W. K., Alam, M., Peterson, V. K., and Sharma, N. (2015). Structural evolution of electrodes in the NCR and CGR cathode-containing commercial lithium-ion batteries cycled between 3.0 and 4.5 V: an operando neutron powder-diffraction study. *J. Mater. Res.* 30, 373–380. doi: 10.1557/jmr.2014.297

Pang, W. K., Kalluri, S., Peterson, V. K., Dou, S. X., and Guo, Z. (2014a). Electrochemistry and structure of the cobalt-free Li $_{1+x}$ MO $_2$ (M = Li, Ni, Mn, Fe) composite cathode. *Phys. Chem. Chem. Phys.* 16, 25377–25385. doi: 10.1039/C4CP02864C

Pang, W. K., and Peterson, V. K. (2015). A custom battery for *operando* neutron powder diffraction studies of electrode structure. *J. Appl. Crystallogr.* 48, 280–290. doi: 10.1107/S1600576715000679

Pang, W. K., Peterson, V. K., Sharma, N., Shiu, J.-J., and Wu, S. (2014b). Lithium migration in Li_4 Ti_5 O_{12} studied using *in situ* neutron powder diffraction. *Chem. Mater.* 26, 2318–2326. doi: 10.1021/cm5002779

Pang, W. K., Sharma, N., Peterson, V. K., Shiu, J.-J., and Wu, S. (2014c). *In-situ* neutron diffraction study of the simultaneous structural evolution of a LiNi0.5Mn1.5O4 cathode and a Li4Ti5O12 anode in a LiNi0.5Mn1.5O4||Li4Ti5O12 full cell. *J. Power Sour.* 246, 464–472. doi: 10.1016/j.jpowsour.2013.07.114

Peterson, V. K., Auckett, J. E., and Pang, W. K. (2017). Real-time powder diffraction studies of energy materials under non-equilibrium conditions. *IUCrJ* 4, 540–554. doi: 10.1107/S2052252517010363

Robert, R., Villevieille, C., and Novák, P. (2014). Enhancement of the high potential specific charge in layered electrode materials for lithium-ion batteries. *J. Mater. Chem. A* 2:8589. doi: 10.1039/c3ta12643a

Roberts, M., Biendicho, J. J., Hull, S., Beran, P., Gustafsson, T., Svensson, G., et al. (2013). Design of a new lithium ion battery test cell for *in-situ* neutron diffraction measurements. *J. Power Sour.* 226, 249–255. doi: 10.1016/j.jpowsour.2012.10.085

Rodríguez-Carvajal, J. (1993). Recent advances in magnetic structure determination by neutron powder diffraction. *Phys. B Condens. Matter* 192, 55–69. doi: 10.1016/0921-4526(93)90108-I

Rodriguez, M. A., Van Benthem, M. H., Ingersoll, D., Vogel, S. C., and Reiche, H. M. (2010). *In situ* analysis of LiFePO4 batteries: signal extraction by multivariate analysis. *Powder Diffr.* 25, 143–148. doi: 10.1154/1.3393786

Rosciano, F., Holzapfel, M., Scheifele, W., and Novák, P. (2008). A novel electrochemical cell for *in situ* neutron diffraction studies of electrode materials for lithium-ion batteries. *J. Appl. Crystallogr.* 41, 690–694. doi: 10.1107/S0021889808018025

Rozier, P., and Tarascon, J. M. (2015). Review—Li-rich layered oxide cathodes for next-generation Li-ion batteries: chances and challenges. *J. Electrochem. Soc.* 162, A2490–A2499. doi: 10.1149/2.0111514jes

Schipper, F., Erickson, E. M., Erk, C., Shin, J. Y., Chesneau, F. F., and Aurbach, D. (2017). Recent advances and remaining challenges for lithium ion battery cathodes I. Nickel-Rich, LiNixCoyMnzO2. *J. Electrochem. Soc.* 164, A6220–A6228. doi: 10.1149/2.0351701jes

Sears, V. F. (1992). Neutron scattering lengths and cross sections. *Neutron News* 3, 26–37. doi: 10.1080/10448639208218770

Senyshyn, A., Mühlbauer, M. J., Dolotko, O., Hofmann, M., Pirling, T., and Ehrenberg, H. (2014). Spatially resolved in operando neutron scattering studies on Li-ion batteries. *J. Power Sour.* 245, 678–683. doi: 10.1016/j.jpowsour.2013.06.158

Shannon, R. D. (1976). Revised effective ionic radii and systematic studies of interatomic distances in halides and chalcogenides. *Acta Crystallogr. Sect. A* 32, 751–767. doi: 10.1107/S0567739476001551

Sharabi, R., Markevich, E., Borgel, V., Salitra, G., Gershinsky, G., Aurbach, D., et al. (2012). Raman study of structural stability of LiCoPO4 cathodes in LiPF6 containing electrolytes. *J. Power Sour.* 203, 109–114. doi: 10.1016/j.jpowsour.2011.12.018

Sharma, N., Du, G., Studer, A. J., Guo, Z., and Peterson, V. K. (2011). *In-situ* neutron diffraction study of the MoS2 anode using a custom-built Li-ion battery. *Solid State Ion* 199–200, 37–43. doi: 10.1016/j.ssi.2011.07.015

Sharma, N., Guo, X., Du, G., Guo, Z., Wang, J., Wang, Z., et al. (2012). Direct evidence of concurrent solid-solution and two-phase reactions and the nonequilibrium structural evolution of LiFePO $_4$. *J. Am. Chem. Soc.* 134, 7867–7873. doi: 10.1021/ja301187u

Sharma, N., Pang, W. K., Guo, Z., and Peterson, V. K. (2015). *In situ* powder diffraction studies of electrode materials in rechargeable batteries. *ChemSusChem* 8, 2826–2853. doi: 10.1002/cssc.201500152

Sharma, N., Peterson, V. K., Elcombe, M. M., Avdeev, M., Studer, A. J., Blagojevic, N., et al. (2010). Structural changes in a commercial lithium-ion battery during electrochemical cycling: an *in situ* neutron diffraction study. *J. Power Sour.* 195, 8258–8266. doi: 10.1016/j.jpowsour.2010.06.114

Sharma, N., Yu, D. H., Zhu, Y., Wu, Y., and Peterson, V. K. (2017). In operando neutron diffraction study of the temperature and current rate-dependent phase evolution of LiFePO 4 in a commercial battery. *J. Power Sour.* 342, 562–569. doi: 10.1016/j.jpowsour.2016.12.048

Sharma, N., Yu, D., Zhu, Y., Wu, Y., and Peterson, V. K. (2013). Non-equilibrium structural evolution of the lithium-rich Li $_{1+\ y}$ Mn $_2$ O $_4$ cathode within a battery. *Chem. Mater.* 25, 754–760. doi: 10.1021/cm303851w

Taminato, S., Yonemura, M., Shiotani, S., Kamiyama, T., Torii, S., Nagao, M., et al. (2016). Real-time observations of lithium battery reactions—operando neutron diffraction analysis during practical operation. *Sci. Rep.* 6: 28843. doi: 10.1038/srep28843

Tarascon, J. M., and Armand, M. (2010). "Issues and challenges facing rechargeable lithium batteries," in *Materials for Sustainable Energy*, ed V. Dusastre (London: Nature Publishing Group), 171–179. doi: 10.1142/9789814317665_0024

Van der Ven, A., Aydinol, M. K., Ceder, G., Kresse, G., and Hafner, J. (1998). First-principles investigation of phase stability in Li x CoO 2. *Phys. Rev. B* 58, 2975–2987. doi: 10.1103/PhysRevB.58.2975

Yabuuchi, N., and Ohzuku, T. (2003). Novel lithium insertion material of LiCo1/3Ni1/3Mn1/3O2 for advanced lithium-ion batteries. *J. Power Sour.* 119–121, 171–174. doi: 10.1016/S0378-7753(03)00173-3

Yin, S. C., Rho, Y. H., Swainson, I., and Nazar, L. F. (2006). X-ray/neutron diffraction and electrochemical studies of lithium De/Re-intercalation in $Li_{1-x}Co_{1/3}Ni_{1/3}Mn_{1/3}O_2$ ($x = 0 \rightarrow 1$). *Chem. Mater.* 18, 1901–1910. doi: 10.1021/cm0511769

Yoon, W. S., Chung, K. Y., McBreen, J., and Yang, X.-Q. (2006). A comparative study on structural changes of $LiCo_{1/3}Ni_{1/3}Mn_{1/3}O_2$ and $LiNi_{0.8}Co_{0.15}Al_{0.05}O_2$ during first charge using *in situ* XRD. *Electrochem. Commun.* 8, 1257–1262. doi: 10.1016/j.elecom.2006.06.005

Yu, H., Qian, Y., Otani, M., Tang, D., Guo, S., Zhu, Y., et al. (2014). Study of the lithium/nickel ions exchange in the layered $LiNi_{0.42}Mn_{0.42}Co_{0.16}O_2$ cathode material for lithium ion batteries: experimental and first-principles calculations. *Energy Environ. Sci.* 7:1068. doi: 10.1039/C3EE42398K

Zhao, E., Fang, L., Chen, M., Chen, D., Huang, Q., Hu, Z., et al. (2017). New insight into Li/Ni disorder in layered cathode materials for lithium ion batteries: a joint study of neutron diffraction, electrochemical kinetic analysis and first-principles calculations. *J. Mater. Chem. A* 5, 1679–1686. doi: 10.1039/C6TA08448F

Zheng, H., Sun, Q., Liu, G., Song, X., and Battaglia, V. S. (2012). Correlation between dissolution behavior and electrochemical cycling performance for $LiNi_{1/3}Co_{1/3}Mn_{1/3}O_2$-based cells. *J. Power Sour.* 207, 134–140. doi: 10.1016/j.jpowsour.2012.01.122

Conflict of Interest Statement: The authors declare that the research was conducted in the absence of any commercial or financial relationships that could be construed as a potential conflict of interest.

frontiers | Frontiers in Energy Research

TYPE Original Research
PUBLISHED 14 November 2022
DOI 10.3389/fenrg.2022.1056260

OPEN ACCESS

EDITED BY
Neeraj Sharma,
University of New South Wales, Australia

REVIEWED BY
Jordi Jacas Biendicho,
Energy Research Institute of Catalonia, Spain
Tan Shi,
Apple, United States

*CORRESPONDENCE
William R. Brant,
william.brant@kemi.uu.se

SPECIALTY SECTION
This article was submitted to Electrochemical Energy Conversion and Storage,
a section of the journal
Frontiers in Energy Research

RECEIVED 28 September 2022
ACCEPTED 31 October 2022
PUBLISHED 14 November 2022

CITATION
Gustafsson O, Schökel A and Brant WR (2022), Mind the miscibility gap: Cation mixing and current density driven non-equilibrium phase transformations in spinel cathode materials.
Front. Energy Res. 10:1056260.
doi: 10.3389/fenrg.2022.1056260

Mind the miscibility gap: Cation mixing and current density driven non-equilibrium phase transformations in spinel cathode materials

Olof Gustafsson[1], Alexander Schökel[2] and William R. Brant[1]*

[1]Ångström Laboratory, Department of Chemistry—Ångström, Structural Chemistry, Uppsala University, Uppsala, Sweden, [2]Deutsches Elektronen Synchrotron (DESY), Hamburg, Germany

Cathode materials that exhibit phase transitions with large structural rearrangements during electrochemical cycling are generally seen as disadvantageous. Large volume changes and lattice mismatches between intermediate phases tend to lead to significant kinetic barriers, as well as strain and particle cracking. In this regard, solid solution reactions are more desirable as they provide lower energy barriers and no miscibility gap between co-existing phases. The high-voltage cathode material $LiNi_{0.5}Mn_{1.5}O_4$ is an interesting candidate for high power and rate capability applications, however little is known on how its phase transitions occur on the particle level. In the presented work *operando* X-ray diffraction was utilized together with detailed peak profile analysis to elucidate the phase transition mechanism dependency on transition metal cation order and current density. When fully disordered, the material was found to undergo a bulk single-phase solid solution reaction between the intermediate phases $LiNi_{0.44}Mn_{1.56}O_4$ and $Li_{0.5}Ni_{0.44}Mn_{1.56}O_4$ followed by a first order phase transition with a coherent interphase between the intermediates $Li_{0.5}Ni_{0.44}Mn_{1.56}O_4$ and $Ni_{0.44}Mn_{1.6}O_4$. When fully ordered and slightly less ordered, two separate first order phase transitions with a coherent interphase between the same intermediate phases were observed. On discharge, the fast kinetics of the transition between $Li_{0.5}Ni_{0.44}Mn_{1.56}O_4$ and $LiNi_{0.44}Mn_{1.56}O_4$ resulted in less strain on the former phase. For all samples the miscibility gap between the intermediate phases narrowed with increased current density, suggesting that the solid solution domain formed at the coherent interphase can be extended when the rate of (de)lithiation exceeds the movement speed of the interphase at the phase transition. This effect was found to be larger with increasing cation disorder. The influence of transition metal ordering on the ability to form solid solutions is in good agreement with computational phase diagrams of $LiNi_{0.5}Mn_{1.5}O_4$, showing that disorder is important for promoting and stabilizing solid solutions. These results indicate that the degree of transition metal ordering within the material is of importance for obtaining a material with small lattice mismatches between the involved intermediate phases and for rational design of full solid solution materials.

KEYWORDS

Operando, X-ray diffraction, spinel, high-rate, phase transition

1 Introduction

Battery materials with high power and rate capability are of importance for expanding the application and integration of battery technology into modern energy solutions, e.g., in electric vehicles (EV) and more specifically for fast charging capabilities. Looking at the positive electrode side, most cathode materials exhibit structural re-arrangement and phase transitions during electrochemical cycling, which may limit the performance of the material. In particular, phase transitions involving large volume changes and miscibility gaps, e.g., first-order phase transitions, are typically considered disadvantageous for realizing high-rate performance, due to the associated kinetic barriers. Here, solid solution-type reactions are more desirable due to the elimination of strain propagation from phase boundaries within the active material particles.

A cathode material that exhibits good rate capability and that has seen usage in EV applications is the iron-based olivine-type material $LiFePO_4$ (LFP). LFP undergoes a single first-order phase transition upon (de)lithiation between its two end-members $LiFePO_4$ and $FePO_4$ at low cycling rates. This kinetically limited two-phase reaction was shown, utilizing X-ray diffraction (XRD), to be bypassed in favor of a solid solution reaction at increased cycling rates (Liu et al., 2014; Zhang et al., 2014). Further, it was also shown that LFP can form metastable solid solutions after heating a two-phase mixture of the two end-members (Delacourt et al., 2005; Chen et al., 2007). In a similar fashion the high-voltage spinel cathode material $LiNi_{0.5}Mn_{1.5}O_4$ (LNMO) was found to form metastable solid solutions after heating of two- and three-phase-mixtures of the end members $LiNi_{0.5}Mn_{1.5}O_4$, $Li_{0.5}Ni_{0.5}Mn_{1.5}O_4$ and $Ni_{0.5}Mn_{1.5}O_4$ (Saravanan et al., 2015). Where phase separation was found in the LFP solid solutions upon cooling to room temperature, the LNMO solid solutions exhibited more stability and remained at room temperature. Further, the first-order phase transition in LNMO was also found to move toward a solid solution-type reaction when cycled at elevated rates (≥5C) (Komatsu et al., 2015). However, the situation for LNMO is a little more complicated than for LFP due to the existence of two structural forms. That is, the material exhibits different structural behavior during (de)lithiation depending on the ordering between Ni and Mn within the structure (Kim et al., 2004). The disordered form undergoes a solid solution reaction between $LiNi_{0.5}Mn_{1.5}O_4$ and $Li_{0.5}Ni_{0.5}Mn_{1.5}O_4$ followed by a single two-phase reaction between $Li_{0.5}Ni_{0.5}Mn_{1.5}O_4$ and $Ni_{0.5}Mn_{1.5}O_4$ upon delithiation (and the reversed upon lithiation). The ordered form undergoes two separate two-phase reactions upon delithiation and lithiation. Often, the transition metal ordering in LNMO is not limited to these two discrete cases, but rather a degree of ordering (or cation mixing) is present in the material. How the nature of the phase transitions in LNMO is affected by the degree of cation mixing enables insight into what other parameters can influence the lattice mismatch, i.e., miscibility gap, between phases. More specifically, to what extent the degree of ordering in the material influences transitions from a two-phase reaction to a solid solution reaction.

In both the case of LFP and LNMO the transition from a two-phase reaction to a solid solution is not discrete. That is, a pure two-phase reaction or a full solid solution reaction across the entire Li composition is not observed. Rather, a metastable decrease in the miscibility gap occurs between the two end-members at higher rates (Liu et al., 2014; Komatsu et al., 2015; Strobridge et al., 2016). In the previously mentioned work on LFP (Liu et al., 2014), a detailed analysis of the peak profile was conducted, providing insight into the distribution of lattice parameters and thus quantifying the narrowing of the miscibility gap. For LNMO, such a detailed study on the transition from two-phase to a solid solution-type reaction has not yet been conducted. Further, given the differences in structural behavior of the disordered and ordered form, a comparison of the behavior at higher rates between them is of interest. As such, the aim of the study presented here is to further elucidate how the high rate structural behavior of LNMO is affected by cation ordering in the material. That is, to provide further quantitative insight into the factors which drive miscibility gap narrowing at higher rates and specifically the role of transition metal ordering.

2 Materials and Methods

2.1 Sample preparation

Pristine $LiNi_{0.5}Mn_{1.5}O_4$ powder was provided by Haldor Topsoe. Further, to obtain additional samples with varying degrees of transition metal ordering, the pristine powder was annealed in two separate ways. To obtain a near fully ordered sample, annealing of the pristine powder was performed in a tube furnace under pure O_2 gas flow. The powder was first heated to 760°C in 2 h followed by a temperature decrease to 710°C over 2 h and held for 5 h, followed by a temperature decrease to 300°C over 5 h. Finally, the sample was cooled down to room temperature over 2 h. To obtain a less ordered sample, the powder was heated to 760°C over 2 h, followed by a decrease in temperature to 710°C over 2 h. The temperature was then held at 710°C for 2 h followed by quenching of the powder by rapid dispersion on a stainless-steel plate.

2.2 Cell assembly and electrochemical characterization

Composite electrodes of two different thicknesses were prepared through a combination of ball milling and slurry casting, following the same procedure as described elsewhere (Gustafsson et al., 2021). The electrode composition was 90 wt% active material, 5 wt% carbon black (C65, Imerys) and 5 wt% polyvinylidene fluoride-based binder (Kynar 2801), dissolved in N-Methyl-2-pyrrolidone (≥99.7%, Merck), 2.5 and 4 wt%, for thinner and thicker electrodes respectively. The resulting capacity of the thicker electrodes was 0.7–0.8 mAh/cm^2 with a porosity of around 40%–45%. The resulting capacity of the thinner electrodes was 0.30–0.35 mAh/cm^2 with a porosity of around 40%. The prepared electrodes were then assembled in pouch cells with Li metal foil as the negative electrode in the same manner as in our previous study (Gustafsson et al., 2021). Prior to performing *operando* X-ray diffraction, all cells were pre-conditioned *via* galvanostatic cycling for two full charge/discharge cycles at a C-rate of C/2 (C = 147 mAh/g) between 3.5 and 4.9 V (vs. Li$^+$/Li). This was done on an Arbin BT-2043 battery test system at room temperature.

2.3 Powder X-ray and neutron diffraction

Powder X-ray diffraction data was collected on the P02.1 beamline (Dippel et al., 2015) at the Petra III synchrotron in Hamburg, Germany, with a wavelength of 0.20698 Å. The detector utilized was a Perkin Elmer XRD1621 CN3 - EHS (200 × 200 μm^2 pixel size, 2,048 × 2,048 pixel area). The wavelength and instrumental broadening contribution to the diffracted patterns were determined from measuring on a powder LaB_6 standard (NIST 660c). Powder neutron diffraction data was collected on the Echidna high-resolution powder diffractometer (Avdeev and Hester, 2018) at the OPAL reactor in Sydney, Australia, with a wavelength of 1.6220 Å. All structural analysis of the collected diffraction data was performed using the TOPAS V6 software package (Coelho, 2018).

2.4 *Operando* X-ray diffraction

Operando X-ray diffraction measurements were carried out on the P02.1 beamline at Petra III. For collection of *operando* X-ray diffraction data, the pre-conditioned pouch cells were assembled in a dedicated cell holder, which is described in more detail elsewhere (Gustafsson et al., 2021). Galvanostatic cycling of the assembled pouch cells was performed using a BioLogic VMP3 potentiostat. Cells with higher mass loading were cycled galvanostatically at 1C and 5C between 3.5–4.9 and 3.5–5.1 V vs. Li$^+$/Li, respectively. Cells with lower mass loading were cycled galvanostatically at 10C between 3.5 and 5.2 V vs. Li$^+$/Li. A 60 s rest at open current voltage (OCV) was employed in between each charge and discharge. At 1C, data was collected continuously for 10 s per pattern, followed by a resting period of 10 s where no data was collected. At 5C and 10C, data was continuously collected for 5 s per pattern, with no resting period in between individual collections.

2.5 Diffraction peak shape modeling and Rietveld refinement of X-ray diffraction data

The whole-powder-pattern fitting approach taken by Liu et al. (2014) and Strobridge et al. (2016) was utilized for peak shape modeling of the X-ray diffraction data. A NIST standard material LaB_6 (660c) was used to obtain the instrument profile, which was modeled by a symmetrical modified Thompson-Cox-Hastings pseudo-Voigt peak shape. The broadening contribution from crystallite size (L) was modeled with a Lorentzian peak profile, where the full width at half maximum (FWHM, β) varies with θ as shown in Eq. 1, where λ is the wavelength.

$$\beta = \frac{\lambda}{L\cos\theta} \tag{1}$$

Peak broadening originating from strain and/or compositional heterogeneity was modeled by convolution of a symmetrical and an asymmetrical profile, following the same approach as Liu et al. (2014). The symmetrical broadening was modeled with a Gaussian peak profile where the FWHM as a function of θ is given by Eq. 2.

$$\beta = E\tan\theta \tag{2}$$

Here, E is the refined strain parameter. The asymmetrical broadening was modeled *via* an exponential function, $f(\theta)$, shown in Eq. 3, where ε_{hkl} is the refined strain parameter. Further, θ, is defined in the range $[\theta_{hkl}, +\infty]$ if $\varepsilon_{hkl} > 0$, and $[-\infty, \theta_{hkl}]$ if $\varepsilon_{hkl} < 0$.

$$f(\theta) = exp\left(-\frac{2\theta - 2\theta_{hkl}}{\varepsilon_{hkl}}\right) \tag{3}$$

The total peak profile is then a convolution of the symmetrical Lorentzian and Gaussian parts together with the asymmetric exponential function. The purely compositional/strain induced peak profile was then obtained from convolution of the Gaussian and exponential peak profile functions. The population density function (pdf) as a function of 2θ at a certain reflection hkl for one phase is then given by Eq. 4, where ⊗ denotes convolution and E and $f(\theta)$ are given from the refined peak profiles.

$$pdf(2\theta)_{hkl} = \frac{2\sqrt{\ln(2)/\pi}}{E\ tan\,\theta}\exp\left(\frac{-4\ln(2)(2\theta - 2\theta_{hkl})^2}{(E\ tan\,\theta)^2}\right) \otimes f(\theta) \tag{4}$$

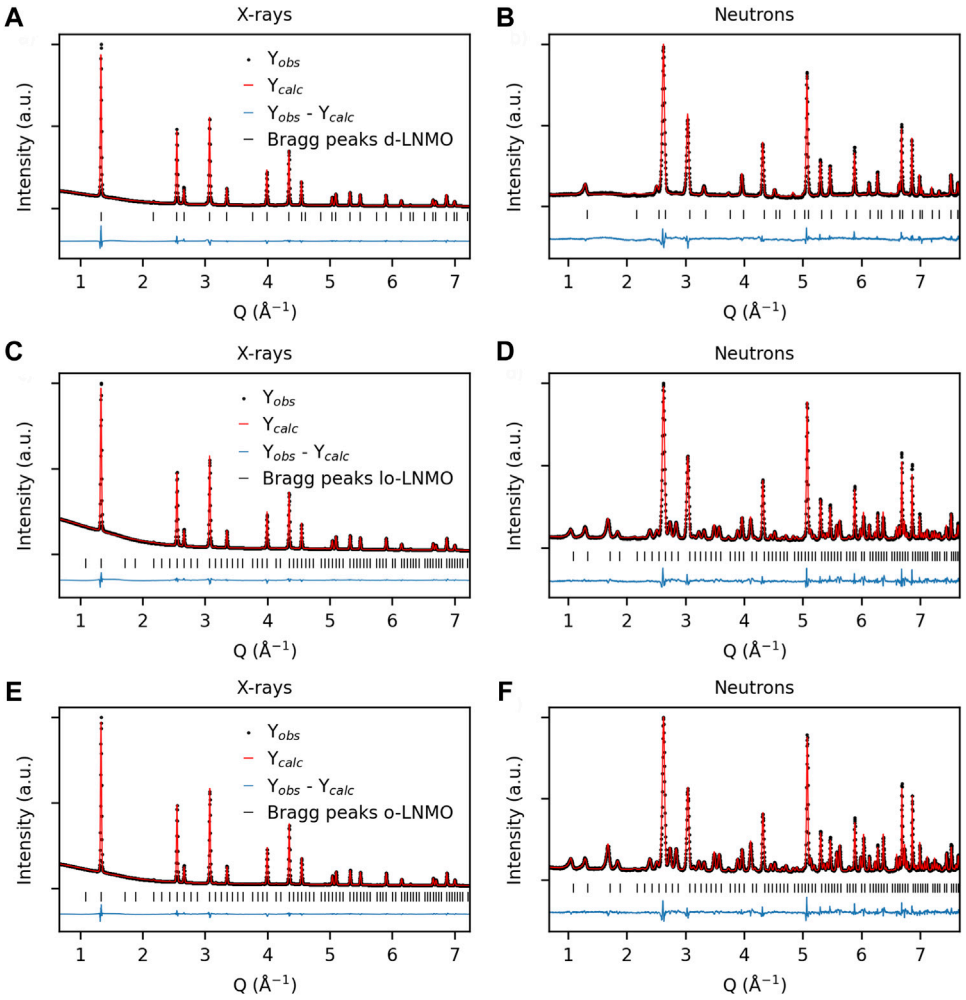

FIGURE 1
Observed and calculated diffraction patterns from combined Rietveld refinement of X-ray and neutron diffraction data for **(A–B)** disordered $LiNi_{0.44}Mn_{1.56}O_4$ (d-LNMO), space group $Fd\bar{3}m$, **(C–D)** less ordered $LiNi_{0.44}Mn_{1.56}O_4$ (lo-LNMO), space group $P4_332$ and **(E–F)** ordered $LiNi_{0.44}Mn_{1.56}O_4$ (o-LNMO), space group $P4_332$.

The total population density function, considering all three LNMO phases, is then given by Eq. 5, where SF_1, SF_2 and SF_3 are the scale factors of the three individual phases.

$$pdf(2\theta) = SF_1 \cdot pdf(2\theta)_{hkl,1} + SF_2 \cdot pdf(2\theta)_{hkl,2} + SF_3 \cdot pdf(2\theta)_{hkl,3} \quad (5)$$

Since the structure of LNMO is cubic, the a parameter can be given from e.g., the (111) reflection. That is, the population density of the lattice parameter a for any of the three phases is given by $\mathrm{pdf}(2\theta)_{111}$ and conversion of 2θ to a *via* Bragg's law.

3 Results

3.1 Powder X-ray and neutron diffraction

The crystalline structure and degree of transition metal ordering for the three LNMO samples were determined *via* a combined refinement of a model to X-ray and neutron powder diffraction data. The resulting observed and calculated patterns are shown in Figure 1. In all three samples, no presence of any crystalline impurity phases, e.g., rock-salt, could be observed. The pristine, as-obtained, transition metal disordered sample (d-LNMO) could be well indexed and modeled in the $Fd\bar{3}m$ space group. No presence of superlattice peaks, mainly in the

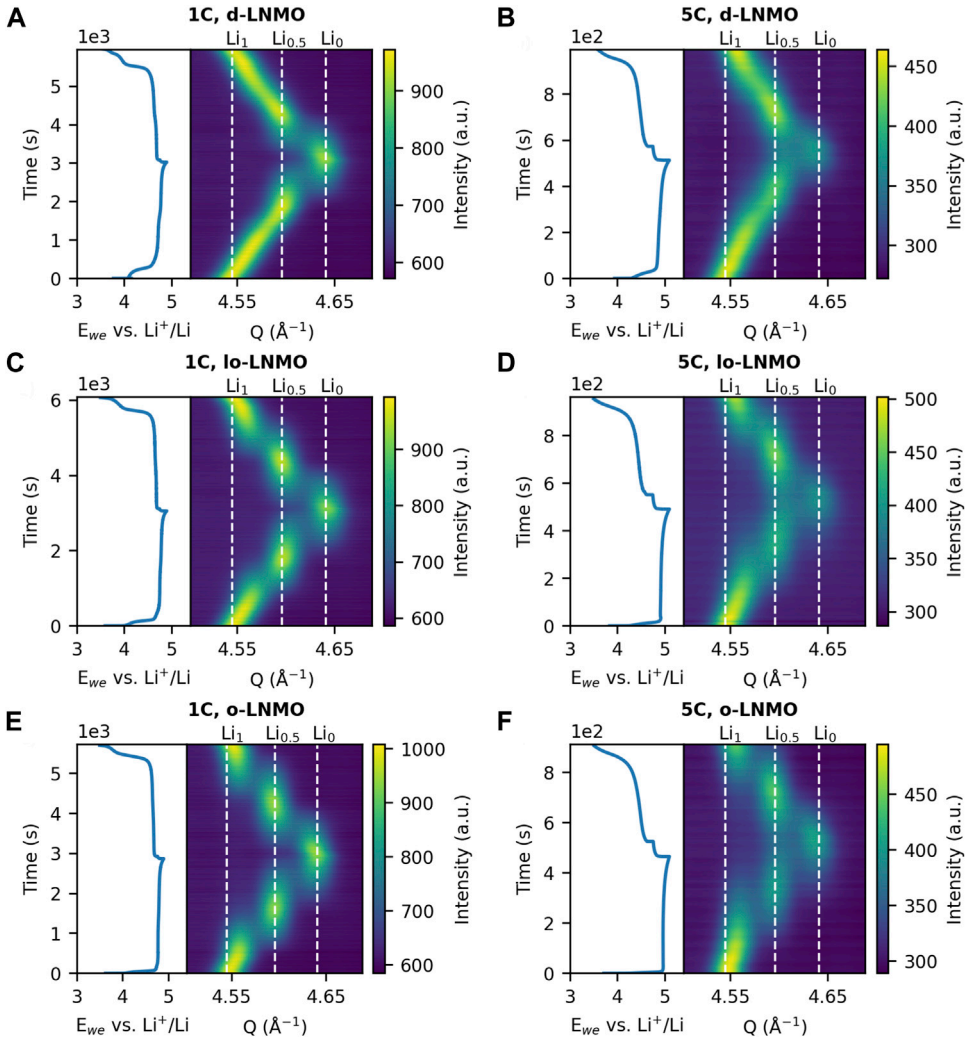

FIGURE 2
Change in Q of the (531) reflection during galvanostatic cycling at 1C and 5C of **(A–B)** disordered LNMO (d-LNMO), **(C–D)** less ordered LNMO (lo-LNMO) and **(E–F)** ordered LNMO (o-LNMO). The peak position of the intermediate phases $LiNi_{0.44}Mn_{1.56}O_4$ (Li_1), $Li_{0.5}Ni_{0.44}Mn_{1.56}O_4$ ($Li_{0.5}$) and $Ni_{0.44}Mn_{1.56}O_4$ (Li_0) are indicated by the dashed white lines.

neutron diffraction data, could be observed, thus confirming that the sample was near fully disordered. A small hump in the background of the neutron diffraction data in the 1.5–2.0 $Å^{-1}$ Q-range is however present, indicating that nanodomains of local ordering could be present in the sample (Kim et al., 2014). The refined occupancies of Ni and Mn on the 16*d* Wyckoff position were 0.2189 (15) and 0.7811 (15), respectively, thus indicating a slightly Mn-rich composition of the sample, i.e., $LiNi_{0.44}Mn_{1.56}O_4$. The two remaining samples exhibited ordering between Ni and Mn, manifested by the presence of additional superlattice peaks in the neutron diffraction data, as compared to the disordered sample. Both ordered samples could be indexed and modeled in the $P4_332$ space group. The degree of Ni and Mn ordering in these two samples was determined from the refined Ni occupancy at the 4*b* Wyckoff position, which is preferably occupied by Ni in the transition metal ordered form of LNMO. Given the slightly Mn-rich nature of the samples, 100% ordering was defined as all available Ni occupying the 4*b* position, which in this case would result in an occupancy of 0.8756. The degree of ordering for the two samples was determined from Rietveld refinement to 99.5% and 87.3% ordering respectively, resulting in a near fully ordered (o-LNMO) and slightly less ordered (lo-LNMO) sample. Further structural details, obtained from Rietveld refinements, of the LNMO samples are given in the Supplementary Tables S1–S3.

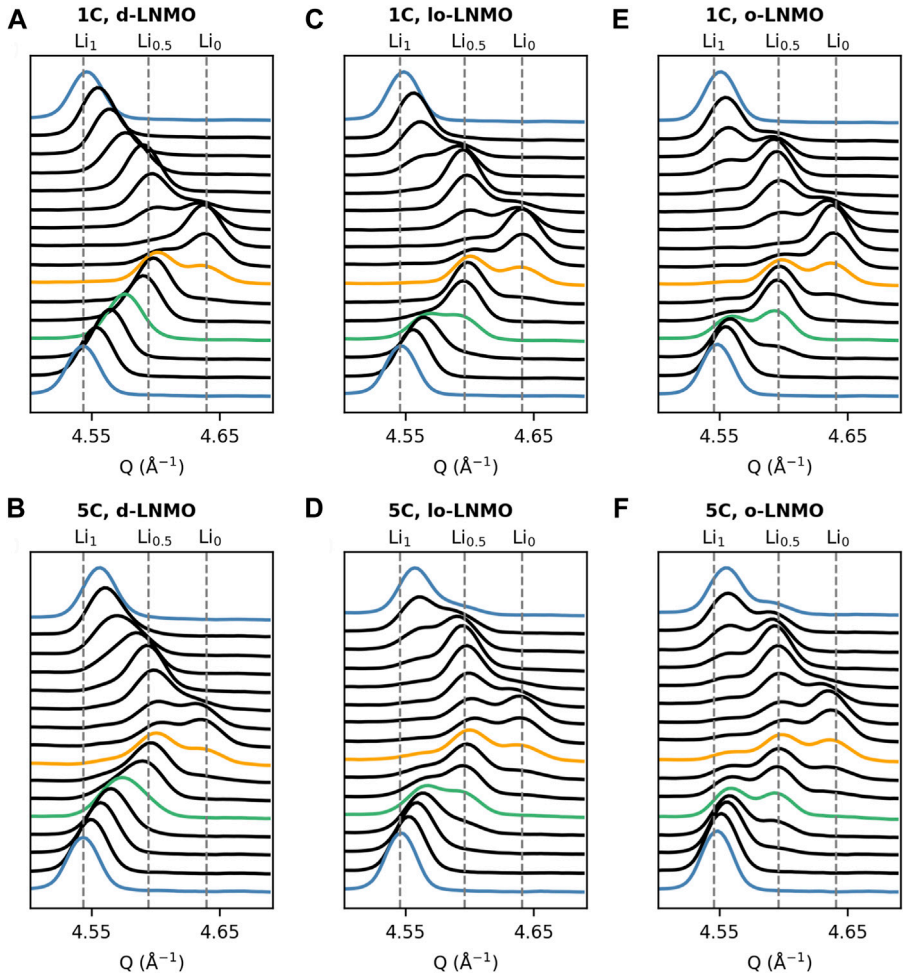

FIGURE 3
Plot of individual X-ray diffraction patterns in the region of the (531) reflection during galvanostatic cycling at 1C and 5C for **(A–B)** disordered LNMO (d-LNMO), **(C–D)** less ordered LNMO (lo-LNMO) and **(E–F)** ordered LNMO (o-LNMO). Patterns at beginning of charge and end of discharge are highlighted as blue. Patterns at a charge capacity of roughly 50 and 100 mAh g^{-1} (corresponding to ≈ 1/3 and 2/3 SOC) are highlighted as green and yellow respectively.

3.2 *Operando* X-ray diffraction

The results of the *operando* XRD measurements are summarized in Figure 2, where the change in Q of the (531) reflection for the three LNMO samples at cycling rates 1C and 5C is shown. As seen in Figure 2, the disordered LNMO sample exhibited, as expected, a solid solution-reaction for the composition $Li_{1-\delta}Ni_{0.44}Mn_{1.56}O_4$ (where typically, $0 \leq \delta \leq 0.5$), indicated by a continuous shift in Q during (dis)charge. The two-phase reaction between $Li_{1-\delta}Ni_{0.44}Mn_{1.56}O_4$ ($\delta \approx 0.5$) and $Ni_{0.44}Mn_{1.56}O_4$ (Li_0, Phase III) then follows, indicated by a discontinuity in the shift of the (531) reflection between the two end members. In the ordered samples, the two separate two-phase reactions between $LiNi_{0.44}Mn_{1.56}O_4$ (Li_1, Phase I) and $Li_{0.5}Ni_{0.44}Mn_{1.56}O_4$ ($Li_{0.5}$, Phase II), and Phase II and Phase III can be identified respectively. Interestingly though, in the less ordered sample, the Phase I reflection appears to extend towards higher Q values, as compared to the fully ordered sample. This becomes more evident when comparing the individual diffraction patterns of the two samples in this region (highlighted as green), as shown in Figure 3. A larger shift in Q would indicate the appearance of a possible solid solution of the Li-rich Phase I, i.e., $Li_{1-\delta'}Ni_{0.44}Mn_{1.56}O_4$ ($0 < \delta' < 0.5$), in the less ordered LNMO sample and a resulting decreased miscibility gap between Phase I and Phase II. When comparing the results between the two cycling rates, one general observation for all three samples can be made. At 5C, less scattering intensity is allocated at the center of the individual reflections, especially in the regions of co-existing phases, hinting toward a possible broadening of the diffraction peaks in all three samples. This broadening can be more clearly observed by studying the individual

diffraction patterns as presented in Figure 3. Here peak broadening appears in all samples at 5C and is especially evident in the patterns where two or more phases co-exist, highlighted as green ($C_{charge} \approx$ 50 mAh g^{-1}, 1/3 SOC) and orange ($C_{charge} \approx$ 100 mAh g^{-1}, 2/3 SOC) in Figure 3. Also, when comparing the peak shape of the Li-rich Phase I at beginning of charge and end of discharge (blue), the broadening is not just symmetric, but rather asymmetric toward higher Q values. Given that the instrumental contribution to the peak profile was determined and then kept fixed, any additional observed broadening originates from the sample (Cheary et al., 2004). Further, since the broadening exhibits asymmetry this must be due to strain and/or compositional variations and not only changes in the crystallite size (Warren, 1990; Liu et al., 2014; Strobridge et al., 2016). Also, compositional variations within individual crystallites due to reaction inhomogeneity can be ruled out when considering the reported high Li-ion diffusivity ($1.41–8.25 \cdot 10^{-9}$ cm^2 s^{-1}) of LNMO (Ma et al., 2010), in combination with the particle size (≈ 5 μm) and applied cycling rates here. To further illustrate this broadening, a fit from Rietveld refinement of the ordered LNMO sample at the co-existence of Phase I, Phase II and Phase III during cycling at 5C (the orange pattern in Figure 3F) is shown in Supplementary Figure S1. When no additional broadening is added, as compared to the refined peak profile on start of charge, the peak profile is clearly too narrow. When adding a combination of symmetrical and asymmetrical broadening, in this case a Gaussian, symmetric broadening from strain and an asymmetrical exponential function, the fit was significantly improved. Due to the physical differences in how symmetrical broadening occurs from strain and size, the respective broadening will vary differently with the scattering angle 2θ. Advanced analysis to separate these contributions, such as the Warren-Averbach Fourier analysis (Warren, 1990) can be undertaken, however, a more straight-forward method is to empirically fit the broadening using either a strain or size dependent model and comparing the two. Here, adding size-modeled broadening to the peak profile routinely gave a worse fit compared to a strain-modeled broadening, as shown in Supplementary Figure S2. As such, we can infer that the broadening occurring here is a product of strain and/or compositional variations within individual crystallites, causing a variation in lattice parameters in the sample. To further investigate how the broadening and the distribution of lattice parameters evolves during cycling of LNMO, a deconvolution of the different sources of broadening is needed and will be dealt with continuing further.

3.3 Quantifying the distribution of lattice parameters and miscibility gap narrowing

To quantify the distribution of lattice parameters, the same approach taken by Liu et al. (2014) was followed by first determining the instrumental broadening contribution and then separating the sample-induced broadening by deconvolution of the peak profile contributors. Broadening from crystallite size was found to be very minor for all samples and could thus be excluded from convolution of the purely sample related peak profile. The sample-induced peak profile was then obtained from a convolution of the symmetric strain and asymmetrical strain/compositional peak profiles, as detailed in the Materials and Methods section. Further, the population density function (pdf) was calculated from the resulting peak profile, depicting the population of lattice parameters for all three intermediate LNMO phases. The resulting evolution of lattice parameter population densities during galvanostatic cycling of d-LNMO, lo-LNMO and o-LNMO are summarized in Figures 4, 5.

3.3.1 Disordered LNMO

The disordered sample exhibits a single-phase solid solution bulk mechanism for the transition between $Li_{1-\delta}Ni_{0.44}Mn_{1.56}O_4$ and Phase II, indicated by a continuous shift in lattice parameter with a narrow distribution at 1C. From the onset of the formation of Phase III, the lattice parameter distribution of Phase II widens both symmetrically, and asymmetrically towards lower values of *a*. The distribution of Phase III also appears wide with slight asymmetry towards higher values of *a*. This observation of asymmetry in the distribution for both phases indicate a distribution of lattice parameters in between the two end members. At 5C there is a clear phase separation between $Li_{1-\delta}Ni_{0.44}Mn_{1.56}O_4$ and Phase II on both charge and discharge. This is likely because of Li-ion diffusion limitations at the electrode level. That is, poor mass transport through the composite electrode, resulting in reaction inhomogeneity between particles closest to the current collector and at the electrolyte interphase. (Strobridge et al., 2015). Interestingly though, at the transition between Phase II and Phase III the miscibility gap is narrowed at 5C, compared to at 1C. This is mainly attributed to an increased asymmetry in the lattice parameter distribution of Phase III.

3.3.2 Ordered LNMO

Looking at the ordered sample, the first-order transition between Phase I and Phase II is accompanied by an asymmetrical broadening toward lower and higher lattice parameters respectively, where the phases extend towards each other. The same is observed for the transition between Phase II and Phase III. For the less ordered sample, this is also the case, however, the miscibility gap here is significantly reduced for both phase transitions as compared to the ordered sample at 1C. The miscibility gap decreases for both samples at 5C, however more so for the transition between Phase I and Phase II. Some hysteretic behavior with regards to phase transitions upon charge and discharge can be observed in both the ordered and less ordered sample. At both 1C and 5C, the less ordered sample exhibits less broadening of Phase II during the transition to Phase

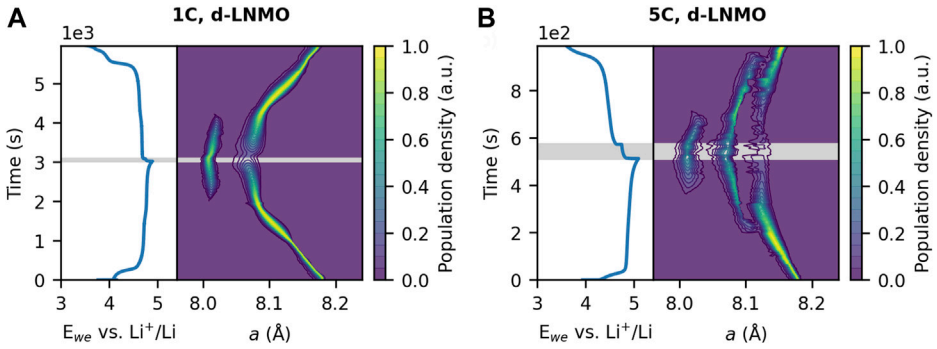

FIGURE 4
Distribution of the lattice parameter *a* during galvanostatic cycling at **(A)** 1C and **(B)** 5C of disordered LNMO (d-LNMO), together with associated voltage profiles respectively. The lowest contour of the population density is drawn at a value of 0.05. The rest period at OCV is indicated by the shaded grey area.

I on discharge compared to on charge. The same observation can be made for the ordered sample at 5C. To further investigate this hysteretic behavior of the two ordered samples and to minimize contributions from reaction inhomogeneity, thinner electrodes with lower mass loading were also studied. These electrodes were cycled at 10C and the resulting lattice parameter distributions are displayed in Figures 5C,F. For both samples the miscibility gap is further decreased compared to at 5C. Also, the hysteretic behavior is gone for both samples, except for the transition between Phase II and Phase III in the ordered sample, where the miscibility gap is bigger between the two phases on discharge, compared to on charge. As a final remark it is also worth noting here that during the rest period at OCV the miscibility gap between Phase II and Phase III increases for the ordered sample.

4 Discussion

During electrochemical cycling of the active cathode material in a composite battery electrode, the individual crystallites may undergo different mechanisms of (de)lithiation which can contribute differently to the observed diffraction peak profile. Broadening from a decrease in the crystallite size, i.e., coherence length, may result from a bulk two-phase reaction, where two phases co-exist within single crystallites (Figure 6A) with a moving phase transition front. Such a decrease in the coherence length will produce a symmetric broadening of the diffracted peaks. Note that this mechanism differs from the domino-cascade model where the phase transition is fast within individual particles, resulting in single-phase crystallites. Broadening from strain and compositional variations may be expressed in similar ways in the peak profile, but their physical origin is different. Strain broadening, or rather microstrain broadening, may arise from a situation similar to the bulk two-phase mechanism, but where there is coherency at the interphase between the two phases (Figure 6B). This results in a distortion of the lattice on both sides of the interphase and a reduction in strain which manifest as an asymmetric broadening of the peak profile (Liu et al., 2014). If the nucleating phase is in minority, it will distort and experience a larger strain relative to the parent phase, resulting in asymmetric broadening of mainly the peak associated with the nucleating phase (Ravnsbæk et al., 2014; Strobridge et al., 2016) (Figure 6D). It should be noted here that the orientation of the interphase within single crystallites may differ from the illustration given in Figure 6, especially if there exist a strong core-shell Li-ion gradient or if the Li-ion diffusion is favored in certain crystallographic directions. However, considering the microstructure of the LNMO samples here, with primary particles of a size ≈ 1 µm (Supplementary Figure S3), in combination with a relatively fast Li-ion diffusion in LNMO (Ma et al., 2010), individual crystallites are not expected to experience a significant core-shell Li-ion gradient. Broadening from compositional variations can occur during high-rate induced solid solution reactions within individual crystallites (Figure 6C) and has been shown to occur in $LiFePO_4$ (Liu et al., 2014; Zhang et al., 2014). In LFP, a solid solution was induced by an overpotential (Malik et al., 2013), resulting in a distribution of crystallites with various lattice parameters, manifested as a mainly asymmetric broadening of the peak profile. Since both the formation of a coherent interphase and a rate-induced solid solution generates an asymmetric peak profile, distinguishing which mechanism is occurring based solely on peak profile analysis is not trivial. However, how the broadening occurs in relation to the evolution of the individual phases involved can provide some indications to which mechanism is more probable. As such, this will be further discussed for the obtained lattice parameter distributions of the three LNMO samples.

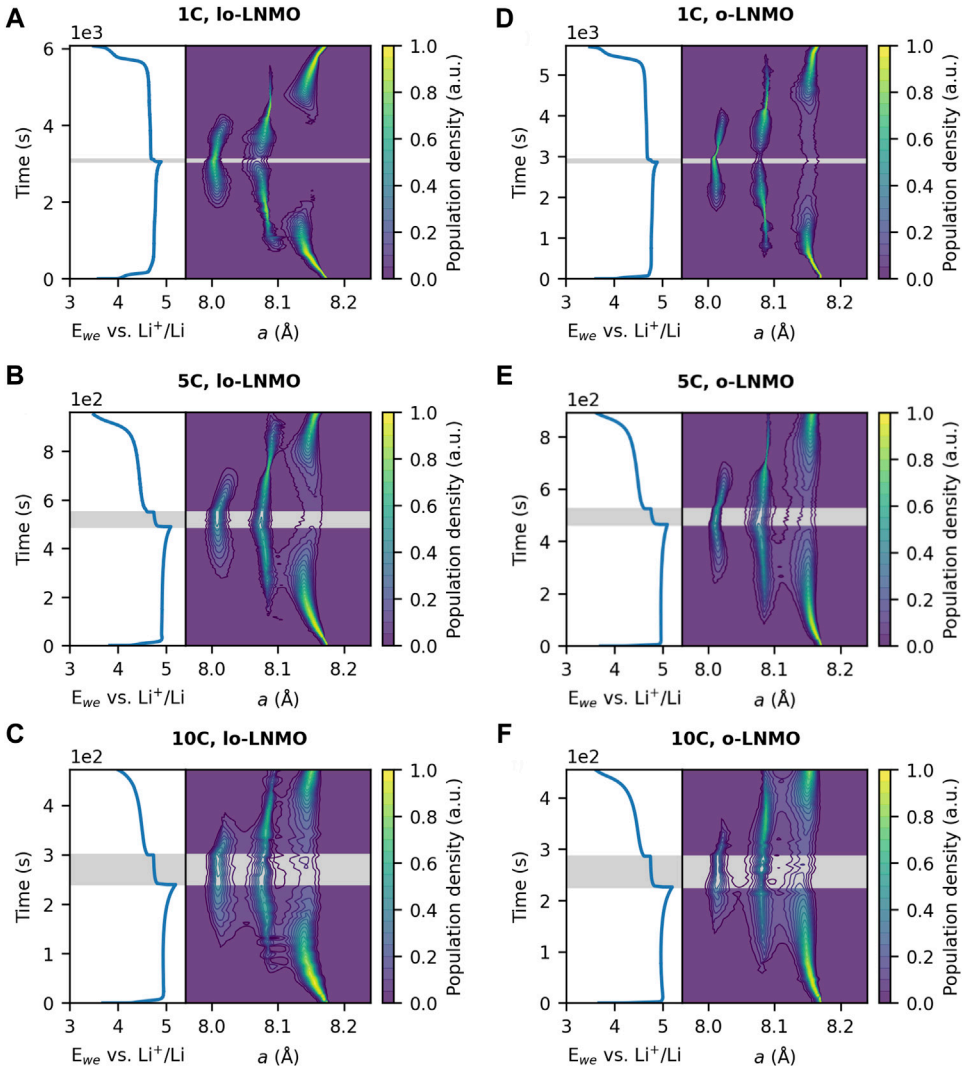

FIGURE 5
Distribution of the lattice parameter *a* during galvanostatic cycling at 1C, 5C and 10C, together with associated voltage profiles respectively, of **(A–C)** less ordered LNMO (lo-LNMO) and **(D–F)** ordered LNMO (o-LNMO). The lowest contour of the population density is drawn at a value of 0.05. The rest period at OCV is indicated by the shaded grey area.

For disordered LNMO, the observed extension of Phase II and Phase III toward each other can be expected assuming a phase transition involving a coherent interphase, as was shown to occur by Komatsu et al. (2015) For a coherent interphase (Figure 6B), broadening should only start to appear when two phases co-exist within a single particle, since a requirement for an interphase to exist is the simultaneous presence of two phases. For both Co- and Mn-substituted $LiFePO_4$, where a coherent interphase was identified as the mechanism for the two-phase transition, an initial lattice distortion of the nucleating phase was found (Ravnsbæk et al., 2014; Strobridge et al., 2016). Such an observation could not be made here, however, the effect in $LiMn_{0.4}Fe_{0.6}PO_4$ was found to diminish significantly at a particle size of ~106 nm (Ravnsbæk et al., 2014). Given the micron-sized particles of LNMO in this study, such an effect is considered to be negligible. Looking at the effect of an increased rate, the overall decrease in the miscibility gap can partly be attributed to the increased number of particles reacting at a single moment in time under higher current densities. Another possible contributor to the decreased miscibility gap is the rate-limiting step in LNMO during phase transitions, which is the rearrangement of chemical bonds at the interphase (Komatsu et al., 2015; Takahashi et al., 2016). The relatively slow rearrangement of these bonds results in the movement speed of the interphase becoming kinetically limiting at high rates (Komatsu et al., 2015). As the

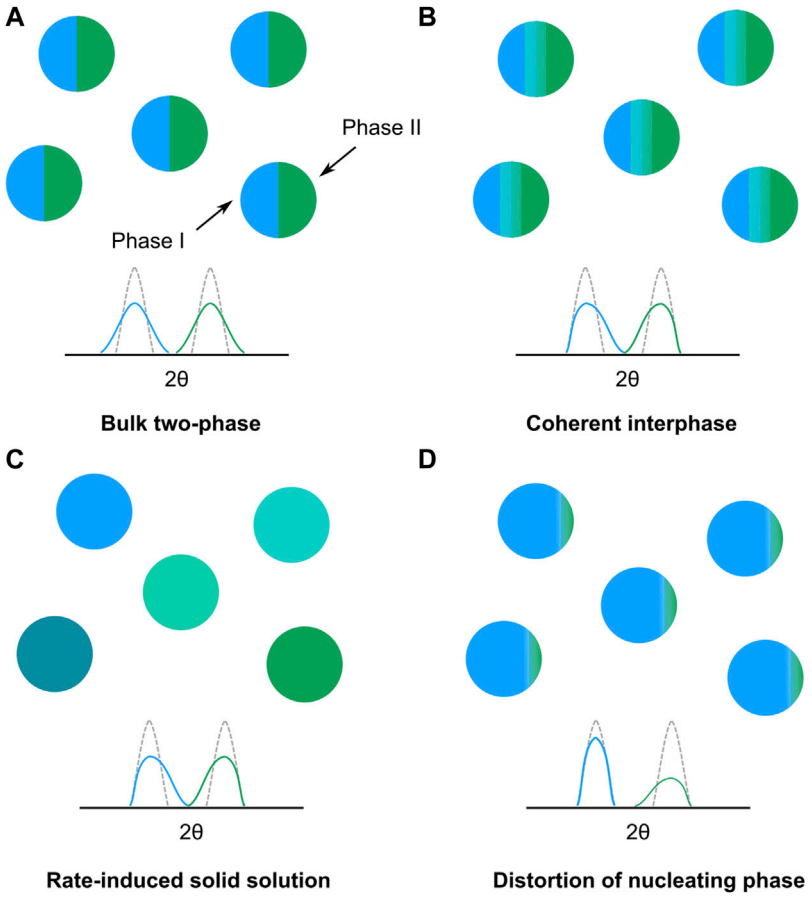

FIGURE 6
Illustration of different phase transition mechanisms during (de)lithiation and their qualitative impact on the observed diffraction peak profiles; **(A)** bulk two-phase mechanism, **(B)** two-phase mechanism with coherent interface, **(C)** rate-induced solid solution in individual crystallites and **(D)** distortion of a nucleating phase.

movement of the interphase becomes rate-limiting, a kinetically more favorable solid solution can be induced, resulting in an increased length of the coherent interphase. The increased length of the interphase results in an increase of the population of intermediate lattice parameters and ultimately a narrowing of the miscibility gap between the two phases. If the rate becomes great enough, the interphase could span the length of the particle, forming a non-equilibrium solid solution following the mechanism depicted in Figure 6C. A solid solution reaction for the transition between Phase II and Phase III in LNMO has been predicted at elevated temperatures from computational work (Lee and Persson, 2013). As such, it is not surprising that an overpotential could promote the formation of a solid solution reaction as suggested by the observations made here.

For both of the ordered samples, the phases involved in both first-order transitions extended towards each other during co-existence of two phases. This would indicate, as mentioned above, the formation of a coherent interphase. However, the smaller miscibility gap for the less ordered sample would imply that the coherent interphase is of a greater length compared to the ordered sample, possibly enabled by a lower energy barrier for formation of a solid solution. In the computational work performed by Lee and Persson (2013), the temperature for formation of a solid solution was significantly lowered, especially in the Phase I and Phase II region, already at a Ni deviation level at the 4*a* position of 1/16, corresponding to a 91.7% degree of ordering. Our results confirm this computational prediction where miscibility gap narrowing is observed already for 87.3% degree of ordering. The reduction of the miscibility gap with increasing current density was larger in both ordered samples for the transition between Phase I and Phase II compared to the transition between Phase II and Phase III. This can be attributed to the lower energy barrier for formation of a solid solution in this compositional region (Lee

and Persson, 2013). As for the disordered sample, the overall decrease in the miscibility gap between Phase II and Phase III with increased current density can be understood from a combination of more particles being active and the rate of (de)lithiation exceeding the movement speed of the interphase at the phase transition. The hysteretic behavior shown for the two ordered samples, in regards to the phase transition between Phase I and Phase II, can be attributed to the differences in activation barriers of this transition upon charge and discharge. The transition from Phase I to Phase II have been shown to be kinetically faster than the transition between Phase II and Phase III (Arai et al., 2013; Takahashi et al., 2014; Takahashi et al., 2016), as a result of their respective activation barriers, leading to the immediate formation of Phase I as soon as the transition to Phase II is completed. Interestingly though, while Phase II shows little to no asymmetric broadening toward Phase I, the lattice parameter distribution of Phase I still extend toward Phase II. This observation would suggest a mechanism where the nucleating Phase I experiences a larger distortion as it starts to form in the pre-existing Phase II, as depicted in Figure 6D. The full conversion from Phase II to Phase I then follows quickly, due to the favorable kinetics of this transition. As a result, the metastable coherent interphase is not maintained (or at least travels too fast to be observed here *via* diffraction) in the same way as it is on charge, leading to the hysteretic behavior. At increasing current density, the hysteretic behavior is less apparent for both the less ordered and the ordered sample, suggesting that the increased rate of lithiation can compete with the faster kinetics of the phase transition, leading to the observation of the metastable coherent interphase again. However, at a similar current density, e.g., 5C, the hysteretic behavior is clearly visible for the ordered sample while diminished for the less ordered sample. This would suggest that the activation barriers vary with the degree of ordering in the material, especially also when comparing to the disordered sample, which does not exhibit any hysteresis.

Looking further into the perceived (in)stability during the rest at OCV for all three samples, an interesting observation can be made. The decreased miscibility gap seems to be maintained, to some degree, during the rest period at OCV in all cases, also at 10C for the ordered sample. Thus, the coherent interphase between the co-existing Phase II and Phase III, and the solid solution region spanning across it, appears to be at least metastable. This observation is in agreement with previous findings on stable room temperature solid solutions in LNMO, where the solid solution formed from a two-phase mixture at elevated temperature was stable also upon cooling down to ambient temperature (Saravanan et al., 2015). The formed interphase, and solid solutions, appear as such to be somewhat stable within the particles, providing a pathway for further solid solution reactions to occur in the material. For the ordered sample, the decrease in the miscibility gap during rest following charge at 10C suggests that Li redistributes in the material, resulting in an interphase of shorter length. Such an observation is not completely surprising, given a greater energy barrier for the formation of a solid solution in this compositional region for a fully ordered configuration in LNMO (Lee and Persson, 2013).

As a final remark, it should be stated that due to diffraction being a bulk sensitive technique, the results observed here reflect that. It is possible that multiple mechanisms may occur on the local, i.e., crystallite and particle, scale. Locally greater than average overpotentials may lead to the formation of a coherent interphase spanning across the crystallite/particle leading to a phase transition like the high-rate induced non-equilibrium solid solution in Figure 6C. Also, size-effects seen for LFP, such as differences in Li solubility and the ability to host a stable interphase (Ravnsbæk et al., 2014; Zhang et al., 2014), may also be present here although not visible in the diffracted pattern due to the low volume fraction of smaller particles. Size effects can however be expected to remain limited in the samples studied here, due to the relative size homogeneity for both the primary and secondary particles, as depicted from SEM imaging (Supplementary Figure S3). Further, since broadening from crystallite size was found to be very minor in all samples, the overall contribution from smaller crystallites to the observed peak profiles should remain small, also during electrochemical cycling. How the reaction mechanism varies on the local scale could be better probed by e.g., microbeam X-ray diffraction.

5 Conclusion

The reaction mechanism and changes in the miscibility gap as a function of rate and degree of transition metal ordering has been studied in LNMO utilizing *operando* X-ray diffraction. Detailed peak profile analysis and deconvolution was undertaken to separate broadening contributions and to quantify the distribution of lattice parameters in the material during cycling. Asymmetric broadening in the peak profiles was observed during two-phase transitions, indicating that domains within the active material populate lattice parameters that lie in between the equilibrium intermediate phases in LNMO. The suggested bulk mechanism for this is the formation of a coherent interphase between intermediate phases with an associated solid solution region across the length of the interphase. Disordered LNMO was found to undergo a single bulk-phase solid solution transition for the composition $Li_{1-\delta}Ni_{0.44}Mn_{1.56}O_4$ ($0 \leq \delta \leq 0.5$), followed by a two-phase transition with a coherent interphase between intermediates $Li_{0.5}Ni_{0.44}Mn_{1.56}O_4$ and $Ni_{0.44}Mn_{1.56}O_4$ at both 1C and 5C. At increased current density, the coherent interphase appears to be of greater length with an extended Li compositional range of the solid solution region across the interphase, indicated by a decrease in the miscibility gap. Both

the ordered and the less ordered sample exhibited two separate two-phase transitions with a coherent interphase between the intermediate phases $LiNi_{0.44}Mn_{1.56}O_4$, $Li_{0.5}Ni_{0.44}Mn_{1.56}O_4$ and $LiNi_{0.44}Mn_{1.56}O_4$ upon charge. Upon discharge, some hysteretic behavior was observed in the phase transition between the $Li_{0.5}Ni_{0.44}Mn_{1.56}O_4$ and $LiNi_{0.44}Mn_{1.56}O_4$ phases compared to on charge, where the former phase exhibited less broadening. This was attributed to the lower activation barrier of this phase transition on discharge, leading to an initial distortion of the nucleating $LiNi_{0.44}Mn_{1.56}O_4$ phase followed by a fast conversion of the $Li_{0.5}Ni_{0.44}Mn_{1.56}O_4$ phase. For the less ordered sample, the decrease in the miscibility gap is greater compared to the ordered sample, and the solid solution region across the interphase appear to span a greater Li compositional range. The miscibility gap decreased for both of the ordered samples at increased cycling rates, similar to the disordered sample, however more so for the transition between the intermediate phases $LiNi_{0.44}Mn_{1.56}O_4$ and $Li_{0.5}Ni_{0.44}Mn_{1.56}O_4$. As such, for all three samples the miscibility gap decreased with elevated current densities, showing that solid solution behavior can be induced when the movement speed of the interphase at the phase transition becomes rate-limiting. This effect was greater with more disorder, highlighting that introducing disorder in the material, even to smaller extents, can both promote the formation and improve the stability of solid solutions in LNMO. The results indicate that the degree of transition metal ordering within the material is especially important for obtaining a material with low miscibility gaps between end member phases. Further introduction of disorder *via* off-stoichiometric compositions, high temperature synthesis or other cation substitutions could thus be beneficial for obtaining true solid solution reactions and improving the rate capability of the material.

Data availability statement

The raw data supporting the conclusions of this article will be made available by the authors, without undue reservation.

Author contributions

WB framed the original research idea, defined the experimental direction, helped with planning, supervised the project and revised the manuscript. OG designed the synchrotron experiment, constructed all batteries, performed all analysis and plotting and wrote the manuscript. AS performed the entire synchrotron experiment independently and revised the final manuscript.

Funding

The authors gratefully acknowledge funding from the Strategic Research Area StandUp for Energy, Swedish Energy Agency (grant no. 48678 1) and Batteries Sweden (BASE).

Acknowledgments

We acknowledge DESY (Hamburg, Germany), a member of the Helmholtz Association HGF, for the provision of experimental facilities. Parts of this research were carried out at Petra III. Beamtime was allocated on P02.1 for proposal I-20191244. We would also like to acknowledge ANSTO (Sydney, Australia) for allocation of beamtime related to proposal 13421 and Maxim Avdeev for carrying out neutron diffraction measurements. Haldor Topsoe is acknowledged for providing $LiNi_{0.5}Mn_{1.5}O_4$ for this study. Ida Nielsen is acknowledged for carrying out SEM imaging.

Conflict of interest

The authors declare that the research was conducted in the absence of any commercial or financial relationships that could be construed as a potential conflict of interest.

Publisher's note

Supplementary material

The Supplementary Material for this article can be found online at: https://www.frontiersin.org/articles/10.3389/fenrg.2022.1056260/full#supplementary-material

References

Arai, H., Sato, K., Orikasa, Y., Murayama, H., Takahashi, I., Koyama, Y., et al. (2013). Phase transition kinetics of $LiNi_{0.5}Mn_{1.5}O_4$ electrodes studied by *in situ* X-ray absorption near-edge structure and X-ray diffraction analysis. *J. Mat. Chem. A Mat.* 1 (35), 10442–10449. doi:10.1039/C3TA11637A

Avdeev, M., and Hester, J. R. (2018). Echidna: A decade of high-resolution neutron powder diffraction at OPAL. *J. Appl. Crystallogr.* 51(6), 1597–1604. doi:10.1107/S1600576718014048

Cheary, R. W., Coelho, A. A., and Cline, J. P. (2004). Fundamental parameters line profile fitting in laboratory diffractometers. *J. Res. Natl. Inst. Stand. Technol.* 109 (1), 1–25. doi:10.6028/jres.109.002

Chen, G., Song, X., and Richardson, T. J. (2007). Metastable solid-solution phases in the $LiFePO_4/FePO_4$ system. *J. Electrochem. Soc.* 154 (7), A627. doi:10.1149/1.2732189

Coelho, A. (2018). TOPAS and TOPAS-academic: An optimization program integrating computer algebra and crystallographic objects written in C++. *J. Appl. Crystallogr.* 51 (1), 210–218. doi:10.1107/S1600576718000183

Delacourt, C., Poizot, P., Tarascon, J.-M., and Masquelier, C. (2005). The existence of a temperature-driven solid solution in $LixFePO_4$ for $0 \leq x \leq 1$. *Nat. Mat.* 4, 254–260. doi:10.1038/nmat1335

Dippel, A.-C., Liermann, H.-P., Delitz, J. T., Walter, P., Schulte-Schrepping, H., Seeck, O. H., et al. (2015). Beamline P02.1 at PETRA III for high-resolution and high-energy powder diffraction. *J. Synchrotron Radiat.* 22(3), 675–687. doi:10.1107/S1600577515002222

Gustafsson, O., Schökel, A., and Brant, W. R. (2021). Design and operation of an operando synchrotron diffraction cell enabling fast cycling of battery materials. *Batter. Supercaps* 4, 1599–1604. doi:10.1002/batt.202100126

Kim, J.-H., Huq, A., Chi, M., Pieczonka, N. P. W., Lee, E., Bridges, C. A., et al. (2014). Integrated nano-domains of disordered and ordered spinel phases in $LiNi_{0.5}Mn_{1.5}O_4$ for Li-ion batteries. *Chem. Mat.* 26 (15), 4377–4386. doi:10.1021/cm501203r

Kim, J. H., Myung, S. T., Yoon, C. S., Kang, S. G., and Sun, Y. K. (2004). Comparative study of $LiNi_{0.5}Mn_{1.5}O_4$-δ and $LiNi_{0.5}Mn_{1.5}O_4$ cathodes having two crystallographic structures: Fd3̄m and P4332. *Chem. Mat.* 16 (5), 906–914. doi:10.1021/cm035050s

Komatsu, H., Arai, H., Koyama, Y., Sato, K., Kato, T., Yoshida, R., et al. (2015). Solid solution domains at phase transition front of $LixNi_{0.5}Mn_{1.5}O_4$. *Adv. Energy Mat.* 5 (17), 1500638. doi:10.1002/aenm.201500638

Lee, E., and Persson, K. A. (2013). Solid-solution Li intercalation as a function of cation order/disorder in the high-voltage $LixNi_{0.5}Mn_{1.5}O_4$ spinel. *Chem. Mat.* 25 (14), 2885–2889. doi:10.1021/cm4014738

Liu, H., Strobridge, F. C., Borkiewicz, O. J., Wiaderek, K. M., Chapman, K. W., Chupas, P. J., et al. (2014). Batteries. Capturing metastable structures during high-rate cycling of $LiFePO_4$ nanoparticle electrodes. *Science* 344 (6191), 1252817. doi:10.1126/science.1252817

Ma, X., Kang, B., and Ceder, G. (2010). High rate micron-sized ordered $LiNi_{0.5}Mn_{1.5}O_4$. *J. Electrochem. Soc.* 157 (8), A925–A931. doi:10.1149/1.3439678

Malik, R., Abdellahi, A., and Ceder, G. (2013). A critical review of the Li insertion mechanisms in $LiFePO_4$ electrodes. *J. Electrochem. Soc.* 160 (5), A3179–A3197. doi:10.1149/2.029305jes

Ravnsbæk, D. B., Xiang, K., Xing, W., Borkiewicz, O. J., Wiaderek, K. M., Gionet, P., et al. (2014). Extended solid solutions and coherent transformations in nanoscale olivine cathodes. *Nano Lett.* 14 (3), 1484–1491. doi:10.1021/nl404679t

Saravanan, K., Jarry, A., Kostecki, R., and Chen, G. (2015). A study of room-temperature $LixMn_{1.5}Ni_{0.5}O_4$ solid solutions. *Sci. Rep.* 5, 8027. doi:10.1038/srep08027

Strobridge, F. C., Liu, H., Leskes, M., Borkiewicz, O. J., Wiaderek, K. M., Chupas, P. J., et al. (2016). Unraveling the complex delithiation mechanisms of olivine-type cathode materials, $LiFe_xCo_{1-x}PO_4$. *Chem. Mat.* 28 (11), 3676–3690. doi:10.1021/acs.chemmater.6b00319

Strobridge, F. C., Orvananos, B., Croft, M., Yu, H.-C., Robert, R., Liu, H., et al. (2015). Mapping the inhomogeneous electrochemical reaction through porous $LiFePO_4$-electrodes in a standard coin cell battery. *Chem. Mat.* 27 (7), 2374–2386. doi:10.1021/cm504317a

Takahashi, I., Arai, H., Murayama, H., Sato, K., Komatsu, H., Tanida, H., et al. (2016). Phase transition kinetics of $LiNi_{0.5}Mn_{1.5}O_4$ analyzed by temperature-controlled operando X-ray absorption spectroscopy. *Phys. Chem. Chem. Phys.* 18 (3), 1897–1904. doi:10.1039/C5CP05535K

Takahashi, I., Murayama, H., Sato, K., Naka, T., Kitada, K., Fukuda, K., et al. (2014). Kinetically asymmetric charge and discharge behavior of $LiNi_{0.5}Mn_{1.5}O_4$ at low temperature observed by *in situ* X-ray diffraction. *J. Mat. Chem. A* 2 (37), 15414–15419. doi:10.1039/C4TA01130A

Warren, B. E. (1990). *X-ray diffraction*. New York: Dover.

Zhang, X., van Hulzen, M., Singh, D. P., Brownrigg, A., Wright, J. P., van Dijk, N. H., et al. (2014). Rate-induced solubility and suppression of the first-order phase transition in olivine $LiFePO_4$. *Nano Lett.* 14 (5), 2279–2285. doi:10.1021/nl404285y

frontiers in Energy Research

ORIGINAL RESEARCH
published: 10 September 2018
doi: 10.3389/fenrg.2018.00089

Effect of AlF_3-Coated $Li_4Ti_5O_{12}$ on the Performance and Function of the $LiNi_{0.5}Mn_{1.5}O_4$||$Li_4Ti_5O_{12}$ Full Battery—An *in-operando* Neutron Powder Diffraction Study

Gemeng Liang[1], Anoop Somanathan Pillai[1], Vanessa K. Peterson[1,2], Kuan-Yu Ko[3], Chia-Ming Chang[3], Cheng-Zhang Lu[3], Chia-Erh Liu[3], Shih-Chieh Liao[3], Jin-Ming Chen[3], Zaiping Guo[1] and Wei Kong Pang[1]**

[1] Faculty of Engineering, Institute for Superconducting & Electronic Materials, University of Wollongong, Wollongong, NSW, Australia, [2] Australian Centre for Neutron Scattering, Australian Nuclear Science and Technology Organization, Sydney, NSW, Australia, [3] Department of Nanomaterials for Energy Storage, Material & Chemical Research Laboratory, Industrial Technology Research Institute, Hsinchu, Taiwan

OPEN ACCESS

Edited by:
Verónica Palomares, University of the Basque Country, Spain

Reviewed by:
Stephen Hull, Science and Technology Facilities Council, United Kingdom
Jordi Jacas Biendicho, Institut de Recerca de l'Energia de Catalunya, Spain

***Correspondence:**
Vanessa K. Peterson
vanessa.peterson@ansto.gov.au
Wei Kong Pang
wkpang@uow.edu.au

Specialty section:
This article was submitted to Energy Storage, a section of the journal Frontiers in Energy Research

Received: 01 April 2018
Accepted: 17 August 2018
Published: 10 September 2018

Citation:
Liang G, Pillai AS, Peterson VK, Ko K-Y, Chang C-M, Lu C-Z, Liu C-E, Liao S-C, Chen J-M, Guo Z and Pang WK (2018) Effect of AlF_3-Coated $Li_4Ti_5O_{12}$ on the Performance and Function of the $LiNi_{0.5}Mn_{1.5}O_4$||$Li_4Ti_5O_{12}$ Full Battery—An in-operando Neutron Powder Diffraction Study. Front. Energy Res. 6:89. doi: 10.3389/fenrg.2018.00089

The $LiNi_{0.5}Mn_{1.5}O_4$ ||$Li_4Ti_5O_{12}$ (LMNO||LTO) battery possesses a relatively-high energy density and cycle performance, with further enhancement possible by application of an AlF_3 coating on the LTO electrode particles. We measure the performance enhancement to the LMNO||LTO battery achieved by a AlF_3 coating on the LTO particles through electrochemical testing and use *in-operando* neutron powder diffraction to study the changes to the evolution of the bulk crystal structure during battery cycling. We find that the AlF_3 coating along with parasitic Al doping slightly increases capacity and greatly increases rate capability of the LTO electrode, as well as significantly reducing capacity loss on cycling, facilitating a gradual increase in capacity during the first 50 cycles. Neutron powder diffraction reveals a structural response of the LTO and LNMO electrodes consistent with a greater availability of lithium in the battery containing AlF_3-coated LTO. Further, the coating increases the rate of structural response of the LNMO electrode during charge, suggesting faster delithiation, and enhanced Li diffusion. This work demonstrates the importance of studying such battery performance effects within full configuration batteries.

Keywords: lithium ion battery, *in-operando*, neutron powder diffraction, real-time analysis, electrochemistry, protective coating, AlF_3

INTRODUCTION

Lithium ion batteries (LIBs) are the main choice of power source for portable electronic devices, including emerging electric vehicle (EV) and hybrid electric vehicle (HEV) technologies, as a result of their low cost, high energy/power density, and relatively long cycle life (Wang and Cao, 2008; Choi and Aurbach, 2016; Li et al., 2017a,b). The first commercial LIBs used lithium cobalt oxide ($LiCoO_2$) as the positive electrode and graphite as the negative electrode, however, the low energy density of this battery is insufficient to satisfy the demands of developing technology (Su et al., 2014; Li et al., 2017b), stimulating the exploration of novel electrode materials with higher energy/power capabilities than the existing state-of-the-art.

The performance limitation in existing LIB technology is the positive electrode, with new materials possessing both higher capacity and average working voltage required to further improve battery energy densities (Fergus, 2010; Liu et al., 2016). In recent years, layered positive electrode materials related to $LiCoO_2$, such as $LiNi_{1/3}Mn_{1/3}Co_{1/3}O_2$ (NMC) and $LiNi_{0.8}Co_{0.15}Al_{0.05}O_2$ (NCA), have been extensively studied and are now used commercially as a result of their relatively-high capacity (Li et al., 2018). However, these materials possess a relatively-low working potential (∼3.7 V vs. Li/Li^+) and suffer from severe voltage decay, limiting their application (Gu et al., 2012; Zheng et al., 2013). Other positive electrode materials with high voltage such as $LiMn_2O_4$ (4.0 V vs. Li/Li^+) (Kim et al., 2008; Xia et al., 2016), $LiNi_{0.5}Mn_{1.5}O_4$ (LNMO) (∼4.7 V vs. Li/Li^+) (Liu et al., 2016; Ma et al., 2016; Pang et al., 2016), and $LiCoAsO_4$ (4.6 V vs. Li/Li^+) (Arroyo-de Dompablo and Amador, 2006; Satya Kishore and Varadaraju, 2006), have also been studied with the aim of improving LIB performance. The LNMO material is arguably the most promising positive electrode material for the next-generation of high-energy-density LIBs, due to its high working voltage, low fabrication cost, relative environmental friendliness, and reasonable cycle stability (Liu et al., 2016; Pang et al., 2016). Moreover, LNMO possesses a practical capacity of more than 140 mAh g^{-1} and an average working voltage of 4.7 V (vs. Li/Li^+), resulting in an exceptionally high energy density, reaching as high as 650 Wh kg^{-1}, beyond that of most other LIB positive electrode materials such as $LiFePO_4$ at ∼560 Wh kg^{-1}, $LiMn_2O_4$ at ∼480 Wh kg^{-1}, and $LiMn_{1/3}Ni_{1/3}Co_{1/3}O_2$ at ∼510 Wh kg^{-1} (Croy et al., 2014; Pang et al., 2016).

LNMO crystalizes into a cubic structure which can have two different atom arrangements, one being a phase with $P4_332$ space group and the other having $Fd\bar{3}m$ space group symmetry (Ariyoshi et al., 2004; Kim et al., 2004; Santhanam and Rambabu, 2010; Feng et al., 2011; Pang et al., 2014b). Both these phases exhibit similar electrochemical performance, with the $Fd\bar{3}m$ phase being slightly more favorable due to faster Li ion diffusion and high structural stability (Feng et al., 2011), where the $P4_332$ space group phase suffers multiple cubic/cubic two-phase reactions during cycling, resulting in phase segregation and grain boundary movement, limiting the Li diffusion rate.

Positive electrode materials such as LNMO are commonly paired with a carbonaceous negative electrode in a full LIB, but this negative electrode suffers from lithium dendrite growth, especially at high rate, and the formation of a thick solid electrolyte interphase (SEI) at voltage <0.8 V vs. Li/Li^+, further deteriorating rate performance and cycle life (Wang et al., 2001; Zhang, 2006). Another negative electrode commonly paired with LNMO is the so-called "zero-strain" $Li_4Ti_5O_{12}$ (LTO) material, with a plateau at 1.55 V vs. Li/Li^+ and superb structural stability and stable cycle performance (Pang et al., 2014b). Although the working voltage of a LIB containing LTO is reduced a little relative to the carbonaceous negative electrode, the issues associated with lithium dendrite and SEI formation can be effectively avoided, enabling superior cycle life.

Consequently, full LIBs containing LTO counter electrodes have been intensively studied, with the $LiMn_2O_4||Li_4Ti_5O_{12}$ full-cell noted to have good safety and electrochemical performance (Belharouak et al., 2007; Wang et al., 2014). However, a major drawback of the $LiMn_2O_4||Li_4Ti_5O_{12}$ system is its relatively low working voltage of ∼2.5 V, limiting its high-energy application. Alternative LNMO||LTO systems with higher working voltages have been investigated, aiming for a working voltage of ∼3.2 V (Ariyoshi and Ohzuku, 2007; Xiang et al., 2008; Wu et al., 2009; Li et al., 2013; Zhang et al., 2013). Ariyoshi and Ohzuku (2007) first reported a 3 V LNMO||LTO system, expected to be widely used in lead-free accumulators, EVs, and HEVs. A further barrier to achieving high voltage LNMO||LTO is the stability of organic-carbonate-based electrolytes, and Xiang et al. enhanced the operational safety of this electrode combination by using a non-flammable dimethyl methylphosphonate (DMMP) based electrolyte (Xiang et al., 2007).

Nevertheless, even with these advancements, the performance of the LNMO||LTO system remains limited by the cycle life of the spinel positive electrode, where the material undergoes two-phase behavior at higher voltages, and suffers from Jahn-Teller distortion resulting in the dissolution of Mn into the electrolyte (Xiao et al., 2013). To resolve these issues, electrode modifications have been adopted, such as doping LNMO with the aim of avoiding Jahn-Teller distortion and coating the active material particle surface to minimize attack of the hydrofluoric acid produced during electrolyte decomposition (Deng et al., 2014; Kim et al., 2014, 2015). Compared with doping strategies, surface coating is more popular due to its simplicity and high efficiency. AlF_3 is commonly used as protecting layer on electrode particles, avoiding the direct exposure to the electrolyte (Wu et al., 2015) and effectively mitigating against the hydrofluoric acid produced by electrolyte decomposition at high voltage (Zheng et al., 2014; Sun et al., 2015; Zhou et al., 2017), as well as against severe gassing behavior of LTO known to occur during cycling (Li et al., 2014). LNMO and $Li[Li_{0.2}Ni_{0.17}Co_{0.07}Mn_{0.56}]O_2$ coated with AlF_3 exhibit better electrochemical performance (Sun et al., 2015; Wu et al., 2015). However, the majority of research into the effect of AlF_3 coatings on electrode particles focus on the positive electrode, and work studying the modified LTO material in a full-configuration battery is lacking.

In this work, we performed a comparative study to investigate how an AlF_3 coated LTO enhances the electrochemical performance of a LNMO||LTO full-configuration battery using high-resolution and *in-operando* neutron powder diffraction (NPD). NPD has been widely employed to perform mechanistic studies of active electrode materials in LIBs. The nuclear scattering mechanism sometimes results in elemental contrast that is difficult to achieve using X-ray diffraction, such as a high sensitivity to lighter elements (i.e., Li and O) in the presence of heavier elements and to transition metals with a similar number of electrons. For example, the elements in a LNMO||LTO battery, Li, Ni, Mn, O, and Ti, have coherent neutron scattering lengths of −1.9, 10.3, −3.7, 5.8, and −3.4 fm, respectively, making NPD one of the most powerful analytical tools for this study (Pang et al., 2014b, 2017; Zhao et al., 2017). Further, the high penetration depth and non-destructive nature of neutrons, as well as advanced modern detectors and instrumentation, enable the real-time monitoring of structural changes of active electrode materials inside functioning LIBs

(Pang et al., 2014a,b, 2016, 2017). Using NPD, the Li content and location within the LNMO and LTO electrodes can be measured, yielding information that is crucially important to understand the functional mechanism of the LNMO||LTO battery. For example, Zhao et al. (2017) explored the relationship between the Li^+/Ni^{2+} ion exchange rate and electrochemical performance of the $LiNi_xMn_yCo_{1-x-y}O_2$ positive electrode, and our previous work (Pang et al., 2014b, 2017) revealed the structural evolution in detail of LNMO and Li diffusion path within the LTO electrode in a LNMO||LTO full battery using *in-operando* NPD. We note the capability of NPD to examine in detail 18650-standard full-configuration batteries, making the approach of industrial relevance in the analysis of the real-time phase transformation and structural change inside commercial batteries.

Our present NPD study of the AlF_3 coated LTO within a LNMO||LTO full-configuration battery reveals that the AlF_3 coated LTO enhances cycle stability of the battery as well as inducing faster structural response of the LNMO counter electrode during its solid solution behavior during charge.

EXPERIMENTAL DETAILS

LNMO powders were prepared by a co-precipitation method. $NiSO_4{\cdot}6H_2O$ (98%, Sigma Aldrich) and $MnSO_4{\cdot}H_2O$ (98%, Sigma Aldrich) (1:3 mole ratio) were added into distilled water and stirred to obtain a homogenous aqueous solution. The solution was pumped into a reactor at 50°C and the pH was kept at 10.5 by adding NH_4OH aqueous solution (28%, Sigma Aldrich) to obtain the homogenous $Ni_{0.25}Mn_{0.75}(OH)_2$ precursors. These precursors were then thoroughly mixed with lithium carbonate (Li_2CO_3) powders (99%, Sigma Aldrich) and calcined at 750°C for 12 h to obtain LNMO powders.

To synthesize LTO, a sol-gel method was used. Lithium acetate (98%, Sigma Aldrich) and tetrabutyltitanate (98%, Sigma Aldrich) (4:5 mole ratio) were mixed with citric acid (99%, Sigma Aldrich) in ethanol (99.5%, Sigma Aldrich). A homogenous white gel was formed after aging the mixed solution for 3 h. The white gel was then heated at 80°C to obtain an organic precursor and the precursor was further calcined at 800°C for 3 h to yield fine LTO powders.

To prepare AlF_3-modified LTO, ammonium fluoride (99%, Aldrich) and aluminum nitrate nonahydrate (99%, Aldrich) were dissolved in distilled water. LTO powders were immersed into the aluminum nitrate solution and the ammonium fluoride solution was slowly added to achieve a ratio of Al:F of 1:3 where the amount of AlF_3 in the solution corresponded to 10 wt% of LTO. The solution containing the LTO powders was constantly stirred at 80°C for 5 h and then filtered using distilled water. Subsequently, the obtained LTO powders were heated at 400°C for 3 h under flowing nitrogen to avoid the formation of Al_2O_3.

The morphology of LNMO, LTO, and AlF_3-coated LTO were investigated by scanning electron microscopy (SEM) using a JEOL JSM7500 and transmission electron microscopy (TEM) using a 200 kV JEOL 2011. Elemental mapping using energy dispersive spectroscopy (EDS) was performed using a JEOL ARM-200F aberration-corrected transmission electron microscope. The phase and composition of the LNMO, LTO, and AlF_3-coated LTO were also characterized using a combination of laboratory XRPD carried out on a Shimadzu Corporation 6000 X-ray diffractometer equipped with a Cu source and high-resolution NPD performed on the high-resolution neutron powder diffractometer ECHIDNA (Liss et al., 2006) at the Open Pool Australian Light water (OPAL) research reactor at the Australian Nuclear Science and Technology Organization (ANSTO). High-resolution NPD data were collected over the 2θ angular range 4–164° with a step size of 0.125° with neutrons of wavelength 1.6218(3) Å as determined using the $La^{11}B_6$ National Institute of Standards and Technology (NIST) standard reference material 660b. Structural analysis was performed using a joint refinement against both XRPD and NPD data using the GSAS-II software (Toby and Von Dreele, 2013). Refined parameters included the background coefficients, zero offset, peak shape parameters. Refined phase parameters included the lattice parameter, oxygen positional parameter, isotropic atomic displacement parameters, and site occupancy factors.

Positive electrodes were prepared by mixing LNMO, polyvinylidene difluoride (PVDF), and carbon black (super P) in a weight ratio of 83:7:10 with N-methyl-2-pyrrolidinone (NMP). After continuously stirring for 3 h the homogenous slurry was coated onto aluminum foil and dried in vacuum at 120°C for 12 h. Negative electrodes were prepared by mixing LTO, PVDF, and super P in a weight ratio of 80:10:10 in NMP, which was stirred, and then coated onto copper foil, and then dried using that same procedure as for the positive electrode preparation.

The electrochemical performance of the LNMO, LTO, and AlF_3-LTO as working electrodes in half-configuration coin cells was tested. Half cells were assembled using Li foil as counter electrode and Celgard® 2400 polypropylene membrane as separator. The electrolyte used was 1M $LiPF_6$ in ethylene carbonate (EC) and dimethyl carbonate (DMC) in a 1:1 ratio by volume. The cell was assembled in an Ar-filled glove box ($O_2 < 1$ ppm, $H_2O < 1$ ppm) and prepared cells galvanostatically tested using a LAND multichannel battery testing system (CT2001A).

18650-standard full-configuration 900–1000 mAh batteries were assembled at the Industrial Technology Research Institute (ITRI) in Taiwan. The performance of the LNMO||LTO systems were evaluated in these batteries between 0.5 and 3.3 V (vs. LTO) using a Maccor series 4000 (USA). These 18650-standard full-configuration batteries were also used in *in-operando* NPD experiments with WOMBAT (Studer et al., 2006), the high-intensity neutron powder diffractometer at ANSTO (a schematic is shown in **Figure S1**). Data were collected every minute over a 2θ angular range 20-136.9° using neutrons of 2.4123(2) Å, as determined using the $La^{11}B_6$ NIST standard reference material 660b, during cycling within 2.0–3.4 V at a current of 0.09 A (equivalent to ∼0.1 C). Single-peak fitting of LTO and LNMO reflections was performed using the Large Array Manipulation Program (Richard et al., 1996).

RESULTS AND DISCUSSION

The morphology and particle size of LTO and AlF_3-coated LTO as characterized using SEM and TEM are shown in **Figures 1a,c**

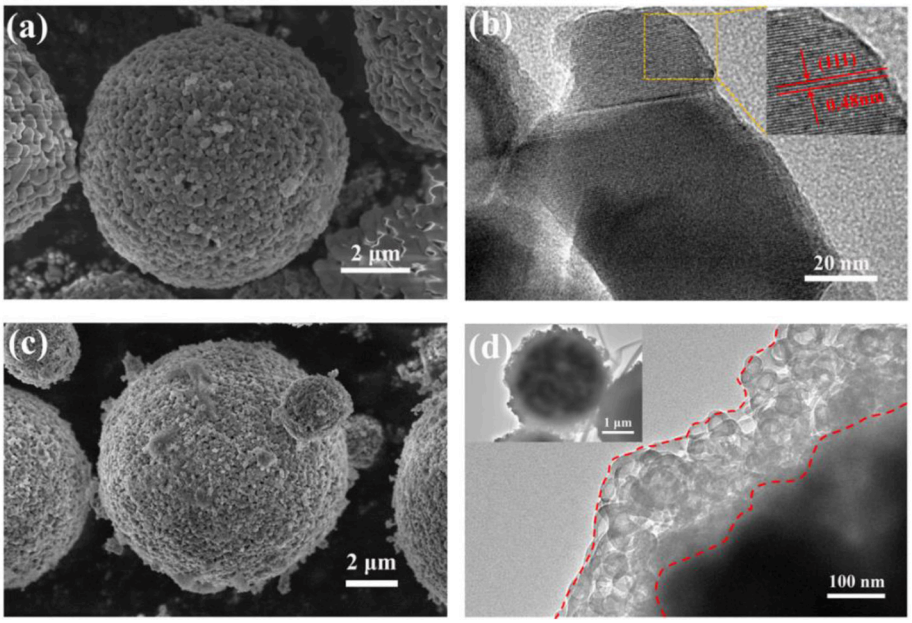

FIGURE 1 | SEM micrographs of **(a)** LTO and **(c)** AlF_3-coated LTO; TEM micrographs of **(b)** LTO with inset showing a magnification of the area outlined in yellow with fringes across the (111), and **(d)** AlF_3-coated LTO with inset showing a whole particle at lower magnification.

and **Figures S2a,b**, revealing that the secondary particles of both LTO and AlF_3-coated LTO are highly porous microspheres with a diameter of 3–10 μm and composed of primary particles of ∼50 nm in diameter. These morphology features promote electrolyte permeation. **Figure 1b** reveals crystalline pristine LTO where the observed (111) lattice (inset) has a spacing of approximately ∼0.48 nm, as consistent with the LTO structure (Cao et al., 2015; Wang et al., 2015). **Figure 1d** shows a uniform coating on the LTO particle, of thickness 100∼200 nm. Results of elemental mapping using EDS are shown in **Figure S3**, clearly revealing a uniform distribution of Al and F around a particle with a central core of Ti and O, confirming a uniform AlF_3 coating. The morphology of the LNMO material is shown in **Figures S2c,d**, where LNMO microspheres are 3-12 μm in diameter and composed of bar-like primary particles ∼500 nm in diameter and ∼2 μm in length.

Structural refinement results for LTO and AlF_3 coated LTO, as well as LNMO materials performed using both high-resolution NPD and XRPD data are shown in **Table 1** and **Table S1**, respectively, and the corresponding Rietveld refinement profiles in **Figure 2** and **Figure S3**, respectively. The LTO and AlF_3 coated LTO phase are both found to be cubic with a $Fd\bar{3}m$ space group (Pang et al., 2014b). The lattice parameter of the LTO is slightly smaller in the coated material, possibly as a result of the doping of ∼3% Al into the LTO structure, as found in the crystallographic analysis and in good agreement with previous work reporting the partial substitution of Al at the 16*c* site in the LTO spinel (Xu et al., 2013; Li et al., 2014). We identify the parasitic doping of Al into the LTO structure in our crystallographic analysis, which was not performed in previous studies of AlF_3-coated electrodes (Sun et al., 2007; Tron et al., 2016), despite Al doping in LTO being associated with improved cycling stability and better rate capability (Xu et al., 2013). We note the possibility of the doping of F onto the O site, however, the determination of this is very difficult given the low contrast for these elements in both NPD and XRPD data, as noted in a previous study (Pang et al., 2017).

Our analysis also revealed that both LTO samples contain minor phases of Li_2O (space group $Fm\bar{3}m$, Inorganic Crystal Structure Database entry number 54368), Li_2O_2 (space group $P6_3/mmc$, Inorganic Crystal Structure Database entry number 50658) and rutile-type TiO_2 (space group $P4_2/mnm$, Inorganic Crystal Structure Database entry number 31324) in the phase composition reported in **Table 2**. We note a larger fraction of rutile in the AlF_3-coated LTO, further supporting the doping of Al in the LTO. Although these minor phases result in a slight reduction in capacity, we focus on the LTO behavior in the following discussion.

The inherently lower resolution of the NPD data relative to the XRPD data meant that the AlF_3 was only detectable in the XRPD data. The Rietveld refinement profile using XRPD data of the AlF_3-coated LTO sample is shown in **Figure S4**, revealing weight fractions of LTO:AlF_3 to be 89(1):11(1) in good agreement with the nominal composition used in the synthesis.

The LNMO sample is found to be composed of both $P4_332$ and $Fd\bar{3}m$ space group phases of amounts 22(2) and 78(2)%, respectively (**Table S1** and **Figure S5**). The lattice and atomic parameters of both phases of LNMO are summarized in **Table S1**. The charge-discharge curve of half cells containing LNMO appear similar to that of those for cells containing only the $Fd\bar{3}m$ space group LNMO phase (**Figure S6**), confirming that the

TABLE 1 | Crystallographic details of LTO and AlF_3-coated LTO obtained from joint Rietveld analysis using XRPD and NPD data. U_{iso} is the isotropic atomic displacement parameter.

$Li_4Ti_5O_{12}$ Space Group = $Fd\bar{3}m$						
a = 8.3505(2)Å, Volume = 582.30(4) Å^3						
Atom	**Site**	***x***	***y***	***z***	**U_{iso} (Å^2)**	**Site occupancy factor**
Li	8*a*	0.375	0.375	0.375	0.015(1)	1
Li	16*d*	0	0	0	0.0100(3)[a]	0.167
Ti	16*d*	0	0	0	0.0100(3)[a]	0.833
O	32*e*	0.23754(4)[b]	0.23754(4)[b]	0.23754(4)[b]	0.0087(2)	1
AlF_3-coated $Li_4Ti_5O_{12}$ Space Group = $Fd\bar{3}m$						
a = 8.3447(2)Å, Volume = 581.07(5) Å^3						
Atom	**site**	***x***	***y***	***z***	**U_{iso} (Å^2)**	**Site occupancy factor**
Li	8*a*	0.375	0.375	0.375	0.025(1)	1
Li	16*d*	0	0	0	0.0106(4)[c]	0.167
Ti	16*d*	0	0	0	0.0106(4)[c]	0.802(3)[e]
Al	16*d*	0	0	0	0.0106(4)[c]	0.031(3)[e]
O	32*e*	0.23752(4)[d]	0.23752(4)[d]	0.23752(4)[d]	0.0121(2)	1

[a,b,c,d] *constrained to be the same.* [e] *constrained to sum to 0.833.*

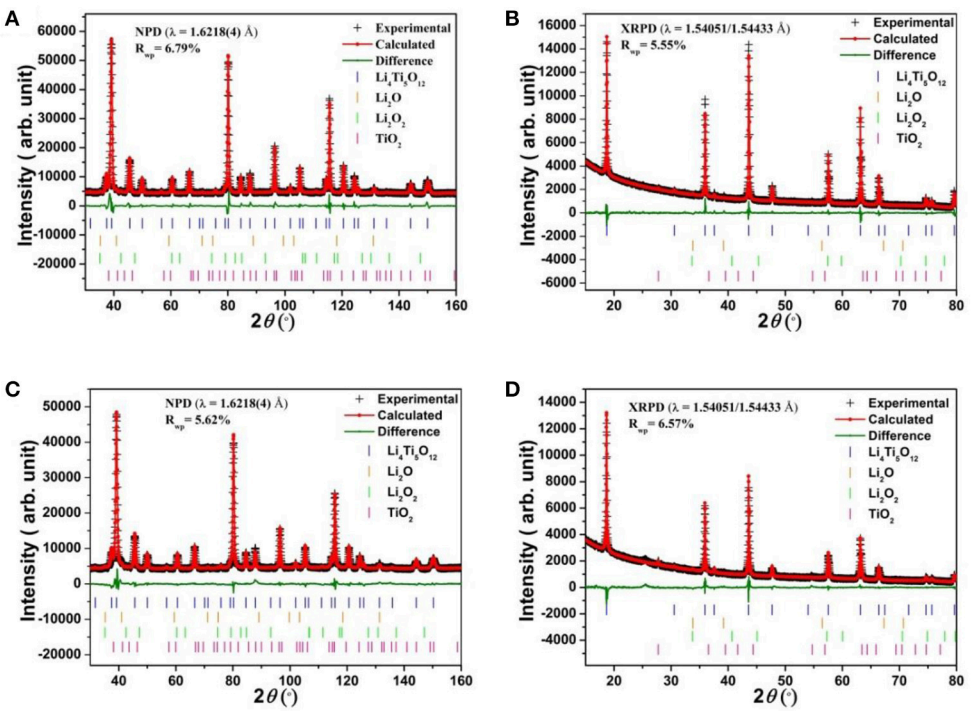

FIGURE 2 | Rietveld refinement profiles for **(A)** NPD and **(B)** XRPD data of LTO, and **(C)** NPD and **(D)** XRPD data of AlF_3-coated LTO. The combined goodness-of-fit (GOF) are 2.58 and 2.15, respectively, and R_{wp} is the weighted profile R-factor.

majority of the sample is composed of LNMO with $Fd\bar{3}m$ space group, which is considered in the following discussion.

The electrochemical performance of the pristine LTO and AlF_3-coated LTO in half-cells are shown in **Figure 3**. **Figure 3A** shows the cycling performance of both LTO at a current density of 1 C (1 C = 175 mA g^{-1}). The uncoated LTO delivers a similar but slightly higher capacity performance (discharge capacity of 162 mAh g^{-1} and charge capacity of 149 mAh g^{-1}) than the

TABLE 2 | Phase composition of LTO and AlF_3-coated LTO samples (AlF_3 excluded).

	Weight fraction (%)			
	LTO	Li_2O	Li_2O_2	TiO_2 (rutile)
LTO	94.66(5)	4.0(1)	0.44(4)	0.9(1)
AlF_3-coated LTO	93.10(5)	3.6(2)	0.40(4)	2.9(2)

AlF_3-coated LTO, which has a capacity of 157 mAh g^{-1} and a charge capacity of 142 mAh g^{-1}. The slightly lower charge capacity of the coated LTO is attributed to the addition of the AlF_3 [11(1) wt.%], which makes no contribution to lithium storage. When the LTO component only is considered, the charge capacity of AlF_3-coated LTO is 159 mAh g^{-1}, ∼85 and 91% of the theoretical charge capacity in the uncoated and coated LTO, respectively.

In terms of cycling performance, the AlF_3-coated LTO retains ∼93% of capacity after 265 cycles compared with ∼81% by the uncoated LTO. The average capacity decay per cycle of LTO and AlF_3-coated LTO is ∼0.070 and ∼0.025%, respectively, with the nearly 300% improvement in the cycling stability of the coated sample attributed to protection against hydrofluoric acid attack. Whilst the underlying mechanism for the known issue of gassing of LTO is yet to fully understood, it is thought to originate from a reaction of Ti and electrolyte, initiating the electrolyte decomposition (Han et al., 2017), and the AlF_3-coating may also help to prevent this behavior. Further contributing to this enhanced cycling stability may be the parasitic Al doping induced by the coating, where the Al-O bond strengthens the MO_6 octahedron (Huang et al., 2007).

Figure 3B compares the rate capabilities of the uncoated and coated LTO. We note that our reported capacities are only for the LTO content of the electrode. The uncoated LTO delivers a capacity of 158, 154, and 146 mAh g^{-1} at a current density of 0.2 C, 0.5 C, and 1 C, respectively, lower than those of the AlF_3-coated LTO of 163, 158, and 156 mAh g^{-1} when the LTO component is considered only, respectively. However, at larger current densities of 2 C and 4 C, the AlF_3-coated LTO anode delivers a capacity of 153 and 147 mAh g^{-1} (considering only the LTO component), respectively, much higher than for the uncoated LTO (122 and 90 mAh g^{-1}, respectively). The improved rate capability of the AlF_3-coated LTO is ascribed to enhanced ionic conductivity as a result of both the coating and Al doping into the structure. We note that the capacity of both uncoated and coated LTO recovered to almost their original value in the first ten cycles at 0.2 C, of 157 and 143 (161 for only the LTO component) mAh g^{-1}, respectively.

Figures 3C,D show the 1st, 50th, and 200th charge-discharge curves of the uncoated and AlF_3-coated LTO at 1 C. In the 1st cycle, the typical plateaus of LTO (∼1.6 V during charge and ∼1.4 V during discharge) are observed for both samples. The AlF_3-coated LTO is found to have a lower degree of polarization (0.17 V) than the uncoated LTO (0.25 V). Upon cycling, the polarization of the uncoated LTO increases dramatically after 200 cycles, where the curve becomes distorted without recognizable plateaus. On the contrary, plateaus in 200th charge-discharge curve for AlF_3-coated LTO are observed at 1.58 V and 1.51 V during delithiation and lithiation process, respectively, indicating enhanced structural stability and cycling performance.

Full battery test results using 18650-type LNMO||LTO batteries are shown in **Figure S7**. At 0.1 C, the LNMO||AlF_3-coated LTO battery delivered a charge capacity of 1097 mAh and a discharge capacity of 944 mAh, constituting ∼86% coulombic efficiency in the first cycle (**Figure S7a**). The first-cycle irreversible capacity was 153 mAh and the overlapped discharge curves of the first and second cycle indicate a stable cycling performance. **Figure S7b** shows the rate performance of the full battery, where the rate-induced potential polarization only increases slightly with increasing current density and the curve retaining obvious plateaus during both charge and discharge. These results reveal superior reaction kinetics of the LNMO||AlF_3-coated LTO full battery relative to the battery containing uncoated LTO. A comparison of the electrochemical performance of the 18650-type full cells containing uncoated and coated LTO is shown in **Figures S7c,d**, respectively. The battery containing the coated LTO has a slightly lower capacity, commensurate with the reduced amount of active LTO, and greatly enhanced cycle performance. Further, unlike the uncoated LTO battery, a gradual increasing capacity during cycling at 1 C was observed in the battery with the coated LTO during the first 50 cycles (**Figures S7c,d**).

To elucidate the mechanism for the enhanced performance of the LNMO||LTO battery achieved by the AlF_3 coating of the LTO, we employed *in-operando* NPD to investigate the phase and structure evolution of the electrodes in 18650 batteries containing LNMO and either coated or uncoated LTO. Full-angular-range contour plots of *in-operando* NPD data in different cycles of the LNMO||LTO batteries and LNMO||AlF_3-coated LTO batteries are shown in **Figure S8**. To show the structural response of the electrodes in more detail, **Figure 4** shows contour plots of the NPD data for both batteries in a selected 2θ range. The 18650-type batteries contain conventional organic hydrogenated electrolyte and Celgard® 2400 separator, both of which are rich in hydrogen and lead to a significant background in the NPD data. Nevertheless, the evolution of the LTO 222 and LNMO 222 reflections during cycling are clearly observed. As LTO is a "zero strain" lithium insertion electrode, the LTO 222 reflection position change during battery cycling is expected to be small. Despite this, the minor lattice change (peak shift) can be clearly observed. We employ single peak fitting of this LTO 222 reflection to understand further the structural evolution of the LTO phase, with the results shown in **Figures 5**, **6** for the LNMO||LTO and LNMO||AlF_3-coated LTO batteries, respectively.

The positional shift of the LTO 222 reflection during the 1st and 2nd cycle is shown in **Figure 5A**, and for the 51st cycle in **Figure 5B**. The positional shift is similar for the first and second cycle, where during lithiation, the LTO 222 reflection shifts to lower 2θ, then to the higher 2θ, indicating the LTO lattice first expands and then contracts. As the end of lithiation is approached, the LTO 222 reflection shows a minor shift to lower 2θ before its final maximum is reached at the charged

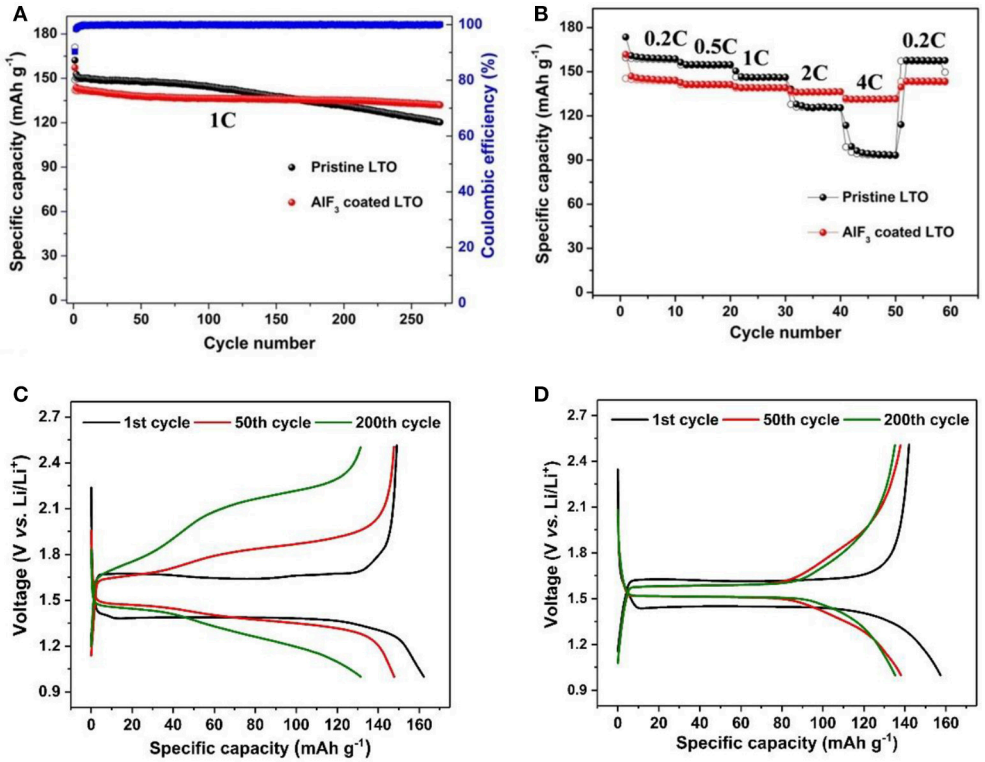

FIGURE 3 | (A) Cycling performance and coulombic efficiency of LTO and AlF_3-coated LTO at 1 C up to 260 cycles; **(B)** rate performance of LTO and AlF_3-coated LTO; 1st, 50th, and 200th charge-discharge curves of **(C)** LTO and **(D)** AlF_3-coated LTO at 1 C. The capacity of AlF_3-coated LTO sample is measured for the composite, including electrochemically active LTO and inactive AlF_3.

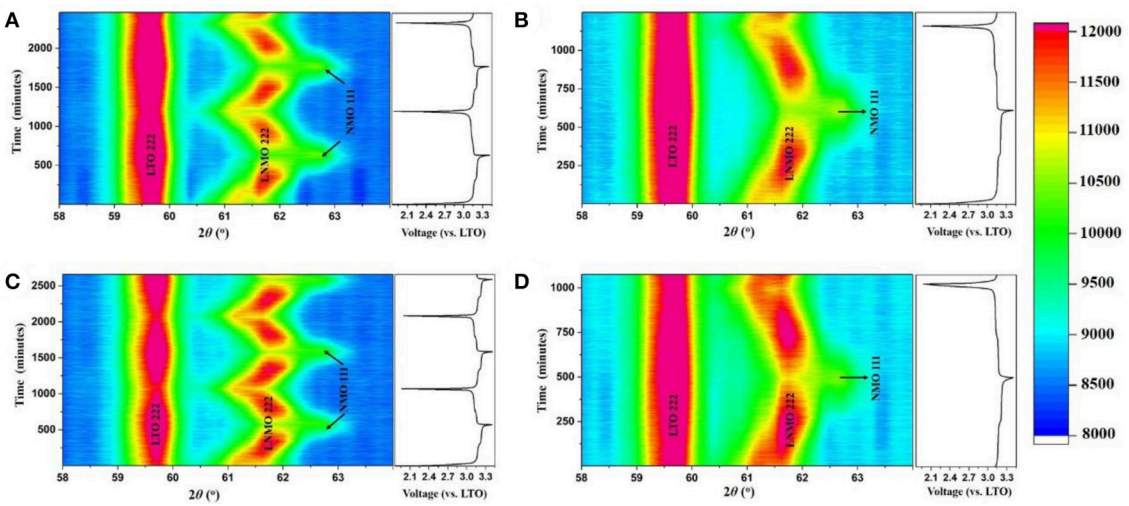

FIGURE 4 | Contour plot of *in-operando* NPD data of the LNMO||LTO battery **(A)** for the first two cycles and **(B)** for the 51st cycle, and of the LNMO||AlF_3-coated LTO battery **(C)** for the first two cycles and **(D)** for the 51st cycle, with intensity (arb.) shown in color with the scale and corresponding voltage curve on the right. LTO 222 and LNMO 222 as well as NMO 111 reflections are labeled.

state. This response is completely consistent with that previously reported, where during lithiation lithium is transferred from the 8*a*, through 32*e*, to the 16*c* crystallographic sites, and the change in structure captured by the LTO 222 reflection position corresponds to the changing population of lithium at these sites, in addition to the repositioning of the O atom in response to lithiation of the 16*c* site (Pang et al., 2014a,b). In the 51st cycle the behavior of the LTO 222 reflection is reproduced, except the

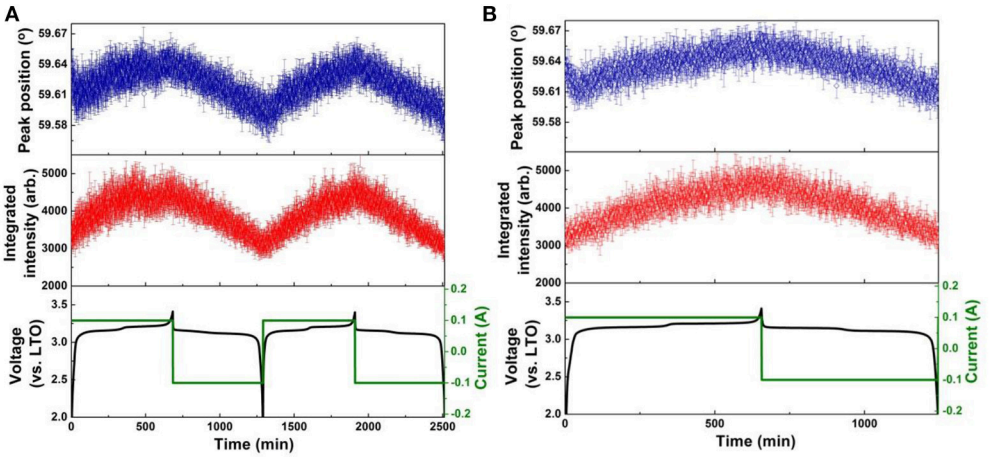

FIGURE 5 | Results of single peak fitting of the LTO 222 reflection in NPD data of the LNMO||LTO battery, including peak position and intensity for **(A)** the first two cycles, and **(B)** the 51st cycle. Battery voltage and current are shown alongside.

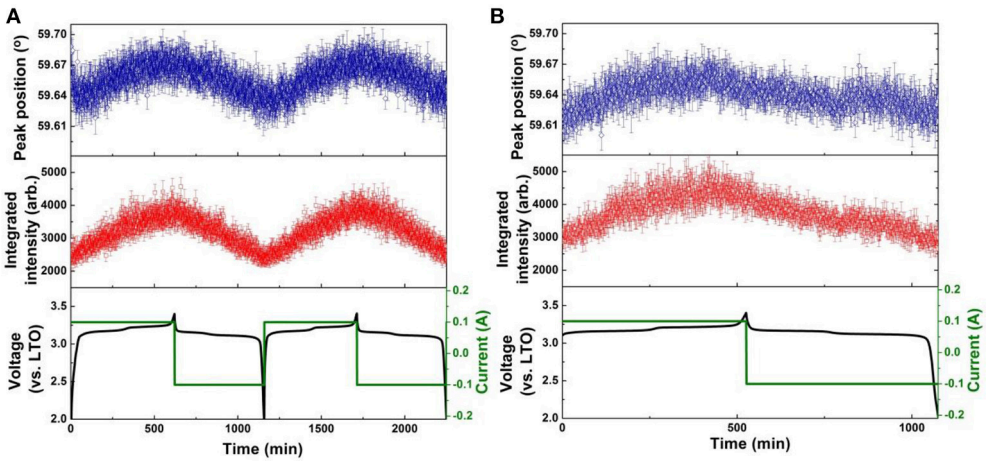

FIGURE 6 | Results of single peak fitting of the LTO 222 reflection in NPD data of the LNMO||AlF_3-LTO battery, including peak position and intensity for **(A)** the first two cycles, and **(B)** the 51st cycle. Battery voltage and current are shown alongside.

transitions are less marked, suggesting some decay of electrode function. Delithiation during discharge induces a relatively linear shift in the LTO 222 reflection position to lower 2θ (expansion), as consistent again with previous work and the known behavior of the LTO electrode (Pang et al., 2014a,b).

The positional shift of the AlF_3-coated LTO 222 reflection in the first and second cycles (**Figure 6A**) shows a similar trend to that of the uncoated LTO, except the minor shift to lower 2θ (expansion) prior to the end of lithiation is only barely observable. The position shift of the AlF_3-coated LTO 222 reflection reaches a maximum plateau before the end of lithiation, implying that the capacity of LTO in this battery has not been fully delivered (Pang et al., 2014b). In the 51st cycle (**Figure 6B**), the minor shift to lower 2θ just prior to the fully charged battery state observed clearly in the 1st and 2nd charge for the uncoated LTO, is just beginning to appear for the coated LTO. In contrast to the uncoated LTO, the position shift of the AlF_3-coated LTO 222 reflection during delithiation exhibits two partially discernible stages for the 1st and 2nd discharge, with this behavior becoming more pronounced in the 51st discharge (**Figure 6B**). The maximum difference in lattice parameter during the 1st, 2nd, and 51st cycle for the coated and uncoated LTO was calculated from the positional shift of the LTO 222 reflection and is shown **Table 3**. These results clearly show that the AlF_3 coating alongside the parasitic doping of Al that occurs reduces the overall LTO lattice change during battery cycling.

The integrated intensity of the LTO 222 reflection is closely associated with the amount of lithium residing at 8*a* and 16*c*, as well as the 32e, crystallographic sites, as well as the position of the oxygen responding to the changing lithium concentration at these sites (Pang et al., 2014a). The intensity of this reflection for both coated and uncoated samples increases during lithiation. The anomalous shift in the LTO 222 reflection position just prior

to the maximum lithiated state is mimicked by the reflection intensity, where a decrease followed by an increase just prior to its maximum is observed. As consistent with the differences in the trend of the LTO 222 reflection position between the uncoated and coated LTO, the intensity change just prior to maximum lithiation is also more pronounced in the uncoated LTO, being hardly visible for the coated LTO. The evolution of the LTO 222 reflection intensity also becomes less pronounced at the 51st cycle, particularly for the uncoated LTO. Similar to the evolution of the LTO 222 reflection position during delithiation, the intensity evolution is more monotonic for the uncoated sample and somewhat staged for the coated LTO in the 51st cycle.

We note that in the AlF_3-coated LTO it may be possible for Al^{3+} to migrate from the 16*d* site occupied by the Ti to the 16*c* site normally occupied by Li^+, resulting in different oxygen repositioning known to occur for the undoped (uncoated) LTO. Such effects may contribute to differences in both the LTO 222 reflection position and intensity evolution. The coherent neutron-scattering length of Al is +3.4 fm, while that of Li is −1.9 fm. Hence, the migration of Al to the 16*c* site is expected to reduce reflection intensity, consistent with a premature finish of the lithiation, although it is difficult to disentangle this effect from that of the O repositioning. A premature completion of lithiation due to Al migration may also explain the gradual increasing capacity observed for the coated LTO-containing battery during cycling at 1 C in the first 50 cycles (**Figures S7c,d**), where an activation process enabling full capacity (∼175 mAh g^{-1}) is correlated with the slight shift to lower 2θ (expansion) near the end of lithiation (just observable in the 51st cycle for the coated LTO).

The evolution of LNMO counter electrode structure in the LNMO||LTO and LNMO||AlF_3-coated LTO batteries is also examined using single peak fitting of the LNMO 222 reflection with results shown in **Figures 7**, **8**. Our previous work (Pang et al., 2014b) revealed that $Fd\bar{3}m$ LNMO undergoes a solid-solution reaction during the redox Ni^{2+}/Ni^{3+} reaction between 3.06 and 3.16 V vs. LTO with a lattice change associated with lithium extraction and insertion. In the present work, we quantify the rate of lithium extraction from the LNMO during the initial charge process by the rate of change of the peak position (° per min) extracted from linear fitting of the time evolution of the LNMO 222 reflection position (**Figures S9, S10**), with the result given in **Table 3**. The LNMO delithiation rate in the LNMO||LTO battery remains nearly unchanged for 50 cycles, but increases gradually in the AlF_3-coated LTO battery. This result implies that the AlF_3 coating promotes faster lithium transport between the electrodes, possibly via a protection by the AlF_3 of the LTO against both hydrofluoric acid and deposition of Mn known to be released by the LNMO, a cause of capacity fade in graphite counter electrodes (Tsunekawa et al., 2002), and allowing the LNMO to continue lithiation/delithation unhindered on continued cycling. We also note that the LNMO||AlF_3-LTO battery, unlike the LNMO||LTO battery, exhibits a capacity increase during cycling (see **Figures S7c,d**), which indicates an increased availability of lithium to shuttle between the electrodes. **Table 3** shows the maximal change

TABLE 3 | Comparison of maximum change of the coated and uncoated LTO lattice parameter, as well as the corresponding rate of change and maximum position change in the counter electrode LNMO 222 reflection position during the charging solid-solution-reaction stage when cycling.

	1st cycle	2nd cycle	51st cycle
Maximum lattice parameter change of LTO and AlF_3-coated LTO (%)			
Uncoated LTO	0.044(1)	0.042(1)	0.040(1)
AlF_3-coated LTO	0.040(1)	0.037(1)	0.035(1)
Rate of change of LNMO 222 reflection position (° per min)			
LNMO||LTO	0.001330(9)	0.001340(9)	0.001300(7)
LNMO||AlF_3-coated LTO	0.001200(7)	0.001370(9)	0.001440(1)
Maximum change of LNMO 222 reflection position (%)			
LNMO||LTO	0.0045(1)	0.0040(1)	0.0033(2)
LNMO||AlF_3-coated LTO	0.0015(2)	0.0016(2)	0.0032(2)

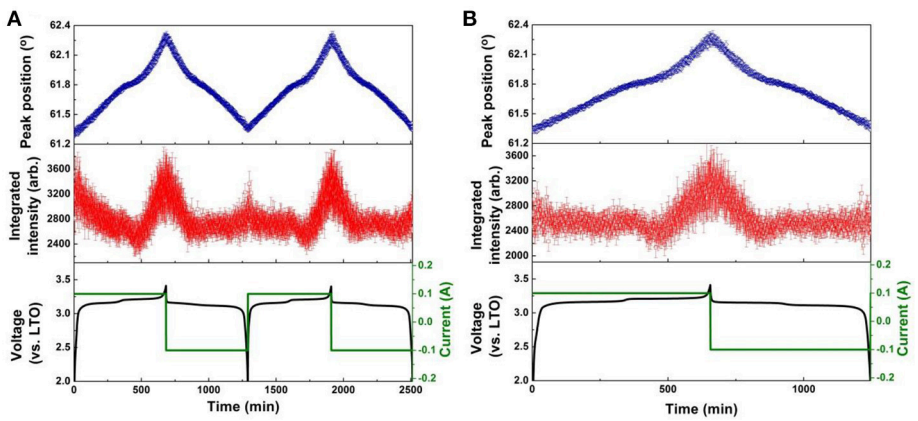

FIGURE 7 | Results of single peak fitting of the LNMO 222 reflection of NPD data for the LNMO||LTO battery, including peak position and intensity, for **(A)** the first two cycles, and **(B)** the 51st cycle. Battery voltage and current are also shown.

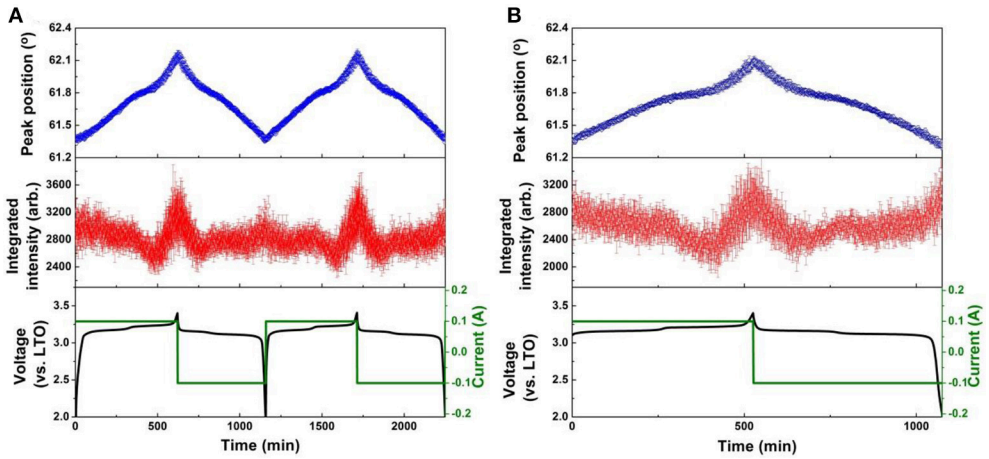

FIGURE 8 | Results of single peak fitting of the LNMO 222 reflection of NPD data for the LNMO||AlF_3-LTO battery, including peak position and intensity, for **(A)** the first two cycles, and **(B)** the 51st cycle. Battery voltage and current are also shown.

of the LNMO 222 reflection position at different cycles in the battery containing the coated and uncoated LTO. The maximum positional change of the LNMO 222 reflection in the LNMO||LTO battery decreases on cycling, while that in the LNMO||AlF_3-LTO battery increases during cycling, consistent with a higher reservoir of active lithium in the battery containing the coated LTO. Further, this result is also corroborated by the structural response of the LTO lattice parameter, where the co-distribution of Li at 8*a* and 16*c* crystallographic sites results in a lattice expansion followed by contraction during lithiation, and therefore a lower maximal lattice change at higher degree of lithiation (Pang et al., 2014a), evidencing higher lithiation in both electrodes in the battery containing the coated LTO.

CONCLUSIONS

The effect of an AlF_3 coating on LTO within a LTO||LNMO battery on the performance and structural evolution of electrodes was investigated by a combination of electrochemical testing and *in-operando* neutron powder diffraction. The coating is found to cause the doping of approximately 3% Al onto the 16*c* crystallographic site of the disordered LTO phase structure. Our examination of the structural response of LTO and LNMO during battery cycling reveals that the AlF_3 coating alongside the induced parasitic doping of Al enhances capacity of the LTO, and suppresses capacity decay in the battery. We measure changes to the structural response of the LTO and LNMO electrodes within the battery containing the coated LTO that are consistent with a greater availability of lithium, and an enhanced rate of lithium extraction from the LNMO counter electrode during its solid-solution behavior on charge. This work demonstrates the feasibility of an LNMO||AlF_3-coated LTO full battery, and our study of the effect of the AlF_3 coating within the full battery configuration reveals new insights into the mechanism of battery performance enhancement.

AUTHOR CONTRIBUTIONS

K-YK prepared the AlF_3 coated LTO. C-MC prepared the 18650 batteries. GL and AP performed preliminary characterization of samples as well as prepared and tested coin cells. C-ZL, C-EL, J-MC, and S-CL performed full battery performance characterization. GL, VP, and WP collected and analyzed the neutron data and prepared the manuscript. WP, VP, and ZG directed the research.

ACKNOWLEDGMENTS

The authors acknowledge the financial support funded from the Ministry of Economic Affairs (MOEA) of TAIWAN, the Australia Neutron Science and Technology Organization (ANSTO) for neutron beamtime, and the Australian Research Council for FT150100109, FT160100251, and DP170102406. In addition, the authors would like to thank the Australian Institute of Nuclear Science and Engineering (AINSE) Limited for providing financial assistance in the form of a Post Graduate Research Award (PGRA) to enable this work. The authors would also be grateful to the Electron Microscopy Centre (EMC) at the University of Wollongong for the support and equipment assistance.

SUPPLEMENTARY MATERIAL

The Supplementary Material for this article can be found online at: https://www.frontiersin.org/articles/10.3389/fenrg.2018.00089/full#supplementary-material

REFERENCES

Ariyoshi, K., Iwakoshi, Y., Nakayama, N., and Ohzuku, T. (2004). Topotactic two-phase reactions of $Li[Ni_{1/2}Mn_{3/2}]O_4$ ($P4_332$) in nonaqueous lithium cells. *J. Electrochem. Soc.* 151, A296–A303. doi: 10.1149/1.1639162

Ariyoshi, K., and Ohzuku, T. (2007). Conceptual design for 12V "lead-free" accumulators for automobile and stationary applications. *J. Power Sources* 174, 1258–1262. doi: 10.1016/j.jpowsour.2007.06.085

Arroyo-de Dompablo, M. E., and Amador, U. (2006). A computational investigation on the electrochemical properties of spinel-like $LiCoAsO_4$ as positive electrode for lithium-ion batteries. *Solid State Sci.* 8, 916–921. doi: 10.1016/j.solidstatesciences.2006.02.051

Belharouak, I., Sun, Y. K., Lu, W., and Amine, K. (2007). On the safety of the $Li_4Ti_5O_{12}$/ $LiMn_2O_4$ lithium-ion battery system. *J. Electrochem. Soc.* 154, A1083–A1087. doi: 10.1149/1.2783770

Cao, L., Hui, Y., Ouyang, H., Huang, J., Xu, Z., Li, J., et al. (2015). $Li_4Ti_5O_{12}$ hollow mesoporous microspheres assembled from nanoparticles for high rate lithium-ion battery anodes. *RSC Adv.* 5, 35643–35650. doi: 10.1039/C5RA03158C

Choi, J. W., and Aurbach, D. (2016). Promise and reality of post-lithium-ion batteries with high energy densities. *Nat. Rev. Mater.* 1:16013. doi: 10.1038/natrevmats.2016.13

Croy, J. R., Abouimrane, A., and Zhang, Z. (2014). Next-generation lithium-ion batteries: the promise of near-term advancements. *MRS Bull.* 39, 407–415. doi: 10.1557/mrs.2014.84

Deng, H., Nie, P., Luo, H., Zhang, Y., Wang, J., and Zhang, X. (2014). Highly enhanced lithium storage capability of $LiNi_{0.5}Mn_{1.5}O_4$ by coating with Li_2TiO_3 for Li-ion batteries. *J. Mater. Chem. A* 2, 18256–18262. doi: 10.1039/C4TA03802A

Feng, X., Shen, C., Fang, X., and Chen, C. (2011). Synthesis of $LiNi_{0.5}Mn_{1.5}O_4$ by solid-state reaction with improved electrochemical performance. *J. Alloys Compounds* 509, 3623–3626. doi: 10.1016/j.jallcom.2010.12.116

Fergus, J. W. (2010). Recent developments in cathode materials for lithium ion batteries. *J. Power Sources* 195, 939–954. doi: 10.1016/j.jpowsour.2009.08.089

Gu, M., Belharouak, I., Zheng, J., Wu, H., Xiao, J., Genc, A., et al. (2012). Formation of the spinel phase in the layered composite cathode used in Li-ion batteries. *ACS Nano* 7, 760–767. doi: 10.1021/nn305065u

Han, C., He, Y. B., Liu, M., Li, B., Yang, Q. H., Wong, C. P., et al. (2017). A review of gassing behavior in $Li_4Ti_5O_{12}$-based lithium ion batteries. *J. Mater. Chem. A* 5, 6368–6381 doi: 10.1039/C7TA00303J

Huang, S., Wen, Z., Zhu, X., and Lin, Z. (2007). Effects of dopant on the electrochemical performance of $Li_4Ti_5O_{12}$ as electrode material for lithium ion batteries. *J. Power Sources* 165, 408–412. doi: 10.1016/j.jpowsour.2006.12.010

Kim, D. K., Muralidharan, P., Lee, H. W., Ruffo, R., Yang, Y., Chan, C. K., et al. (2008). Spinel $LiMn_2O_4$ nanorods as lithium ion battery cathodes. *Nano Lett.* 8, 3948–3952. doi: 10.1021/nl8024328

Kim, J. H., Myung, S. T., Yoon, C. S., Kang, S. G., and Sun, Y. K. (2004). Comparative study of LiNi0.5Mn1.5O4-δ and LiNi0.5Mn1.5O4 cathodes having two crystallographic structures: $Fd\bar{3}m$ and $P4_332$ *Chem. Mater.* 16, 906–914. doi: 10.1021/cm035050s

Kim, J. H., Pieczonka, N. P. W., Sun, Y. K., and Powell, B. R. (2014). Improved lithium-ion battery performance of $LiNi_{0.5}Mn_{1.5-x}Ti_xO_4$ high voltage spinel in full-cells paired with graphite and $Li_4Ti_5O_{12}$ negative electrodes. *J. Power Sources* 262, 62–71. doi: 10.1016/j.jpowsour.2014.03.107

Kim, J. W., Kim, D. H., Oh, D. Y., Lee, H., Kim, J. H., Lee, J. H., et al. (2015). Surface chemistry of $LiNi_{0.5}Mn_{1.5}O_4$ particles coated by Al_2O_3 using atomic layer deposition for lithium-ion batteries. *J. Power Sources* 274, 1254–1262. doi: 10.1016/j.jpowsour.2014.10.207

Li, S., Chen, C., Xia, X., and Dahn, J. (2013). The impact of electrolyte oxidation products in $LiNi_{0.5}Mn_{1.5}O_4/Li_4Ti_5O_{12}$ cells. *J. Electrochem. Soc.* 160, A1524–A1528. doi: 10.1149/2.051309jes

Li, W., Dolocan, A., Oh, P., Celio, H., Park, S., Cho, J., et al. (2017a). Dynamic behaviour of interphases and its implication on high-energy-density cathode materials in lithium-ion batteries. *Nat. Commun.* 8:14589. doi: 10.1038/ncomms14589

Li, W., Li, X., Chen, M., Xie, Z., Zhang, J., Dong, S., et al. (2014). AlF_3 modification to suppress the gas generation of $Li_4Ti_5O_{12}$ anode battery. *Electrochim. Acta* 139, 104–110. doi: 10.1016/j.electacta.2014.07.017

Li, W., Liu, X., Celio, H., Smith, P., Dolocan, A., Chi, M., et al. (2018). Mn versus Al in layered oxide cathodes in lithium-ion batteries: a comprehensive evaluation on long-term cyclability. *Adv. Energy Mater.* 8:1703154. doi: 10.1002/aenm.201703154

Li, W., Song, B., and Manthiram, A. (2017b). High-voltage positive electrode materials for lithium-ion batteries. *Chem. Soc. Rev.* 46, 3006–3059. doi: 10.1039/C6CS00875E

Liss, K. D., Hunter, B., Hagen, M., Noakes, T., and Kennedy, S. (2006). Echidna–the new high-resolution powder diffractometer being built at OPAL. *Phys. B: Condensed Matter* 385–386, 1010–1012. doi: 10.1016/j.physb.2006.05.322

Liu, H., Wang, J., Zhang, X., Zhou, D., Qi, X., Qiu, B., et al. (2016). Morphological evolution of high-voltage spinel $LiNi_{0.5}Mn_{1.5}O_4$ cathode materials for lithium-ion batteries: the critical effects of surface orientations and particle size. *ACS Appl. Mater. Interfaces* 8, 4661–4675. doi: 10.1021/acsami.5b11389

Ma, J., Hu, P., Cui, G., and Chen, L. (2016). Surface and interface issues in spinel $LiNi_{0.5}Mn_{1.5}O_4$: insights into a potential cathode material for high energy density lithium ion batteries. *Chem. Mater.* 28, 3578–3606. doi: 10.1021/acs.chemmater.6b00948

Pang, W. K., Lin, H. F., Peterson, V. K., Lu, C. Z., Liu, C. E., Liao, S. C., et al. (2017). Effects of fluorine and chromium doping on the performance of lithium-rich $Li_{1+x}MO_2$ (M= Ni, Mn, Co) positive electrodes. *Chem. Mater.* 29, 10299–10311. doi: 10.1021/acs.chemmater.7b02930

Pang, W. K., Lu, C. Z., Liu, C. E., Peterson, V. K., Lin, H. F., Liao, S. C., et al. (2016). Crystallographic origin of cycle decay of the high-voltage $LiNi_{0.5}Mn_{1.5}O_4$ spinel lithium-ion battery electrode. *Phys. Chem. Chem. Phys.* 18, 17183–17189. doi: 10.1039/C6CP00947F

Pang, W. K., Peterson, V. K., Sharma, N., Shiu, J. J., and Wu, S. H. (2014a). Lithium migration in $Li_4Ti_5O_{12}$ studied using in situ neutron powder diffraction. *Chem. Mater.* 26, 2318–2326. doi: 10.1021/cm5002779

Pang, W. K., Sharma, N., Peterson, V. K., Shiu, J. J., and Wu, S. H. (2014b). In-situ neutron diffraction study of the simultaneous structural evolution of a $LiNi_{0.5}Mn_{1.5}O_4$ cathode and a $Li_4Ti_5O_{12}$ anode in a $LiNi_{0.5}Mn_{1.5}O_4||Li_4Ti_5O_{12}$ full cell. *J. Power Sources* 246, 464–472. doi: 10.1016/j.jpowsour.2013.07.114

Richard, D., Ferrand, M., and Kearley, G. (1996). Analysis and visualisation of neutron-scattering data. *J. Neutron Res.* 4, 33–39. doi: 10.1080/10238169608200065

Santhanam, R., and Rambabu, B. (2010). Research progress in high voltage spinel $LiNi_{0.5}Mn_{1.5}O_4$ material. *J. Power Sources* 195, 5442–5451. doi: 10.1016/j.jpowsour.2010.03.067

Satya Kishore, M. V. V. M., and Varadaraju, U. V. (2006). Synthesis, characterization and electrochemical studies on $LiCoAsO_4$. *Mater. Res. Bull.* 41, 601–607. doi: 10.1016/j.materresbull.2005.09.005

Studer, A. J., Hagen, M. E., and Noakes, T. J. (2006). Wombat: the high-intensity powder diffractometer at the OPAL reactor. *Phys. B: Condensed Matter* 385–386, 1013–1015. doi: 10.1016/j.physb.2006.05.323

Su, X., Wu, Q., Li, J., Xiao, X., Lott, A., Lu, W., et al. (2014). Silicon-based nanomaterials for lithium-ion batteries: a review. *Adv. Energy Mater.* 4:1300882. doi: 10.1002/aenm.201300882

Sun, S., Yin, Y., Wan, N., Wu, Q., Zhang, X., Pan, D., et al. (2015). AlF_3 surface-coated $Li[Li_{0.2}Ni_{0.17}Co_{0.07}Mn_{0.56}]O_2$ nanoparticles with superior electrochemical performance for lithium-ion batteries. *ChemSusChem* 8, 2544–2550. doi: 10.1002/cssc.201500143

Sun, Y. K., Cho, S. W., Lee, S. W., Yoon, C., and Amine, K. (2007). AlF_3-coating to improve high voltage cycling performance of $Li[Ni_{1/3}Co_{1/3}Mn_{1/3}]O_2$ cathode materials for lithium secondary batteries. *J. Electrochem. Soc.* 154, A168–A172. doi: 10.1149/1.2422890

Toby, B. H., and Von Dreele, R. B. (2013). GSAS-II: the genesis of a modern open-source all purpose crystallography software package. *J. Appl. Crystallogr.* 46, 544–549. doi: 10.1107/S0021889813003531

Tron, A., Park, Y. D., and Mun, J. (2016). AlF_3-coated $LiMn_2O_4$ as cathode material for aqueous rechargeable lithium battery with improved cycling stability. *J. Power Sources* 325, 360–364. doi: 10.1016/j.jpowsour.2016.06.049

Tsunekawa, H., Tanimoto, S., Marubayashi, R., Fujita, M., Kifune, K., and Sano, M. (2002). Capacity fading of graphite electrodes due to the deposition of manganese ions on them in Li-ion batteries. *J. Electrochem. Soc.* 149, A1326–A1331. doi: 10.1149/1.1502686

Wang, C., Appleby, A. J., and Little, F. E. (2001). Electrochemical impedance study of initial lithium ion intercalation into graphite powders. *Electrochim. Acta* 46, 1793–1813. doi: 10.1016/S0013-4686(00)00782-9

Wang, C., Wang, S., He, Y. B., Tang, L., Han, C., Yang, C., et al. (2015). Combining fast li-ion battery cycling with large volumetric energy density: grain boundary induced high electronic and ionic conductivity in $Li_4Ti_5O_{12}$ spheres of densely packed nanocrystallites. *Chem. Mater.* 27, 5647–5656. doi: 10.1021/acs.chemmater.5b02027

Wang, Y., and Cao, G. (2008). Developments in nanostructured cathode materials for high-performance lithium-ion batteries. *Adv. Mater.* 20, 2251–2269. doi: 10.1002/adma.200702242

Wang, Z., Wang, Z., Peng, W., Guo, H., and Li, X. (2014). An improved solid-state reaction to synthesize Zr-doped $Li_4Ti_5O_{12}$ anode material and its application in $LiMn_2O_4$/$Li_4Ti_5O_{12}$ full-cell. *Ceramics Int.* 40, 10053–10059. doi: 10.1016/j.ceramint.2014.04.011

Wu, H., Belharouak, I., Deng, H., Abouimrane, A., Sun, Y. K., and Amine, K. (2009). Development of $LiNi_{0.5}Mn_{1.5}O_4$/$Li_4Ti_5O_{12}$ system with long cycle life. *J. Electrochem. Soc.* 156, A1047–A1050. doi: 10.1149/1.3240197

Wu, Q., Yin, Y., Sun, S., Zhang, X., Wan, N., and Bai, Y. (2015). Novel AlF_3 surface modified spinel $LiMn_{1.5}Ni_{0.5}O_4$ for lithium-ion batteries: performance characterization and mechanism exploration. *Electrochim. Acta* 158, 73–80. doi: 10.1016/j.electacta.2015.01.145

Xia, H., Xia, Q., Lin, B., Zhu, J., Seo, J. K., and Meng, Y. S. (2016). Self-standing porous $LiMn_2O_4$ nanowall arrays as promising cathodes for advanced 3D microbatteries and flexible lithium-ion batteries. *Nano Energy* 22, 475–482. doi: 10.1016/j.nanoen.2016.01.022

Xiang, H. F., Jin, Q. Y., Chen, C. H., Ge, X. W., Guo, S., and Sun, J. H. (2007). Dimethyl methylphosphonate-based nonflammable electrolyte and high safety lithium-ion batteries. *J. Power Sources* 174, 335–341. doi: 10.1016/j.jpowsour.2007.09.025

Xiang, H. F., Zhang, X., Jin, Q. Y., Zhang, C. P., Chen, C. H., and Ge, X. W. (2008). Effect of capacity matchup in the $LiNi_{0.5}Mn_{1.5}O_4$/$Li_4Ti_5O_{12}$ cells. *J. Power Sources* 183, 355–360. doi: 10.1016/j.jpowsour.2008.04.091

Xiao, X., Ahn, D., Liu, Z., Kim, J. H., and Lu, P. (2013). Atomic layer coating to mitigate capacity fading associated with manganese dissolution in lithium ion batteries. *Electrochem. Commun.* 32, 31–34. doi: 10.1016/j.elecom.2013.03.030

Xu, W., Chen, X., Wang, W., Choi, D., Ding, F., Zheng, J., et al. (2013). Simply AlF_3-treated $Li_4Ti_5O_{12}$ composite anode materials for stable and ultrahigh power lithium-ion batteries. *J. Power Sources* 236, 169–174. doi: 10.1016/j.jpowsour.2013.02.055

Zhang, S. S. (2006). The effect of the charging protocol on the cycle life of a Li-ion battery. *J. Power Sources* 161, 1385–1391. doi: 10.1016/j.jpowsour.2006.06.040

Zhang, Z., Hu, L., Wu, H., Weng, W., Koh, M., Redfern, P. C., et al. (2013). Fluorinated electrolytes for 5 V lithium-ion battery chemistry. *Energy Environ. Sci.* 6, 1806–1810. doi: 10.1039/c3ee24414h

Zhao, E., Fang, L., Chen, M., Chen, D., Huang, Q., Hu, Z., et al. (2017). New insight into Li/Ni disorder in layered cathode materials for lithium ion batteries: a joint study of neutron diffraction, electrochemical kinetic analysis and first-principles calculations. *J. Mater. Chem. A* 5, 1679–1686. doi: 10.1039/C6TA08448F

Zheng, J., Gu, M., Xiao, J., Polzin, B. J., Yan, P., Chen, X., et al. (2014). Functioning mechanism of AlF_3 coating on the Li-and Mn-rich cathode materials. *Chem. Mater.* 26, 6320–6327. doi: 10.1021/cm502071h

Zheng, J., Gu, M., Xiao, J., Zuo, P., Wang, C., and Zhang, J. G. (2013). Corrosion/fragmentation of layered composite cathode and related capacity/voltage fading during cycling process. *Nano Lett.* 13, 3824–3830. doi: 10.1021/nl401849t

Zhou, Y., Lee, Y., Sun, H., Wallas, J. M., George, S. M., and Xie, M. (2017). Coating solution for high-voltage cathode: AlF_3 atomic layer deposition for freestanding $LiCoO_2$ electrodes with high energy density and excellent flexibility. *ACS Appl. Mater. Interfaces* 9, 9614–9619. doi: 10.1021/acsami.6b15628

Conflict of Interest Statement: The authors declare that the research was conducted in the absence of any commercial or financial relationships that could be construed as a potential conflict of interest.

frontiers in Energy Research

ORIGINAL RESEARCH
published: 31 July 2018
doi: 10.3389/fenrg.2018.00064

Insight Into the Formation of Lithium Alloys in All-Solid-State Thin Film Lithium Batteries

Damian Goonetilleke[1], Neeraj Sharma[1], Justin Kimpton[2], Jules Galipaud[3,4], Brigitte Pecquenard[3,4] and Frédéric Le Cras[5]*

[1] School of Chemistry, University of New South Wales, Sydney, NSW, Australia, [2] Australian Synchrotron, Clayton, VIC, Australia, [3] Centre National de la Recherche Scientifique, University of Bordeaux, ICMCB, UPR 9048, Pessac, France, [4] Bordeaux INP, ICMCB, UPR 9048, Pessac, France, [5] CEA, LETI, Université Grenoble Alpes, Grenoble, France

Solid-state thin film batteries utilize electrode and electrolyte components which are nanometers or micrometers thick, enabling the production of novel devices with new form factors. Here, *in situ* X-ray diffraction is used to carry out the first study of a solid-state thin film lithium-ion battery containing a solid-state LiPON electrolyte and Bi negative electrode. The structure-electrochemistry relationships in the Li-Bi system are revealed and details of cell construction, data collection, and data analysis is presented to guide for research.

Keywords: solid-state battery, *in situ*, X-ray diffraction, structure-properties relationships, electrochemistry, electrode materials, thin-film

OPEN ACCESS

Edited by:
Jian Liu,
University of British Columbia Okanagan, Canada

Reviewed by:
Qian Sun,
University of Western Ontario, Canada
Biqiong Wang,
General Motors, United States

****Correspondence:***
Neeraj Sharma
neeraj.sharma@unsw.edu.au

Specialty section:
This article was submitted to Energy Storage, a section of the journal Frontiers in Energy Research

Received: *20 February 2018*
Accepted: *14 June 2018*
Published: *31 July 2018*

Citation:
Goonetilleke D, Sharma N, Kimpton J, Galipaud J, Pecquenard B and Le Cras F (2018) Insight Into the Formation of Lithium Alloys in All-Solid-State Thin Film Lithium Batteries. Front. Energy Res. 6:64. doi: 10.3389/fenrg.2018.00064

INTRODUCTION

All-solid-state microbatteries are an interesting development of conventional Li-ion batteries (LIBs), which operate in the same potential window and by similar reaction mechanisms. All-solid-state thin film lithium batteries (microbatteries) are becoming an essential component of emerging autonomous miniaturized electronic devices, allowing a maximized integration of their power source. Microbatteries are electrochemical cells in which thin films of the different cell components are stacked by various deposition techniques to form a functional electrochemical device, with individual layers having thicknesses ranging from tens of nanometers to a few micrometers. Typically, thin film battery systems consist of crystalline lithium intercalation compounds as the cathode, and metallic lithium negative electrodes (lithium thin film battery) or inorganic compounds in which the initial charge is used to form a negative electrode by lithium plating ("lithium-free thin film batteries") (Dudney and Neudecker, 1999; Bates et al., 2000). Thin films are generally prepared by vacuum deposition techniques such as sputtering or evaporation, which are already under widespread use in microelectronics fabrication (Kanehori et al., 1983; Dudney and Neudecker, 1999). The patterning of each material level, from the current collectors to the encapsulation layers, can be achieved either by shadow masking or by photolithography, allowing for customizable footprints with areas ranging from mm^2 to cm^2.

In thin film batteries, where diffusion lengths are minimized, solid-state electrolytes are favorable. Solid-state electrolytes are inherently advantageous over liquid electrolytes in terms of safety and handling thanks to their electrochemical, mechanical and thermal stability (Takada, 2013; Teng et al., 2014). Issues with capacity fade caused by the formation of a solid-electrolyte interface (SEI) are also avoided by using a solid-state electrolyte. This contributes to the cell

achieving a long calendar life, good capacity retention and stable electrochemical response (Bates et al., 2000; Fleutot et al., 2011; Cras et al., 2015). Electrochemical stability of solid-state electrolytes typically over a wider voltage window also allows for cells to operate at high voltages enabling higher energy densities to be achieved. Further, parasitic electrochemical reactions between the electrolyte and electrode are drastically reduced, if not suppressed (Bates et al., 1994).

Another useful asset of these cells is their 2D design, which can minimize large changes in the volume of the electrodes during (de-)lithiation (Zhao et al., 2015). Deposition techniques allow for a large variety of electrode materials to be used, from amorphous to crystalline, from thermodynamically stable to metastable forms, and from simple to complex multi-phase compounds. The thickness of the layers can also be finely controlled which can be useful to counterbalance low ionic/electronic conductivity. Electrode materials that can be prepared by sputtering or by pulsed laser deposition are indeed numerous and include well-known intercalation materials $LiCoO_2$ (Neudecker et al., 2000; Yoon et al., 2013), $LiMn_2O_4$ (Jones et al., 1994), $LiNi_{0.5}Mn_{1.5}O_4$ (Xia et al., 2007), $LiFePO_4$ (Bajars et al., 2011), V_2O_5 (West et al., 1992), conversion reaction materials FeS_2 (Pelé et al., 2015), CuO (Pecquenard et al., 2014), and pure or mixed Li-alloying materials (Dimov, 2009). In bulk battery systems, the use of lithium alloy negative electrodes has generally been avoided due to the significant volume changes which occur during the alloying process as a result of lithium insertion/removal (Besenhard et al., 1997). However, the high packing density of metallic lithium and lithium alloys makes it attractive to re-consider the use of lithium alloy negative electrodes for thin film batteries, where the volume change will not be nearly as significant as the bulk, and the increased specific capacity could be especially useful. A number of lithium binary alloy systems have been explored (Massalski et al., 1986), including Li-Al (Yao et al., 1971; Bang et al., 2001), Li-Si (Wen and Huggins, 1981), Li-Sn, and Li-Cd among others (Huggins, 1999). The high-packing density achieved when lithium is inserted into the metallic lattice is favorable for achieving better specific and volumetric capacities compared with lithium intercalation into carbonaceous materials (Besenhard et al., 1997).

Several systems using a lithium alloy negative electrode have been reported to date (Besenhard et al., 1997; Huggins, 1999; Bang et al., 2001; Zhang, 2011). In particular, Bi is an interesting candidate for use in thin film batteries for powering new, emerging microelectronics devices (Crosnier et al., 2001). Moreover Bi, which is a non-toxic material, has a high sputtering yield allowing the growth of several hundred nanometer thick thin films in a limited period of time. Li-Bi alloys form at relatively low potentials (0.8–0.6 V) which avoids electrochemical activity from other cell components vs. lithium (Crosnier et al., 2001; Xianming et al., 2002). Bi also offers a good theoretical specific capacity of 385 mAh g^{-1}, which is comparable to that of graphite (372 mAh g^{-1}) (Zhang, 2011), and a high volumetric capacity of 3,800 mAh cm^{-3}. The galvanostatic cycle curve of Bi vs. Li^+/Li is in agreement with the phase diagram, displaying two discharge plateaus corresponding to the formation of an LiBi phase, followed by the formation of Li_3Bi upon further Li insertion. Recently, it has also been clearly demonstrated that lithium binary alloy systems, especially Li-Si, may have a great interest in all-solid-state thin film configuration despite the large volume variation (300 % from Si to $Li_{15}Si_4$) occurring during Li insertion (Phan et al., 2012).

Several *in situ* structural studies of LIB systems have been carried out using both synchrotron X-ray diffraction (XRD) and neutron powder diffraction (NPD) (Sharma and Peterson, 2012; Hu et al., 2013; Pang et al., 2015; Sharma et al., 2015a; Goonetilleke et al., 2017). These studies allow the structural changes which take place in active materials to be related to the devices' electrochemical activity in real-time. While most *in situ* structural studies have focused on conventional LIBs using a liquid electrolyte (Sharma et al., 2015b), *in situ* structural characterization of a thin film battery utilizing a polymer electrolyte has been reported (Gustafsson et al., 1992). Solid-state batteries are ideal for diffraction studies as the absence of a liquid electrolyte and amorphous components such as separators removes large background contributions. Thus, considering their excellent electrochemical behavior, their versatility in terms of materials and their simple design, 2D all-solid-state thin film lithium microbatteries appear as promising devices to carry out *in situ* structural studies of various electrode materials. *In situ* and/or *operando* characterization of electrode materials operating in all-solid-state cells are rare. They mainly focus on chemical depth profiling by means of neutron techniques (Oudenhoven et al., 2011; Wang et al., 2017) or chemical analysis of solid-solid interfaces by means of scanning tunneling electron microscopy-electron energy loss spectroscopy (STEM-EELS, (Ma et al., 2016; Wang et al., 2016; Gong et al., 2017). To our knowledge, no *in situ* structural characterization has been carried out by X-ray diffraction on ceramic all-solid-state batteries so far.

We focused our study on the following stack: Bi | LiPON | Li, because it constitutes a model stack for *in situ* analysis, Bi being a heavy element and a crystalline material (well-adapted for X-ray analysis) and a potential candidate to replace Li as a negative electrode in all-solid-state thin film batteries. We report for the first time an *in situ* X-ray diffraction study of Bi/LiPON/Li all-solid-state cells. This preliminary study was achieved to follow the formation of lithium alloys during cycling of the cell.

EXPERIMENTAL

Cell Design

As all-solid-state thin film batteries do not contain any liquid, conductive additives or polymeric binders, their format is thus well suited for *in situ* diffraction studies (Zhou et al., 2013). Nevertheless, particular attention was devoted to the cell design considerations to ensure high quality diffraction data, including thickness of the electrode and electrolyte films, thickness and nature of substrate and encapsulation layers and surface and positioning of the cells on the substrate and the sample holder. As detailed below, the thickness of the active material is about a few hundred nanometers. A LiPON electrolyte (Bates et al., 1992) was chosen as it is an amorphous solid-state electrolyte for lithium ion batteries that

induces little-to-no scattering. This electrolyte offers high ionic conductivity and chemical stability against metallic lithium, which has led to its reported application in several solid-state LIB systems (Dudney, 2005; Jacke et al., 2010; Senevirathne et al., 2013). The thickness of substrate and encapsulation layers can contribute to a reduction in cell performance. Both were slimmed down as much as possible while keeping sufficient mechanical properties.

Four 9 × 9 mm^2 all-solid-state cells were prepared on thin glass substrate (50 µm thick, AF32 borosilicate glass, Schott Gmbh) by ICMCB and CEA in a chamber connected to a glove-box. The deposition of all levels of the stack was made through a shadow mask to localize each layer. A 200 nm Cr thin film was first deposited by sputtering to favor the adhesion of Bi thin film on the glass substrate. The Bi (250 nm) thin film was grown by radiofrequency sputtering under Ar on the Cr current collector. The Li-Bi binary diagram displays two definite compounds LiBi and Li_3Bi (Sangster and Pelton, 1991). These compounds have a melting temperature higher than the maximum temperature applied during the solder-reflow process used to connect the electronic components on the printed circuit board (about 260°C). This feature constitutes a great advantage for practical use compared to metallic Li. The LiPON solid electrolyte film, 1.4 µm thick, was then deposited by RF reactive sputtering under pure nitrogen atmosphere. To complete the active part of the microbattery, a metallic lithium film, 3 µm thick, was then deposited on the LiPON film by thermal evaporation. More thorough characterization of similarly prepared solid-state thin film microbatteries has been published in previous studies (Fleutot et al., 2011; Phan et al., 2012; Cras et al., 2015). To protect the active stack from moisture and oxygen, the whole group of 4 cells was capped by a second layer of thin glass. A polymer seal was interposed between the two glass sheets, on the rim of the group of cells to limit the X-ray absorption in this area. The glass substrate was then attached to a rigid printed circuit board and the electrical connection with the cells was achieved using silver-filled epoxy.

In Situ X-Ray Diffraction

High-intensity synchrotron radiation is a necessity to ensure that sufficient intensity can be achieved given the small interaction volume, while allowing for adequate time resolution between each collection. *In situ* X-ray diffraction data were collected in transmission geometry using the Powder Diffraction Beamline at the Australian Synchrotron (Wallwork et al., 2007), using a wavelength of 0.618952(7) Å determined using the NIST 660b LaB_6 standard reference material (Black et al., 2011). The incident beam, with a profile of 1.2 × 3 mm, was focused at the center of a single microbattery cell, see **Figure 1**. Data were collected in the range $5^\circ < 2\theta < 84^\circ$ with collection times of 4 min that were continuously recorded. The microbattery was charged potentiostatically by applying a 0.8 V potential to the cell using a Neware BTS3000 Battery Testing System. Rietveld refinements (Rietveld, 1969) using the *in situ* XRD data were carried out using GSAS-II (Toby and Von Dreele, 2013). Single peak fits were carried out using Gaussian peak shapes with a linear background in LAMP (Richard et al., 1996).

RESULTS AND DISCUSSION

Rietveld Refinement

In order to investigate how the structures of the different phases present within the cell evolve over time, sequential Rietveld refinement of structural models against the collected XRD data was undertaken. Due to the nature of the data, which contains contributions from multiple phases which may exhibit preferred orientation, and background contributions from amorphous phases, it is important to note that several constraints are applied to the data. When carrying out sequential refinement, a number of parameters are refined for only

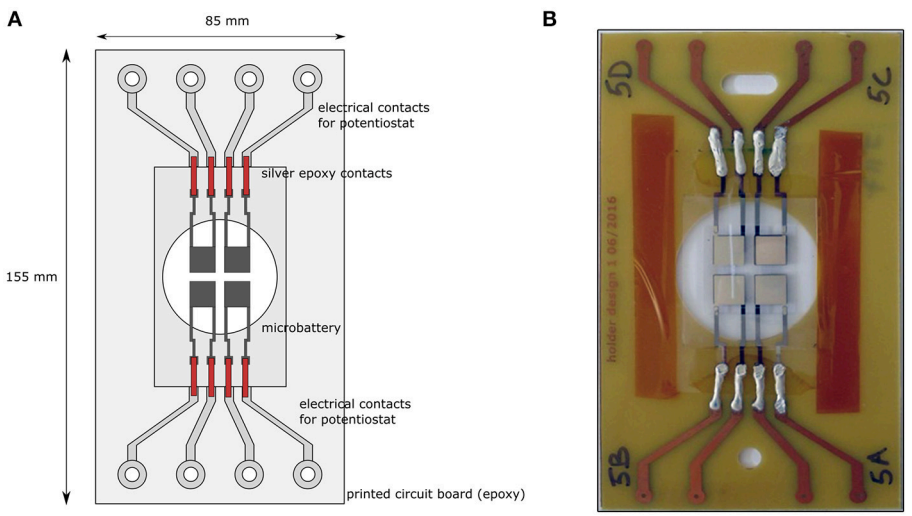

FIGURE 1 | (A) Circuit schematic and **(B)** an example of a printed circuit board with all solid-state microbatteries prepared by sputtering.

one dataset and fixed, while others are allowed to refine throughout the electrochemical process. The fixed parameters include the peak profile parameters, sample parameters, and atomic parameters of the various phases. Peak profile parameters and sample parameters, such as the overall scale factor, sample displacement and sample absorption are fixed as their

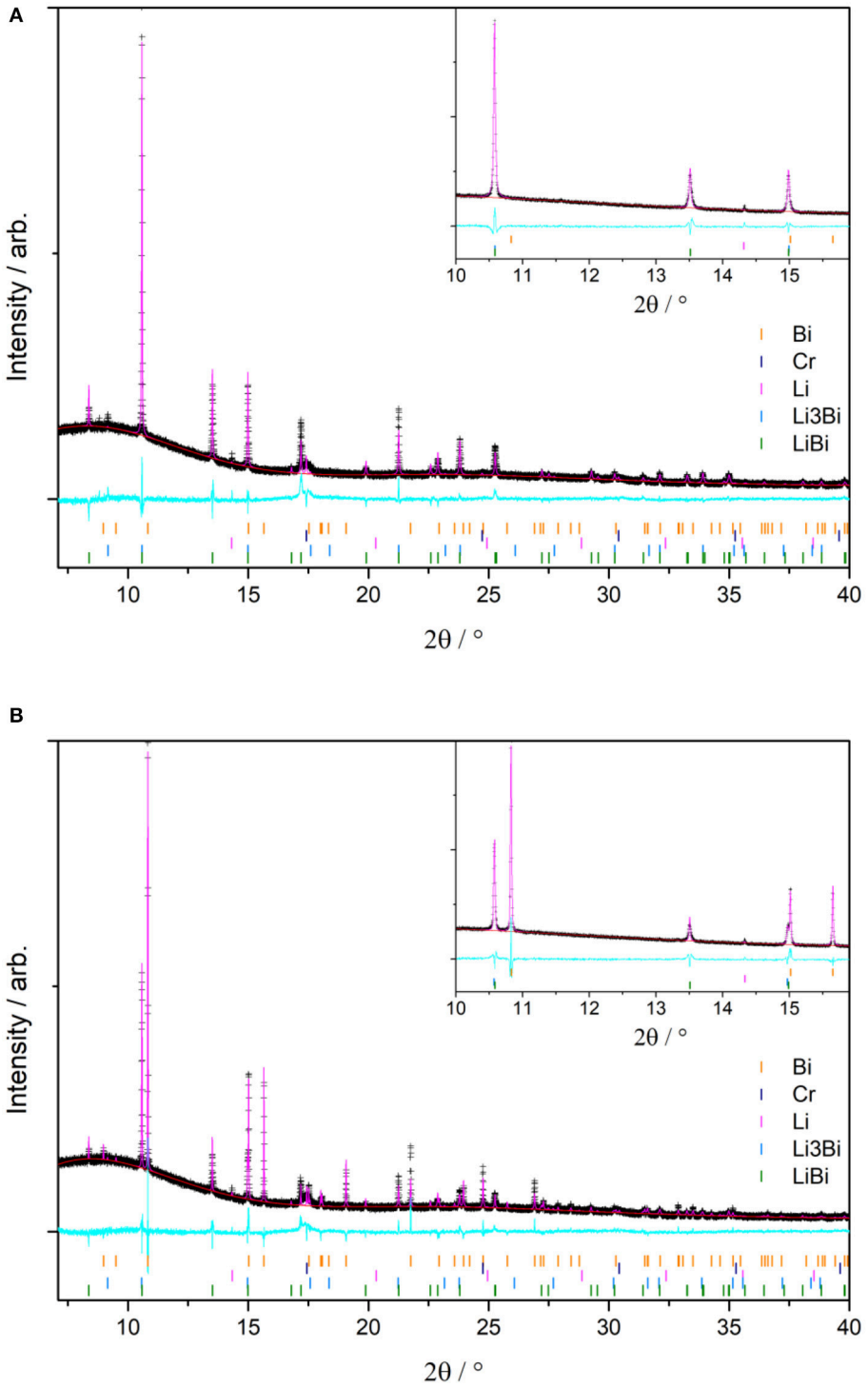

FIGURE 2 | Rietveld refinement profile of the **(A)** first dataset (discharged state) and **(B)** the last dataset (charged state). Reflections from all three major phases are present in the last dataset. Observed data are represented as crosses (+), calculated model as pink line, background function as red line, and difference as cyan line below.

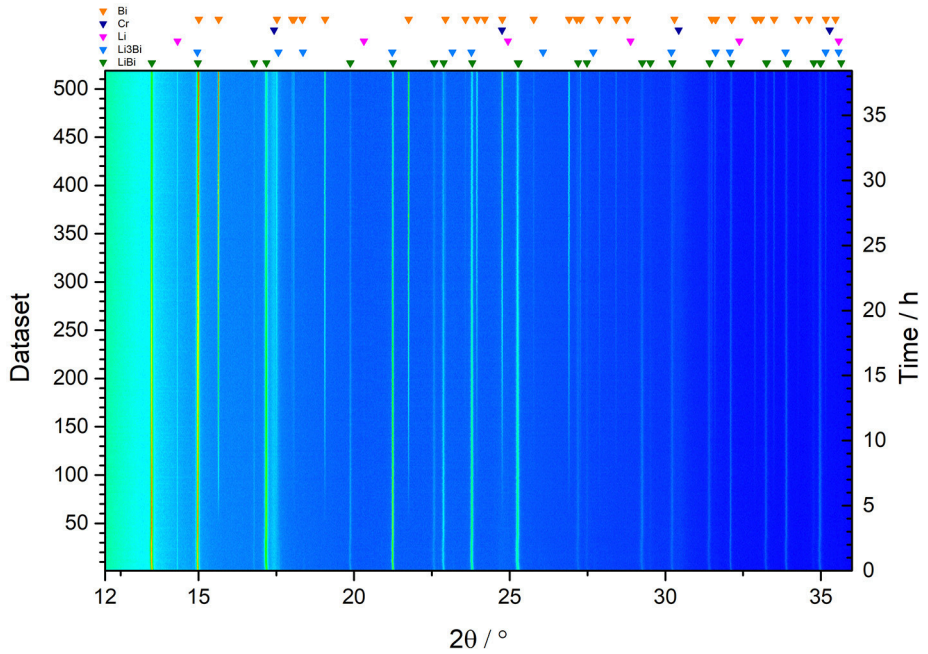

FIGURE 3 | Contour map showing evolution of the collected diffraction data during the 0.8 V potentiostatic hold.

TABLE 1 | Space groups and refined lattice parameters of phases identified in the diffraction data shown in **Figure 2B**.

Phase	Space group	a (Å)	b (Å)	c (Å)	Vol (Å^3)
Bi	*R*–3 *m*	4.54604 (18)	4.54604 (18)	11.86117 (22)	212.287 (12)
LiBi	*P* 4/ *m m m*	3.35667 (8)	3.35667 (8)	4.24097 (19)	47.784 (3)
Li_3Bi	*F m*–3 *m*	6.72065 (25)	6.72065 (25)	6.72065 (25)	303.552 (32)
Li	*I m*–3 *m*	3.50897 (117)	3.50897 (117)	3.50897 (117)	43.205 (43)
Cr	*I m*–3 *m*	2.8881 (2)	2.8881 (2)	2.8881 (2)	24.091 (5)

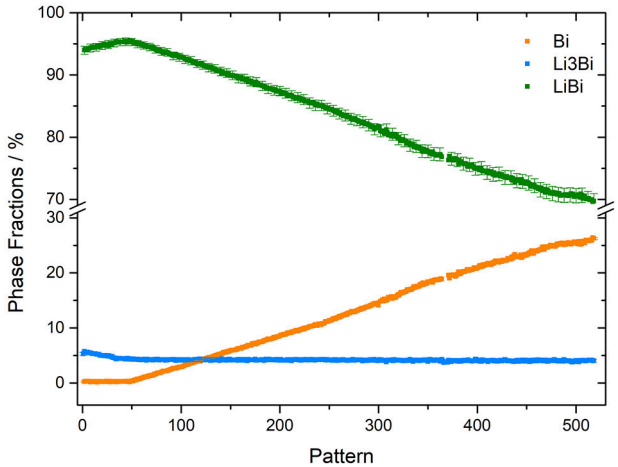

FIGURE 4 | Phase fractions as a function of pattern number as determined by Rietveld refinement.

contributions are known to remain constant throughout the experiment, e.g., the intensity and profile of the incident X-ray beam remain essentially constant, and the sample position relative to the detector remains fixed. Due to the number of phases and low sensitivity of X-rays toward Li, precise structural characterization of the phases present is not possible, and so atomic parameters such as atomic co-ordinates and atomic displacement parameters (ADPs) were fixed. Parameters allowed to refine throughout include the background (Chebyschev function, 13 terms), scale factors for each phase, and structural lattice parameters, apart from Cr and Li which are not expected to undergo expansion/contraction during cycling.

Figures 2A,B show refinements of the first and last datasets, showing the phases present in the discharged and charged state respectively. The observed data is represented by black crosses, while the calculated model is represented by the line through the data. The line below shows the difference between the observed and calculated data. Large spikes in the difference line indicate regions where the least squares refinement approach struggles to model the intensity of particular reflections, in particular the Bi reflection at $2\theta \approx 10.8^\circ$ in **Figure 2B**. The statistics for the refinements shown in **Figures 2A,B** are $wR_p = 7.70\%$ and $wR_p = 9.19\%$, respectively. The wR_p value was found to increase over time, indicating the difficulty in modeling the intensity of the Bi phase which appears as the cell was charged. In this system the discrepancy between the calculated intensity and observed intensity can be attributed primarily

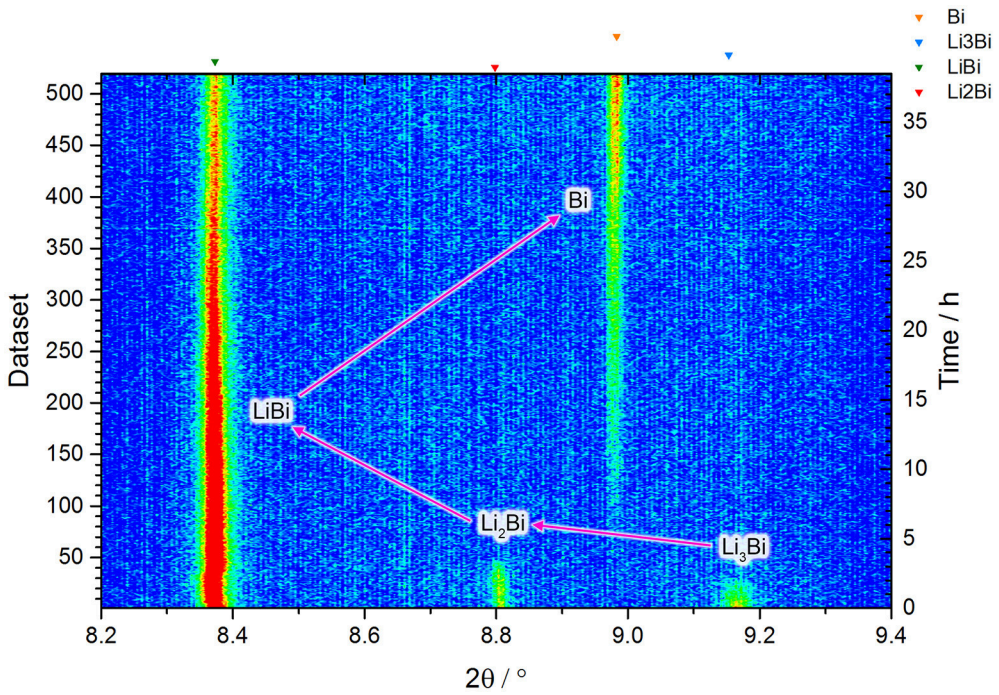

FIGURE 5 | Contour map focusing on the $8.2° < 2\theta < 9.4°$ region, highlighting the range of lithiated bismuth reflections. Arrows indicate a possible reaction pathway.

to two contributions, micro-absorption and sample texturing. Micro-absorption which can arise in systems where there is a large difference in X-ray absorption coefficients between two phases (Taylor and Matulis, 1991), e.g., between Li and Bi in this system. Due to the nature of thin film samples, in which growth of films can occur along particular crystallographic planes, sample texturing can also lead to mismatch between the intensity of calculated models and the observed data for particular reflections (Zolotoyabko, 2009). Sample texturing can be modeled using a preferred orientation model. In this analysis, the strength and direction (along a particular crystallographic plane) of the orientation effects were accounted for using the March-Dollase approach (Von Dreele, 1997). Discrepancies in reflection intensities due to sample texturing can be modeled for each phase individually. Despite "rocking" of the sample stage to improve powder averaging, refinement results suggest strong preferred orientation in the data. It is important to note such contributions which can introduce difficulty in fitting the data, however information about the structural changes taking place within the microbattery such as lattice parameters and phase composition can still be extracted with good confidence. Another consideration to make is that the significant volume expansion often observed during alloying reactions could cause the cell to be displaced relative to the incident beam and affect the cell parameters determined by Rietveld refinement. However, given the nanoscale dimensions of the cell, the magnitude of the volume change is expected to be negligible relative to what would be required to cause issues in the collection of diffraction data, and this is confirmed by the fact that no shift in the position of reflections from the electrochemically inactive cell components is observed during electrochemical cycling.

Structural Evolution

Figure 3 shows the evolution of the diffraction data over time. The alloys formed through electrochemical alloying are known to be identical to those formed metallurgically (Dey, 1971), and in the Li-Bi system. The LiBi and Li_3Bi phases may be formed at ambient temperatures (Zintl and Brauer, 1935; Sangster and Pelton, 1991). In this study, reflections corresponding to the lithiated bismuth phases LiBi, Li_3Bi were observed as well as Bi. Additional reflections can also be seen from the Li metal, and the Cr current collectors, as indicated by the markers above the contour plot. The structures and lattice parameters of the observed phases as determined by Rietveld refinement are detailed in in **Table 1**, and examples of refined fits are shown in **Figure 2**.

The cell was charged potentiostatically at 0.8 V to drive the lithium de-intercalation reactions in the electrode materials. We can observe a series of two-phase reactions occurring. **Figure 4** shows how phase fractions of the three major phases change over time. As the battery is charged, Li is removed from the Bi-Li negative electrode material, resulting in a gradual decrease in the amount of the Li-rich Li_3Bi phase, which reacts to form LiBi, and hence a rapid increase in the amount of LiBi is observed near the beginning of the experiment. As the cell is charged further, the LiBi content begins to decrease and a concurrent increase in the amount of Bi present is observed. A possible reaction pathway is described in **Figure 5**, where we observe reversal of the lithium alloying with Bi via the following

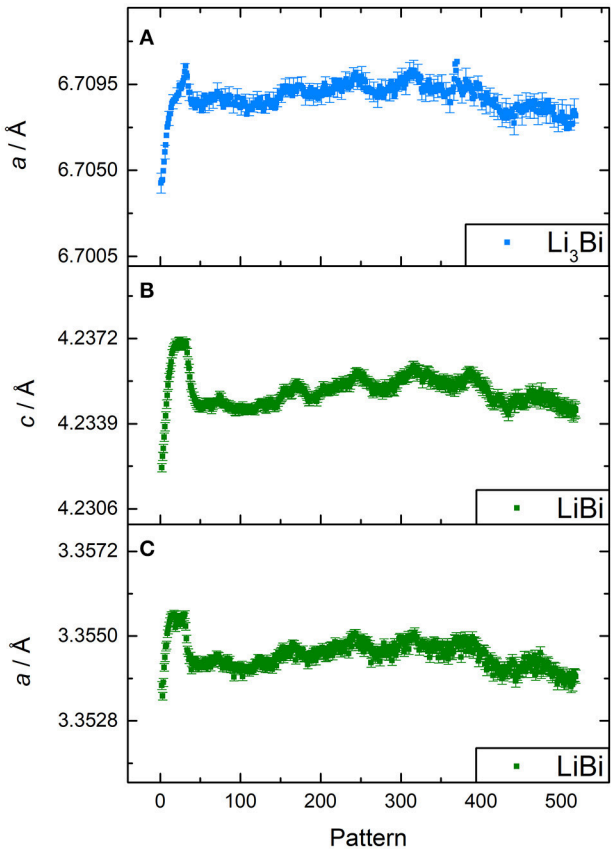

FIGURE 6 | Lattice parameters of the **(A)** Li_3Bi and **(B,C)** LiBi phases as a function of time.

reactions,

$$Li_3Bi \rightarrow LiBi + 2Li^+ + 2e^- \quad (1)$$

$$LiBi \rightarrow Bi + Li^+ + e^- \quad (2)$$

Figure S1 shows an example of a typical charge-discharge curve of a Bi/LiPON/Li all-solid-state cell. The potential profile exhibits two plateaus corresponding to two reactions described above. A similar reaction pathway has been demonstrated for sodium-ion batteries (NIBs) utilizing Bi as a negative electrode material (Gao et al., 2018). The reversibility of the alloying process has been demonstrated previously (Xianming et al., 2002), however it could not be demonstrated during the available beamtime, given the low current densities which thin film batteries were exposed to in this case.

An additional reflection is also observed at $2\theta \approx 8.8^\circ$, see **Figure 5**, resulting from the (1 1 0) plane in Li_2Bi. This Li_2Bi phase forms in small quantities during conversion from Li_3Bi at the discharged state to LiBi during charge. The Li_2Bi structure was recently reported in an amendment to the Li-Bi phase diagram (Pavlyuk et al., 2015). Li_2Bi adopts a hexagonal unit with space group $P-6\ 2\ c$, and in our cell was found to have lattice parameters of $a = 8.061(5)$ Å and $c = 6.835(3)$ Å. In **Figure 5** we also observe reflections corresponding to the (1 1 1), (0 0 1) and (0 0 3) planes of Li_3Bi, LiBi, and Bi respectively.

Closer inspection of the diffraction data in **Figure 5** shows a slight shift in the position of the LiBi 001 reflection ($2\theta \approx 8.37^\circ$) at the beginning of the experiment. Beyond this point, the lattice parameters of the lithiated bismuth phases remain constant, see **Figure 6**, and reaction proceeds via a two-phase mechanism as Bi is formed. The *a* and *c* lattice parameters of LiBi, see **Figures 6B,C**, behave nearly identically as the insertion of lithium into Li_x Bi causes an isotropic expansion of the unit cell.

CONCLUSIONS

The use of *in situ* diffraction to study structural evolution in thin film devices is demonstrated. A series of phase transitions from lithiated bismuth to bismuth metal were identified as the device was charged. This preliminary study of a Bi/LiPON/Li all-solid-state cell demonstrates that these thin film devices can be used to explore the phase transformations which occur within the electrodes during cell operation. Further, the ability to resolve these phase transformations highlights that electrochemical insertion could provide a novel way to explore the phase diagrams of binary alloy systems at ambient temperatures.

AUTHOR CONTRIBUTIONS

DG performed the *in-situ* experiment, analyzed the data and wrote a significant proportion of the manuscript. NS instigated the research and performed the *in-situ* experiment. JK experimental design at the Australian Synchrotron. JG made and tested the *in-situ* cells and designs. BP instigated the research and provided research support throughout the project. FL instigated the research and developed the *in-situ* cell design.

ACKNOWLEDGMENTS

This research was undertaken on the Powder Diffraction beamline at the Australian Synchrotron, Victoria, Australia. DG acknowledges the support of the Australian Government Research Training Program Scholarship. NS would like to thank the Australian Research Council for financial support provided via grants DE160100237 and DP170 100269.

SUPPLEMENTARY MATERIAL

The Supplementary Material for this article can be found online at: https://www.frontiersin.org/articles/10.3389/fenrg.2018.00064/full#supplementary-material

REFERENCES

Bajars, G., Kucinskis, G., Smits, J., and Kleperis, J. (2011). Physical and electrochemical properties of LiFePO 4/C thin films deposited by direct current and radiofrequency magnetron sputtering. *Solid State Ionics* 188, 156–159. doi: 10.1016/j.ssi.2010.10.022

Bang, H. J., Kim, S., and Prakash, J. (2001). Electrochemical investigations of lithium-aluminum alloy anode in Li/polymer cells. *J. Power Sources* 92, 45–49. doi: 10.1016/S0378-7753(00)00522-X

Bates, J. B., Dudney, N. J., Gruzalski, G. R., Zuhr, R. A., Choudhury, A., Luck, C. F., et al. (1992). Electrical properties of amorphous lithium electrolyte thin films. *Solid State Ionics* 53, 647–654. doi: 10.1016/0167-2738(92)90442-R

Bates, J., Dudney, N., Neudecker, B., Ueda, A., and Evans, C. (2000). Thin-film lithium and lithium-ion batteries. *Solid State Ionics* 135, 33–45. doi: 10.1016/S0167-2738(00)00327-1

Bates, J., Gruzalski, G., Dudney, N., Luck, C., and Yu, X. (1994). Rechargeable thin-film lithium batteries. *Solid State Ionics* 70, 619–628. doi: 10.1016/0167-2738(94)90383-2

Besenhard, J., Yang, J., and Winter, M. (1997). Will advanced lithium-alloy anodes have a chance in lithium-ion batteries? *J. Power Sources* 68, 87–90. doi: 10.1016/S0378-7753(96)02547-5

Black, D. R., Windover, D., Henins, A., Filliben, J., and Cline, J. P. (2011). Certification of standard reference material 660B. *Powder Diffract.* 26, 155–158. doi: 10.1154/1.3591064

Cras, F. L., Pecquenard, B., Dubois, V., Phan, V.-P., and Guy-Bouyssou, D. (2015). All-solid-state lithium-ion microbatteries using silicon nanofilm anodes: high performance and memory effect. *Adv. Energy Mater.* 5:1501061. doi: 10.1002/aenm.201501061

Crosnier, O., Brousse, T., Devaux, X., Fragnaud, P., and Schleich, D. (2001). New anode systems for lithium ion cells. *J. Power Sources* 94, 169–174. doi: 10.1016/S0378-7753(00)00599-1

Dey, A. (1971). Electrochemical alloying of lithium in organic electrolytes. *J. Electrochem. Soc.* 118, 1547–1549. doi: 10.1149/1.2407783

Dimov, N. (2009). "Development of metal alloy anodes," in *Lithium-Ion Batteries,* eds Em. M. Yoshio, A. Kozawa, and R. J. Brodd (New York, NY: Springer), 241–265. doi: 10.1007/978-0-387-34445-4_11

Dudney, N. J. (2005). Solid-state thin-film rechargeable batteries. *Mater. Sci. Eng.* 116, 245–249. doi: 10.1016/j.mseb.2004.05.045

Dudney, N. J., and Neudecker, B. J. (1999). Solid state thin-film lithium battery systems. *Curr. Opin. Solid State Mater. Sci.* 4, 479–482. doi: 10.1016/S1359-0286(99)00052-2

Fleutot, B., Pecquenard, B., Le Cras, F., Delis, B., Martinez, H., Dupont, L., et al. (2011). Characterization of all-solid-state Li/LiPONB/TiOS microbatteries produced at the pilot scale. *J. Power Sour.* 196, 10289–10296. doi: 10.1016/j.jpowsour.2011.07.018

Gao, H., Ma, W., Yang, W., Wang, J., Niu, J., Luo, F., et al. (2018). Sodium storage mechanisms of bismuth in sodium ion batteries: an operando X-ray diffraction study. *J. Power Sour.* 379, 1–9. doi: 10.1016/j.jpowsour.2018.01.017

Gong, Y., Zhang, J., Jiang, L., Shi, J.-A., Zhang, Q., Yang, Z., et al. (2017). *In situ* atomic-scale observation of electrochemical delithiation induced structure evolution of LiCoO2 cathode in a working all-solid-state battery. *J. Am. Chem. Soc.* 139, 4274–4277. doi: 10.1021/jacs.6b13344

Goonetilleke, D., Pramudita, J. C., Hagan, M., Al Bahri, O. K., Pang, W. K., Peterson, V. K., et al. (2017). Correlating cycling history with structural evolution in commercial 26650 batteries using in operando neutron powder diffraction. *J. Power Sour.* 343, 446–457. doi: 10.1016/j.jpowsour.2016.12.103

Gustafsson, T., Thomas, J. O., Koksbang, R., and Farrington, G. C. (1992). The polymer battery as an environment for *In Situ* X-ray diffraction studies of solid-state electrochemical processes. *Electrochim. Acta* 37, 1639–1643. doi: 10.1016/0013-4686(92)80128-9

Hu, C.-W., Sharma, N., Chiang, C.-Y., Su, H.-C., Peterson, V. K., Hsieh, H.-W., et al. (2013). Real-time investigation of the structural evolution of electrodes in a commercial lithium-ion battery containing a V-added LiFePO4 cathode using *In-Situ* neutron powder diffraction. *J. Power Sour.* 244, 158–163. doi: 10.1016/j.jpowsour.2013.02.074

Huggins, R. A. (1999). Lithium alloy negative electrodes. *J. Power Sour.* 81–82, 13–19. doi: 10.1016/S0378-7753(99)00124-X

Jacke, S., Song, J., Cherkashinin, G., Dimesso, L., and Jaegermann, W. (2010). Investigation of the solid-state electrolyte/cathode LiPON/LiCoO2 interface by photoelectron spectroscopy. *Ionics* 16, 769–775. doi: 10.1007/s11581-010-0479-1

Jones, S. D., Akridge, J. R., and Shokoohi, F. K. (1994). Thin film rechargeable Li batteries. *Solid State Ionics* 69, 357–368. doi: 10.1016/0167-2738(94)90423-5

Kanehori, K., Matsumoto, K., Miyauchi, K., and Kudo, T. (1983). Thin film solid electrolyte and its application to secondary lithium cell. *Solid State Ionics* 9, 1445–1448. doi: 10.1016/0167-2738(83)90192-3

Ma, C., Cheng, Y., Yin, K., Luo, J., Sharafi, A., Sakamoto, J., et al. (2016). Interfacial Stability of Li metal–solid electrolyte elucidated via *in situ* electron microscopy. *Nano Lett.* 16, 7030–7036. doi: 10.1021/acs.nanolett.6b03223

Massalski, T. B., Okamoto, H., Subramanian, P., Kacprzak, L., and Scott, W. W. (1986). *Binary Alloy Phase Diagrams*. Metals Park, OH: American Society for Metals.

Neudecker, B., Dudney, N., and Bates, J. (2000). "Lithium-free" thin-film battery with *in situ* plated li anode. *J. Electrochem. Soc.* 147, 517–523. doi: 10.1149/1.1393226

Oudenhoven, J., Labohm, F., Mulder, M., Niessen, R., Mulder, F., and Notten, P. (2011). *In situ* neutron depth profiling: a powerful method to probe lithium transport in micro-batteries. *Adv. Mater.* 23, 4103–4106. doi: 10.1002/adma.201101819

Pang, W. K., Kalluri, S., Peterson, V. K., Sharma, N., Kimpton, J., Johannessen, B., et al. (2015). Interplay between electrochemistry and phase evolution of the P2-type Na x (Fe1/2Mn1/2) O2 cathode for use in sodium-ion batteries. *Chem. Mater.* 27, 3150–3158. doi: 10.1021/acs.chemmater.5b00943

Pavlyuk, V., Sozanskyi, M., Dmytriv, G., Indris, S., and Ehrenberg, H. (2015). Amendment of the Li-Bi phase diagram crystal and electronic structure of Li2Bi. *J. Phase Equilib. Diffus.* 36, 544–553. doi: 10.1007/s11669-015-0409-z

Pecquenard, B., Le Cras, F. D. R., Poinot, D., Sicardy, O., and Manaud, J.-P. (2014). Thorough characterization of sputtered CuO thin films used as conversion material electrodes for lithium batteries. *ACS Appl. Mater. Interfaces* 6, 3413–3420. doi: 10.1021/am4055386

Pelé, V., Flamary, F., Bourgeois, L., Pecquenard, B., and Le Cras, F. (2015). Perfect reversibility of the lithium insertion in FeS 2: the combined effects of all-solid-state and thin film cell configurations. *Electrochem. Commun.* 51, 81–84. doi: 10.1016/j.elecom.2014.12.009

Phan, V. P., Pecquenard, B., and Le Cras, F. (2012). High-performance all-solid-state cells fabricated with silicon electrodes. *Adv. Funct. Mater.* 22, 2580–2584. doi: 10.1002/adfm.201200104

Richard, D., Ferrand, M., and Kearley, G. (1996). Lamp, the large array manipulation program. *J. Neutron Res.* 4, 33–39. doi: 10.1080/10238169608200065

Rietveld, H. (1969). A profile refinement method for nuclear and magnetic structures. *J. Appl. Crystallogr.* 2, 65–71. doi: 10.1107/S0021889869006558

Sangster, J., and Pelton, A. (1991). The Bi-Li (Bismuth-Lithium) system. *J. Phase Equilibria* 12, 447–450. doi: 10.1007/BF02645966

Senevirathne, K., Day, C. S., Gross, M. D., Lachgar, A., and Holzwarth, N. A. W. (2013). A new crystalline LiPON electrolyte: synthesis, properties, and electronic structure. *Solid State Ionics* 233, 95–101. doi: 10.1016/j.ssi.2012.12.013

Sharma, N., Gonzalo, E., Pramudita, J. C., Han, M. H., Brand, H. E. A., Hart, J. N., et al. (2015a). The unique structural evolution of the O3-phase Na2/3Fe2/3Mn1/3O2during high rate charge/discharge: a sodium-centred perspective. *Adv. Funct. Mater.* 25, 4994–5005. doi: 10.1002/adfm.201501655

Sharma, N., Pang, W. K., Guo, Z., and Peterson, V. K. (2015b). *In situ* powder diffraction studies of electrode materials in rechargeable batteries. *ChemSusChem.* 8, 2826–2853. doi: 10.1002/cssc.201500152

Sharma, N., and Peterson, V. K. (2012). *In situ* neutron powder diffraction studies of lithium-ion batteries. *J. Solid State Electrochem.* 16, 1849–1856. doi: 10.1007/s10008-011-1567-5

Takada, K. (2013). Progress and prospective of solid-state lithium batteries. *Acta Mater.* 61, 759–770. doi: 10.1016/j.actamat.2012.10.034

Taylor, J., and Matulis, C. (1991). Absorption contrast effects in the quantitative XRD analysis of powders by full multiphase profile refinement. *J. Appl. Crystallogr.* 24, 14–17. doi: 10.1107/S002188989000841X

Teng, S., Tan, J., and Tiwari, A. (2014). Recent developments in garnet based solid state electrolytes for thin film batteries. *Curr. Opin. Solid State Mater. Sci.* 18, 29–38. doi: 10.1016/j.cossms.2013.10.002

Toby, B. H., and Von Dreele, R. B. (2013). GSAS-II: the genesis of a modern open-source all purpose crystallography software package. *J. Appl. Crystallogr.* 46, 544–549. doi: 10.1107/S0021889813003531

Von Dreele, R. (1997). Quantitative texture analysis by Rietveld refinement. *J. Appl. Crystallogr.* 30, 517–525. doi: 10.1107/S0021889897005918

Wallwork, K. S., Kennedy, B. J., and Wang, D. (2007). "The high resolution powder diffraction beamline for the Australian Synchrotron," in *AIP Conference Proceedings: AIP* (Clayton), 879–882. doi: 10.1063/1.2436201

Wang, C., Gong, Y., Dai, J., Zhang, L., Xie, H., Pastel, G., et al. (2017). *In situ* neutron depth profiling of lithium metal–garnet interfaces for solid state batteries. *J. Am. Chem. Soc.* 139, 14257–14264. doi: 10.1021/jacs.7b07904

Wang, Z., Santhanagopalan, D., Zhang, W., Wang, F., Xin, H. L., He, K., et al. (2016). *In situ* STEM-EELS observation of nanoscale interfacial phenomena in all-solid-state batteries. *Nano Lett.* 16, 3760–3767. doi: 10.1021/acs.nanolett.6b01119

Wen, C. J., and Huggins, R. A. (1981). Chemical diffusion in intermediate phases in the lithium-silicon system. *J. Solid State Chem.* 37, 271–278. doi: 10.1016/0022-4596(81)90487-4

West, K., Zachau-Christiansen, B., Skaarup, S., and Poulsen, F. (1992). Lithium insertion in sputtered vanadium oxide film. *Solid State Ionics* 57, 41–47. doi: 10.1016/0167-2738(92)90062-T

Xia, H., Meng, Y., Lu, L., and Ceder, G. (2007). Electrochemical properties of nonstoichiometric LiNi0. 5Mn1. 5O4– δ thin-film electrodes prepared by pulsed laser deposition. *J. Electrochem. Soc.*154, A737–A743. doi: 10.1149/1.2741157

Xianming, W., Nishina, T., and Uchida, I. (2002). Lithium alloy formation at bismuth thin layer electrode and its kinetics in propylene carbonate electrolyte. *J. Power Sour.* 104, 90–96. doi: 10.1016/S0378-7753(01)00876-X

Yao, N., Heredy, L., and Saunders, R. (1971). Emf measurements of electrochemically prepared lithium-aluminum alloy. *J. Electrochem. Soc.* 118, 1039–1042. doi: 10.1149/1.2408242

Yoon, Y., Park, C., Kim, J., and Shin, D. (2013). Lattice orientation control of lithium cobalt oxide cathode film for all-solid-state thin film batteries. *J. Power Sour.* 226, 186–190. doi: 10.1016/j.jpowsour.2012.10.094

Zhang, W.-J. (2011). A review of the electrochemical performance of alloy anodes for lithium-ion batteries. *J. Power Sour.* 196, 13–24. doi: 10.1016/j.jpowsour.2010.07.020

Zhao, Y., Li, X., Yan, B., Li, D., Lawes, S., and Sun, X. (2015). Significant impact of 2D graphene nanosheets on large volume change tin-based anodes in lithium-ion batteries: a review. *J. Power Sour.* 274, 869–884. doi: 10.1016/j.jpowsour.2014.10.008

Zhou, Y.-N., Xue, M.-Z., and Fu, Z.-W. (2013). Nanostructured thin film electrodes for lithium storage and all-solid-state thin-film lithium batteries. *J. Power Sour.* 234, 310–332. doi: 10.1016/j.jpowsour.2013.01.183

Zintl, E., and Brauer, G. (1935). Konstitution der lithium-wismut-legierungen: 14. mitteilung über metalle u. legierungen. *Berichte Bunsengesellschaft Physikalische Chemie* 41, 297–303.

Zolotoyabko, E. (2009). Determination of the degree of preferred orientation within the March–Dollase approach. *J. Appl. Crystallogr.* 42, 513–518. doi: 10.1107/S0021889809013727

Conflict of Interest Statement: The authors declare that the research was conducted in the absence of any commercial or financial relationships that could be construed as a potential conflict of interest.

frontiers in Energy Research

PERSPECTIVE
published: 20 November 2018
doi: 10.3389/fenrg.2018.00121

In-situ Studies of High Temperature Thermal Batteries: A Perspective

Julia L. Payne[1], Kyriakos Giagloglou[1], George M. Carins[1], Christina J. Crouch[1,2], Julia D. Percival[2], Ronald I. Smith[3], Richard K. B. Gover[2] and John T. S. Irvine[1]*

[1] School of Chemistry, Faculty of Science, University of St Andrews, St Andrews, United Kingdom, [2] AWE Aldermaston, Reading, United Kingdom, [3] ISIS Facility STFC Rutherford Appleton Laboratory, Didcot, United Kingdom

Here we present a perspective on *in-situ* studies of high temperature batteries. We focus on a primary battery technology- the thermal battery- which possesses a molten salt electrolyte. We discuss aspects of sample environment design, data collection and will briefly look at some case studies. We aim to highlight the importance of using *in-situ* techniques in studying electrochemical devices such as high temperature batteries.

Keywords: *in-situ*, neutron diffraction, thermal battery, transition metal sulfides, high temperature batteries

OPEN ACCESS

Edited by:
Neeraj Sharma, University of New South Wales, Australia

Reviewed by:
Xiangyu Zhao, Nanjing Tech University, China
Verónica Palomares, Universidad del País Vasco, Spain
Donna Claire Arnold, University of Kent, United Kingdom

****Correspondence:***
Julia L. Payne
jlp8@st-andrews.ac.uk

Specialty section:
This article was submitted to Energy Storage, a section of the journal Frontiers in Energy Research

Received: *04 May 2018*
Accepted: *25 October 2018*
Published: *20 November 2018*

Citation:
Payne JL, Giagloglou K, Carins GM, Crouch CJ, Percival JD, Smith RI, Gover RKB and Irvine JTS (2018) In-situ Studies of High Temperature Thermal Batteries: A Perspective. Front. Energy Res. 6:121. doi: 10.3389/fenrg.2018.00121

INTRODUCTION

In recent years, the study of battery technologies using *in-situ* techniques has become increasingly important (Sharma et al., 2015). This has been driven by a desire for the precise understanding of the processes occurring during battery operation, which may be used to optimize batteries or inform the future synthetic targets of new battery materials with improved performance. This has been accompanied by improvements in the design of cells which allow collection of both electrochemical data and the data of interest (Bergstrom et al., 1998; Berg and Thomas, 1999; Sharma and Peterson, 2012; Roberts et al., 2013; Biendicho et al., 2014; Sharma et al., 2015; Brant et al., 2016). Techniques such as powder X-ray diffraction (PXRD), powder neutron diffraction (PND), Nuclear Magnetic Resonance (NMR) and X-ray absorption spectroscopy (XAS) have all been used (Bergstrom et al., 1998; Berg and Thomas, 1999; Balasubramanian et al., 2001; Morcrette et al., 2003; Yoon et al., 2003; Borkiewicz et al., 2012; Herklotz et al., 2013; Roberts et al., 2013; Biendicho et al., 2014; Brant et al., 2016; Kim et al., 2016; Gu et al., 2017; Pecher et al., 2017). This has been accompanied by improvements in instrumentation at synchrotron and neutron facilities, along with a willingness to accommodate unusual sample environments and set-ups on the beamline.

With the lithium-ion battery revolutionizing the portable electronics market in recent years, it is unsurprising that the majority of these *in-situ* studies have focused on batteries which operate at room temperature. However, batteries are required for a wide range of applications and there remain several battery technologies that have not been studied using *in-situ* techniques.

One battery technology which we are currently investigating is the thermal battery. Thermal batteries are primary batteries which are used in emergency power supplies in aircraft, ejector seats, and other military applications (Guidotti and Masset, 2006). Applications which utilize thermal batteries require a constant power to be drawn over a length of time, so as a result, materials that operate *via* conversion reactions, rather than intercalation reactions are usually preferred. Typically they consist of a cathode, anode, molten salt electrolyte, separator and a pyrotechnic ignition source to heat the battery (Masset and Guidotti, 2007, 2008a,b; Guidotti and Masset, 2008). Due to the use of a molten salt electrolyte, thermal batteries must operate at a temperature above the melting point of the electrolyte, which means that they often operate at temperatures

close to 500°C. The high temperature operation, in addition to the fact that air/moisture-sensitive transition metal sulfides are the most commonly used cathodes, means that structural studies of this battery technology would be best performed using *in-situ* techniques, and would require a complex cell design. To the best of our knowledge no such studies have been reported.

Our current research interests have focused on the *in-situ* study of thermal batteries which use transition metal sulfides as the cathode material, $Li_{13}Si_4$ as the anode material, KCl-LiCl eutectic as an electrolyte and MgO as the separator. In particular the transition metal disulfides, MS_2 (where M = Fe, Co, and Ni) are the most commonly used cathode materials in thermal batteries and they offer a particularly intriguing study, as the discharge mechanisms are thought to be different depending on the transition metal present in the cathode, with only cells using FeS_2 as a cathode forming lithiated compounds upon battery discharge (Preto et al., 1983).

EXPERIMENTAL CONSIDERATIONS

Design of Sample Environment

The purpose of our experiments was to carry out combined battery discharge and powder neutron diffraction studies. A sample environment for combined conductivity and neutron diffraction studies of hydride ion conductors was designed by one of us, so this sample environment was modified to enable it to be used for *in-situ* thermal battery studies instead (Payne et al., 2017; Carins et al., in preparation). A photograph of the sample environment is shown in **Figure 1A**. This sample environment is able to maintain an inert atmosphere around the sample, which is important when looking at air/moisture sensitive species. During each experiment, Argon gas was continuously flowed through the sample environment.

The sample environment consists of a closed-end quartz tube, which has thinned walls near the sample area to allow for beam entry and exit. There is a gas inlet/outlet on the top of the tube. Wires for electrical connections run from the top of the tube to the sample holder and are sheathed in Al_2O_3.

By modifying the sample environment using vanadium plates as both current collectors and sample holder (**Figure 1B**) we were able to simplify the data analysis by reducing the number of phases that will be observed in the diffraction pattern [vanadium's very low neutron scattering length (−0.39 fm) compared to those of the atomic species making up the other phases present means that it contributes very little to the neutron diffraction pattern of the battery]. Neutron diffraction is particularly appropriate when studying lithium-containing materials in the presence of much higher Z-number atoms because unlike X-ray scattering (which depends on the number of electrons) neutrons scatter from the atomic nucleus and this results in the scattering power of lithium being comparable to the other species in the battery. Recesses in the vanadium plates hold the sample in position for optimum beam convergence on the sample. A diagram of the vanadium plate sample holder is shown in **Figure 1B**.

The design of an equivalent cell for the equivalent X-ray diffraction experiment would be non-trivial. A suitable current collector is difficult to find and existing sample environments designed to work at room temperature use beryllium windows which would oxidize at the high temperatures required for this study.

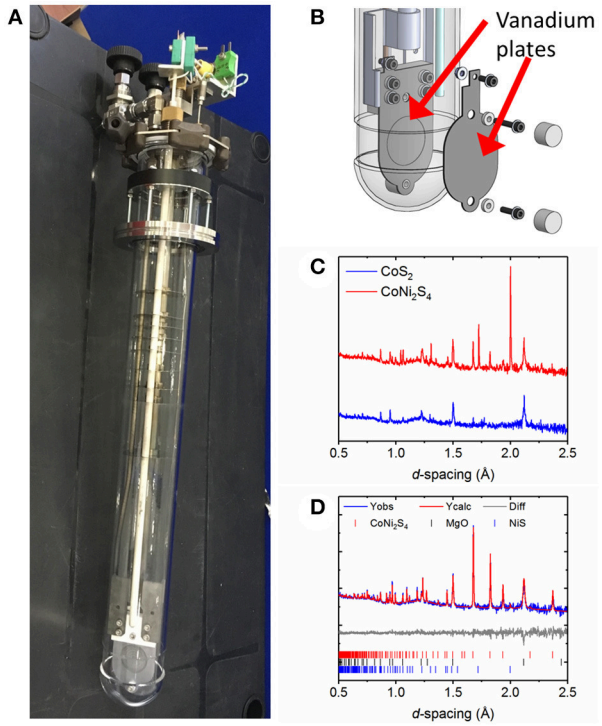

FIGURE 1 | (A) Photograph of the *in-situ* sample environment used for studies of thermal batteries which allows the flow of an inert gas during the course of the experiment to maintain an inert atmosphere. **(B)** Shows a diagram of vanadium plate current collector which doubles as a sample holder. Screws are used to help hold the sample in place. **(C)** Comparison of powder diffraction data obtained in 5 min on the Polaris diffractometer for two cells using two different cathode materials: CoS_2 and $CoNi_2S_4$ **(D)** multi-phase Rietveld fit to data collected in 5 min on the Polaris diffractometer during the discharge of a thermal battery which uses $CoNi_2S_4$ as the cathode material. Please note that differences in intensity of the $CoNi_2S_4$ data are due to the data being collected at different states of discharge. Broad features in the background of the diffraction pattern are due to the amorphous quartz outer container of the *in-situ* sample environment and molten salt eutectic.

Choice of Instrument

Our *in-situ* experiments have been carried out on the Polaris diffractometer at the ISIS facility, Rutherford Appleton Laboratory, UK. Polaris is a high flux, medium resolution diffractometer, which is particularly suited to fast data collection and unusual sample environments, making it the ideal choice for the *in-situ* experiment. The recent upgrade of Polaris enables the collection of good quality diffraction data, even with very small samples (Lindsay-Scott et al., 2014).

Data Collection Protocols

With any *in-situ* experiment, there is balance to be achieved between the electrochemistry and the structural data that will be collected. Neutron powder diffraction requires larger samples than the corresponding X-ray diffraction experiment. In our first

experiments we decided to preserve the electrochemistry as much as possible, which resulted in the use of a thinner pellet shaped cell (∼1–2 mm thickness) than would normally be required for neutron diffraction. This led to limitations in the parameters that could be extracted from multi-phase Rietveld refinement, such as meaningful thermal parameters. **Figure 1C** shows the data quality from 5 min neutron powder diffraction data collections on CoS_2 and $CoNi_2S_4$ based cells. Much better data quality could be obtained for the $CoNi_2S_4$ cell which benefitted from both being a slightly thicker sample, along with the higher neutron scattering length of nickel (10.3 fm) in comparison to cobalt (2.49 fm) and sulfur (2.85 fm). Data were analyzed by carrying out multi-phase Rietveld refinements. **Figure 1D** shows a multi-phase Rietveld fit to a 5 min data set collected during discharge of a thermal battery which used $CoNi_2S_4$ as the cathode material. This indicates that good quality data can often be obtained in times as short as a few minutes when using neutron diffraction, but it is dependent on the sample being studied.

During an *in-situ* experiment, it is important to minimize the contributions to the diffraction pattern from parts of the sample environment, and we were able to do this by adjusting the dimensions of the incident neutron beam to match the geometry of the thermal battery sample as well as utilizing neutron shielding materials (boron nitride) to cover parts of the sample environment that may scatter (and would contribute to the diffraction pattern). The reliability of a spallation neutron source can also be challenging during such *in-situ* experiments, where short interruptions to the beam due to minor accelerator faults may result in "gaps" in the data, but fortunately for our experiments carried out to date, this has not been problematic.

In terms of carrying out the battery discharge, two approaches have been used. Firstly, potentiostatic discharge has been used, where data are collected at fixed isopotentials. The isopotentials are determined by an *ex-situ* battery discharge in our home laboratory before our *in-situ* experiment, in order to ensure that diffraction data are collected at the key plateaux on the discharge profile. Longer diffraction datasets are collected at the isopotentials, and on switching between isopotentials faster data collection takes place. Alternatively, galvanostatic discharge maybe carried out, during which a large number of diffraction patterns are collected continuously over short periods of time (e.g., 5 mins each), and which subsequently may be summed to obtain higher quality datasets on plateaux in the discharge profile. We have had success with both types of measurement, but we found that it was difficult to get meaningful capacities from our *in-situ* experiments to date.

Sample Preparation

The samples for the experiments were prepared by sequentially pressing the powders for the anode, electrolyte/separator and cathode into pellets. The sequential pressing offers the opportunity to make good contacts between each layer. It is then relatively straightforward to handle the pellet and load it into the *in-situ* sample environment inside the glovebox. The eutectic of choice for the electrolyte is the KCl-LiCl eutectic (melting point = 352°C). At room temperature, peaks from the electrolyte are present in the neutron powder diffraction pattern, but on heating above the melting point of the electrolyte, the peaks disappear, which again simplifies the data analysis by reducing the number of phases observed in the neutron diffraction pattern.

CASE STUDIES: THERMAL BATTERIES USING TRANSITION METAL SULFIDES, AS CATHODES

As discussed earlier, transition metal disulfides MS_2 (where M = Fe, Co, and Ni) are some of the most commonly used cathode materials for thermal batteries, and indeed it was these materials which have formed the basis of our first *in-situ* studies on thermal batteries (Payne et al., 2017; Payne et al., in preparation). In addition, our recent synthetic and electrochemical work has looked at some other transition metal sulfides as potential cathodes for thermal batteries (Giagloglou et al., 2016, 2017; Giagloglou et al., in preparation).

Our first *in-situ* study looked at the discharge of a thermal battery which used NiS_2 (a conversion material) as the cathode, $Li_{13}Si_4$ as the anode, KCl-LiCl eutectic as the electrolyte and MgO as the separator (Payne et al., 2017). This experiment was carried out at 520°C, which to the best of our knowledge, is the highest temperature *in-situ* battery experiment carried out to date. **Figure 2** shows some of the results from this experiment, including a film plot of the diffraction data collected during battery discharge, a plot of the evolution of phase fraction and discharge profile over the course of the experiment and finally the changes in crystal structure of Ni-containing species during discharge. In our study, we were able to correlate the evolution of crystalline phases with plateaux observed in the battery discharge profile and a total of four nickel containing phases were observed in the diffraction patterns. A film plot of the diffraction data shows evolution of the crystalline phases upon discharge and is shown in **Figure 2A**. Rietveld refinement was used to extract phase fractions from the diffraction data. This allows us to correlate the phase fractions with the electrochemical data, and in particular with the plateau in the voltage discharge profile. **Figure 2B** shows the evolution of phase fraction and cell voltage during discharge. This shows that the plateau in the voltage discharge profile at ∼1.7 V was due to the NiS_2 to NiS transformation, whilst the plateau at ∼1.4–1.3 V was due to the NiS to Ni_3S_2 transformation. We did not observe Ni_7S_6, which had previously been observed in cells examined at room temperature and this led us to propose a new discharge mechanism for NiS_2 when it is used as a cathode (Payne et al., 2017). The structures of the Ni-containing phases that were identified during discharge are shown in **Figure 2C**. We should also point out that we also observed changes in cell parameter of the NiS phase, which provides evidence for a region of solid solution, and although the changes in composition of this phase could not be accurately determined it is possible that this change in cell parameter was due to either a non-stoichiometric $Ni_{1-x}S$ phase or some Li incorporation in NiS. It was particularly useful to collect synchrotron powder X-ray diffraction data on the cathode after our *in-situ* neutron diffraction data, as this enabled conclusive identification of all cell components present,

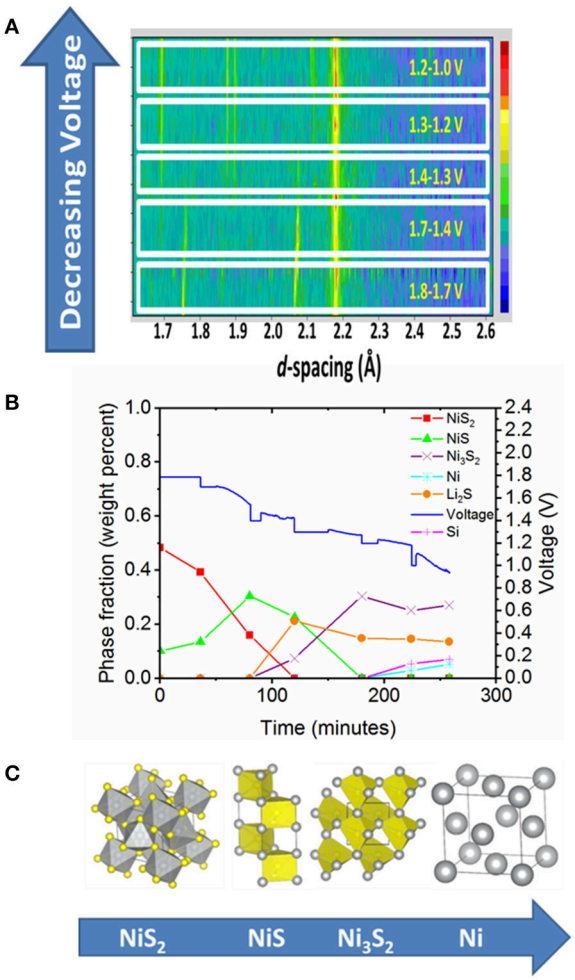

FIGURE 2 | Results from the *in-situ* thermal battery discharge using NiS_2 as the cathode (Payne et al., 2017). **(A)** Film plot of neutron diffraction data collected during battery discharge. Please note that the *y*-axis is not a linear function of time. **(B)** Evolution of phase fraction and voltage over the course of the experiment. **(C)** Crystal structures of Ni containing species observed during the course of battery discharge. **(A,B)** Copyright Wiley-VCH Verlag GmbH & Co. KGaA and are reproduced from Payne et al. (2017) with permission.

as we benefitted from the high intensity and resolution of the synchrotron source. This emphasizes the importance of using complementary techniques (where possible) to enhance the understanding of the system under study.

$Li_{13}Si_4$ is an anode commonly used in thermal batteries. However, in our *in-situ* studies to date, the combination of a large unit cell and low symmetry of the $Li_{13}Si_4$ structure, which is then pressed into a pellet, means that it is particularly difficult to study the changes in the structure of the anode material during discharge. Although the lithium silicides have been well-studied by a variety of techniques, including single crystal diffraction and NMR, much less is known about their high temperature behavior, including the high temperature crystallography (Key et al., 2009, 2011; Zeilinger and Faessler, 2013; Zeilinger et al., 2013a,b). It is also possible that $Li_{13}Si_4$ (and related phases) are largely amorphous during battery discharge, as electrochemically driven amorphisation is known to occur in lithium ion batteries upon lithium uptake when Si is used as an anode (Limthongkul et al., 2003a,b). The challenges in studying the anode material highlights that often questions still remain after an *in-situ* experiment, meaning that such experiments may often need follow up studies, in order to fully understand the system of interest.

Restricting *in-situ* studies to diffraction based techniques means that it can be easy to neglect any components which are amorphous. In the case of the thermal battery, the presence of molten salt electrolytes can simplify data analysis, due to the reduction in the number of crystalline phases observed in the diffraction pattern at device operating temperature. However, there may be occasions when we are interested in the amount of amorphous material in the battery. The use of a crystalline ceramic separator in thermal batteries is particularly useful as it can be used as an internal standard to quantify the amorphous content the battery. The importance of gaining an understanding of non-crystalline phases has recently been highlighted in a study of the *in-situ* synthesis of the $Li_7La_3Zr_2O_{12}$ Li-ion conductor. This quantified the fraction of molten/amorphous phases present in this system and found that the presence of a carbonate melt assists the synthesis of $Li_7La_3Zr_2O_{12}$ (Rao et al., 2015).

OTHER HIGH-TEMPERATURE BATTERY TECHNOLOGIES: SODIUM METAL HALIDE BATTERIES

We should point out that thermal batteries are not the only high temperature battery technology. Sodium-metal halide batteries, which are also often referred to as "ZEBRA" (Zero-Emission Battery Research Activities) cells are another high temperature battery technology which have been studied using *in-situ* techniques (Zinth et al., 2015, 2016). These cells typically operate at around 300°C and have also been studied by *in-situ* neutron diffraction (Zinth et al., 2015). Spatially resolved neutron diffraction data were collected at different points within the cathode of such a cell, enabling reaction fronts to be monitored as they move through the battery (Zinth et al., 2015). *In-situ* neutron tomography and radiography have been used to probe the changes in morphology of the cell components during battery cycling (Zinth et al., 2016). The phase evolution in sodium metal halide batteries and the presence of intermediates have also been studied using *in-situ* energy dispersive X-ray diffraction and this has allowed both spatial and kinetic information to be obtained on the battery charge/discharge process (Russenbeek et al., 2011).

CONCLUSIONS

Although most *in-situ* studies of batteries have focused on batteries which operate at room temperature, other battery technologies, such as the thermal battery and the sodium metal halide battery, operate at higher temperatures and require *in-situ* studies to be carried out at elevated temperature, in order to gain a better understanding of the processes taking place in them. Our recent *in-situ* work has successfully probed and

shed light on the processes occurring in thermal batteries during discharge at their high operating temperatures of around 500°C. To the best of our knowledge we believe that these are the highest temperature *in-situ* battery studies carried out to date. We should also point out that studies using complementary techniques such as synchrotron PXRD post battery testing offer advantages such as high resolution and intensity, which can help to unambiguously identify products formed during battery discharge. Although improvements can be envisioned and there are still many questions to be answered, this work paves the way for future high temperature *in-situ* studies of batteries.

AUTHOR CONTRIBUTIONS

JLP co-wrote the article, carried out experiments, and analyzed data. KG prepared samples and carried out experiments. GC developed the sample environment and carried out experiments. CC carried out experiments. JDP and RS carried out experiments and co-wrote manuscript. RG and JI co-wrote manuscript and oversaw research.

FUNDING

We thank AWE and EPSRC (EP/P007821/1) for supporting this programme of research.

ACKNOWLEDGMENTS

We thank the STFC for provision of neutron diffraction beam-time and Diamond Light Source for the provision of X-ray diffraction beam-time.

REFERENCES

Balasubramanian, M., Sun, X., Yang, X. Q., and McBreen, J. (2001). *In situ* X-ray diffraction and X-ray absorption studies of high-rate lithium-ion batteries. *Power Sources J.* 92, 1–8. doi: 10.1016/s0378-7753(00)00493-6

Berg, H., and Thomas, J. O. (1999). Neutron diffraction study of electrochemically delithiated $LiMn_2O_4$ spinel. *Solid State Ionics*, 126, 227–234.doi: 10.1016/s0167-2738(99)00235-0

Bergstrom, O., Andersson, A. M., Edstrom, K., and Gustafsson, T. (1998). A neutron diffraction cell for studying lithium-insertion processes in electrode materials. *J. Appl. Crystallogr.* 31, 823–825. doi: 10.1107/s00218898980 0538x

Biendicho, J. J., Roberts, M., Offer, C., Noreus, D., Widenkvist, E., Smith, R. I., et al. (2014). New *in-situ* neutron diffraction cell for electrode materials. *Power Sources J.* 248, 900–904. doi: 10.1016/j.jpowsour.2013.09.141

Borkiewicz, O. J., Shyam, B., Wiaderek, K. M., Kurtz, C., Chupas, P. J., and Chapman, K. W. (2012). The AMPIX electrochemical cell: a versatile apparatus for *in situ* X-ray scattering and spectroscopic measurements. *J. Appl. Crystallogr.* 45, 1261–1269. doi: 10.1107/s0021889812042720

Brant, W. R., Roberts, M., Gustafsson, T., Biendicho, J. J., Hull, S., Ehrenberg, H., et al. (2016). A large format in operando wound cell for analysing the structural dynamics of lithium insertion materials. *Power Sources J.* 336, 279–285. doi: 10.1016/j.jpowsour.2016.10.071

Giagloglou, K., Payne, J. L., Crouch, C., Gover, R. K. B., Connor, P. A., and Irvine, J. T. S. (2016). Zirconium trisulfide as a promising cathode material for Li primary thermal batteries. *J. Electrochem. Soc.* 163, A3126–A3130. doi: 10.1149/2.1351614jes

Giagloglou, K., Payne, J. L., Crouch, C., Gover, R. K. B., Connor, P. A., and Irvine, J. T. S. (2017). Synthesis and electrochemical study of $CoNi_2S_4$ as a novel cathode material in a primary Li thermal battery. *J. Electrochem. Soc.* 164, A2159–A2163. doi: 10.1149/2.1171709jes

Gu, Q. F., Kimpton, J. A., Brand, H. E. A., Wang, Z. Y., and Chou, S. L. (2017). Solving key challenges in battery research using *in situ* synchrotron and neutron techniques. *Adv. Energy Mater.* 7:1602831. doi: 10.1002/aenm.201602898

Guidotti, R. A., and Masset, P. (2006). Thermally activated ("thermal") battery technology - Part I: An overview. *Power Sources J.* 161, 1443–1449. doi: 10.1016/j.jpowsour.2006.06.013

Guidotti, R. A., and Masset, P. J. (2008). Thermally activated ("thermal") battery technology - Part IV. Anode materials. *Power Sources J.* 183, 388–398. doi: 10.1016/j.jpowsour.2008.04.090

Herklotz, M., Scheiba, F., Hinterstein, M., Nikolowski, K., Knapp, M., Dippel, A. C., et al. (2013). Advances in *in situ* powder diffraction of battery materials: a case study of the new beamline P02.1 at DESY, Hamburg. *J. Appl. Crystallogr.* 46, 1117–1127. doi: 10.1107/s0021889813013551

Key, B., Bhattacharyya, R., Morcrette, M., Seznéc, V., Tarascon, J. M., and Grey, C. P. (2009). Real-time NMR investigations of structural changes in silicon electrodes for lithium-ion batteries. *J. Am. Chem. Soc.* 131, 9239–9249. doi: 10.1021/ja8086278

Key, B., Morcrette, M., Tarascon, J. M., and Grey, C. P. (2011). Pair Distribution function analysis and solid state NMR studies of silicon electrodes for lithium ion batteries: understanding the (De)lithiation mechanisms. *J. Am. Chem. Soc.* 133, 503–512. doi: 10.1021/ja108085d

Kim, T., Song, B. H., Lunt, A. J. G., Cibin, G., Dent, A. J., Lu, L., et al. (2016). Operando X-ray absorption spectroscopy study of atomic phase reversibility with wavelet transform in the lithium-rich manganese based oxide cathode. *Chem. Mater.* 28, 4191–4203. doi: 10.1021/acs.chemmater.6b00522

Limthongkul, P., Jang, Y. I., Dudney, N. J., and Chiang, Y. M. (2003a). Electrochemically-driven solid-state amorphization in lithium-metal anodes. *Power Sources J.* 119, 604–609. doi: 10.1016/s0378-7753(03)00303-3

Limthongkul, P., Jang, Y. I., Dudney, N. J., and Chiang, Y. M. (2003b). Electrochemically-driven solid-state amorphization in lithium-silicon alloys and implications for lithium storage. *Acta Mater.* 51, 1103–1113. doi: 10.1016/s1359-6454(02)00514-1

Lindsay-Scott, A., Dobson, D., Nestola, F., Alvaro, M., Casati, N., Liebske, C., et al. (2014). Time-of-flight neutron powder diffraction with milligram samples: the crystal structures of $NaCoF_3$ and $NaNiF_3$ post-perovskites. *J. Appl. Crystallogr.* 47, 1939–1947. doi: 10.1107/s1600576714021803

Masset, P., and Guidotti, R. A. (2007). Thermal activated (thermal) battery technology - Part II. Molten salt electrolytes. *Power Sources J.* 164, 397–414. doi: 10.1016/j.jpowsour.2006.10.080

Masset, P. J., and Guidotti, R. A. (2008a). Thermal activated ("thermal") battery technology - Part IIIa: FeS_2 cathode material. *Power Sources J.* 177, 595–609. doi: 10.1016/j.jpowsour.2007.11.017

Masset, P. J., and Guidotti, R. A. (2008b). Thermal activated ("thermal") battery technology. Part IIIb. Sulfur and oxide-based cathode materials. *Power Sources J.* 178, 456–466. doi: 10.1016/j.jpowsour.2007.11.073

Morcrette, M., Leriche, J. B., Patoux, S., Wurm, C., and Masquelier, C. (2003). *In situ* X-ray diffraction during lithium extraction from rhombohedral and monoclinic Li3V2(PO4)3. *ECS Solid State Lett.* 6, A80–A84. doi: 10.1149/1.1563871

Payne, J. L., Percival, J. D., Giagloglou, K., Crouch, C. J., Carins, G. M., Smith, R. I., et al. (2017). *In-situ* thermal battery discharge using NiS_2 as a cathode material. *Chemelectrochem.* 4, 1916–1923. doi: 10.1002/celc.201700095

Pecher, O., Carretero-Gonzalez, J., Griffith, K. J., and Grey, C. P. (2017). Materials' methods: NMR in battery research. *Chem. Mater.* 29, 213–242. doi: 10.1021/acs.chemmater.6b03183

Preto, S. K., Tomczuk, Z., Vonwinbush, S., and Roche, M. F. (1983). Reactions of FeS_2, CoS_2, and NiS_2 electrodes in molten LiCl-KCl electrolytes. *J. Electrochem. Soc.* 130, 264–273. doi: 10.1149/1.2119692

Rao, R. P., Gu, W. Y., Sharma, N., Peterson, V. K., Avdeev, M., and Adams, S. (2015). *In situ* neutron diffraction monitoring of $Li_7La_3Zr_2O_{12}$ formation: toward a rational synthesis of garnet solid

electrolytes. *Chem. Mater.* 27, 2903–2910. doi: 10.1021/acs.chemmater.5b00149

Roberts, M., Biendicho, J. J., Hull, S., Beran, P., Gustafsson, T., Svensson, G., et al. (2013). Design of a new lithium ion battery test cell for *in-situ* neutron diffraction measurements. *Power Sources J.* 226, 249–255. doi: 10.1016/j.jpowsour.2012.10.085

Russenbeek, J., Gao, Y., Zhong, Z., Croft, M., Jisrawi, N., Ignatov, A., et al. (2011). *In situ* X-ray diffraction of prototype sodium metal halide cells Time and space electrochemical profiling. *Power Sources J.* 196, 2332–2339. doi: 10.1016/j.jpowsour.2010.10.023

Sharma, N., Pang, W. K., Guo, Z. P., and Peterson, V. K. (2015). *In situ* powder diffraction studies of electrode materials in rechargeable batteries. *Chemsuschem*, 8, 2826–2853. doi: 10.1002/cssc.201500152

Sharma, N., and Peterson, V. K. (2012). *In situ* neutron powder diffraction studies of lithium-ion batteries. *J. Solid State Electrochem.* 16, 1849–1856. doi: 10.1007/s10008-011-1567-5

Yoon, W. S., Grey, C. P., Balasubramanian, M., Yang, X. Q., and McBreen, J. (2003). *In situ* X-ray absorption spectroscopic study on $LiNi_{0.5}Mn_{0.5}O_2$ cathode material during electrochemical cycling. *Chem. Mater.* 15, 3161–3169. doi: 10.1021/cm030220m

Zeilinger, M., Benson, D., Haussermann, U., and Fassler, T. F. (2013a). Single crystal growth and thermodynamic stability of $Li_{17}Si_4$. *Chem. Mater.* 25, 1960–1967. doi: 10.1021/cm400612k

Zeilinger, M., and Fässler, T. F. (2013). Revision of the $Li_{13}Si_4$ structure. *Acta Cryst. E.* 69, i81–i82. doi: 10.1107/S1600536813029759

Zeilinger, M., Kurylyshyn, I. M., Haussermann, U., and Fassler, T. F. (2013b). Revision of the Li-Si phase diagram: discovery and single-crystal X-ray structure determination of the high-temperature phase $Li_{4.11}Si$. *Chem. Mater.* 25, 4623–4632. doi: 10.1021/cm4029885

Zinth, V., Schulz, M., Seidlmayer, S., Zanon, N., Gilles, R., and Hofmann, M. (2016). Neutron tomography and radiography on a sodium metal halide cell under operating conditions. *J. Electrochem. Soc.* 163, A838–A845. doi: 10.1149/2.0181606jes

Zinth, V., Seidlmayer, S., Zanon, N., Crugnola, G., Schulz, M., Gilles, R., et al. (2015). *In situ* spatially resolved neutron diffraction of a sodium metal halide battery. *J. Electrochem. Soc.* 162, A384–A391. doi: 10.1149/2.0421503jes

Conflict of Interest Statement: The authors declare that the research was conducted in the absence of any commercial or financial relationships that could be construed as a potential conflict of interest.

frontiers in Energy Research

BRIEF RESEARCH REPORT
published: 12 July 2018
doi: 10.3389/fenrg.2018.00069

New Opportunities for Air Cathode Batteries; *in-Situ* Neutron Diffraction Measurements

Jordi Jacas Biendicho[1]*, *Dag Noréus*[2], *Colin Offer*[3], *Gunnar Svensson*[2], *Ronald I. Smith*[3] *and Stephen Hull*[3]

[1] *Catalonia Institute for Energy Research, Sant Adrià de Besòs, Spain,* [2] *Department of Material and Environmental Chemistry, Stockholm University, Stockholm, Sweden,* [3] *ISIS Neutron and Muon Source, STFC Rutherford Appleton Laboratory, Didcot, United Kingdom*

Batteries with air electrodes are gaining interest as Energy Storage Systems (ESSs) for Electrical Vehicles (EVs) because of their high specific energy density. The electrochemical performance of these batteries is limited by the metallic electrode, which suffers structural transformations and corrosion during cycling that reduces the cycle life of the battery. In this context, relevant information on the discharge products may be obtained by *in-situ* neutron diffraction, a suitable technique to study electrodes that contain light elements or near neighbor elements in the periodic table. Case studies of MH-air and Fe-air batteries are highlighted.

Keywords: metal-air battery, metal hybrid air battery, *in-situ* neutron diffraction, rechargeable batteries, fuel cells

OPEN ACCESS

Edited by:
Verónica Palomares, University of the Basque Country (UPV/EHU), Spain

Reviewed by:
Branimir Nikola Grgur, University of Belgrade, Serbia
Wei Kong Pang, University of Wollongong, Australia

***Correspondence:**
Jordi Jacas Biendicho
jjacas@irec.cat

Specialty section:
This article was submitted to Energy Storage, a section of the journal Frontiers in Energy Research

Received: *19 March 2018*
Accepted: *25 June 2018*
Published: *12 July 2018*

Citation:
Jacas Biendicho J, Noréus D, Offer C, Svensson G, Smith RI and Hull S (2018) New Opportunities for Air Cathode Batteries; in-Situ Neutron Diffraction Measurements. Front. Energy Res. 6:69. doi: 10.3389/fenrg.2018.00069

INTRODUCTION

Air cathode-based batteries are promising energy storage systems for Electrical Vehicles (EVs) because they are lighter and, theoretically, may store higher electrochemical capacity than Li-ion batteries. This, in turn, maximizes the specific energy density ($kWkg^{-1}$) of the battery and may lead to a substantial increase of the range capability of EVs beyond the present limit of ~300 Km (Science and Technology, 2017). Tesla has recently obtained patent(s) on this technology (Herman et al., 2017), with the aim of developing new chemistries and optimizing the existing ones which, unfortunately, are not yet competitive enough to replace current technology, especially in terms of cycle life.

An air cathode battery is a hybrid system that falls into two technologies; fuel cells and rechargeable batteries. The positive electrode or cathode is a light electrode that requires a continuous source of fuel or gaseous reactant to release the stored energy, as in Solid Oxide Fuel Cells (SOFCs) (Singhal, 2000). The anode is a metallic electrode which usually contains additives to improve its electrochemical performance and it is immersed in the electrolyte, typically an aqueous one. This hybrid configuration overcomes some of the problems associated with fuel cells and rechargeable batteries, when considered individually. For instance, air cathode batteries do not rely on H_2 gas, so safety issues and costs associated with hydrogen storage using highly-pressurized cylinders are not a limitation in Metal-air batteries. Or the electrochemical capacity of a rechargeable Nickel-Metal Hydride battery (NiMH) may be significantly increased by the use of an air-electrode instead of $Ni(OH)_2$ (Dong et al., 2010), hence a MH-air battery.

Half-cell reactions in an aqueous air cathode battery are presented below. For the positive air electrode, oxygen or air is supplied during discharge and the oxygen reduction reaction takes place giving 2 hydroxide molecules. It is difficult to develop air-electrodes able to withstand

the electrochemical evolution and reduction of oxygen (OER and ORR) at high current rates (Jörissen, 2006). For our work investigating phase formation and transformations during charge/discharge using *in-situ* powder diffraction methods, Ni mesh may be used at the anode. The use of nickel mesh is motivated by its relatively simple diffraction pattern, which minimizes the number of Bragg reflections contaminating the neutron diffraction patterns collected *in-situ*. Concerning half-cell reactions at the metallic electrode, two reactions are presented which generally describe the chemistry at this electrode, which is the limiting one in terms of battery electrochemical capacity. In the case where the metallic electrode is a hydrogen-absorbing metal or metal-hydride as in MH-air batteries, reaction 2, protons diffuse to the particle surface and recombine with OH- at the interface with the electrolyte during discharge, forming H_2O and releasing electrons (Young and Nei, 2013; Yartys et al., 2016). Or, alternatively, the metallic electrode oxidizes forming hydroxides and/or oxide compounds, depending on the depth-of-discharge, reaction 3. In this category, Al-air, Mg-air, Zn-air or Fe-air batteries are included (Rahman Md et al., 2013).

Air electrode: $2OH^- \leftrightarrow {}^1/_2O_2 + H_2O + 2e^-$ reaction 1

MH -electrode: $2M + 2H_2O + 2e^- \leftrightarrow 2MH + 2OH^-$ reaction 2

Metallic electrode $2M(OH)_x + 2e^- \leftrightarrow 2M + 2OH^-$ reaction 3

The cycle life of an air cathode battery is limited by the reactions taking place at the metallic electrode. In MH-air batteries, the stored electrochemical capacity is high ($\sim$300 $mAhg^{-1}$ for AB_5-type alloys) and may be increased if superlattice A_2B_7-type alloys are used, which also show lower self-discharge (Yartys et al., 2016). However, these materials corrode in alkaline solutions, forming insulating phases such as $La(OH)_2$ at the particle/electrolyte interface, which reduce the diffusivity of protons to the bulk and, as the electrochemical reaction proceeds, capacity rapidly decreases. Corrosion also affects Metal-air batteries. In Li-Air batteries (Aurbach et al., 2016), the chemical interaction between Li metal and the electrolyte is critical to avoid formation of irreversible phases, and aprotic electrolytes have shown better performance than aqueous ones. Critically, the latter one needs passivation of the metallic lithium in order to operate safely. The highly irreversible formation of discharge products at the metallic electrodes in Al-air, Zn-air, Fe-air and Mg-air batteries affect their performance and, in addition, H_2 gas evolution occurs at the discharge potentials, which reduces the efficiency of the batteries (Rahman Md et al., 2013). In the case of Fe-air, addition of K_2SnO_3 to the aqueous electrolyte improves the electrochemical performance of the battery (Chamoun et al., 2017).

Powder diffraction experiments are a fundamental method of determining phase composition and structures in multi-component systems such as batteries, of which the metallic compounds contained inside, are one example. However, corrosion products in Li and Na-based batteries may be difficult to characterize using X-rays due to the low atomic number elements contained in them. In a similar way there is very little contrast between elements adjacent to each other in the periodic table, e.g., transition metals, when X-ray radiation is used, so limiting the structural information that can be obtained from Rietveld refinement of the crystal structure(s). With neutron diffraction, however, the scattering power of nuclei can vary dramatically between elements of similar atomic number, and also between isotopes of the same element. Furthermore, neutrons are highly penetrating compared to X-rays, meaning that information is gained from the bulk of a sample rather than near-surface regions. Consequently *in-situ* neutron diffraction is the ideal technique to obtain accurate structural information on the phases commonly found in air cathode batteries in real time as they are charged and discharged in the neutron beam. However, air cathode electrodes have additional requirements compared to rechargeable batteries which need to be implemented into cell design e.g. O_2 or H_2 evolution.

In this manuscript, the use of *in-situ* neutron diffraction to characterize Metal-air batteries is highlighted in two case studies, MH-air and Fe-air, using a customized electrochemical cell for air cathode.

METHODS

In-situ neutron diffraction data were collected at the Polaris diffractometer (Hull et al., 1992) at ISIS, and diffraction data were analyzed by the Rietveld method using GSAS least-squares refinement software (Larson and Von Dreele, 1990). Neutron diffraction data were collected using the backscattering detector ($135^\circ \leq 2\theta \leq 168^\circ$, $d_{max} = 2.7$ Å). Further information of cell design and components may be found in (Biendicho et al., 2014, 2015; Chamoun et al., 2017).

RESULTS AND DISCUSSION

The electrochemical cell originally constructed to conduct *in-situ* studies in a NiMH battery (Biendicho et al., 2014, 2015), may be easily adapted to other energy storage systems due to its modular and flexible configuration. As presented in previous publications, the cell is based in a planar design stacking the components on top of each other, as in coin cells used in a laboratory to characterize electrode materials *ex-situ*. However, the dimensions of the *in-situ* cell are significantly larger compared to standard coin cells to maximize the amount of electrode material exposed to the neutron beam; the outer cell diameter of the cell is 84 mm and usually accommodates rectangular-shaped electrodes of 1–2 g. **Figures 1A,B** show an expanded view of the *in-situ* cell and a sketch of the cell components and their position with respect to the incident neutron beam, respectively. Further details of the cell components and materials used to collect neutron diffraction patterns with an increased peak-to-background ratio may be found in previous publications (Roberts et al., 2013; Biendicho et al., 2014, 2015).

As discussed above, the positive electrode in a metal-air battery requires a constant source of fuel to release the stored energy. It is necessary, therefore, to take into account this requirement at the cell design stage, especially if long-term stability studies are considered. A special separator module was designed and is presented in **Figure 1C**. The upper part of the

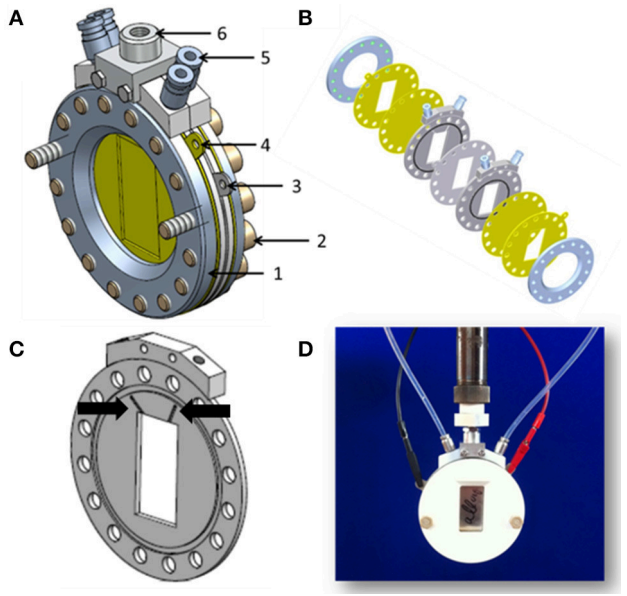

FIGURE 1 | (A) Expanded view of the *in-situ* cell; 1 and 2 correspond to the alloy clamp rings and PEEK screws used to seal the cell after assembly, 3 and 4 are the two windows which hold the thin Ni metal sheets used as positive and negative electrodes, 5 are inlet/outlet connections for the tubing to pump in gas fuel or electrolyte and 6 is the threaded block used to mount the cell on the diffractometer; **(B)** sketch of the cell components and their position with respect to the incident neutron beam; **(C)** close-up detail of the separator module; the two apertures that connect the inner compartment of the battery with the cell exterior (indicated by the black arrows); **(D)** assembled cell with tubing connections prior *in-situ* experiment.

separator module has two apertures, indicated by black arrows, which connect the inner compartment of the battery to the cell exterior, allowing either gas fuel or electrolyte to be pumped in and out of the cell during *in-situ* diffraction measurements. These apertures are also used to avoid cell over-pressure during discharge at the positive electrode (H_2 evolution). **Figure 1D** shows the assembled *in-situ* cell with inlet and outlet connections, which was constructed prior to one of the experiments conducted at the ISIS neutron spallation source. Considering the positive electrode, a nickel mesh is preferred since it is the same material as current collector. Other catalytic materials could be used as electrodes but they would either add extra Bragg peaks to the neutron diffraction patterns or increase the background, potentially masking reflections from the negative electrode.

Two examples are presented in the following paragraphs i.e., MH-air and Fe-air, to show the quality of diffraction patterns obtained by the customized electrochemical cell, and the type of structural information that may be extracted by *in-situ* measurements, respectively.

Figure 2A shows neutron diffraction patterns of the cell assembled with an AB_5-type alloy as anode as a function of discharge state using a current of ∼30 mA. Because the incoherent neutron scattering from hydrogen atoms would produce a large background signal, deuterated 6 M KOD electrolyte was used instead during battery construction. The most intense sharp diffraction peaks correspond to nickel from the thin current collectors and Ni mesh used as counter electrode, and the small background contribution is related to a Polypropylene membrane. The cell was loaded with 1.8 gr of alloy with composition $MmNi_{3.6}Al_{0.4}Mn_{0.3}Co_{0.7}$ where Mm denotes Misch metals. Additional information of cell assembly, cycling conditions and components may be found in Biendicho et al. (2014, 2015).

As discharge proceeds, the intensity of the reflections corresponding to the β-phase with lattice parameters a ∼5.26 Å and c ∼4.17 Å decrease and other reflections appear that can be indexed using a smaller unit cell corresponding to the α-phase, with a ∼5.00 Å and c ∼4.04 Å. Because of the good signal-to-noise ratio of the *in-situ* neutron diffraction patterns, it is also possible to observe differences in diffraction line widths between the charged phase and the discharged one. Bragg Peaks of β-phase are broader than the ones corresponding to the α-phase, demonstrating a substantial disorder of the deuterium atoms in the crystal structure of the charged material. For this alloy composition, an intermediate an intermediate phase (γ-phase) has been detected, in addition to the β- and α- phases, during charge and its appearance has been related to an improved stability of the electrode to corrosion and, in turn, to a better cycle life (Latroche et al., 1999).

Figure 2B shows phase fraction (weight %) as a function of cell potential for a Fe-air battery. Blue, red and black markers correspond to Fe, Fe_3O_4 and a new intermediate hydride phase that was identified during *in-situ* measurements. The electrolyte composition was deuterated 6 KOD and 0.1 M K_2SO_3 which was used as additive to reduce H2 evolution and no membrane was used to separate the Fe and Ni mesh electrodes. Instead, physical separation with a 5 mm distance between the electrodes was provided. The total weight of the Fe electrode was 1.25 g. Additional information of cell assembly, cycling conditions and components may be found in Chamoun et al. (2017).

Structural refinements of the new phase observed in the Fe electrode showed a good agreement between observed and calculated data (see Chamoun et al., 2017). The new metastable phase was refined using a tetragonal unit cell and with composition being a solid solution of Fe, Sn, Bi, and C. its weight fraction was then monitored *in-situ*, as for the other phases. *In-situ* structural information, which may also involve lattice or atomic displacement parameters, are interesting because they give in-deep understanding of the redox chemistry in the electrode, otherwise inaccessible by *ex-situ* techniques.

CONCLUSIONS

In-situ neutron diffraction is, therefore, a technique that contributes to a better understanding of charge/discharge mechanism in the metallic alloys presently used in many battery systems. Such knowledge is vital in allowing the development of new materials and compositions having improved capacity retention, fewer irreversible side-reaction and better efficiency.

The updated electrochemical cell presented in this paper provides the requirements to characterize the structure of

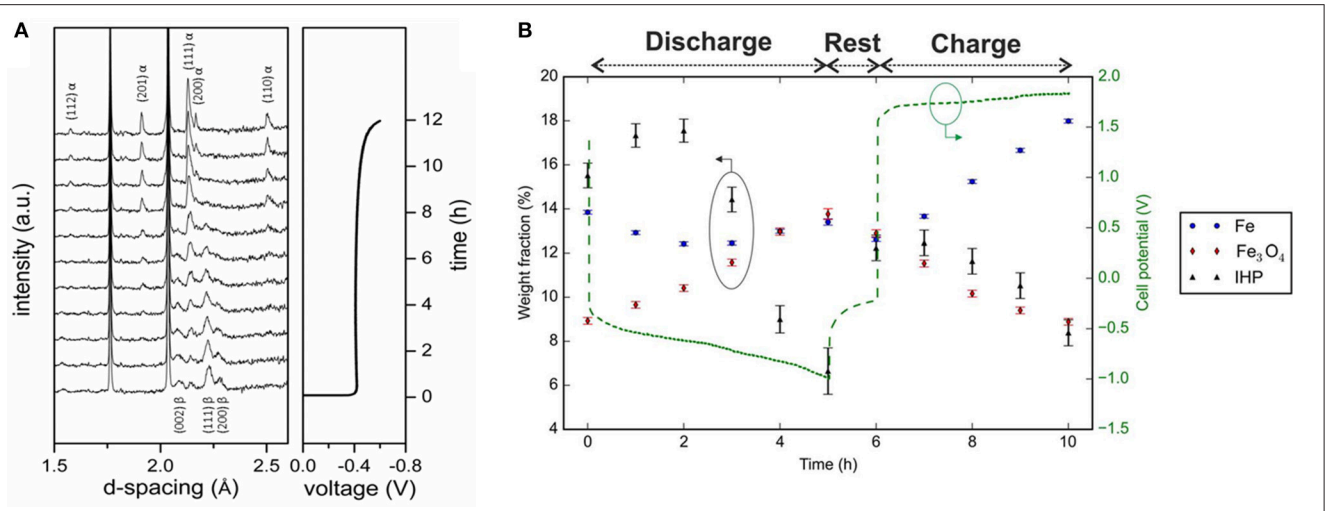

FIGURE 2 | (A) Neutron diffraction patterns from the cell collected *in-situ* using an MH electrode (AB_5-type alloy) and Ni mesh as negative and positive electrodes, respectively. The cell potential vs O_2/H_2 measured during the *in-situ* experiment is also presented, **(B)** Plot showing weight fraction and the cell potential vs. O_2/H_2 as a function of time using a Fe electrode and Ni mesh as anode and cathode, respectively.

metallic electrodes in an air cathode battery *in-situ*. The specially designed separator module, the choice of Ni mesh as cathode and the use of deuterated aqueous electrolyte are key components to obtain neutron diffraction patterns with good signal-to-noise ratio, which may be used to extract relevant structural information such as phase stability or phase fraction as highlighted for an MH-air and a Fe-air battery, respectively.

AUTHOR CONTRIBUTIONS

Cell design and construction were conducted at ISIS and Stockholm university. For this task, JJ, SH, GS, and CO contributed equally. Material preparation and *ex-situ* battery testing were conducted at Stockholm University by JJ and DN. *In-situ* experiments presented in the paper were obtained at ISIS neutron and Muon source by JJ, SH, and RS.

REFERENCES

Aurbach, D., McCloskey, B. D., Nazar, L. F., and Bruce, P. G. (2016). Advances in understanding mechanism underpinning lithium-air batteries. *Nat. Energy* 1:16128. doi: 10.1038/NENERGY.2016.128

Biendicho, J. J., Roberts, M., Noréus, D., Lagerqvist, U., Smith, R. I., Svensson, G., et al. (2015). *In situ* investigation of commercial $Ni(OH)_2$ and $LaNi_5$-baesed electrodes by neutron powder diffraction. *J. Mater. Res.* 30, 407–215. doi: 10.1557/jmr.2014.317

Biendicho, J. J., Roberts, M., Offer, C., Noréus, D., Widenkvist, E., Smith, R. I., et al. (2014). New *in-situ* neutron diffraction cell for electrode materials. *J. Power Sour.* 248, 900–904. doi: 10.1016/j.jpowsour.2013.09.141

Chamoun, M., Skarman, B., Vidarsson, H., Smith, R. I., Hull, S., Lelis, M., et al. (2017). Stannate increases hydrogen evolution overpotential on rechargeable alkaline iron electrodes. *J. Electrochem. Soc.* 164, *A*1251–A1257. doi: 10.1149/2.1401706jes

Dong, H., Kiros, Y., and Noréus, D. (2010). An air-metal hydride battery using MmNi3.6Mn0.4Al0.3Co0.7 in the anode and a perovskite in the cathode. *Int. J. Hydrogen Energy* 35, 4336–4341.doi: 10.1016/j.ijhydene.2010.02.007

Herman, W. A., Straubel, J. B., and Beck, D. G. (2017). *Charge Rate Modulation of Metal-Air Cells as a Function of Ambient Oxygen Concentration*. Patent no: US 9559532 B2

Hull, S., Smith, R. I., David, W. I. F., Hannon, A. C., Mayers, J., Cywinski, R., et al. (1992). The polaris powder diffractometer at ISIS. *Physica B* 180–181, 1000–1002. doi: 10.1016/0921-4526(92)90533-X

Jörissen, L. (2006). Bifunctional oxygen/air electrodes. *J. Power Sour.* 155, 23–32. doi: 10.1016/j.jpowsour.2005.07.038

Larson, A. C., and Von Dreele, R. B. (1990). *Report LA-UR-86-748*. Los Alamos, NM: Los Alamos National Laboratory, NM87545.

Latroche, M., Percheron-Guégan, A., and Chabre, Y. (1999). Influence of cobalt in MmNi4.3-xMn0.3Al0.4Cox alloy (x=0.36 and 0.69) on its electrochemical behavior studied by *in situ* neutron diffraction. *J. Alloys Compd.* 293–295, 637–642.

Rahman Md, A., Wang, X., and Wen, C. (2013). High energy density metal-air batteries: a review. *J. Electrochem. Soc.* 160, A1759–A1771. doi: 10.1149/2.062310jes

Roberts, M., Biendicho, J. J., Hull, S., Beran, P., Gustafsson, T., Svensson, G., et al., (2013). Design of a new lithium ion battery test cell for *in-situ* neutron diffraction measuraments. *J. Power Sour.* 226, 249–255. doi: 10.1016/j.jpowsour.2012.10.085

Science and Technology (2017) (September 2017). Electric vehicles powered by fuel-cells get a second look. *The Economist*, p. 25.

Singhal, S. C. (2000). Advances in solid oxide fuel cell technology. *Solid State Ionics* 135, 305–313. doi: 10.1016/S0167-2738(00)00452-5

Yartys, V., Noréus, D., and Latroche, M. (2016). Metal hydrides as negative electrode materials for Ni-MH batteries. *Appl. Phys. A* 122, 43. doi: 10.1007/s00339-015-9538-9.

Young, K.-H., and Nei, J. (2013). The current status of hydrogen storage alloy development for electrochemical applications. *Materials (Basel).* 6, 4574–4608. doi: 10.3390/ma6104574

Conflict of Interest Statement: The authors declare that the research was conducted in the absence of any commercial or financial relationships that could be construed as a potential conflict of interest.

Advantages of publishing in Frontiers

OPEN ACCESS
Articles are free to read for greatest visibility and readership

FAST PUBLICATION
Around 90 days from submission to decision

HIGH QUALITY PEER-REVIEW
Rigorous, collaborative, and constructive peer-review

TRANSPARENT PEER-REVIEW
Editors and reviewers acknowledged by name on published articles

Frontiers
Avenue du Tribunal-Fédéral 34
1005 Lausanne | Switzerland

Visit us: www.frontiersin.org
Contact us: info@frontiersin.org | +41 21 510 17 00

REPRODUCIBILITY OF RESEARCH
Support open data and methods to enhance research reproducibility

DIGITAL PUBLISHING
Articles designed for optimal readership across devices

FOLLOW US
@frontiersin

IMPACT METRICS
Advanced article metrics track visibility across digital media

EXTENSIVE PROMOTION
Marketing and promotion of impactful research

LOOP RESEARCH NETWORK
Our network increases your article's readership